Universidade do Minho
Escola de Engenharia

Alexandre Coumiotis Moreira Peixoto

High-aspect-ratio tridimensional electrode arrays for neural applications

Junho de 2015

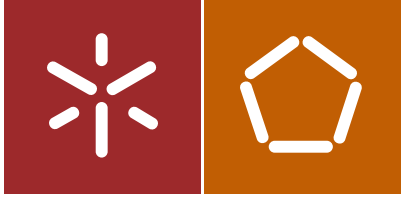

Universidade do Minho
Escola de Engenharia

Alexandre Coumiotis Moreira Peixoto

High-aspect-ratio tridimensional electrode arrays for neural applications

Tese de Doutoramento
Programa Doutoral em Engenharia Biomédica

Trabalho efectuado sob a orientação do
Professor Doutor José Higino Correia

Junho de 2015

Statement of integrity

I hereby declare having conducted my thesis with integrity. I confirm that I have not used plagiarism or any form of falsification of results during the thesis elaboration.

I further declare that I have fully acknowledged the Code of Ethical Conduct of the University of Minho.

University of Minho, _____

Full name: _____

Signature: _____

…Arts, crafts and sciences uplift the world of being, and are conducive to its exaltation. Knowledge is as wings to man's life, and a ladder for his ascent. Its acquisition is incumbent upon everyone. The knowledge of such sciences, however, should be acquired as can profit the peoples of the earth, and not those which begin with words and end with words…

Bahá'u'lláh

*To my wonderful **parents** and my lovely **wife***

ACKNOWLEDGMENTS

I would like to express my sincere gratitude to the University of Minho and all its governing bodies for being a host institution with high-quality environment for research.

A special thank you, to my supervisor Professor José Higino Correia for believing and giving me an opportunity of a lifetime to work in this wonderful area of micro and nanofabrication and at the same time introduce me to the research world.

My uttermost appreciation to Alexandre Ferreira for being above all a good friend with an upbeat spirit, for the innumerable insights and support throughout the PhD, especially during the most challenging and hopeless moments.

Sincere thanks to Nuno Mendes for introducing me to the world of neuroscience, for encouraging me to work in micro and nanotechnology, and also for helpful insights about neural electrodes.

A special thank you note to my research colleague Beatriz Gonçalves, for being a wonderful friend and valuable researcher, for all the help in designing and developing the various prototypes, experiments and tests throughout this work.

Many thanks to João Ribeiro, Manuel Silva, Rui Sousa, Luís Jacinto, Pedro Libânio, Professor Senentxu Méndez, Professor Luís Rocha, Professor Luís Gonçalves, Marino Maciel, Carlos Torres, Joel Almeida, Ângela Macedo for helping with the development and execution of some experiments that enabled the success of this work. A gratitude note to Professor João Paulo Carmo for the interesting discussions about scientific subjects and publishing skills.

To my lab mates Miguel Gomes, Catarina Costa, Rui Rocha and lately Eliana Vieira a kind thank you note for the wonderful companionship moments and contribution to the joy and efficiency of our lab.

To my dearly beloved wife, Jaleh Zandieh and my amazing parents Aspasia Coumiotis and José Peixoto, and my syster Andrea Peixoto a heartfelt thank you for the limitless love, encouragement and support. A special thanks to my uncle Afonso Rocha for inspiring me since childhood for the love of science.

Lastly, I would like to thank the support provided by Portuguese Foundation for Science and Technology (SFRH/BD/89509/2012).

ABSTRACT

Neural electrodes are a valuable tool that allows neuroscientists to monitor the neural activity of the brain with great spatial and temporal resolution. Micro and nanotechnology has allowed the development of high-density neural electrode arrays.

In the present work, two different materials were used to perform neural arrays, namely silicon and aluminum. The main objective was the ability to reach areas of the brain between 2 mm and 4 mm deep due to its importance in small animal models such as the rat. In such animals, important brain structures such as the hippocampus are situated in this range of depth. Another key objective was the fabrication of probes with high-aspect-ratio in order to minimize tissue displacement and consequent adverse reactions caused by implantation.

Four different prototypes each using a specific fabrication approach, were performed and described in detail. Two of these prototypes were performed with aluminum while the other two were performed with silicon. Standard microfabrication processes such as dicing, wet-etching, physical vapor deposition, and non-standard processes such as thermomigration, aluminum anodizing, polymer casting, and sanding were used. The combination of these standard and non-standard processes allowed a simpler and cheaper fabrication approach when compared with commercially available arrays.

The first aluminum prototype was composed by 100 micropillars with a gold electrode at each tip. The aluminum micropillars were encapsulated by aluminum oxide and were 3 mm long with an aspect-ratio of 12:1. The second version was composed by 25 micropillars encapsulated with medical grade epoxy each with a platinum electrode at the tip. Each micropillar was 3 mm long with an aspect-ratio of 19:1. The first silicon prototype was composed by 100 silicon micropillars, each 3 mm long with an aspect-ratio of 5:1. The second version was composed by 36 silicon micropillars encapsulated with medical grade epoxy, each with a platinum electrode at the tip. Each micropillar was 4 mm long with an aspect-ratio of 22:1. A slanted version of the second prototype was also fabricated, allowing progressively increasing penetration depths.

Mechanical characterization was performed by implantation in agar gel and porcine cadaver brain while electrical characterization was performed by electrochemical impedance tests as well as cyclic voltammetry.

Overall, aluminum showed to be a suitable alternative to silicon in terms of structural material. Also, a dicing based approach proved to be a cost-effective method able to perform high-aspect-ratio neural arrays.

RESUMO

Os elétrodos neuronais são uma ferramenta que proporciona aos neurocientistas a capacidade de monitorizar a atividade neuronal do cérebro com uma grande resolução temporal e espacial. As micro e nanotecnologias proporcionaram o desenvolvimento de matrizes de elétrodos neuronais com alta densidade.

No presente trabalho dois materiais foram usados para fabricar matrizes de elétrodos neuronais, nomeadamente o silício e o alumínio. O objetivo principal foi a capacidade de chegar a zonas do cérebro entre os 2 mm e 4 mm de profundidade devido a sua importância em modelos animais de pequeno porte como o rato. Nestes animais, estruturas cerebrais importantes como o hipocampo estão situadas nesta gama de profundidades. Outro objetivo chave foi o fabrico de elétrodos com alta razão de aspeto, de forma a minimizar a compressão de tecido neuronal e consequentes reações adversas causadas pela implantação.

Quatro protótipos, cada um utilizando um tipo de fabrico específico foram desenvolvidos e descritos em detalhe. Dois desses protótipos foram fabricados com alumínio, enquanto os outros dois foram feitos em silício. Foram usados processos de microfabrico *standard* como corte com disco, corrosão química, deposição de filmes finos, e também processos não standard como termomigração, anodização do alumínio, molde de polímeros e lixamento. A combinação de processos standard e não standard permitiram uma abordagem de fabrico mais simples e barata quando comparada com a abordagem utilizada em elétrodos comercialmente disponíveis.

O primeiro protótipo de alumínio foi composto por 100 micropilares com um elétrodo de ouro na ponta. Os micropilares de alumínio foram encapsulados com óxido de alumínio e tinham 3 mm de comprimento resultando numa razão de aspeto de 12:1. A segunda versão foi composta por 25 micropilares encapsulados com epóxi biocompatível, cada com um elétrodo de platina na ponta. Cada micropillar tinha 3 mm de comprimento com uma razão de aspeto de 5:1. O primeiro protótipo de silício foi composto por 100 micropilares de silício, cada com 3 mm de comprimento e com razão de aspeto de 5:1. A segunda versão foi composta por 36 micropilares de silício encapsulados com epóxi biocompatível e cada com um elétrodo de platina na ponta. Cada micropillar tinha 4 mm de comprimento resultando numa razão de aspeto de 22:1. Uma versão inclinada do segundo protótipo também foi fabricada, permitindo profundidades de penetração progressivas.

A caracterização mecânica foi feita através de implantações em gelatina de agar e em cérebro de porco, enquanto a caracterização elétrica foi feita através de testes de impedância eletroquímica assim como testes de voltametria cíclica.

No geral, o alumínio demonstrou ser uma alternativa viável ao silício em termos de material estrutural. A abordagem baseada no corte com disco provou ser um método económico capaz de realizar matrizes de elétrodos neuronais de grande razão de aspeto.

TABLE OF CONTENTS

LIST OF FIGURES

LIST OF TABLES

LIST OF SYMBOLS

Symbol	Description	Unit
I	Area moment of inertia	m^4
P	Buckling load	N
R_{ct}	Charge transfer resistance	Ω
V	Electric potential	Volt
e^-	Electron	---
L	Length of the pillar	m
Z_{CPA}	Phase angle impedance	Z
R_s	Solution resistance	Ω
s	Unit of time	Second
E	Young's Modulus	Pa

LIST OF ABBREVIATIONS

Abbreviation	Description
AC	Alternate Current
Al_2O_3	Aluminum Oxide
BCI	Brain Computer Interface
CNS	Central Nervous System
CSC	Charge Storage Capacity
R_{ct}	Charge transfer resistance
CVD	Chemical Vapor Deposition
CE	Counter electrode
CV	Cyclic Voltammetry
EIS	Electrochemical Impedance Spectroscopy
E-Beam	Electron Beam
EDS	Energy-Dispersive x-ray Spectroscopy
Au	Gold
MEMS	Micro Electro Mechanical Devices
PNS	Peripheral Nervous System
Z_{CPA}	Phase angle impedance
PBS	Phosphate Buffered Saline
PVD	Physical Vapor Deposition
Pt	Platinum
KOH	Potassium Hydroxide
RIE	Reactive Ion Etching
RE	Reference Electrode
rpm	Rotations Per Minute
SEM	Scanning Electron Microscope
Si	Silicon
R_s	Solution resistance
sccm	Standard Cubic Centimeters per Minute
H_2SO_4	Sulfuric Acid

TE	Test Electrode
USEA	Utah Slanted Electrode Array

Chapter 1

Introduction

Luigi Galvani's pioneer work opened an era of discoveries in bioelectricity. Technological advancements such as the metallic electrodes served as an invaluable tool in the discovery and understanding of the nervous system functions. The electrodes not only enabled many discoveries in electrophysiology but also became a medical tool for treating some neurological disorders. Deep brain stimulation has become an accepted treatment for Parkinson's disease and essential tremor, with over 100,000 patients having received these implants worldwide [1]. Another widespread neuro-engineering technology is the cochlear implant, so far allowing the recovery of hearing of more than 320,000 patients worldwide [2]. Encouraged by these achievements, unprecedented resources are being provided to study the brain through big research projects such as: the BRAIN initiative proposed by the Obama administration [3], the Human Brain Project by the European Commission [4], and Revolutionizing Neuroprosthetics by the Defense Advanced Research Projects Agency (DARPA) [5]. The development of new neural probes supported by a deep understanding of the nervous system will allow further advancements in the brain's undiscovered physiology in health and illness, and also a reliable and long lasting electronic interface with it.

1.1 The nervous system

The nervous system is responsible for coordinating voluntary and involuntary actions and also for the transmission of signals between different parts of the body. It consists of two main parts, the central nervous system (CNS) and the peripheral nervous system (PNS).

The CNS is composed by the brain and the spinal cord [6]. The spinal cord is responsible for receiving and processing sensory information from the skin, joints, muscles of the limbs and trunk, and also responsible for the control of the movements of these body parts. The brain is responsible for receiving sensory information from the skin and muscles of the head as well as providing the motor control for the muscles of the head. It regulates levels of arousal and awareness, processes information from the hearing, balance, and taste. It controls the digestion, breathing, heart rate, force, learning of motor skills, coordination of visual and auditory reflexes, regulates autonomic, endocrine and visceral functions, memory storage, reasoning, among others [7].

The brain regions responsible for our cognitive abilities are primarily in the cerebral cortex and also in the hippocampus and amygdala. The cerebral cortex is the outermost layered structure of the brain and is responsible for functions such as planning future actions, control of movement, vision processing and hearing (Figure 1.1). The hippocampus and the amygdala are situated below the cortex and play an important role in learning, memory and emotions [7].

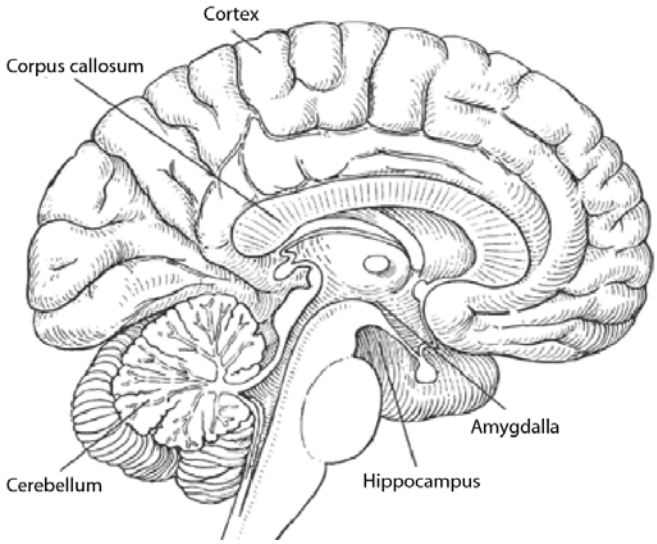

Figure 1.1: Illustration of a sagittal slice of a human brain. Some important structures are labeled (adapted from [8]).

The PNS is composed of spinal nerves, cranial nerves, autonomic nerves and supporting cells. These nerves usually contain different combinations of axons, motor neurons and sensory neurons [9]. The main function of the PNS is to connect the central nervous system (CNS) to the limbs and organs, essentially serving as a communication pathway between the brain and the extremities.

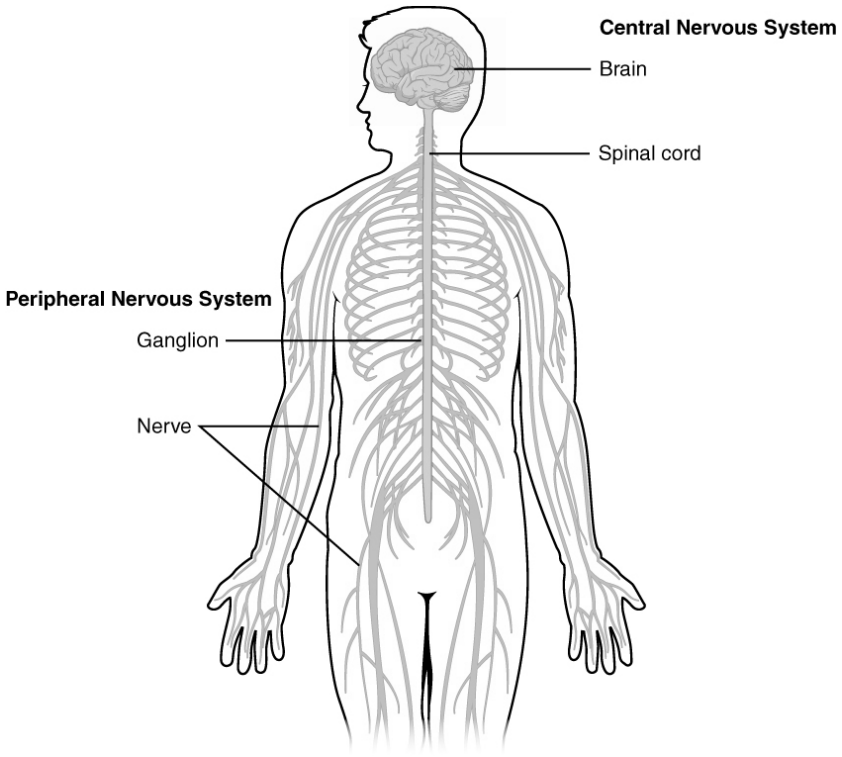

Figure 1.2: Illustration of the CNS and the PNS, note that the CNS is composed by the brain and the spinal cord (reprinted from [10]).

1.1.1 Signal Conduction in the Brain

The entire nervous system is composed of neurons, which are characterized by their ability to receive, conduct and transmit signals in the form of electrical impulses (action potentials). A neuron has a cell body with its nucleus and organelles that support its functions and processes. Dendrites are the numerous short structures that carry an action potential toward the neuron's cell body, and an axon is a long structure that carries the action potential away from the cell body. One neuron communicates with other neurons and also other cells through an electrochemical structure called the synapse. These structures can be classified in two major groups: chemical and electrical synapses. In the chemical synapses communication is performed between an axon and a dendrite with the aid of neurotransmitters, while in electrical synapses the electrical signal is directly transmitted between dendrites through structures called gap junction

channels. Axons are typically sheathed with concentric layers of a lipid-rich material called myelin, which acts as an electrical insulator between the nerve and the surrounding environment. The myelinated sheath is periodically interrupted by segments lacking myelin, called the nodes of Ranvier, which allows the saltatory conduction. Due to this type of conduction, myelinated axons transmit impulses much faster than non-myelinated axons. The CNS regions that contain myelinated axons are termed white matter because myelinated nerves appear white in color, whereas the portions of the CNS composed mostly of nerve cell bodies appear gray and are therefore called gray matter [6].

1.1.2 The action potential

The action potential is a short-lasting event in which the electrical membrane potential of a cell rapidly rises and falls, following a consistent trajectory (Figure 1.3a). The membrane potential is the difference in voltage between the inside and the outside of a neuron caused by the different concentration of ions. These action potentials are also known as “spikes” and reflect the electrical activity of a single neuron.

Action potentials are generated mainly by the flow of ions through voltage-gated sodium and potassium channels embedded in the cell's membrane (Figure 1.3b). Both sodium and potassium channels are shut when the membrane potential is near the resting potential of the cell (approximately -70 mV) until the moment when the membrane receives an electrical stimulus. If this stimulus is strong enough the sodium channels start to open and the membrane potential increases over the threshold value (approximately -55 mV). This allows an inward flow of positively charged sodium ions, leading to the depolarization of the membrane. The process proceeds until all of the available ion channels are open, resulting in a large upswing in the membrane potential. This potential rises until it reaches a peak potential of approximately 40 mV, which is almost equal to the Sodium equilibrium potential. The rapid influx of sodium ions causes the polarity of the plasma membrane to reverse, and the ion channels rapidly inactivate. As the sodium channels close, sodium ions can no longer enter the neuron, and are progressively transported out of the plasma membrane. At the same time potassium channels are activated, and there is an outward flow of potassium ions, leading to the repolarization of the membrane. After repolarization of the membrane, there is a transient negative shift, called the after hyperpolarization or refractory period, due to additional potassium flow of ions. This is the mechanism that prevents an action potential from traveling back the way it came.

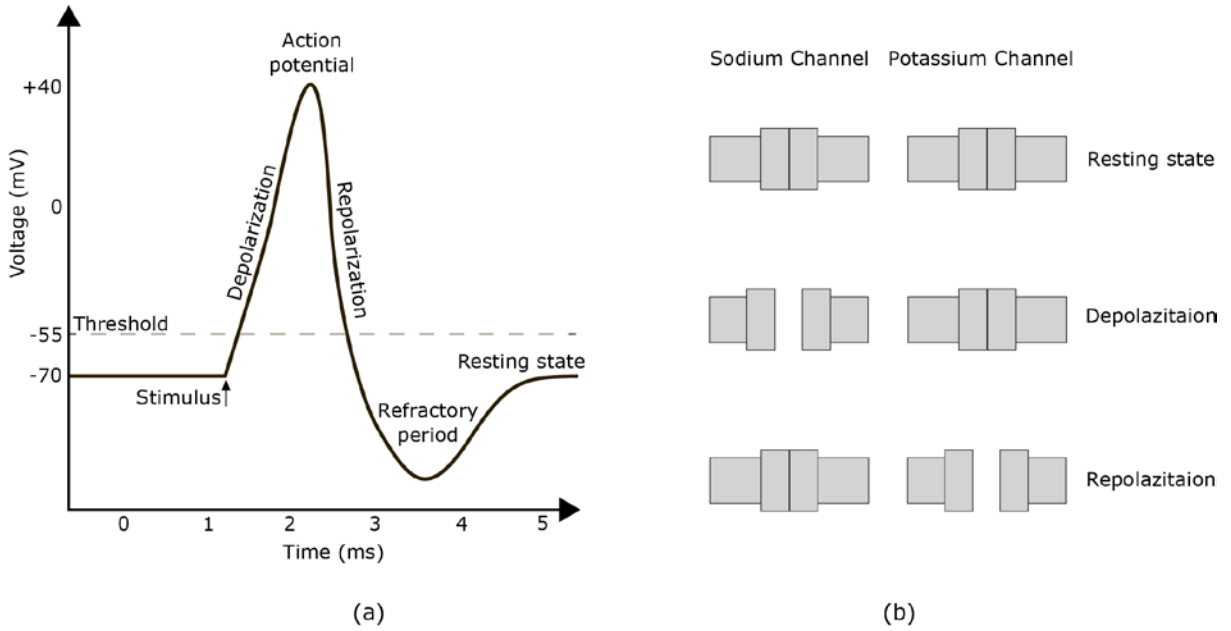

Figure 1.3: Action potential and voltage-gated channels with key moments highlighted. (a) Plot of an action potential, (b) Ion channels states (adapted from [11]).

1.1.3 Recording of Action Potentials

The action potential is of fundamental importance to better understand the mechanisms by which neurons communicate and process information. An action potential can be measured extracellularly with the aid of an electrode. When this electrode is placed in the vicinity of a firing neuron it can measure the electric potential difference between itself (recording electrode) and a distant electrode (reference electrode). The shape of the acquired signal will be inverted and its amplitude significantly smaller than the transmembrane potential. This electrical potential difference is typically between 50 and 500 µV in amplitude and has a duration between 1 and 10 ms [12]. This electrical potential difference can be acquired, amplified and processed with the aid of electronic instrumentation. The waveform of extracellular recorded signals have an inversed polarity when compared to the transmembrane action potential because it measures the difference in potential between the vicinity of the axon and the extracellular medium (Figure 1.4) [13].

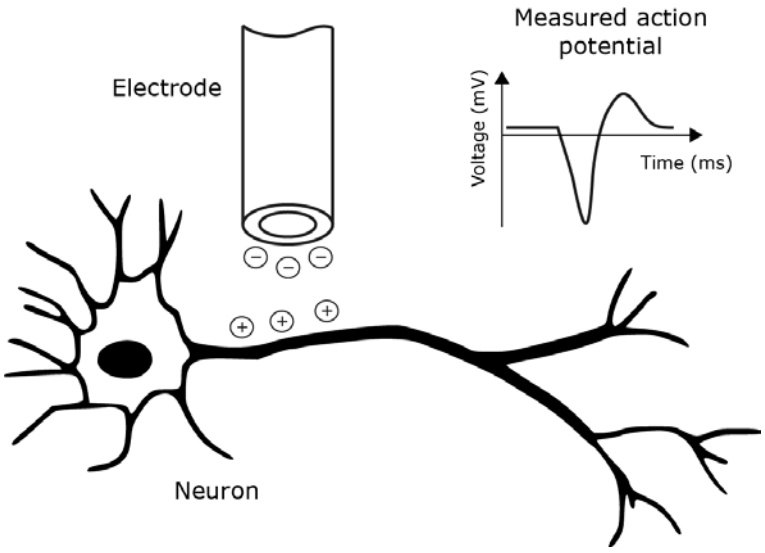

Figure 1.4: Measurement of an action potential with a extracellular microwire electrode (adapted from [14]).

It is also possible to record the sum of action potentials from a small volume of neural tissue with a single electrode. This kind of recording is known as local field potential (LFP) and requires an electrode with lower impedance than the single-unit recording electrodes. Due to their low impedance, these electrodes can record from all neurons that are situated within a radius of a few hundred micrometers away from the recording site. After undergoing a low-pass filter, the acquired signal can provide invaluable information about cortical functions [15].

1.2 Neural Probes

Neural probes usually consist of a support structure and a metallic interface that can transduce bioelectrical signals into electrical signals and vice versa. These probes can be made of different materials and also have different shapes and sizes, according to their application and target area. They can help physicians in the treatment of neurological disorders such as Parkinson's disease, essential tremor, epilepsy and other disorders [16]. Some probes are meant to be implanted inside the cortex and are known as intracortical probes. Recently, these probes have been used in clinical trials for the restoration of movement control from patients with paralysis when the motor cortex is disconnected from the muscles, this application is also known as brain machine interfaces (BMI) [17]. They have also been an invaluable tool for neuroscience research, providing insight on motor control, memory formation and other brain processes [18]. These probes can be classified according to their fabrication methods and design.

1.2.1 Microwire probes

Microwire probes enabled the first recording of action potentials in living animals in the 1950s [19]. Nowadays they are used on a variety of applications, especially as a research tool for neuroscience [20]. They consist of a metallic wire, typically made of tungsten or platinum-iridium (Pt-Ir) alloys, and an encapsulation layer of a biocompatible polymer (e.g. Teflon, Polyimide and Parylene-C). These wires have very small dimensions, ranging from 30 to 50 µm in diameter and many millimeters in length. The encapsulation layer has a very thin thickness ranging from 1 to 3 µm [20]. These microwires can be assembled in arrays, enabling the recording of hundreds of action potentials (Figure 1.5a) [21]. They are the cheapest and most simple type of probes, many times being manually assembled [22]. Enabled by the development of microfabrication technology, advances have been made in the manufacturing process of these types of probes (Figure 1.5b). These advances allowed better control of the length, thickness and spacing of the microwires, and also the use of new types of materials with improved characteristics for encapsulation [23]. Materials such as conductive polymers have also been developed to replace the traditional metallic wires [24]. These polymers allow wires with smaller dimensions, better mechanical match to the brain tissue and better biointegration. Microwire probes have some limitations, particularly when assembled on an array format. Their assembly process increases considerably the cost of production and decreases the reproducibility yield. The resulting arrays usually have bulky connectors to the external electronic instrumentation.

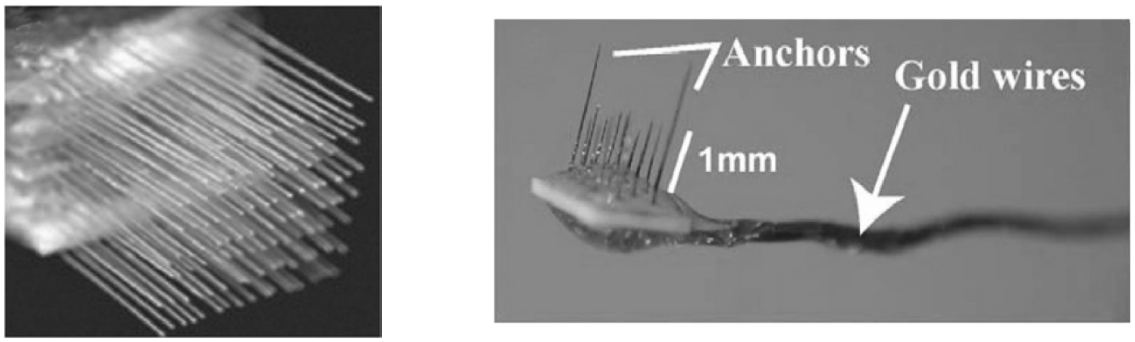

(a) **(b)**

Figure 1.5: Example of two microwire arrays. (a) High-density microwire assembly (reprinted from [25] with permission from The National Academy of Sciences). (b) Tungsten microelectrode array (reprinted from [23] with permission from Elsevier).

1.2.2 Planar Probes

With the advancement of microfabrication technology, a new kind of neural probe was developed in the early 1970s [26]. This probe was proposed to overcome limitations in terms of reproducibility and precision of microwire electrodes by introducing industrial manufacturing technologies on the fabrication process. These probes were based on a silicon (Si) substrate, used gold as the electrode material and glass for encapsulation. Each probe was composed by a needle-like structure with a planar profile usually called a shank (Figure 1.6a). On the surface of the shank, three electrodes capable of recording and stimulating were patterned. The Si structure was fabricated by selectively removing the undesired areas. Afterwards, the electrodes and the interconnecting leads were patterned over the structure surface. The final step was the deposition of a thin layer of glass on top of the entire structure except on the electrodes' areas (Figure 1.6a).

Due to the posterior advancements on microfabrication technology led by the semiconductor industry, many improvements were made to this type of probe in terms of size, design and materials employed. Currently, probes with tens of electrodes on each shank are possible. Although many modern probes still use Si as the substrate material, other more flexible and biocompatible materials have been employed (polyimide, SU-8 and Parylene-C) [27,28]. The electrodes are usually made of a metallic thin-film with high-charge capacity (Pt, Pt black and iridium oxide) [29]. These materials can be deposited over the substrate with great precision (below 1 μm) and with a defined pattern using a process called photolithography. Typically, the final step is to encapsulate the probe with an electrically insulating and biocompatible material [27]. Recently, an external layer made of bioresorbable materials has been added to the encapsulation layer in order to improve the shanks' stiffness and biocompatibility. Materials such as modified starch, maltose and silk fibroin have been successfully tested [30,31]. This type of probe relies on planar microfabrication technology, which has the advantage of allowing batch fabrication. Tridimensional arrays have also been developed through the assembly of layers of two-dimensional comb-like structures (Figure 1.6b). These structures are precisely stacked using micromanipulation methods. Using this methodology, it has become possible to assemble a tridimensional array with 256 recording electrodes on a single probe [32]. Other advancements include the addition of microfluidic channels in the shank, and optical capabilities, either by assembling optical fibers or micro-light-emitting diodes [33,34]. Probes with the ability to emit light inside the brain are used to an emerging field called ontogenetics. When assembled on a tridimensional format, this type of probe continues to have high reproducibility rates however the fabrication yields decrease. Another limitation is that, when in a tridimensional format, these

probes are limited to 2 mm long shanks, which only allow reaching cortical areas of the brain [35].

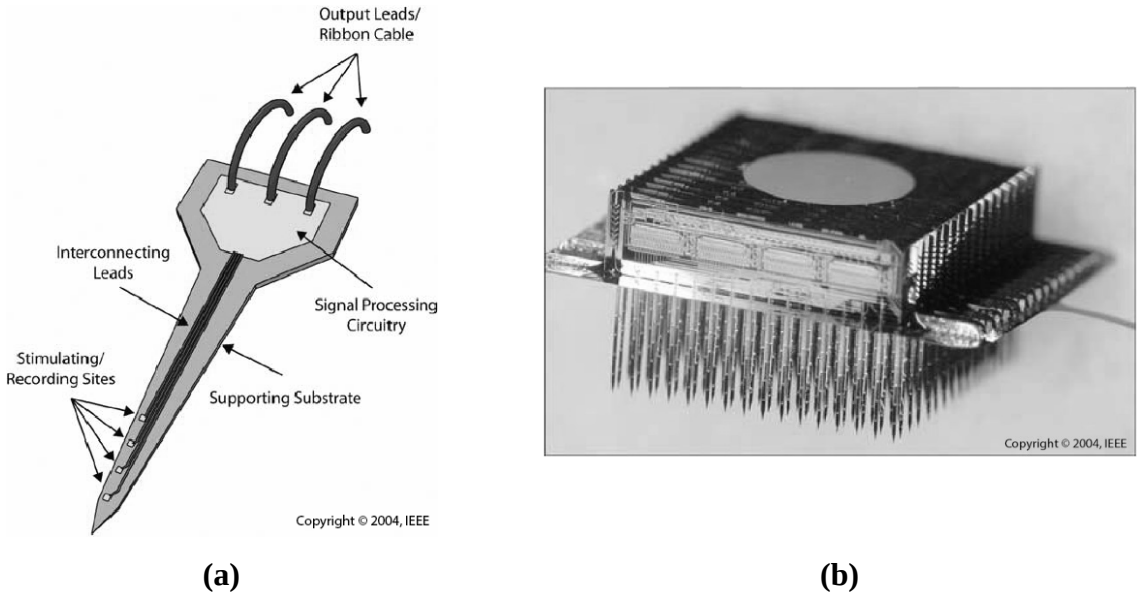

Figure 1.6: Microelectrodes performed by planar microfabrication processes. (a) General structure of a thin-film microelectrode probe, also known as shank. (b) Tridimensional assembly of an array (both pictures were reprinted from [35] with permission from IEEE).

1.2.3 Tridimensional probes

This kind of probe was developed in the early 1990s with the objective of recording signals from the visual cortex of cats [36]. They were developed at the University of Utah and are currently known as the Utah Array (Figure 1.7a). The array is composed of 100 Si shanks, each with an electrode at the tip. The shanks are made of Si and are insulated from each other with glass. Each shank is 1.5 mm long and 86 μm wide at the base and has a metallic electrode at the tip, which is usually platinum. The shank itself is insulated with a biocompatible polymer (Polyimide). Silicon is used as the electrical pathway between the electrodes at the tip and the contact pads at the bottom. The Si is heavily doped with Boron in order to have a good electrical conductance (on the order of milliohms per centimeter) in order to maintain the signal quality within acceptable limits. Although based on Si, the fabrication process of the Utah array is unique, since it does not rely on the assembly of planar structures. The fabrication process begins with a 2 mm thick Si wafer from which the shanks are carved from. In order to do this, a combination microfabrication steps such as dicing and wet-etching is employed. These techniques will be described in the next chapter. Another popular design is the Utah Slanted Electrode Array (USEA), which uses similar fabrication processes and materials. The USEA has different penetrating lengths along the probe (Figure 1.7b). This slanted design is intended for recording from nerve fibers of the PNS [37]. A smaller and higher density version of the USEA

has been developed to target small structures in the sciatic and pudendal nerves of cats [38]. New materials have been used for the probe structure, such as polydimethylsiloxane (PDMS). This polymer of the silicone family has been used instead of glass to add flexibility to the array. The mechanical characteristics of the probe allow it to envelop nerve fibers [39]. These types of probes benefit from the high reproducibility rates that Si microfabrication technology offers. Despite many mechanical advantages, Si also has some limitations. It is a brittle material that can break during insertion. It also has a hardness many orders of magnitude above the brain, which can cause tissue damage due to mechanical mismatch [40]. Moreover, these probes are also limited to recording/stimulating cortical regions, since the shanks have a maximum penetration length of 2 mm.

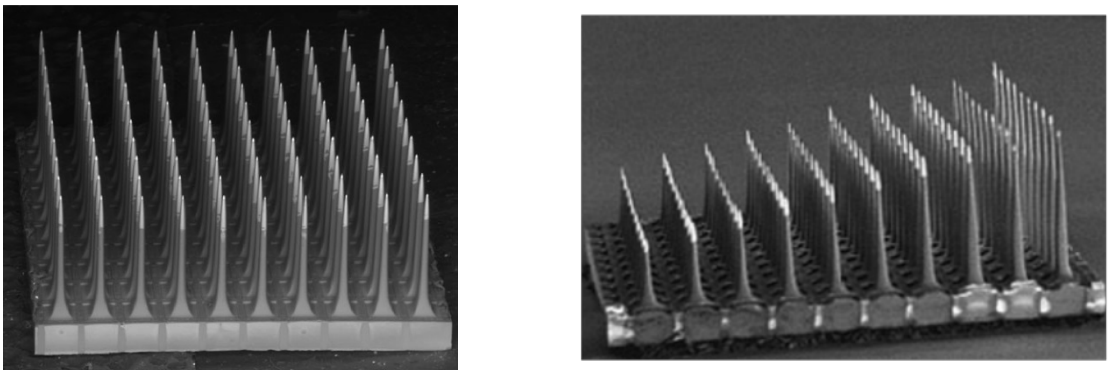

(a) **(b)**

Figure 1.7: Tridimensional probes developed at university of Utah: (a) Utah electrode array (reprinted from [41] with permission from Springer Science and Business Media); (b) Utah slanted electrode array (reprinted from [42] with permission from Macmillan Publishers Ltd).

1.2.4 Neurotrophic probe

The neurotrophic probe was initially developed by Kennedy et al. in the late 1980s with the aim of achieving long-term *in vivo* recordings [43]. These probes have been able to continuously record in human patients for a period of four years [44]. They are made of glass and have the shape of a cone. The probe is manually fabricated by heating and pulling a glass micropipette, forming a very thin tube with a conical shape at its tip. After detaching the conical tip, three to four gold wires are glued inside it (Figure 1.8a). Finally, the resultant cone is filled with nerve growth factors. The nerve growth factors enable the nearby neurons to project axons and dendrites into the cone, allowing the gold electrodes to record their action potentials. With the goal of increasing the number of recording electrodes inside the cone, a new microfabricated probe has been recently developed [45]. This probe was developed using planar processes and used the flexibility of its substrate material to have a conical shape (Figure 1.8b). Although having good biointegration capabilities, this type of probe usually has high manufacturing costs

and low reproducibility yields due to the manual nature of the fabrication method. They also have lower densities of electrodes when compared to all previously mentioned types of probes.

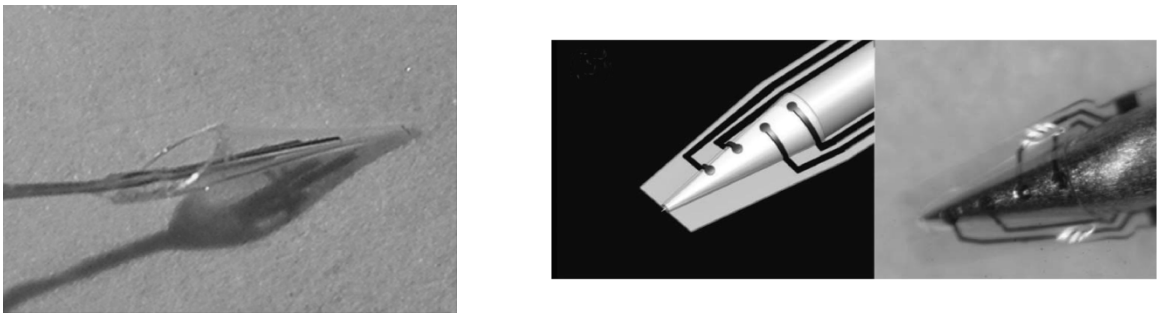

(a) (b)

Figure 1.8: Neurotrophic probe. (a) Close-up of the glass cone tip with the microelectrodes glued inside (reprinted from [44] with permission from Elsevier). (b) Microfabricated neurotrophic electrode (reprinted from [45] with permission from The Royal Society of Chemistry).

1.3 Motivation and Objectives

Tridimensional neural probes are increasingly showing their great potential as a research tool for neurophysiology as well as a tool for advanced prosthetics and for future treatments of different types of paralysis [42]. These probes have been an essential element in the ground-breaking discoveries of how populations of neurons interact, process and store information [22]. This knowledge has been indispensable for the development of BMIs [46]. A great investment is being made by DARPA to advance such probes in order to restore the function of soldiers with lost limbs during war [5]. These high-density probes are limited to interact with superficial structures of the brain such as the cerebral cortex. However probes with longer shanks could reach deeper structures of the brain and offer new insights on their functioning. The hippocampus is a key structure in the brain that plays important roles in the memory and spatial navigation. In order to access areas of the brain below the cortex is of great importance, since areas such as the hippocampus and the amygdala have a key role in learning, memory formation and spatial navigation [7]. New fabrication processes need to be investigated in order to develop high-density tridimensional probes that can achieve deeper brain structures than current ones. Also the use of different materials such as aluminum could introduce new capabilities to the array, since it has the mechanical properties needed for implantation without bending or breaking, and also offers excellent electrical properties for conducting neural signal from the electrode to the exterior without significant signal attenuation.

For the present work, the following goals are proposed:

- A tridimensional fabrication process without the need of assembling components.
- An array with high-fabrication rates and low production costs.
- A methodology that allows the fabrication of high-density probes with 4 mm long and 150 µm wide Si shanks that are able to reach structures like the hippocampus of rats.
- A slanted probe that can reach several layer of the brain cortex (Figure 1.9a).
- The development of high-density tridimensional probes that use aluminum as structural material (Figure 1.9b).

The fabrication process will rely mainly on subtractive techniques on a block of the substrate material (aluminum or silicon), natively producing a tridimensional structure that avoids assembly processes. By simplifying the production and avoiding advanced microfabrication techniques it is possible to increase fabrication rates and reduce costs.

In order to process high-aspect-ratio shanks a new dicing methodology will be applied. This methodology allows the manufacture of shafts with various lengths in the same probe. Deeper structures can be precisely targeted by mounting the array on a stereotaxic apparatus.

A tridimensional aluminum structure will be performed by using new sawing blades to perform the dicing process.

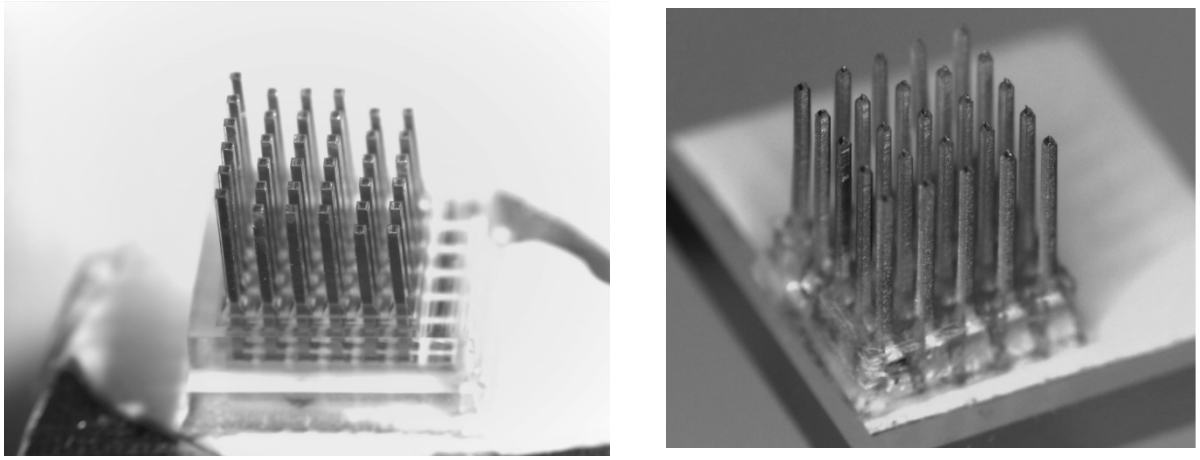

(a) (b)

Figure 1.9: Proposed arrays. (a) Slanted Si array. (b) Aluminum array.

1.4 Organization of the thesis

This chapter introduced the neuroanatomy of certain specific structures of the brain, the neurophysiological principles of action potentials and their recording, and also a concise and complete review on current state-of-the-art probes. Chapter 2 introduces the manufacturing technologies used, describes the proposed design for the neural array, and describes some materials and their use for neural probes. Chapter 3 and 4 discusses the fabrication of the aluminum and silicon arrays respectively, describing each fabrication step in detail and pointing out the achieved solutions to overcome some processes' limitations. The evolution of the prototypes and fabrication methods are also addressed in these two chapters. Chapter 5 describes the mechanical characterization of the arrays and the electrochemical characterization of the electrodes. Finally in Chapter 6, a few conclusions are summarized and recommendations for future work are pointed out.

References

[1] Medtronics, "Deep Brain Stimulation facts," *Retrieved on Jul 2014*. Available at: http://professional.medtronic.com/pt/neuro/dbs-md/index.htm#.U8kQh5RdWSo.

[2] National Institute on Deafness and Other Communication Disorders, "Cochlear Implants facts," *Retrieved on Jan 2014*. Available at: http://www.nidcd.nih.gov/health/hearing/pages/coch.aspx.

[3] National Institute of Health, "BRAIN Initiative," *Retrieved on Jul 2014*. Available at: http://www.nih.gov/science/brain/.

[4] European Commision, "Human Brain Project," *Retrieved on Ago 2014*. Available at: https://www.humanbrainproject.eu/.

[5] Defense Advanced Research Projects Agency, "Revolutionizing Prosthetics Program," *Retrieved on Jul 2014*. Available at: http://www.darpa.mil/Our_Work/BTO/Programs/Revolutionizing_Prosthetics.aspx.

[6] B. I. Bogart and V. Ort, "Introduction to the Peripheral Nervous System," in *Elsevier's Integrated Anatomy and Embryology*, Elsevier, 2007.

[7] E. Kandel, J. Schwartz, and T. Jessell, *Principles of neural science*, 5th Ed. McGraw-Hill Medical, 2000.

[8] S. Tapert and Cladwell, "Brain side view," *Retrieved on Jul 2014*. Available at: http://pubs.niaaa.nih.gov/publications/arh284/205-212.htm.

[9] J. White, *USMLE Road Map Neuroscience*, 2nd Ed. McGraw-Hill Medical, 2008.

[10] O. College, "CNS and PNS," *Wikimedia Commons. Retrieved on Jul 2014*. Available at: http://commons.wikimedia.org/wiki/File:1201_Overview_of_Nervous _System.jpg.

[11] "Action Potential," *Wikimedia Commons. Retrieved on Jul 2014*. Available at: http://commons.wikimedia.org/wiki/File:Action_potential.svg.

[12] G. E. Perlin, "A fully-implantable integrated front-end for neural recording microsystems," Thesis dissertation. University of Michigan, USA, 2008.

[13] D. Henze and Z. Borhegyi, “Intracellular features predicted by extracellular recordings in the hippocampus in vivo,” *J. Neurophysiol.*, vol. 84, pp. 390–400, 2000.

[14] “Neuron,” *Wikimedia Commons. Retrieved on Jul 2014*. Available at: http://commons.wikimedia.org/wiki/File:Neuron_-_annotated.svg.

[15] A. Mazzoni, N. Logothetis, and S. Panzeri, “The information content of Local Field Potentials: experiments and models,” in *Principles of Neural Coding*, 2012.

[16] M. Han and D. B. McCreery, “Microelectrode Technologies for Deep Brain Stimulation,” in *Implantable Neural Prostheses 1*, Springer US, 2009.

[17] N. G. Hatsopoulos and J. P. Donoghue, “The science of neural interface systems.,” *Annu. Rev. Neurosci.*, vol. 32, pp. 249–266, Jan. 2009.

[18] K. C. Cheung, “Implantable microscale neural interfaces,” *Biomed. Microdevices*, vol. 9, no. 6, pp. 923–938, Dec. 2007.

[19] D. H. Hubel, “Tungsten microelectrode for recording from single units,” *Science*, vol. 125, no. 3247, pp. 549–550, 1957.

[20] D. A. Turner, P. G. Patil, and M. A. L. Nicolelis, “Conceptual and Technical Approaches to Human Neural Ensemble Recordings,” in *Methods for Neural Ensemble Recordings. 2nd edition*, 2008.

[21] D. A. Schwarz, M. A. Lebedev, T. L. Hanson, D. F. Dimitrov, G. Lehew, J. Meloy, S. Rajangam, V. Subramanian, P. J. Ifft, Z. Li, A. Ramakrishnan, A. Tate, K. Z. Zhuang, and M. A. L. Nicolelis, “Chronic, wireless recordings of large-scale brain activity in freely moving rhesus monkeys,” *Nat. Methods*, 2014.

[22] M. A. Nicolelis, A. A. Ghazanfar, B. M. Faggin, S. Votaw, and L. M. Oliveira, “Reconstructing the engram: simultaneous, multisite, many single neuron recordings.,” *Neuron*, vol. 18, no. 4, pp. 529–537, Apr. 1997.

[23] S. Musallam, M. J. Bak, P. R. Troyk, and R. a Andersen, “A floating metal microelectrode array for chronic implantation.,” *J. Neurosci. Methods*, vol. 160, no. 1, pp. 122–127, Feb. 2007.

[24] T. Kozai, N. Langhals, P. Patel, and X. Deng, “Ultrasmall implantable composite microelectrodes with bioactive surfaces for chronic neural interfaces,” *Nat. Mater.*, vol. 11, no. December, 2012.

[25] M. A. L. Nicolelis, D. Dimitrov, J. M. Carmena, R. Crist, G. Lehew, J. D. Kralik, and S. P. Wise, “Chronic, multisite, multielectrode recordings in macaque monkeys.,” *Proc. Natl. Acad. Sci. U. S. A.*, vol. 100, no. 19, pp. 11041–11046, Sep. 2003.

[26] K. D. Wise, J. B. Angell, and A. Starr, “An integrated-circuit approach to extracellular microelectrodes,” *IEEE Trans. Bio-medical Eng.*, vol. 17, no. 3, pp. 238–247, 1970.

[27] C. Hassler, T. Boretius, and T. Stieglitz, “Polymers for neural implants,” *J. Polym. Sci. Part B Polym. Phys.*, vol. 49, no. 1, pp. 18–33, Jan. 2011.

[28] N. S. Dias, M. F. Silva, and J. F. Ribeiro, “Gold Coated SU-8-Based Microelectrodes for In Vivo Electrophysiological Studies,” in *Proceedings of the 5th International IEEE EMBS Conference on Neural Engineering*, 2011.

[29] S. F. Cogan, “Neural stimulation and recording electrodes,” *Annu. Rev. Biomed. Eng.*, vol. 10, pp. 275–309, Jan. 2008.

[30] F. Wu, E. Stark, M. Im, I.-J. Cho, E.-S. Yoon, G. Buzsáki, K. D. Wise, and E. Yoon, “An implantable neural probe with monolithically integrated dielectric waveguide and recording electrodes for optogenetics applications.,” *J. Neural Eng.*, vol. 10, no. 5, Oct. 2013.

[31] D. Egert, J. Kaplan, R. L. Peterson, and K. Najafi, “Iodine-treated starch as easy-to-use, biodegradable material with controllable swelling and stiffening properties,” in *IEEE 26th International Conference on Micro Electro Mechanical Systems (MEMS)*, 2013.

[32] Q. Bai, K. D. Wise, and D. J. Anderson, “A high-yield microassembly structure for three-dimensional microelectrode arrays,” *IEEE Trans. Biomed. Eng.*, vol. 47, no. 3, pp. 281–289, Mar. 2000.

[33] T. Kim, J. G. McCall, Y. H. Jung, X. Huang, E. R. Siuda, Y. Li, J. Song, Y. M. Song, H. A. Pao, R.-H. Kim, C. Lu, S. D. Lee, I.-S. Song, G. Shin, R. Al-Hasani, S. Kim, M. P. Tan, Y. Huang, F. G. Omenetto, J. A. Rogers, and M. R. Bruchas, “Injectable, Cellular-Scale Optoelectronics with Applications for Wireless Optogenetics,” *Science*, vol. 340, pp. 211–216, Apr. 2013.

[34] B. Rubehn, S. B. E. Wolff, P. Tovote, A. Lüthi, and T. Stieglitz, "A polymer-based neural microimplant for optogenetic applications: design and first in vivo study.," *Lab on a Chip*, vol. 13, no. 4, pp. 579–88, Jan. 2013.

[35] K. D. Wise, D. J. Anderson, J. F. Hetke, D. R. Kipke, and K. Najafi, "Wireless implantable microsystems: high-density electronic interfaces to the nervous system," *Proc. IEEE*, vol. 92, no. 1, pp. 76–97, 2004.

[36] P. K. Campbell, K. E. Jones, R. J. Huber, K. W. Horch, and R. A. Normann, "A silicon-based, three-dimensional neural interface: manufacturing processes for an intracortical electrode array," *IEEE Trans. Biomed. Eng.*, vol. 38, no. 8, pp. 758–768, Aug. 1991.

[37] A. Branner, R. B. Stein, and R. A. Normann, "Selective stimulation of cat sciatic nerve using an array of varying-length microelectrodes.," *J. Neurophysiol.*, vol. 85, no. 4, pp. 1585–1594, Apr. 2001.

[38] H. A. C. Wark, R. Sharma, K. S. Mathews, E. Fernandez, J. Yoo, B. Christensen, P. Tresco, L. Rieth, F. Solzbacher, R. A. Normann, and P. Tathireddy, "A new high-density (25 electrodes/mm^2) penetrating microelectrode array for recording and stimulating sub-millimeter neuroanatomical structures.," *J. Neural Eng.*, vol. 10, Aug. 2013.

[39] D. Byun, S. J. Cho, and S. Kim, "Fabrication of a flexible penetrating microelectrode array for use on curved surfaces of neural tissues," *J. Micromechanics Microengineering*, vol. 23, Dec. 2013.

[40] V. S. Polikov, P. A. Tresco, and W. M. Reichert, "Response of brain tissue to chronically implanted neural electrodes.," *J. Neurosci. Methods*, vol. 148, pp. 1–18, Oct. 2005.

[41] R. Bhandari, S. Negi, and F. Solzbacher, "Wafer-scale fabrication of penetrating neural microelectrode arrays.," *Biomed. Microdevices*, vol. 12, no. 5, pp. 797–807, Oct. 2010.

[42] R. A. Normann, "Technology insight: future neuroprosthetic therapies for disorders of the nervous system," *Nat. Clin. Pract. Neurol.*, vol. 3, no. 8, pp. 444–452, 2007.

[43] P. R. Kennedy, "The cone electrode: a long-term electrode that records from neurites grown onto its recording surface.," *J. Neurosci. Methods*, vol. 29, no. 3, pp. 181–193, Sep. 1989.

[44] J. Bartels, D. Andreasen, P. Ehirim, H. Mao, S. Seibert, E. J. Wright, and P. Kennedy, "Neurotrophic electrode: method of assembly and implantation into human motor speech cortex.," *J. Neurosci. Methods*, vol. 174, no. 2, pp. 168–176, Sep. 2008.

[45] J. T. W. Kuo, B. J. Kim, S. A. Hara, C. D. Lee, C. A. Gutierrez, T. Q. Hoang, and E. Meng, "Novel flexible Parylene neural probe with 3D sheath structure for enhancing tissue integration.," *Lab on a Chip*, vol. 13, no. 4, pp. 554–561, Feb. 2013.

[46] M. L. Homer, A. V Nurmikko, J. P. Donoghue, and L. R. Hochberg, "Implants and Decoding for Intracortical Brain Computer Interfaces," *Annu. Rev. Biomed. Eng.*, pp. 383–405, 2013.

Chapter 2

Design, Materials and Methods

Neural arrays can have different designs according to their application. Among these designs, the tridimensional array demonstrates a great ability to precisely and simultaneously read from multiple regions of interest. Before fabricating such an array, important parameters such as geometrical, electrical and chemical properties need to be addressed.

The main geometrical parameters to have into account when designing the array are the density of electrodes, implantation depth, and aspect ratio of the shanks. There should also be a careful reflection on the materials to be applied on the array, as they need to perform mechanically, electrically and chemically in accordance with certain requirements. The design and the materials used are interrelated because the material properties can limit the design characteristics and, at the same time, the design may prevent the use of certain materials. The available technologies need to be wisely selected, in order to have a cost-effective and reproducible array. These technologies are also dependent on the selected design and materials, since not all geometric features are possible to be produced nor all materials can be manufactured with current microfabrication technologies. The correct combination of these three parameters will lead to the successful fabrication of the array.

2.1 Design of the Array

The tridimensional design is of great value as a neuro-research tool. One of the underlying principles is that even the simplest of behaviors depends on the interaction of a large population of neurons. A device that has many recording sites overcomes the limitation of recording single neurons, and allows the recording of concurrent time-dependent interactions between large populations of neurons. These interactions are essential for the understanding of processing and storing information [1].

Tridimensional arrays, such as the Utah array, have proven to be the most successful design for implantable neuroprostheses due to the ability of recording simultaneously from multiple neurons with a precise spacing, high-density, and due to the longevity of recording even in human subjects [2].

The design should comply with the following general requirements:

- Be robust enough to withstand implantation process
- Allow chronic recordings
- Be compatible with standard microfabrication technologies
- Allow the implementation of high-reproducible processes and batch fabrication
- Avoid the use of advanced microfabrication techniques using instead simpler and more cost-effective solutions

The fabrication process should be flexible enough to produce arrays for various applications such as recording of action and local field potentials, and stimulation of excitable tissue. This flexibility implies the possibility to adjust important parameters that are required for each specific application.

2.1.1 Design parameters

The requirements for neural recording and stimulation will define the tridimensional array characteristics. The main parameters to be defined are the density and depth of electrodes, and aspect ratio of the shank. Besides these parameters it is important to have in mind the available fabrication processes.

The density of electrodes is defined as the spacing between electrodes. For high-density applications, i.e. applications where a great amount of neurons are sought, it needs a high-density array. There are two types of signals that are targeted, the local field potential, which is the sum of the extracellular activity of many neurons in the vicinity of an electrode, and the single units, which refer to the activity only one neuron at a time.

Local field potentials are generally a localized phenomenon with a maximum radius of influence of approximately 500 µm. This means that electrodes with 1000 µm spacing between them are able to interact simultaneously with two adjacent local field potentials (Figure 2.1a) [3].

The interaction with individual neurons requires very short distances, generally below 20 µm between the electrode tip and the neuron itself (Figure 2.1b) [4]. Ideally a neural array should interact with every individual neuron from a target volume of the brain, but in practical terms, this is not viable due to current technology limitations.

The proposed fabrication approach should allow designs with an interelectrode spacing of 1000 µm for interaction with adjacent local field potentials and also smaller spacing for high-density interaction with single units.

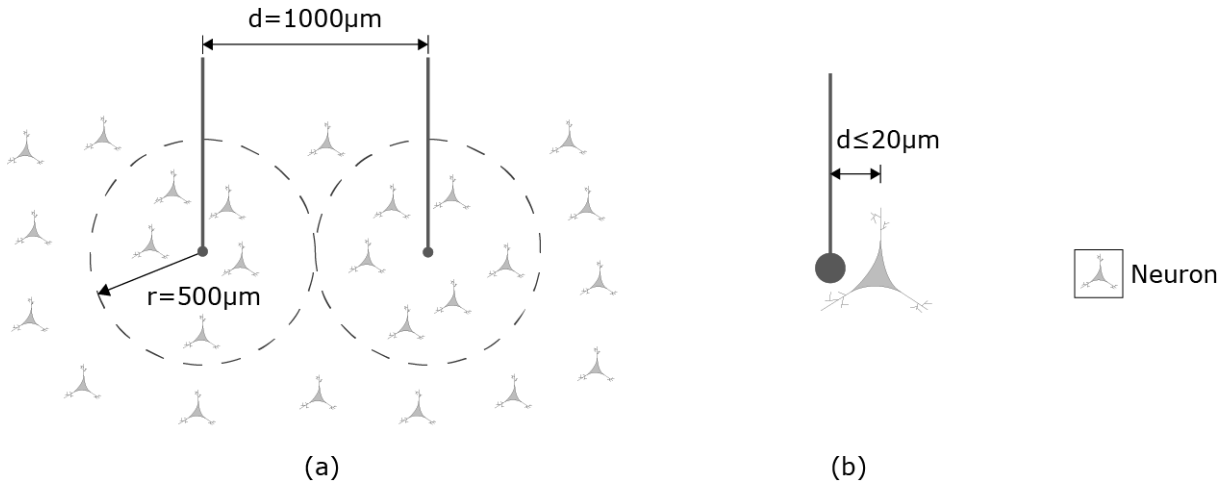

Figure 2.1: Distance between electrodes and neurons. (a) Recording from two adjacent local field potentials. (b) Recording from a single neuron.

Usually neural arrays are tested on animal models for research purposes. Animals such as rats are frequently used in neuroscience as a suitable model for behavioral studies and neurological deficits [5,6]. The array should target two cerebral structures of interest, namely the cortex and hippocampus, which are linked to learning and memory [7]. In rats, the cortex has an approximate maximum depth of 1.8 mm, while below it, the hippocampus can reach 4.4 mm [8,9]. These depths will define the range of lengths that the electrode should have. The electrodes must reach a minimum of 1.8 mm to cover all cortical layers, while superior lengths are desired to reach hippocampal structures (Figure 2.2).

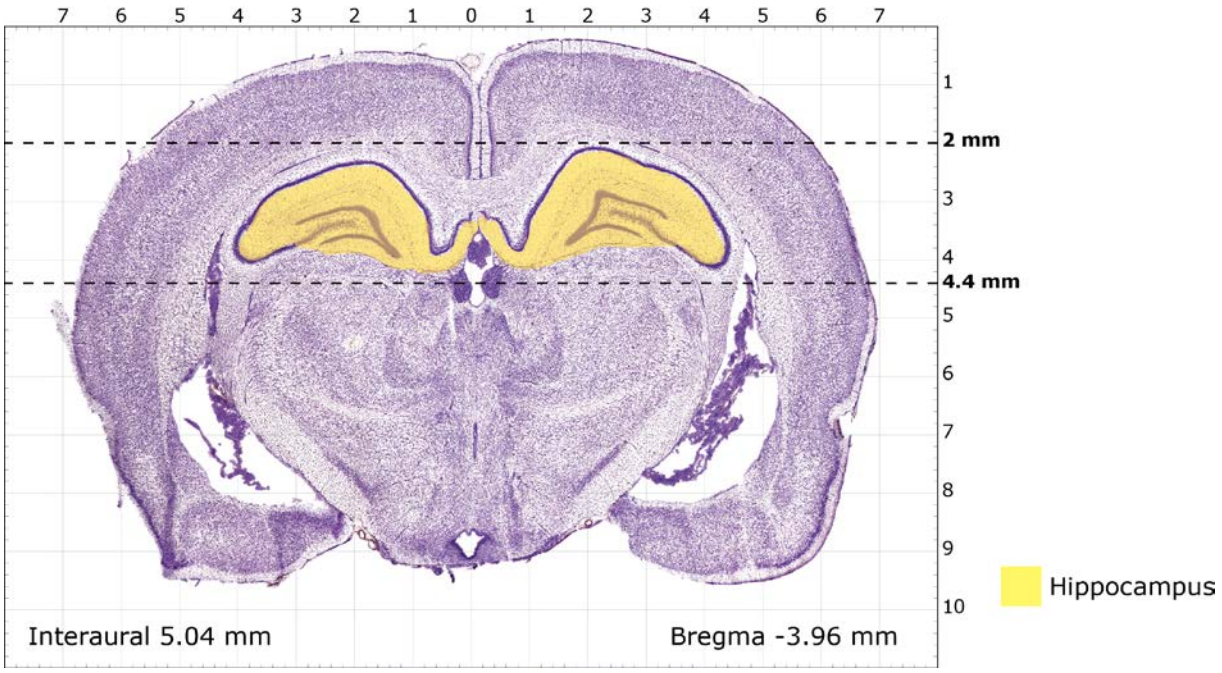

Figure 2.2: A coronal slice of the rat brain with correspondent stereotaxic references. The area highlighted with yellow represents the hippocampus. The depth of interest is limited by two dashed lines. Adapted from [9].

The aspect ratio of the shank is defined by the relation between its cross-section and length. This relation is important since it defines the volume of neural tissue displaced after implantation. In order to displace a minimal amount of neural tissue, it is necessary to have shanks with a small cross-section. Commercially available probes for neural recording and stimulation usually have diameters ranging from 30 to 250 µm for neural recording [10–12]. The width of the proposed shanks should not exceed 250 µm in order to avoid massive tissue trauma [12]. Based on the minimum length and width, the aspect ratio should be at least 17.6 which correspond to a 4.4 mm long divided by a 250 µm wide shaft.

2.1.2 Proposed Design

Two generic designs are proposed based on the parameters described in the previous section, a design with equally-sized shanks (Figure 2.3a), and a design with different-sized shanks (Figure 2.3b). The slanted design is best suited for applications where different layers are targeted, such as the simultaneous recording of different hippocampus structures. The non-slanted design is best suited to interact with neurons at equal depths, such as neurons in the same cortex layer. Each shank should have a sharp tip, in order to facilitate the piercing of the brain's meninges and also minimize tissue dimpling and damage [13]. All shanks are mechanically connected and must be able to connect to external electronics at the bottom side of the array (Figure 2.3c)

These arrays will be performed with a combination of materials and microfabrication

techniques described in sections 2.2 and 2.3.

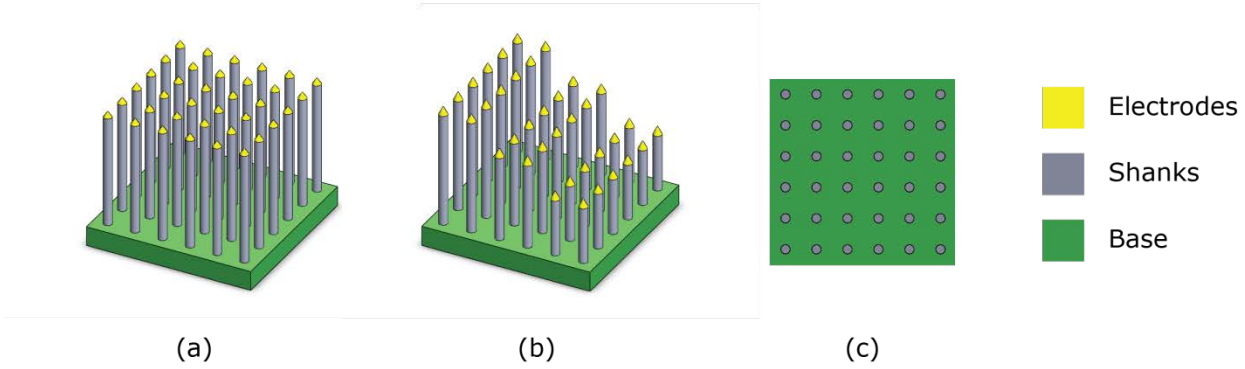

Figure 2.3: Illustration of the two proposed designs. (a) Tridimensional electrode array. (b) Slanted electrode array. (c) Bottom view. Each circle represents the bottom of the shank for connection to the exterior.

2.2 Materials

The array is composed by different materials, each needing particular properties to perform successfully. The choice of a material to a specific part will depend on its mechanical, electrical and chemical properties. Besides these properties, another important factor is the ability to engineer the material for the target purpose. The array can be divided into four parts, namely, the substrate, insulation, encapsulation and electrode.

The substrate will be the main responsible for the structural integrity of the shank, as it will withstand the forces involved during implantation and at the same time transmitting electrical signals to the exterior.

The insulation will avoid electrical contact between shanks while offering a strong adhesion between shanks. The mechanical and electrical properties will determine the choice of material for both substrate and insulation.

The encapsulation will guarantee that only the desired parts of the array are in contact with the external environment, protecting the underlying materials from degradation, and at the same time, preventing the device from causing adverse reactions in the neural tissue. This means that its constituent materials should be biocompatible, biostable, and electrically insulating [14].

Finally, the electrode will perform the signal transduction between the ionic activity from brain cells and the shaft, which will rely mainly on the chemical and electrical properties of the chosen material.

2.2.1 Substrate

The substrate is the main structure in the array and is constituted by the shanks and their base. The shanks have to withstand the axial forces that are applied during implantation and to a

minor degree the shear forces that can occur due to imperfect implantation, namely, angled insertion and movement during penetration (Figure 2.4a and b).

When high-aspect-ratio structures are subjected to an axial load they can bend, this phenomenon is known as buckling (Figure 2.4b) and can be described by the Euler buckling load equation (2.1):

$$P = \pi^2 \times \frac{EI}{L^2} \tag{2.1}$$

where P is the buckling load, π is a mathematical constant, E is the Young's modulus of the material, I is the area moment of inertia and L is the shank's length. The Young's modulus is a measure of the stiffness of an elastic material. The area moment of inertia is a measure of how the geometrical distribution of the material in the shank's cross section resists bending. For a square shank it can be described by equation (1.2).

$$I = \frac{\mathrm{w}^4}{12} \tag{2.2}$$

where w is the shank width. According to equation (2.1) and (2.2), the factor that will determine the resistance of two shanks with equal dimension to buckling is the Young's modulus of the material.

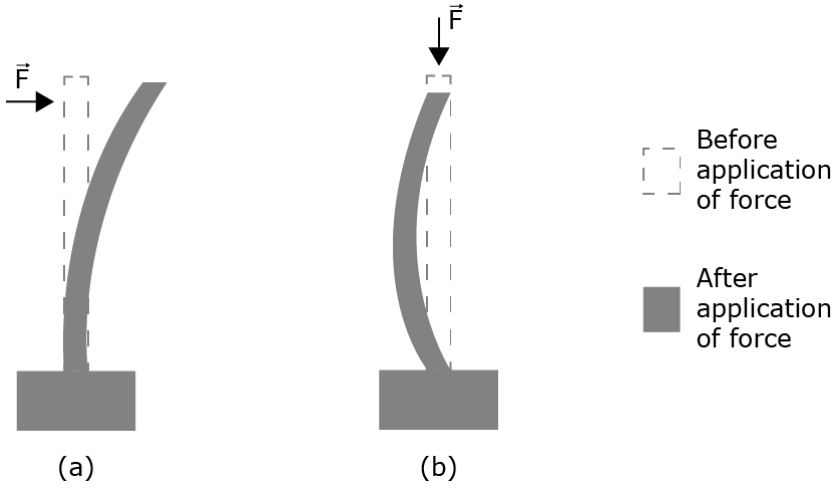

Figure 2.4: Forces applied to the shank during insertion. (a) Bending due to shear force. (b) Buckling due to axial force ($|\vec{F}| > P$).

Another important characteristic concerning the materials to be used as the substrate is whether they are brittle or ductile. Brittle materials tend to have superior Young's modulus and low tolerance to bending, while ductile materials are less stiff and have the ability to bend

considerably before breaking.

Materials such as silicon, platinum-iridium alloys, polymers, and ceramics have been used as substrate materials for neural electrodes. Silicon stands out as the material of choice because of the variety of microfabrication technologies oriented to machine it [15–17].

Silicon is a brittle and stiff material, and has been successfully used as high-aspect-ratio structure that is able to pierce the brain [18]. On the other hand, being a brittle material has some disadvantages, such as the risk of breaking and not bending during insertion.

The substrate material should also be electrically conductive, since the electrical signals acquired from the neurons should flow from the tip to the bottom of the shank with minimal attenuation. Although silicon is a semiconductor, it is possible to increase its conductivity by introducing impurities into its crystal lattice in a process called doping. Heavily-doped silicon wafers that are available in the market can have an electrical resistivity below 1×10^{-5} Ω.m [19], which is acceptable for the purposes of neural recording [20].

Alternatively, aluminum is an excellent electrical conductor, ductile and easily machined. It has a Young's modulus lower than silicon, but still much higher than the brain, which indicates that it can be implanted in the form of a high-aspect-ratio structure (Table 2.1). Also, as a ductile material, it minimizes the risk of breaking during insertion, which can occur when brittle materials are used [21]. Aluminum has an electrical resistivity of 2.69×10^{-8} Ω.m [22], which is one of the lowest of all metals, and by this reason it is a good transmission line, introducing minimal signal attenuation.

Due to their properties, aluminum and silicon will be used as the substrate material for the array.

Table 2.1: Material properties comparison chart

Parameter	**Young's modulus**	**Shear strength**	**Compressive strength**	**Resistivity**	**Cost**
	GPa	N/mm^2	N/mm^2	Ω.m	---
Silicon [23]	190	7000	8300	$*1.3\times10^{-5}$	$$$
Aluminum [22]	70	75	70	2.69×10^{-8}	$
Aluminum oxide [24]	375	330	2600	$>10^{16}$	$$
Brain [25]	19×10^{-6}	---	16×10^{-3}	---	---
Epoxy [26]	3.21	35**	65	3×10^{15}	$$
Cyanoacrylate [12,13]	2.2	0.1	---	10^{17}	$

*Heavily-doped silicon [19]. ** Similar type of epoxy [29]

2.2.2 Insulation

The insulation guarantees that the signal acquired at each electrode, travels through the shank and connects to the exterior without interference from adjacent electrodes. In order to keep the shanks assembled together and electrically independent, a non-conductive adhesive needs to be added between shanks. The adhesion should be strong enough to withstand the shear forces that occur during implantation (Figure 2.5), be stiff enough to avoid the array's deformation, and be flexible enough to reduce the risk of breaking the array during insertion. The adhesive should have a high resistivity in order to be a good electrical insulator and avoid the flow of current between shanks.

Adhesive polymers in general have good adhesive properties and diverse mechanical characteristics with a wide range of compatibility with metals and ceramics. The main properties to have into account when selecting the adhesive is its shear strength, gap size filling, curing time, working temperature, flexibility, electrical resistivity and material processing.

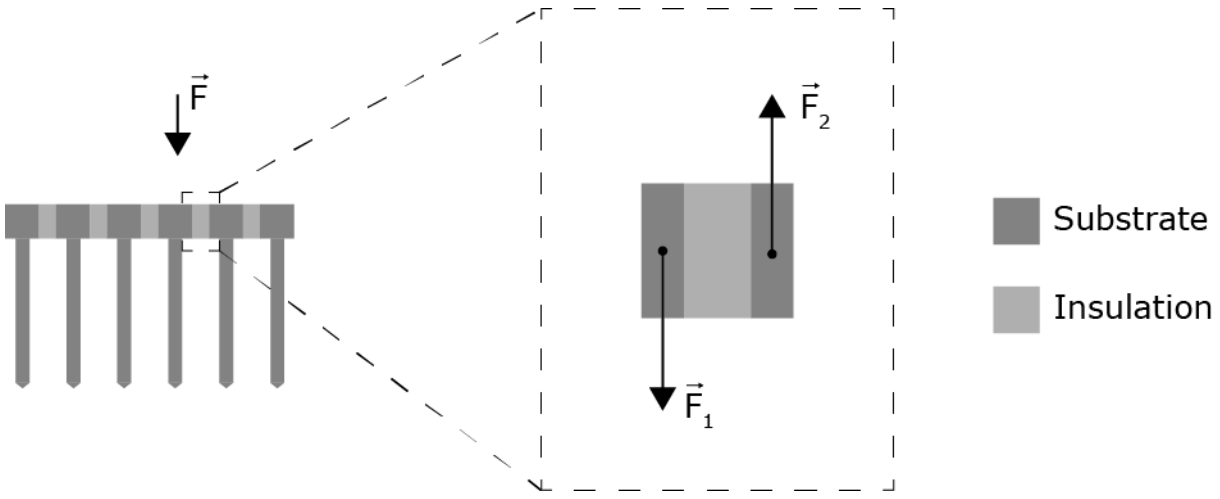

Figure 2.5: Cross-sectional view of the array. Illustration of the shear force applied to the insulation during implantation. $\vec{F}_1$ is the force applied at the base of the shank; $\vec{F}_2$ is the reaction force from the brain surface.

Epoxy resins stand out among the many kinds of adhesive polymers due to their great mechanical and chemical properties [30]. They have high shear strength, which indicates how much force can be applied in the whole structure during manual handling or implantation while keeping the array assembled (Table 2.1). This characteristic is a consequence of the strong adhesion due to mechanical interlocking and chemical bonding of the epoxy to the target substrate.

The insulation that is situated between shanks will determine the epoxy viscosity. High viscosities will hinder the flow of the epoxy inside the inter-shank gap. Epoxies with low viscosities are needed for micrometer scale gaps, allowing an easy flow into these small gaps and

thus completely filling them.

The choice of an epoxy with the adequate curing time at ambient temperature is essential because these adhesives gain small air bubbles during their processing. In order to remove these bubbles, a degassing procedure is necessary. If the curing time is short, the bubbles will not be extracted from the glue, creating porosities and reducing the array's mechanical robustness.

Generally epoxies have a wide working temperature range (between -40 ºC and 80 ºC). This range is more than enough to withstand the human body temperature, but may not be sufficient to withstand higher temperatures that are required in some microfabrication processes like physical vapor deposition.

The epoxy should have enough flexibility to avoid cracks when subjected to large strains and at the same time be stiff enough to maintain the array integrity when being manipulated or implanted.

Since no electric current should flow between shanks, the adhesive should have a high resistivity. Epoxies generally are good electrical insulators with a resistivity in the order of 10^{15} Ω.m. This guarantees that each shank receives the signal from each electrode at the tip without cross communication between electrodes.

The processing of epoxies involves curing and the application method. Generally uncured epoxies have poor mechanical, chemical, and temperature resistance, but when the resin is cured, tridimensional cross linked structures are formed, greatly enhancing its properties. Usually curing is performed by mixing of two components, namely the hardener and the resin itself. Other less common processes such as ultra violet or temperature curing are also possible. As the two-component mixture starts to cure, it produces heat as a byproduct of the chemical reactions. It is important to avoid excessive heating and consequent degradation of the mixture and the surrounding materials. This mixture can be easily applied over the target area with a spatula or with a small dispensing nozzle.

Epoxy resins will be used for the structural bonding of the shanks.

2.2.3 Encapsulation

The encapsulation serves as a chemical and electrical shield between the array and the external environment. This layer guarantees that only the tip of the shanks is in direct contact with the nervous tissue, in this manner avoiding signal interface of the entire shank with the neurons. Because the encapsulation is exposed to the cerebrospinal fluid, it should be biocompatible in order to avoid tissue response and protect the underlying array from the corrosive environment that could damage it. Besides protecting the array, the encapsulation also prevents the production of toxic or injurious effects in the surrounding tissue. It should have a

strong adhesion to the substrate in order to avoid fluid contact with undesired areas due to peeling.

Polymers such as epoxies, Parylene-C, and Polyimide are extensively used in medical implants due to their ability to protect electronics, causing little or no adverse reaction inside the human body [31]. Epoxies are the easiest of these three polymers in terms of material processing and dispensing method, since they can be manually applied without the need of special equipment.

Aluminum oxide can also be used as encapsulation material because of its biocompatibility and high electrical resistivity [32]. This coating can be applied to an aluminum substrate through anodizing processes, thus creating a hard external layer. Beyond these characteristics, aluminum oxide has a very high Young's modulus which can also enhance the structural robustness of the entire shank (Table 2.1).

Cyanoacrylate frequently called super glue is a low-cost, easy to use, hard, translucent, biocompatible polymer (Table 2.1). This encapsulating polymer can be applied through dip coating, spray coating or simply dispensing directly over the substrate with a small nozzle (dropcoating).

Medical grade epoxies, aluminum oxide, Polyimide, and Cyanoacrylate will be tested as encapsulation material for the array.

2.2.4 Electrode

The tip of each shank should be coated with a material that can perform the transduction between ionic charges at the tissue and electrical charges at the shaft. This material must be biocompatible, have good adhesion to the substrate, low electrode-tissue impedance, and high-charge injection capacity. Since neither aluminum nor doped silicon fulfills these requirements, other materials need to be deposited over them.

Platinum and its alloys have been extensively used on neural electrodes due to its chemical stability in saline, high polarization and high charge-injection limits [33].

Gold is a possible alternative to platinum since it is chemically inert, biocompatible, have a stable electrochemical behavior, and provides no native oxide [34].

Platinum and gold can be deposited with the aid of physical vapor deposition technique. These two materials will be deposited at the shanks' tips.

2.3 Technologies

A set of microfabrication processes must be used in order to manufacture the arrays with

the proposed designs. Parameters such as cost, reproducibility, and production yield, should be addressed when selecting the technology to be applied. The adequate combination of available techniques will guarantee a cost-effective and fast fabrication of the prototypes. The main techniques selected to fabricate the proposed array are wafer dicing, wet-etching, physical vapor deposition and aluminum anodizing. Besides these main processes, other techniques such as adhesive bonding, sanding, and microcasting needs to be applied. These latter will be discussed in Chapter 3 and 4.

2.3.1 Wafer Dicing

Wafer dicing or just dicing, is part of the packaging process of microsystems which concerns with the assembly, electrical insulation, mechanical protection, and external communication of the system components. Usually microsystems are manufactured on thin and circular semiconductor substrates called wafers (Figure 2.6a). These wafers vary in size, ranging from 25.4 mm (1 inch) to 300 mm (12 inch) and with thicknesses varying from 275 µm to a few millimeters. Each wafer can have thousands of identical structures patterned over it. The dicing process separates these structures in individual components called dies (Figure 2.6b). The separation process can be performed in three ways, by scribing and breaking the wafer (just like the cutting of window glass), by using high-power lasers to cut the wafer and, finally, through a sawing process that mechanically cuts the wafer.

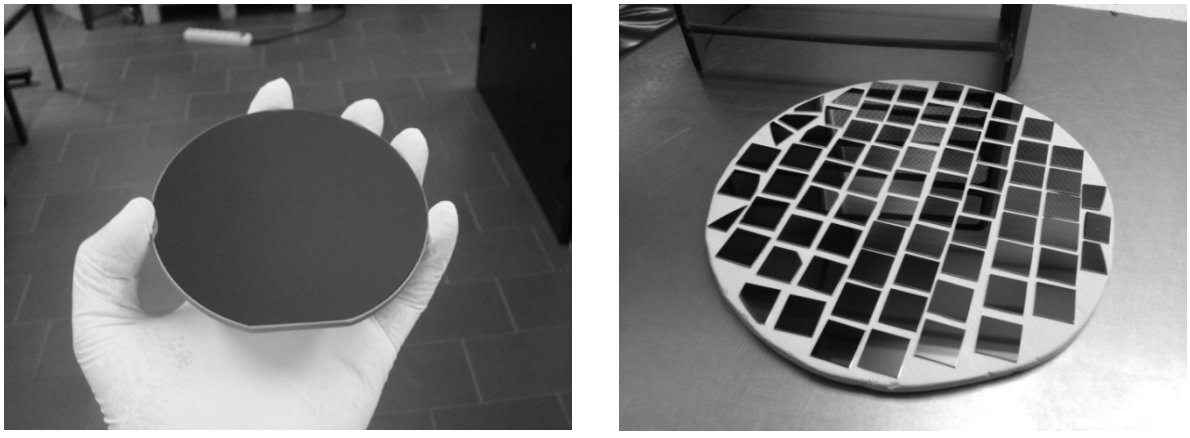

(a) **(b)**

Figure 2.6: Wafer dicing through mechanical sawing. (a) Silicon wafer. (b) Diced silicon wafer over a ceramic support.

The dicing machine that will perform the cutting in the fabrication processes is a Disco DAD 2H/6T (Figure 2.7a). This machine uses diamond-coated blades to cut silicon substrates with blade thicknesses varying from 50 to 250 µm. The blade usually spins at high-rotation

speeds (30,000 rpm) to perform high-quality cuts on silicon. The substrate can move at variable speeds between 0.3 and 10 mm/s. Blade exposure determines the maximum depth of the cuts while blade thickness determines the cut width. The blade is attached to a shaft called spindle which is responsible for the Z and Y movements, while the rotation (R) is performed by the support (Figure 2.7b). The substrate is attached to a sticky tape and placed over the support known as chuck. The wafer is held to the chuck with the aid of suction performed by three small holes in it. The alignment of the blade is performed through a microscope placed over the substrate. Rotation, cutting speed, and blade elevation can be programmed. The cuts can be performed automatically and at various angles.

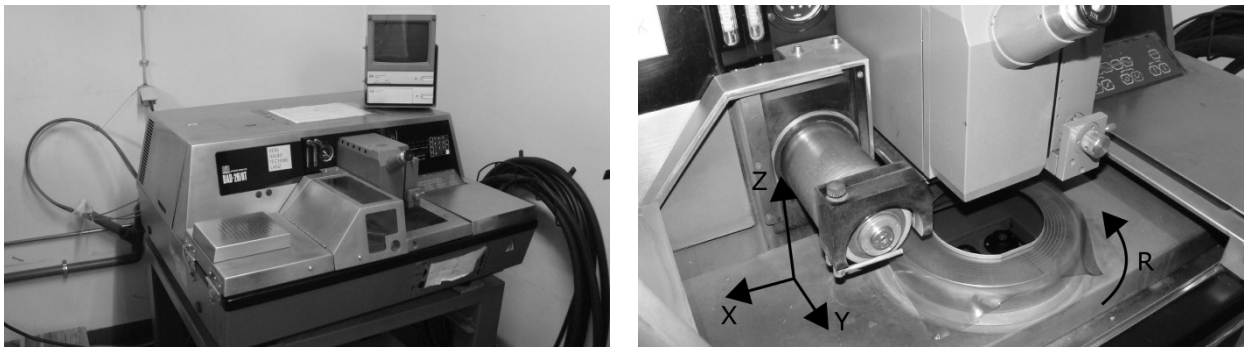

(a) **(b)**

Figure 2.7: Disco DAD 2H/6T dicing machine. (a) Machine picture. (b) Detail of the spindle movements (Y and Z) and rotation of the sample (R).

2.3.2 Wet-etching

Wet-etching is commonly used in microfabrication to clean, make patterns or create structures by chemically removing atoms or molecules from the substrate material at controlled rates. Typically, the parts that are not meant to be removed are protected with a mask. This mask is usually a polymer that is chemically resistant to the etching solution. The etching process starts when the substrate is immersed in the etching solution. At this point, any part of the substrate that is in direct contact with the solution is oxidized and posteriorly dissolved. By controlling the temperature of the solution and etching time, it is possible to accurately control the amount of material to be removed. When the corrosion rate is equal in all directions, it is called isotropic etching, while if there is a preference in direction, it is known as anisotropic etching (Figure 2.8). The anisotropy of the corrosion depends on the way that the atoms are organized in the substrate material (i.e., crystalline structure) and also on the etching solution. For example, silicon being a crystalline material suffers highly anisotropic etching when exposed to potassium hydroxide (KOH) but it can also suffer isotropic etching when exposed to Hydrofluoric acid (HF).

(a) **(b)**

Figure 2.8: Cross section of a substrate undergoing wet-etching, arrows indicates the directionality of the corrosion. (a) Isotropic etching. (b) Anisotropic etching.

All silicon etching will be performed in a Tamson T1000, which allows the control of the temperature of the etching bath (Figure 2.9a). The aluminum etching will be performed in a petri dish over a heated bath. The hot plate has a probe to constantly monitor the bath temperature (Figure 2.9b).

(a) **(b)**

Figure 2.9: Wet-etching equipment and set-up. (a) Tamson T1000 wet-etching system for silicon. (b) Aluminum wet-etching set-up.

2.3.3 Physical Vapor Deposition (PVD)

Physical vapor deposition encompasses a variety of thin-film deposition methods that operate under vacuum. These methods are used in microfabrication to deposit very thin layers of a material over a substrate [35]. These layers can have thicknesses in the nanoscale and are known as thin-films. This section will cover the three methods of PVD that will be used for the fabrication of the array, namely, thermal evaporation, electron beam (e-beam) and sputter deposition.

Thermal evaporation uses the low pressure of the vacuum chamber and the temperature generated by an electrical resistance to vaporize the desired material (target) over a substrate. The target is heated sufficiently to enter the gaseous state, allowing this vapor to move towards the substrate. As the vapor reaches the substrate, it condenses producing a thin-film with the same characteristics of the target material (Figure 2.10a).

Electron beam deposition uses the same principle of thermal evaporation, but instead of heating the entire target it vaporizes only a small area with the aid of a focalized beam of electrons that collide at high speed against it (Figure 2.10b).

Sputter deposition (sputtering) relies on the collision of ions against the target to perform the thin-film deposition. An ionized gas is produced inside the vacuum chamber with a combination of electrical and magnetic fields along with a continuous injection of an inert gas, such as Argon. The ions in the gas collide with the target under the influence of a strong electric field. As the collisions occur the atoms of the target are ejected from the surface and travel towards the substrate where they will be deposited (Figure 2.10c).

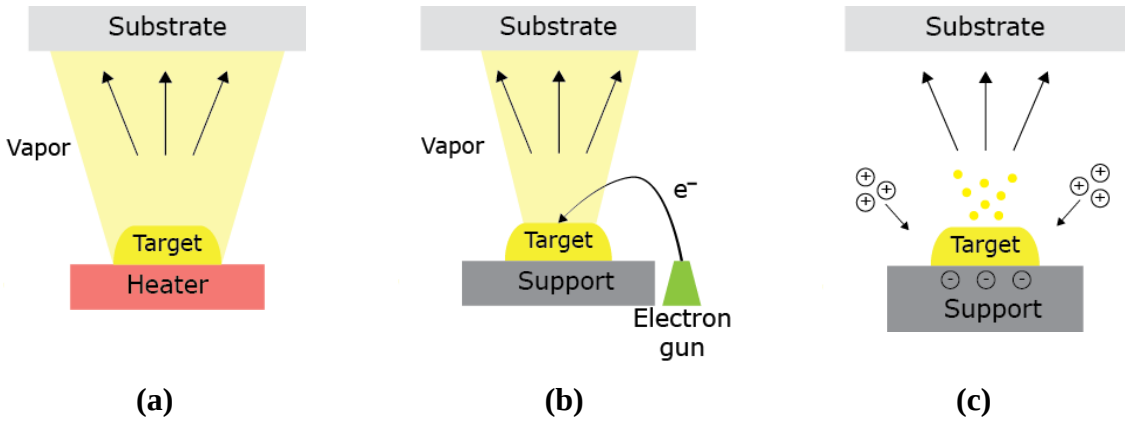

Figure 2.10: Physical vapor deposition techniques. (a) Thermal evaporation. The target is heated and starts to evaporate towards the substrate. (b) e-beam evaporation. A beam of electrons hits the target vaporizing it. (c) Sputter deposition. Positively charged ions bombard the target resulting in the ejection of atoms from the target to the substrate.

These three deposition methods are complimentary since each one is best suited for a specific type of material or application. In the present work, gold will be deposited by thermal

evaporation on a separate chamber, since it is a contaminating material. Titanium will be used as adhesion layer, and will be deposited through e-beam, since this technique can easily vaporize materials with high melting point. Sputtering will be used to deposit platinum, due to the low temperatures involved in the process. Low temperatures imply low film stress and therefore high film quality. Figure 2.11 shows the vacuum chamber that performs thermal evaporation of gold, and Figure 2.12 shows the chamber that performs e-beam and sputter deposition. This last chamber is able to implement both types of deposition under the same vacuum (Figure 2.12b).

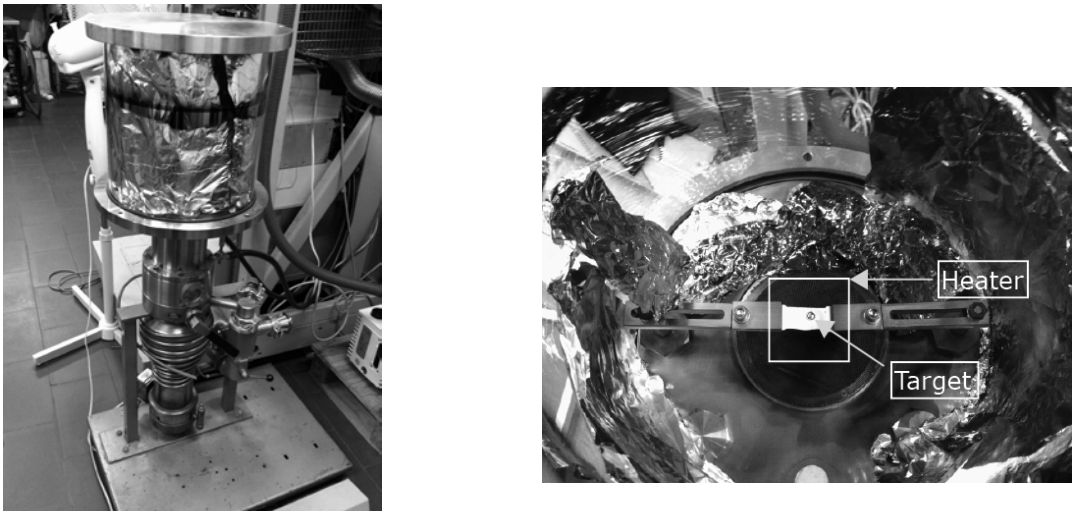

(a) **(b)**

Figure 2.11: Thermal evaporation chamber. (a) External view. (b) Interior view.

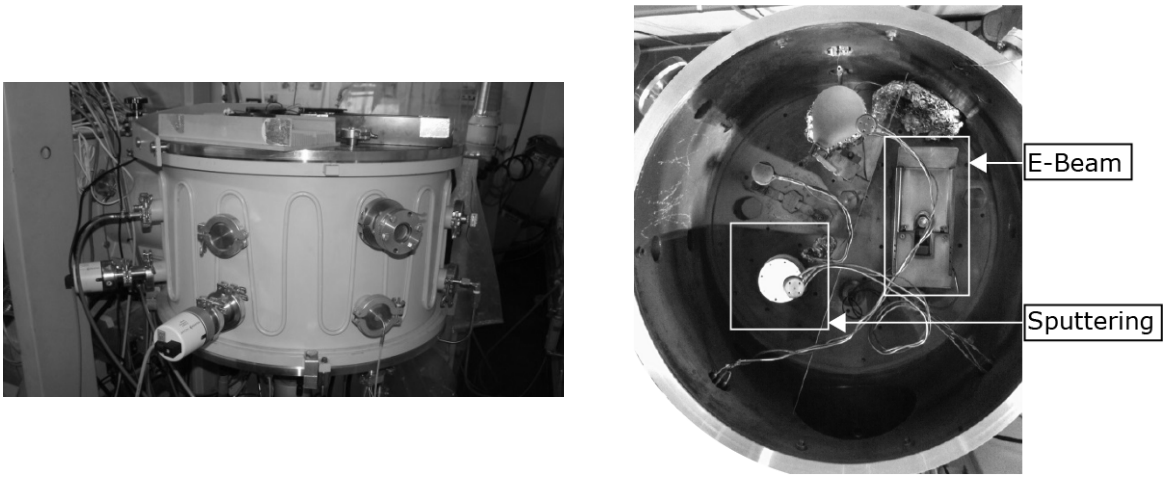

(a) **(b)**

Figure 2.12: E-beam and sputtering chamber. (a) External view. (b) Interior view.

2.3.4 Thermomigration

Thermomigration, also known as the Soret effect, is the movement of a mass under the influence of a temperature gradient.

It is used for the growth of semiconductors such as Gallium phosphide and also for doping semiconductor materials such as silicon. This doping process introduces impurities in a crystalline semiconductor for the purpose of modulating its electrical properties. In this way, if a silicon wafer is doped with a conducting material it will become a better electrical conductor [36].

In the present work, thermomigration will be used to dope silicon wafers with aluminum, this way performing electrically conductive paths through the silicon.

Figure 2.13 describes the thermomigration process of aluminum through silicon. First, aluminum is deposited over the wafer with the desired pattern and placed in a furnace. In order to promote the migration, this furnace has two regions with different temperatures, namely the heat sink and heat source. The temperature at the heat sink will initially melt the aluminum-silicon interface. This interface will enter liquid phase below the individual melting temperature of aluminum and silicon, which is called the eutectic temperature (550 ºC). The heat source has a higher temperature than the heat sink generating a thermal gradient between them. Subjected to this gradient the aluminum-silicon mixture (eutectic mixture) migrates from the heat sink towards the heat source leaving behind a trail of aluminum doped silicon. The temperature gradient has to be at least 0.1 ºC/µm in order to produce a moving eutectic mixture [36]. This trail has a higher conductivity than silicon and can be used as an electric pathway between the two sides of the wafer.

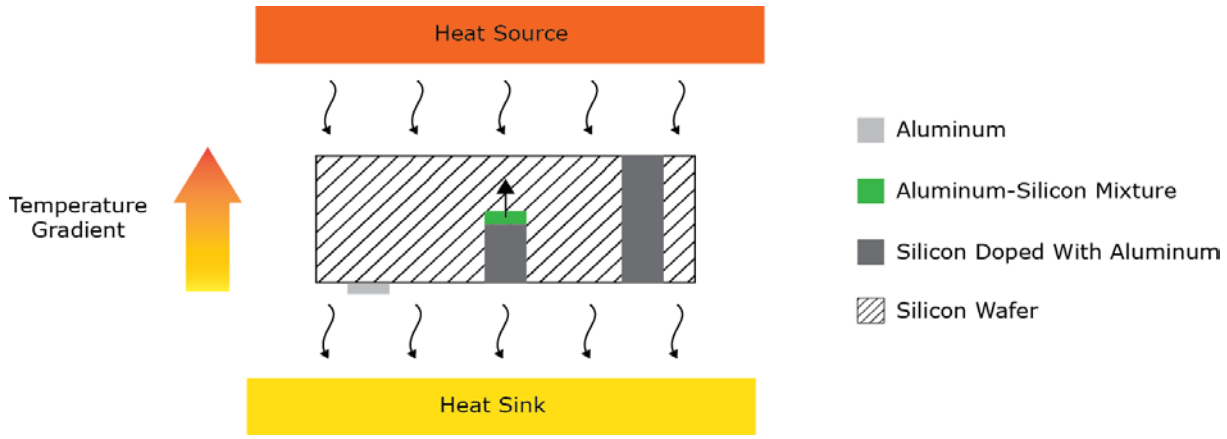

Figure 2.13: Illustration of the thermomigration process.

2.3.5 Aluminum anodizing

The anodizing process is an electrochemical reaction that transforms the surface of an aluminum substrate into aluminum oxide and is widely used in the metal industry for coating purposes [37]. This oxide layer is very hard, resistant to abrasion and corrosion, has excellent adhesion, and is a good electrical insulator (Table 2.1). The anodizing technique is inexpensive when compared to standard microfabrication technologies. The thickness of the oxide usually is situated between 3 and 30 μm and depends on the applied voltage during oxide growth [37]. The anodizing process is performed by injecting a constant current between the aluminum substrate (anode) while it is immersed in the acid solution (electrolyte). Figure 2.14, shows the anodizing set-up used in the present work. The anode consists of an aluminum array, while the cathode is a platinum foil and both anode and cathode are immersed in the acid solution.

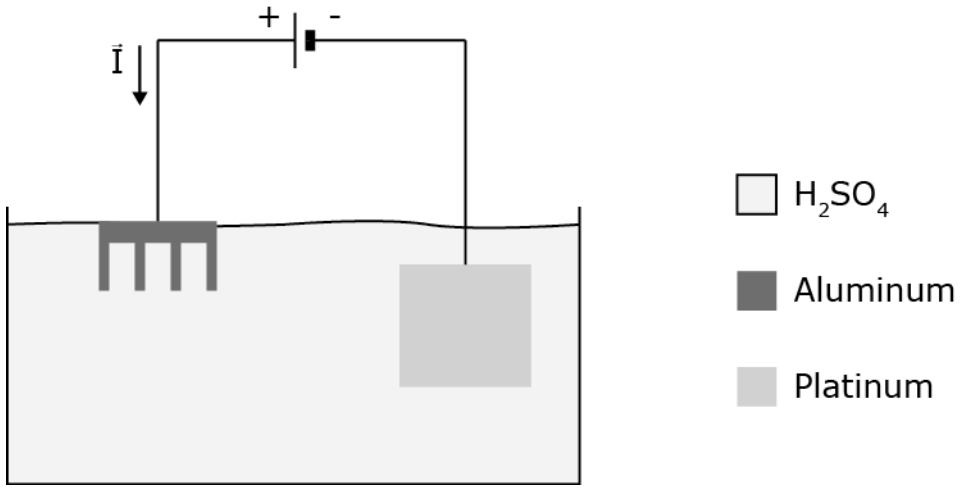

Figure 2.14: Illustration of the aluminum anodizing set-up.

2.4 Proposed Array

Two different arrays are proposed based on the two generic designs, selected materials, and available fabrication technologies. One of the arrays has shanks of the same length (Figure 2.15a), while the other has shanks with different lengths (Figure 2.15b). The shanks are performed by dicing technique, resulting on structures with square and long profile. Due to the format of these structures, they will be referred to as pillars from now on. The tips have a pyramidal profile and can be performed by dicing technique alone or in a combination with wet-etching. In order to simultaneously interact with many neurons, each pillar is electrically insulated from each other with epoxy resin. Polymer or aluminum oxide encapsulation is

deposited along the pillars' length (Figure 2.15c). The backside of the array has flat square regions (pads) to connect to external electronic instrumentation. The pillar's base has a small volume in order to promote a good attachment of the array to the brain avoiding tethering to the skull or possible displacements due to head movements [38]. The base region is also important for the attachment of devices that will perform probe insertion.

The sequence of fabrication steps are described in detail in Chapters 3 and 4.

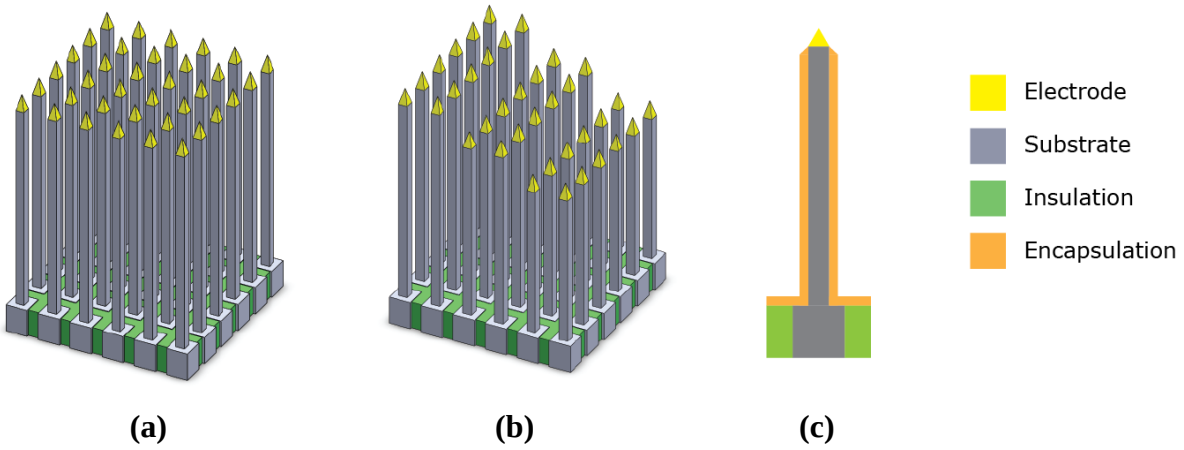

Figure 2.15: Illustration of the two proposed arrays without external encapsulation and a single pillar with encapsulation. (a)Tridimensional electrode array, (b) slanted electrode array, (c) detail of the encapsulation on a single pillar.

References

[1] M. A. Nicolelis, A. A. Ghazanfar, B. M. Faggin, S. Votaw, and L. M. Oliveira, "Reconstructing the engram: simultaneous, multisite, many single neuron recordings.," *Neuron*, vol. 18, no. 4, pp. 529–537, Apr. 1997.

[2] R. A. Normann, "Technology insight: future neuroprosthetic therapies for disorders of the nervous system," *Nat. Clin. Pract. Neurol.*, vol. 3, no. 8, pp. 444–452, 2007.

[3] Y. Kajikawa and C. E. Schroeder, "How local is the local field potential?," *Neuron*, vol. 72, no. 5, pp. 847–858, Dec. 2011.

[4] G. Buzsáki, "Large-scale recording of neuronal ensembles.," *Nat. Neurosci.*, vol. 7, no. 5, pp. 446–451, May 2004.

[5] J. J. Buccafusco, *Methods of Behavior Analysis in Neuroscience*. CRC Press, 2000.

[6] M. A. Cenci, I. Q. Whishaw, and T. Schaller, "Animal models of neurological deficits: how relevant is the rat?," *Nat. Rev. Neurosci.*, no. 3, pp. 574–579, 2002.

[7] E. Dégenètais, A.-M. Thierry, J. Glowinski, and Y. Gioanni, "Synaptic influence of hippocampus on pyramidal cells of the rat prefrontal cortex: an in vivo intracellular recording study.," *Cereb. cortex*, vol. 13, no. 7, pp. 782–792, Jul. 2003.

[8] J. Lee, C. Ehlers, F. Crews, M. Niethammer, F. Budin, B. Paniagua, K. Sulik, J. Johns, M. Styner, and I. Oguz, "Automatic cortical thickness analysis on rodent brain," *Proc. Soc. Photo-Optical Instruments Eng.*, pp. 1–12, 2011.

[9] G. Paxinos and C. Watson, *The Rat Brain in Stereotaxic Coordinates - Part 1*, Sixth Edit. Elsevier Inc., 2007.

[10] Harvard.Apparatus © , "Metal Micro Electrodes," *Retrieved on Ago 2014*. Available at: http://www.harvardapparatus.com/webapp/wcs/stores/servlet/haisku3_10001_11051_53282_-1_HAI_ProductDetail_N_37757_37796_37799.

[11] Science Products GmbH, "Microprobe Electrodes," *Retrieved on Ago 2014*. Available at: http://www.science-products.com/Products/CatalogG/MPI-Electrodes/MPI.html.

[12] MicroProbes©, "Metal Microelectrodes Specifications," *Retrieved on Mar 2015*. Available at: http://www.microprobes.com/index.php/knowledge-center/selection-customization.

[13] A. A. Sharp, A. M. Ortega, D. Restrepo, D. Curran-Everett, and K. Gall, "In vivo penetration mechanics and mechanical properties of mouse brain tissue at micrometer scales," *IEEE Trans. Biomed. Eng.*, vol. 56, no. 1, pp. 45–53, Jan. 2009.

[14] Y.-H. Joung, "Development of implantable medical devices: from an engineering perspective," *Int. Neurourol. J.*, pp. 98–106, 2013.

[15] S. Musallam, M. J. Bak, P. R. Troyk, and R. a Andersen, "A floating metal microelectrode array for chronic implantation.," *J. Neurosci. Methods*, vol. 160, no. 1, pp. 122–127, Feb. 2007.

[16] K. A. Moxon, S. C. Leiser, G. A Gerhardt, K. A Barbee, and J. K. Chapin, "Ceramic-based multisite electrode arrays for chronic single-neuron recording.," *IEEE Trans. Biomed. Eng.*, vol. 51, no. 4, pp. 647–656, Apr. 2004.

[17] T. Kim, J. G. McCall, Y. H. Jung, X. Huang, E. R. Siuda, Y. Li, J. Song, Y. M. Song, H. A. Pao, R.-H. Kim, C. Lu, S. D. Lee, I.-S. Song, G. Shin, R. Al-Hasani, S. Kim, M. P. Tan, Y. Huang, F. G. Omenetto, J. a. Rogers, and M. R. Bruchas, "Injectable, Cellular-Scale Optoelectronics with Applications for Wireless Optogenetics," *Science*, vol. 340, pp. 211–216, Apr. 2013.

[18] W. Jensen, K. Yoshida, and U. G. Hofmann, "In-Vivo Implant Mechanics of Flexible , Silicon-Based ACREO Microelectrode Arrays in Rat Cerebral Cortex," *IEEE Trans. Biomed. Eng.*, vol. 53, no. 5, pp. 934–940, 2006.

[19] S. B. Goncalves, A. C. Peixoto, F. Pinho, A. F. Silva, and J. H. Correia, "High-aspect Ratio Microelectrodes Array With Different Penetrating Length for Neural Applications," in *MME 2013 24th Micromechanics and Microsystems Europe Conference*, 2013.

[20] R. Sharma, P. Tathireddy, S. Lee, and L. Rieth, "Application-specific customizable architectures of Utah neural interfaces," *Procedia Eng.*, vol. 25, pp. 1016–1019, 2011.

[21] K. Najafi and J. F. Hetke, "Strength characterization of silicon microprobes in neurophysiological tissues.," *IEEE Trans. Biomed. Eng.*, vol. 37, no. 5, pp. 474–481, May 1990.

[22] R. Cobden and A. Banbury, "Aluminium: Physical Properties, Characteristics and Alloys," *TALAL*. 1994.

[23] K. E. Petersen, "Silicon as a mechanical material," *Proc. IEEE*, vol. 70, no. 5, pp. 420–457, 1982.

[24] Goodfellow, "Metals, Alloys, Compounds, Ceramics, Polymers, Composites." 1997. Available at: http://www.goodfellow.com/E/Alumina.html

[25] B. Rashid, M. Destrade, and M. Gilchrist, "Mechanical characterization of brain tissue in compression at dynamic strain rates," *J. Mech. Behav. Biomed. Mater.*, 2012.

[26] Henkel AG & Co., "Hysol® 3430™ Technical Datasheet," 2008. Available at: http://www.loctite.co.uk/fullproduct-list-loctite-4995.htm?countryCode=uke&BU=industrial&parentredDotUID=productfinder&redDotUID=1000000IC7Z.

[27] Henkel AG & Co., "Loctite ® 431™ Technical Datasheet," 2010. Available at: http://www.loctite.co.uk/loctite-4087.htm?nodeid=8802626011137.

[28] H. Helbawi, L. Zhang, and I. Zarudi, "Difference in subsurface damage in indented specimens with and without bonding layer," *Int. J. Mech. Sci.*, vol. 43, 2001.

[29] Henkel AG & Co., "Hysol® 9430™ Technical Datasheet," 2001. Available at: http://www.henkelna.com/product-search-1554.htm?nodeid=8797873209345.

[30] DSM Engineering Plastics, "Gluing Guide," 2013. Available at: www.dsm.com/content/dam/dsm/automotive/en_US/documents/gluing-guide.pdf.

[31] C. Hassler, T. Boretius, and T. Stieglitz, "Polymers for neural implants," *J. Polym. Sci. Part B Polym. Phys.*, vol. 49, no. 1, pp. 18–33, Jan. 2011.

[32] D. S. Finch, T. Oreskovic, K. Ramadurai, C. F. Herrmann, S. M. George, and R. L. Mahajan, "Biocompatibility of atomic layer-deposited alumina thin films.," *J. Biomed. Mater. Res. A*, vol. 87, no. 1, pp. 100–106, Oct. 2008.

[33] S. F. Cogan, "Neural stimulation and recording electrodes," *Annu. Rev. Biomed. Eng.*, vol. 10, pp. 275–309, Jan. 2008.

[34] A. Altuna, G. Gabriel, L. Menéndez de la Prida, M. Tijero, A. Guimerá, J. Berganzo, R. Salido, R. Villa, and L. J. Fernández, "SU-8-based microneedles for in vitro neural applications," *J. Micromechanics Microengineering*, vol. 20, no. 6, Jun. 2010.

[35] D. Mattox, *Handbook of Physical Vapour Deposition (PVD) Processing: Film Formation, Adhesion, Surface Preparation and Contamination Control*. 1998.

[36] M. Eslamian and M. Saghir, "Thermodiffusion applications in MEMS, NEMS and solar cell fabrication by thermal metal doping of semiconductors," *Fluid Dyn. Mater. Process.*, vol. 8, no. 4, pp. 353–380, 2012.

[37] J. R. Davis, *Aluminum and Aluminum Alloys*. 1993.

[38] K. D. Wise, "Wireless integrated microsystems: Wearable and implantable devices for improved health care," in *Solid-State Sensors, Actuators and Microsystems Conference*, 2009.

Chapter 3

Aluminum Array Fabrication

This chapter describes the fabrication of two prototypes of neural arrays based on aluminum substrate. Although not a traditional structural material for neural electrodes, aluminum shows some valuable qualities, such as low resistivity, ease of machining and mechanical flexibility. The fabrication of both prototypes relied on a combination of microfabrication technologies such as: dicing, wet-etching, and thin-film deposition. Among these technologies, dicing stands out as the central technique for the structure fabrication as well as the encapsulation. Wet-etching was used to smooth the aluminum surface and decrease the pillars' overall volume, while thin-film deposition transformed the aluminum into functional electrodes.

The first and second prototype achieved 3 mm long pillars, and approximate aspect ratios of 12:1 and 19:1, respectively.

The fabrication of both prototypes required a step by step procedure that was different in the insulation and encapsulation steps. While the first prototype relied on aluminum oxide for encapsulation, the second used a medical grade epoxy. The second prototype represents an evolution of the first in terms of fabrication simplicity and reproducibility.

3.1 First Prototype

3.1.1 Fabrication Process

A fabrication process was developed to produce a prototype with 100 individualized electrodes (10 rows by 10 columns) and 1 mm of spacing between them. The fabrication flow had the 8 following steps:

1. Pads region dicing
2. Adhesive deposition on pads region
3. Removal of excess adhesive on the pads region
4. Pillars dicing
5. Tips dicing
6. Wet-etching
7. Thin-film deposition
8. Array anodizing

Initially, a block of aluminum with the shape of a rectangular parallelepiped was used as the substrate. The surface on which the pillars were machined is called top side, while the opposite surface is called bottom side.

The first dicing step defined the region where the pads are situated and was performed by cutting the bottom side of the substrate, resulting on evenly spaced grooves (Figure 3.1a). The pads serve as electrical connection to the exterior. The blade's thickness determined the grooves' width and influenced the pads size.

Afterwards, a thin layer of the adhesive polymer was deposited over the substrate's bottom side in order to electrically isolate the pads (Figure 3.1b). Due to the uneven profile of the adhesive, a polishing process was implemented to make the bottom side flat, exposing the aluminum pads (Figure 3.1c).

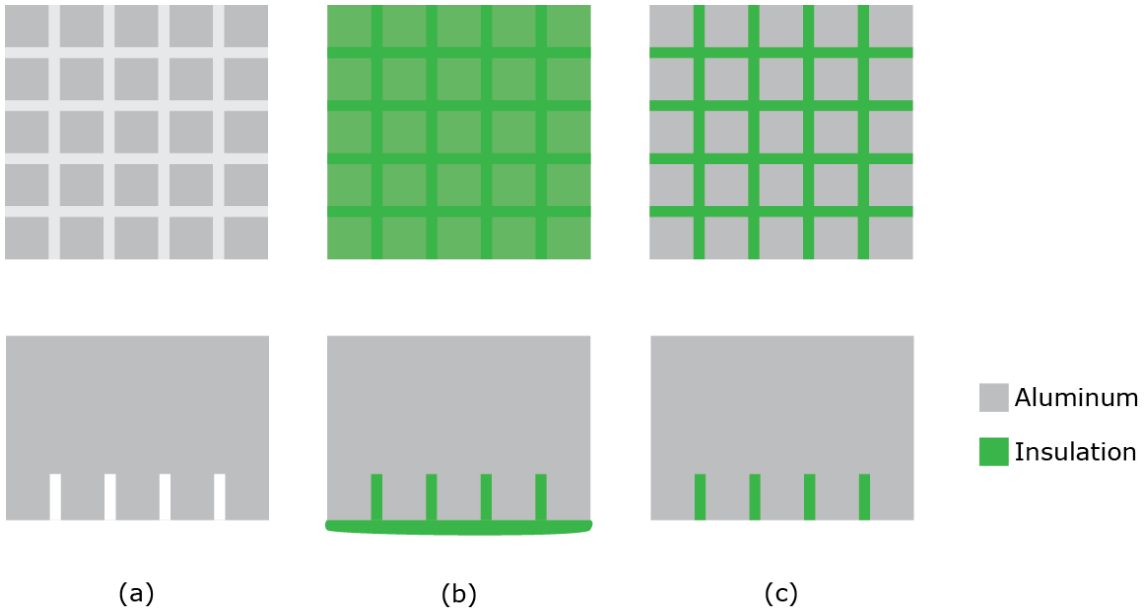

Figure 3.1: Illustration of the first three fabrication processes: *first row*, bottom view; *second row*, side view. For clarity of representation only a 5×5 array is illustrated. (a) Bottom side after dicing. (b) Polymer deposition. (c) Bottom side after polishing.

After having the pads region defined and insulation material set on a grid pattern, the substrate's top side underwent dicing and wet-etching processes that cut and shaped the pillars. Successive cuts were made on the substrate, accomplishing thick aluminum pillars (Figure 3.2a). These cuts were performed with a blade with straight profile (Figure 3.3b). The length and width of the pillars was controlled by the z-axis and y-axis jump (Figure 3.3). Afterwards, the pillars were sharpened by a series of cuts performed at the tips (Figure 3.2b). The tip profile was determined by the v-shaped grooves that the beveled blade performed (Figure 3.3c). The sharp profile at the tips, allows an easier penetration in brain tissue. Next, a wet-etching process was performed to reduce the pillar's width. After the wet-etching stage, the resulting pillars had a thin and long profile (Figure 3.2c). The dimensions of these pillars will be described on section 3.1.2 and further on Chapter 5.

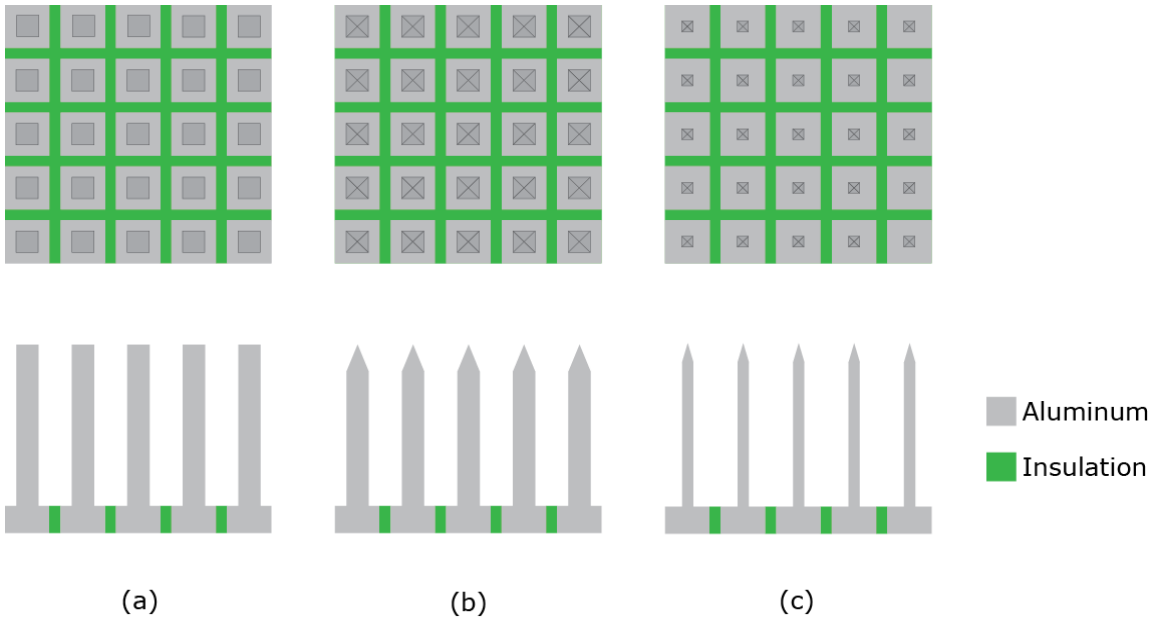

Figure 3.2: Machining of the top side of the substrate: *first row*, top view; *second row*, side view. For clarity of representation only a 5×5 array is illustrated. (a) Diced pillars. (b) Pillars with tip after sharpening. (c) Thin and long pillar after wet-etching.

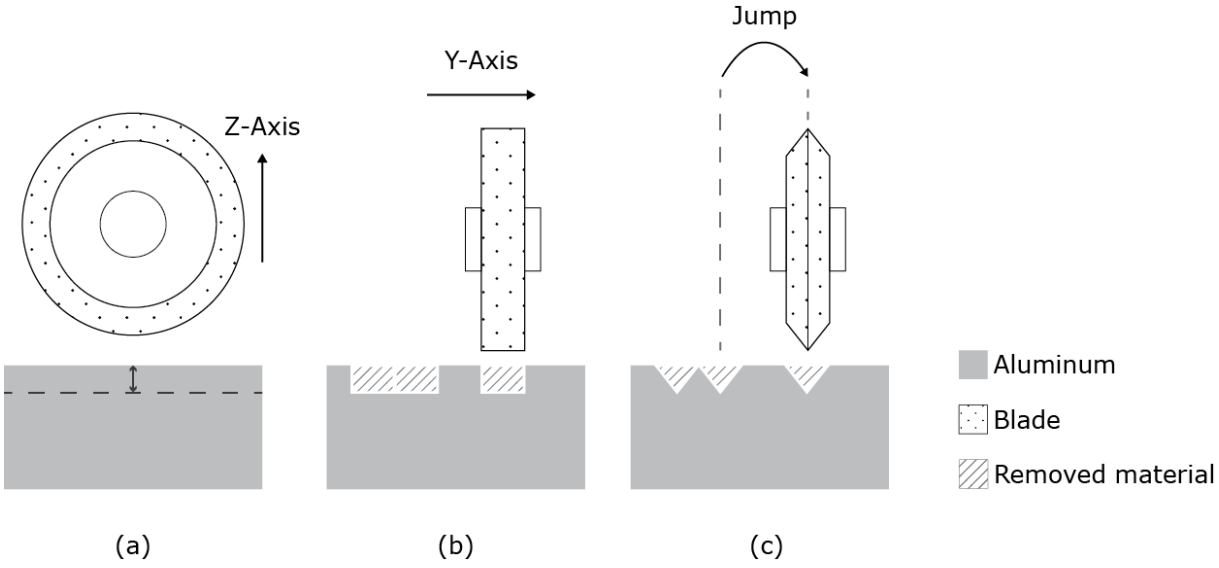

Figure 3.3: Dicing blades and cutting program detail. (a) Side view of dicing blade showing the relation between z-axis level and depth of cut. (b) Front view of dicing blade with straight profile. By successive y-axis jumps the blade performs square grooves. (c) Front view of the beveled blade. Each cut is able to perform v-shaped grooves.

A deposition step followed the top side's micromachining. A thin layer of gold was deposited over the tips using a masking technique to guarantee the deposition of gold only on the pillars' tips (Figure 3.4a). Gold was chosen due to its excellent surface inertness and because it offers no native oxide [1]. The masking technique consisted on pressing an aluminum foil against the sharp pillars until the tips punctured the foil exposing themselves to the deposition vapors (Figure 3.4b).

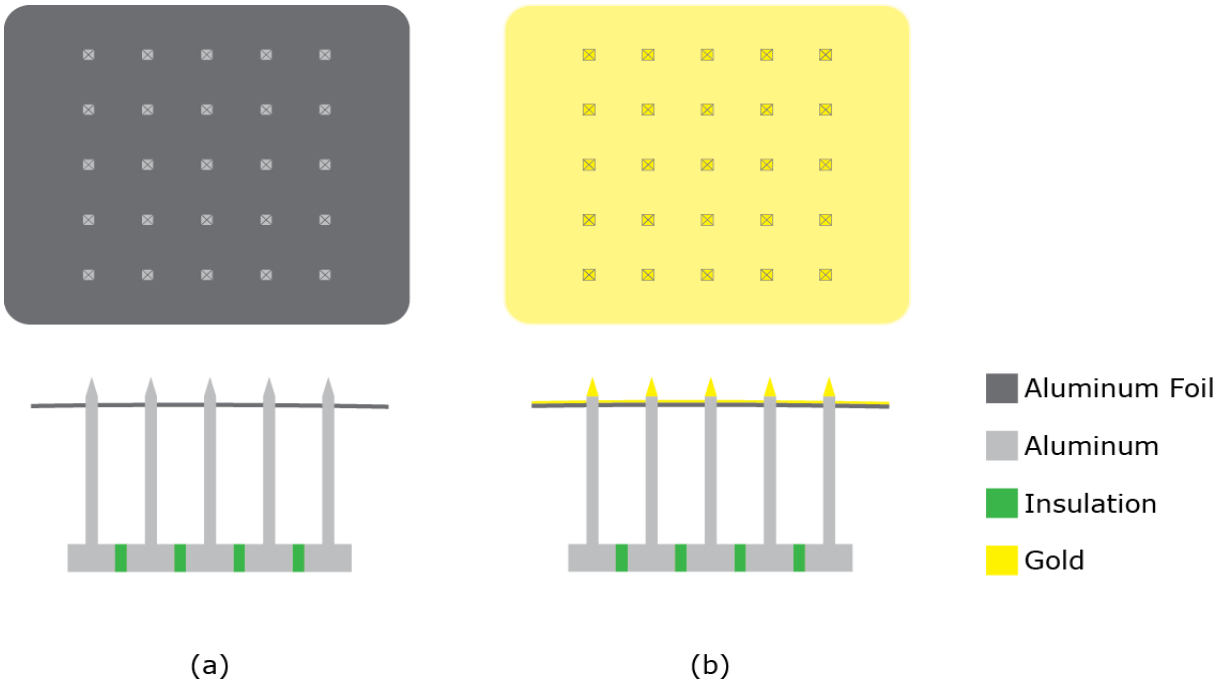

Figure 3.4: Deposition of the thin-film over the pillars': *first row*, top view; *second row*, side view. For clarity of representation only a 5×5 array is illustrated. (a) Before, and (b) after deposition.

The final stage consisted on the encapsulation of the array by anodizing the aluminum substrate. The array was dipped in a sulfuric acid bath at the same time that an electric current was injected into it. The result was the growth of aluminum oxide on any aluminum surface exposed to the acid. At this point, the array had an electrically insulating and biocompatible encapsulation layer made of aluminum oxide (Figure 3.5).

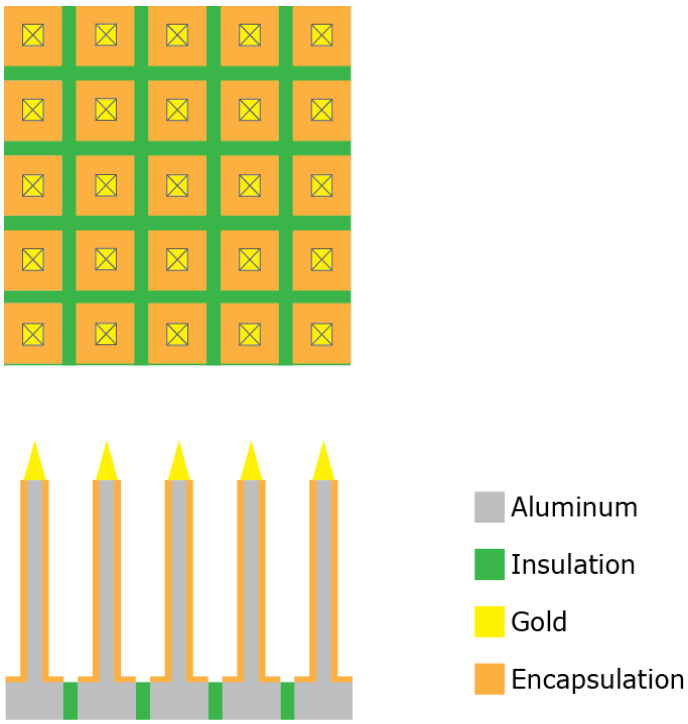

Figure 3.5: Encapsulation of aluminum oxide over the array: *first row*, top view; *second row*, sectional view. For clarity of representation only a 5×5 array is illustrated.

3.1.2 Experimental Results

Two different diamond coated blades were tested to cut aluminum, namely Disco Z09 and ZHDG blades. Z09 blades were recommended by the supplier to cut various types of ceramics and silicon, while ZHDG blades were recommended to cut various semiconductor packages such as ceramics, glass and epoxies. The Z09 blades were only able to cut through 300 µm thick aluminum substrates at the minimum cutting speed (feed speed) available in the machine (0.3 mm/s). All attempts to cut thicker substrates led to blade damage. The ZHDG blades could successfully cut through a 3 mm thick aluminum substrate at a feed speed of 1 mm/s. Some evidences of aluminum residues could be observed on the blade after cutting the aluminum substrates (Figure 3.6). Despite this fact, ZHDG blades were able to continually cut aluminum for tens of hours without suffering damage.

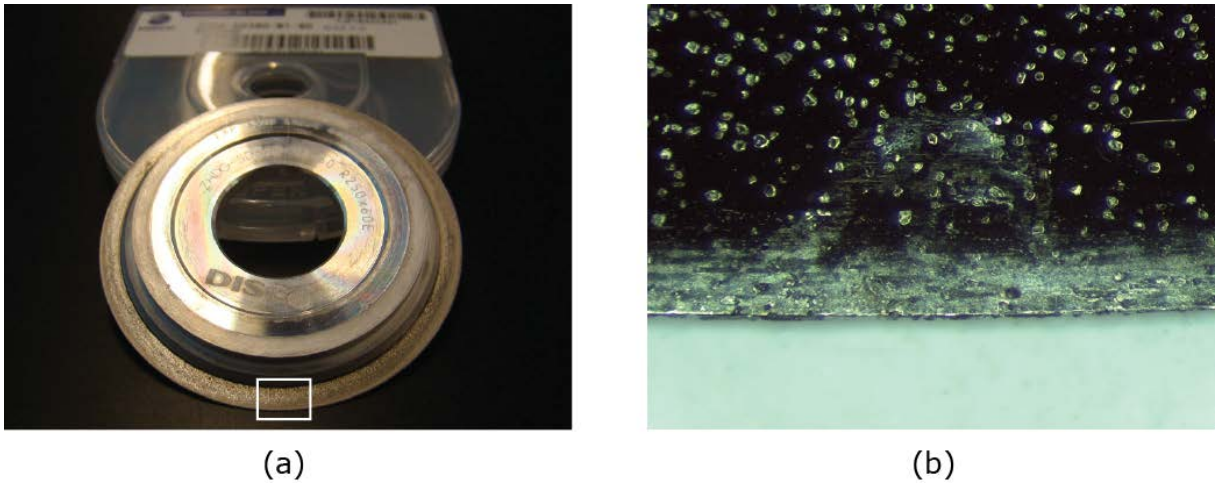

Figure 3.6: Photos of the ZHDG blades after dicing an aluminum substrate. (a) Blade photo with sawing area highlighted. (b) Detail of the sawing area with aluminum residues. The small dots over the blade are diamond grits.

The programming of cuts was based on three variables: speed of cut (feed speed), y-axis step, which determines the distance between two cuts, and the z-axis level, which determines the depth of cut (Figure 3.3). After the completion of a sequence of jumps, the program repeated itself until the entire substrate is diced.

The array was constituted from a 4 mm thick and 10 mm wide aluminum substrate. The bottom side cuts were performed with a 250 µm thick ZHDG blade. Due to the size of the protruding diamond grits, the grooves performed by this blade had an approximate width of 320 µm. The dicing program performed 1 mm spaced and 1 mm deep grooves that defined the pads' region. The dicing machine determined the depth of cut, by measuring the distance between the blade and the reference, known as z-index (Figure 3.7a). Since Disco DAD 2H/6T programming is limited to a 2 mm z-index, an aluminum block with 50 µm tolerance was used to offset the reference (Figure 3.7b). It was placed over the chuck during machine's set-up and removed afterwards. By adding an offset of 2 mm, it became possible to cut at levels (z-blade) between 2 and 4 mm (Figure 3.7c).Table 3.1 summarizes the blade and program parameters used the pads' dicing stage.

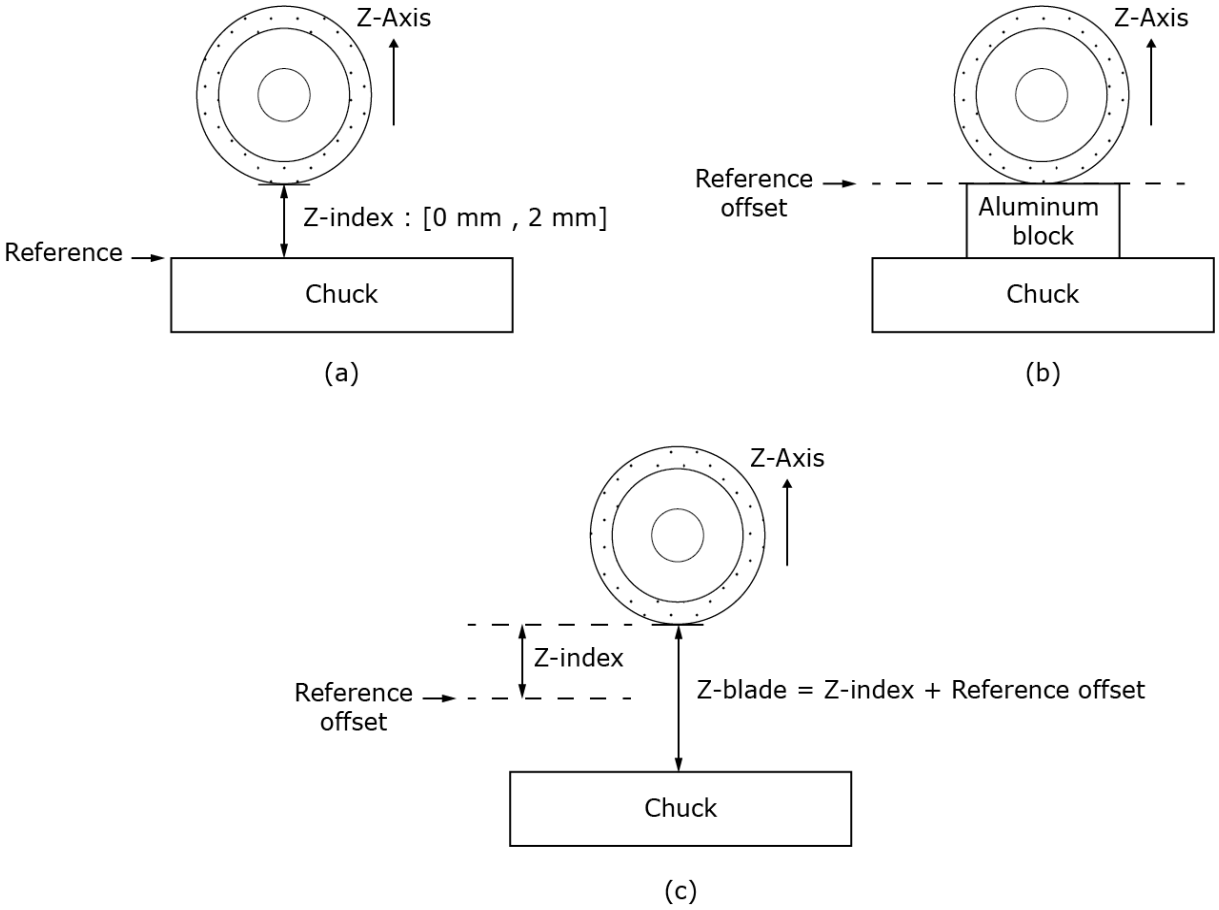

Figure 3.7: Dicer parameters for increased depth of cut. (a) Z-index limits between 0 and 2 mm. (b) Reference offset by adding an aluminum block during set-up. (c) Z-blade level as the sum of z-index and reference offset.

Table 3.1: First prototype's parameters for pads dicing.

Parameter	Value	Comments
Blade thickness	250 µm	V-shaped ZHDG that performs 320 µm wide grooves in aluminum
Jump #1	1 mm	Distance between cuts
Feed speed	1 mm/s	Speed at which the cut is performed
Z-blade	3 mm	Depth of Cut (1 mm) = substrate thickness (4 mm) – z-blade (3 mm) z-blade (3 mm) = reference offset (2 mm) + z-index (1 mm)

The cuts resulted in grooves that had a grid pattern on the bottom side of the substrate (Figure 3.8a and b). An epoxy resin was pressed with a small spatula against the bottom side in order to fill grooves (Figure 3.8c). The epoxy used is strong, translucent, and

has a fast curing time (Hysol® 3430™) [2]. After curing for 24 hours at ambient temperature, the excess epoxy at the backside was removed through manual polishing with a P2000 sandpaper (grit size 10 µm).

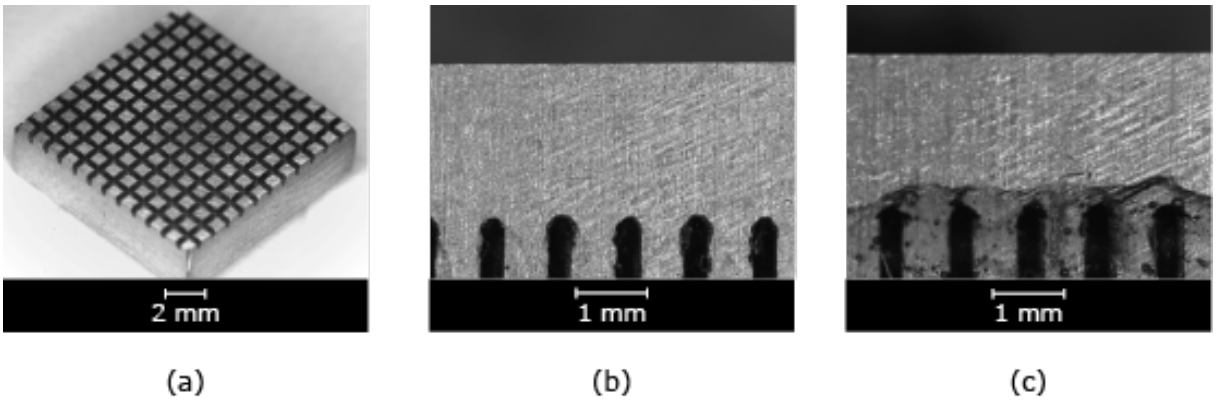

Figure 3.8: Bottom side dicing and insulation results. (a) Photo of the diced pads region facing up. (b) Side view of the grooves before and, (c) after epoxy deposition.

After having the pads' region defined and the insulation set, the substrate was turned over and the second dicing procedure was performed. This procedure performed 330 µm wide and 3 mm long pillars into the substrate (Figure 3.9a). The cutting program had three distinct y-axis jumps (Figure 3.3b). The first defined the width of the pillar, while the second and third removed the excess aluminum between pillars (Table 3.2). The jumps were repeated in cycles until the aluminum substrate was completely diced.

Table 3.2: First prototype's parameters for pillars dicing.

Parameter	Value	Comments
Blade thickness	250 µm	V-shaped ZHDG that performs 320 µm wide grooves in aluminum
Jump #1	650 µm	Pillar width (330 µm) = jump #1 (650 µm) – groove width (320 µm)
Jump #2	320 µm	Removes the excess aluminum between pillars
Jump #3	30 µm	Pillars' spacing (1 mm) = jump #1 (650 µm) + jump #2 (320 µm)
Feed speed	0.5 mm/s	
Z-blade	1 mm	Depth of cut(3 mm) = substrate thickness (4 mm) – z-blade (1 mm)

In order to sharpen the tips, a series of cuts performed 330 µm wide and 300 µm long cuts centered at each pillar (Table 3.3). After this dicing stage the sharp pillars had a considerable amount of burr (Figure 3.9b).

Table 3.3: First prototype's parameters for tips dicing.

Parameter	Value	Comments
Blade thickness	250 µm	V-shaped ZHDG
Jump #1	330 µm	Tip width (330 µm) = pillar width (330 µm)
Jump #2	670 µm	Tips spacing (1 mm) = jump #1 (330 µm) + jump #2 (670 µm)
Feed speed	0.5 mm/s	
Z-blade	3.7 mm	Tip length (300 µm) = substrate thickness (4 mm) – z-blade (3.7 mm)

The array was afterwards immersed in acid solution that performed the wet-etching. The aluminum etchant was in constant movement with the aid of a magnetic stirrer, and kept at a constant temperature of 50ºC. The solution used was a Transene type A aluminum etchant, composed by phosphoric acid, acetic acid, nitric acid, and water [3]. The wet-etching stage removed the burr accumulated at the pillars edges and at the same time decreased the pillar's cross-section. The array was kept on the acid for 30 minutes, reducing the width of the pillars from 320 µm to 250 µm (Figure 3.9c).

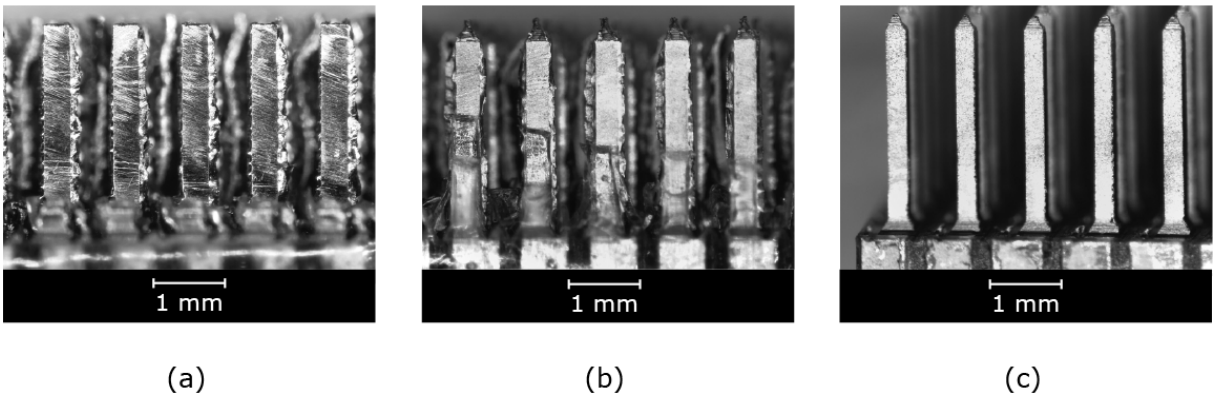

Figure 3.9: Photos of the top side dicing stage. (a) Pillars with a square profile. (b) Pillars after tip sharpening. (c) Pillars after wet-etching.

In the next stage, gold was deposited at the tips. In order to guarantee that only the tips were exposed to the vapor, an aluminum foil was used as a shadow mask. The foil was pressed against the array until the pillars punctured it (Figure 3.10b). The array was fixed on the substrate holder inside the vacuum chamber for the thermal evaporation of gold (Figure 3.10a). The deposition started with an internal pressure of 2.2×10^{-6} mbar inside the chamber

and the target was heated by supplying 170 W. The process lasted for 16 minutes with a deposition rate of 0.32 nm/s. The result was a 307 nm thick gold film over each tip.

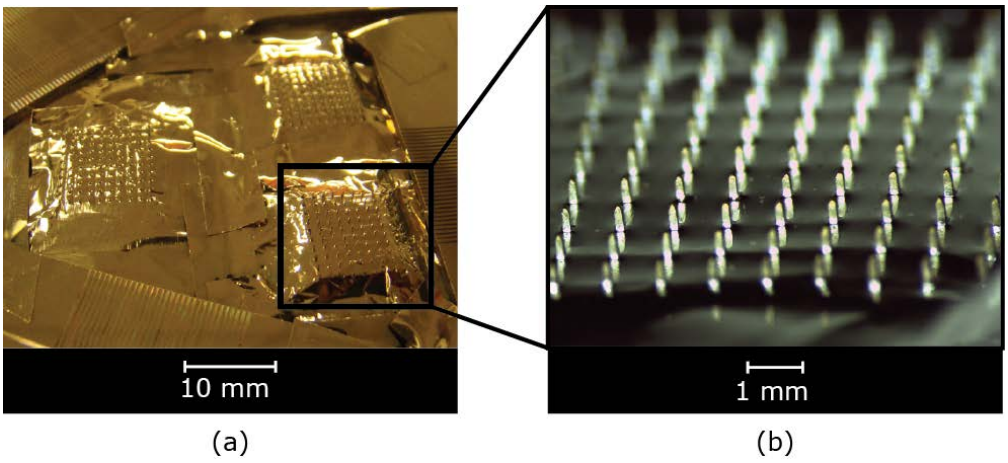

Figure 3.10: Photos after thermal deposition of gold. (a) Substrate holder with three arrays masked with aluminum foil. (b) Detail of the exposed tips.

The last stage consisted on the encapsulation of the array. The bare aluminum at the pillars was insulated with a layer of aluminum oxide. This layer was grown by immersing the array in a 15% solution of sulfuric acid, while injecting an anodic current density of 13 mA/cm^2 for 30 minutes. The cathode was a 250 µm thick platinum foil with an area of 4 cm × 4 cm. The result was a biocompatible and electrically insulating encapsulation layer [4].

The insulated array can be seen on Figure 3.11a, while the detail on the golden tips can be seen on Figure 3.11b.

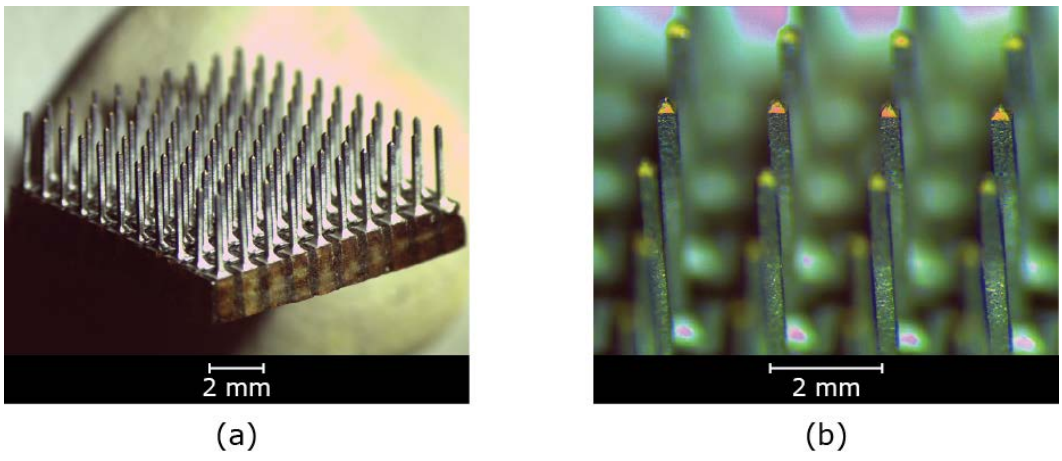

Figure 3.11: Photographs of the final array. (a) View of the entire array. (b) Zoom on the golden tips.

3.2 Second Prototype

3.2.1 Fabrication Process

The second prototype design consisted of 25 individualized electrodes (5 rows by 5 columns) with 600 µm of spacing between them. The reduced number, and spacing between electrodes, increased the density and reduced the area of implantation. The fabrication sequence was similar to the first prototype, with some differences in the last four steps, which also offered better control on the electrode area. The following steps were implemented:

1. Pads region dicing
2. Adhesive deposition on the pads region
3. Removal of excess adhesive on the pads region
4. Pillars dicing
5. Wet-etching
6. Encapsulation deposition
7. Tips dicing
8. Thin-film deposition
9. Removal of encapsulation excess

Similarly to the first prototype, the first dicing stage performed evenly spaced, grid patterned grooves on the substrate's bottom side (Figure 3.1a). Afterwards, a thin layer of the adhesive polymer was deposited over the substrate's bottom side (Figure 3.1b). A polishing process was performed to make the bottom side flat (Figure 3.1c).

The next step performed the pillars by dicing and etching the substrate's top side Thick aluminum pillars were accomplished on the substrate by making successive cuts (Figure 3.12a). The pillars' thickness was reduced by employing a wet-etching process resulting on long and thin pillars (Figure 3.12b). The dimensions of these pillars will be described in section 3.2.2 and further in Chapter 5. The next step added a biocompatible and electrically insulating epoxy over the top side. The material filled all empty spaces between pillars, resulting on a rigid block (Figure 3.12c). This approach avoided the use of an aluminum foil and anodizing for encapsulation purposes.

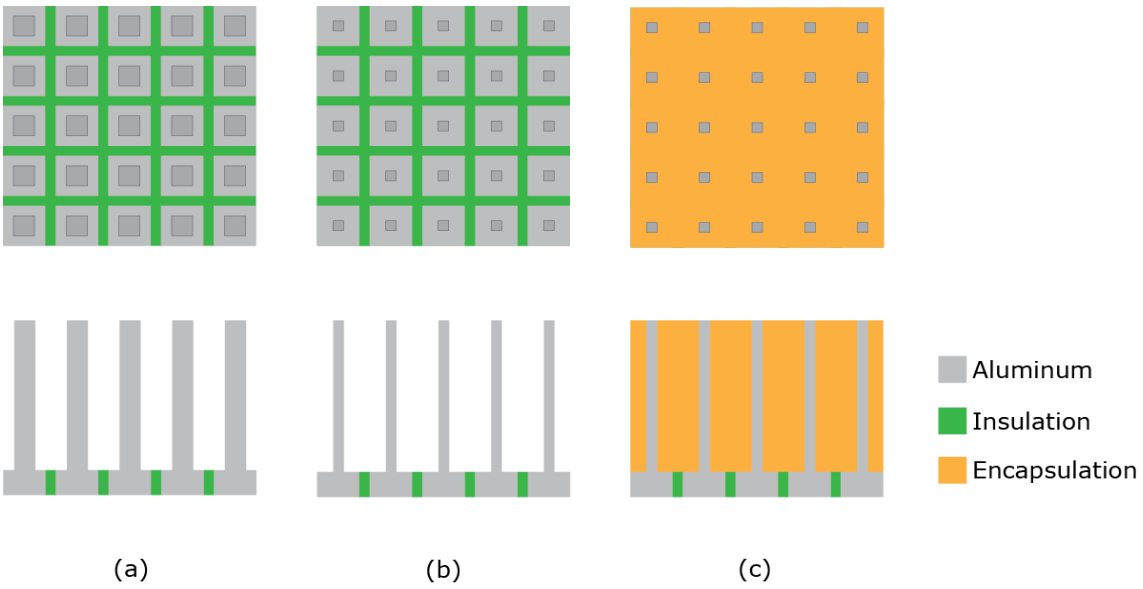

Figure 3.12: Machining of the top side of the substrate: *first row*, top view; *second row*, side view. (a) Diced pillars. (b) Pillars after wet-etching. (c) Resulting block after encapsulation deposition.

A series of cuts was performed at the top side performing tips at the top of each pillar (Figure 3.13a). The array underwent a thin-film deposition step in order to make the tips functional electrodes. The epoxy served as a selective mask for deposition since after the dicing step only the aluminum at the tips were exposed (Figure 3.13b). Platinum was used as electrode material due to its' biocompatibility, biostability and high-charge density threshold which is important for stimulation purposes [5]. The final step used dicing to remove the excess inter-pillar epoxy, leaving only a thin layer around each pillar. The result was an array with encapsulated high-aspect-ratio pillars with electrodes at the tips (Figure 3.13c).

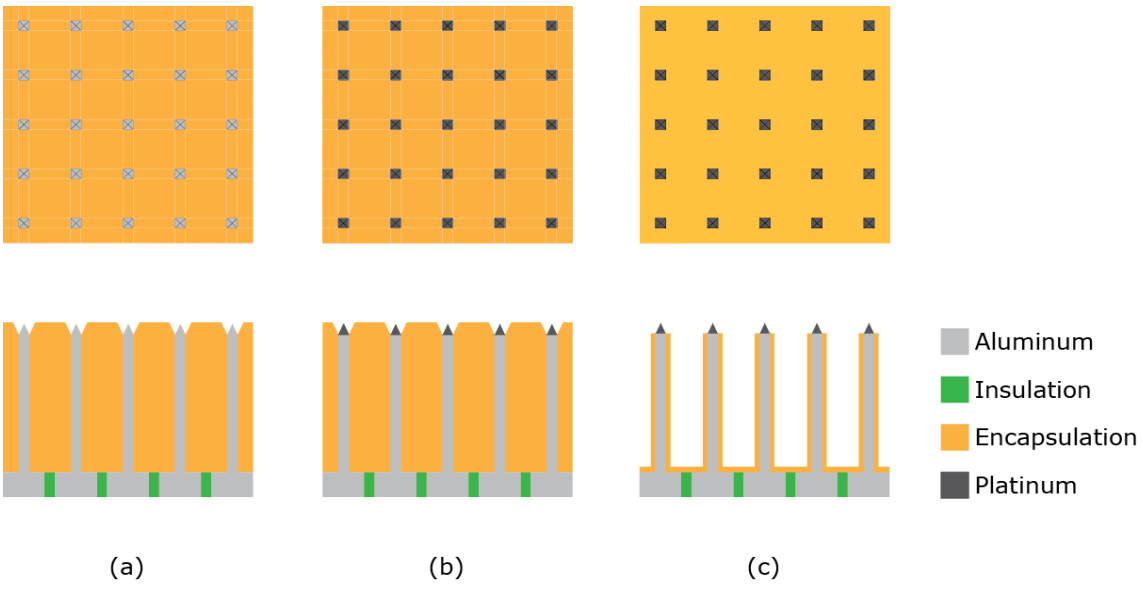

Figure 3.13: Final dicing steps: *first row*, top view; *second row*, side view. (a) Tips after surface dicing with beveled blade. (b) After deposition of platinum. (c) Final array after removal of excess encapsulation.

3.2.2 Experimental Results

The second prototype was made from a 4 mm thick and 4.2 mm wide aluminum substrate. In order to have a higher density of electrodes on the second prototype, a thinner blade (120 µm thick) was used to perform the bottom side cuts. A thinner blade implies thinner grooves, which allowed more closely spaced pillars. Due to the size of the protruding diamond grits, the grooves performed by this blade had an approximate width of 150 µm. The cutting program performed 600 µm spaced and 1 mm deep grooves. Just like in the first prototype, a reference offset of 3 mm was used to allow cuts above 2 mm (Table 3.4). The result was grid patterned grooves on the bottom side of the substrate that delineated the pads region (Figure 3.14a).

Table 3.4: Second prototype's parameters for pads dicing.

Parameter	Value	Comments
Blade thickness	120 µm	ZHDG that performs 150 µm wide grooves in aluminum
Jump #1	600 µm	Distance between cuts
Feed speed	1 mm/s	Speed at which the cut is performed
Z-blade	3 mm	Z-blade (3 mm) = reference offset (3 mm) + z-index (1 mm)

The grooves were filled with an epoxy resin by pressing with a small spatula against the bottom side (Figure 3.14b). For increased temperature resistance, an epoxy with a working temperature of 180 ºC was used (Hysol® 9492™) [6]. An epoxy with superior working temperature than the previous one was chosen in order to better withstand thin-film processing. After curing for 24 hours at ambient temperature, the excess epoxy at the backside was removed through manual polishing with a P2000 sandpaper.

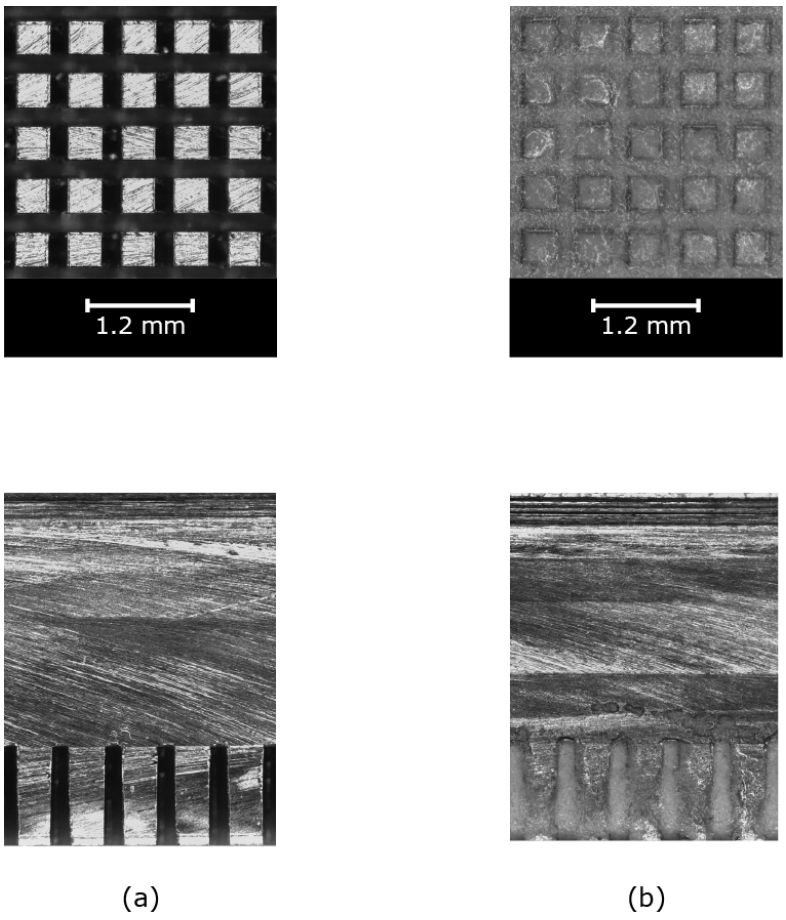

Figure 3.14: Photos after the first dicing and deposition stage with scale bar: *first row*, bottom view; *second row*, side view. The scale bar is equal for both rows. (a) Array after dicing and (b) after epoxy deposition.

After having the pads region defined and the insulation set, the substrate was turned over and the second dicing procedure was executed (Figure 3.15a). The cutting program performed 280 µm wide and 3 mm long pillars (Table 3.5).

Table 3.5: Second prototype's parameters for pillars dicing.

Parameter	Value	Comments
Blade thickness	250 µm	V-shaped ZHDG that performs 320 µm wide grooves in aluminum
Jump #1	600 µm	Pillar width (280 µm) = jump #1 (600 µm) – groove width (320 µm)
Feed speed	0.5 mm/s	
Z-blade	1 mm	Pillar length (3 mm) = substrate thickness (4 mm) – z-blade (1 mm)

Afterwards, the wet-etching of the array was performed by immersing it, in Transene type A aluminum etchant [3]. The etchant was in constant movement with the aid of a

magnetic stirrer, and kept at a constant temperature of 50ºC. The wet-etching stage removed the burr accumulated at the pillars edges and, at the same time, decreased the pillar's cross-section. The array was kept on the acid for 70 minutes, reducing the width of the pillars from approximately 280 µm to 120 µm before and after the etching, respectively (Figure 3.15b).

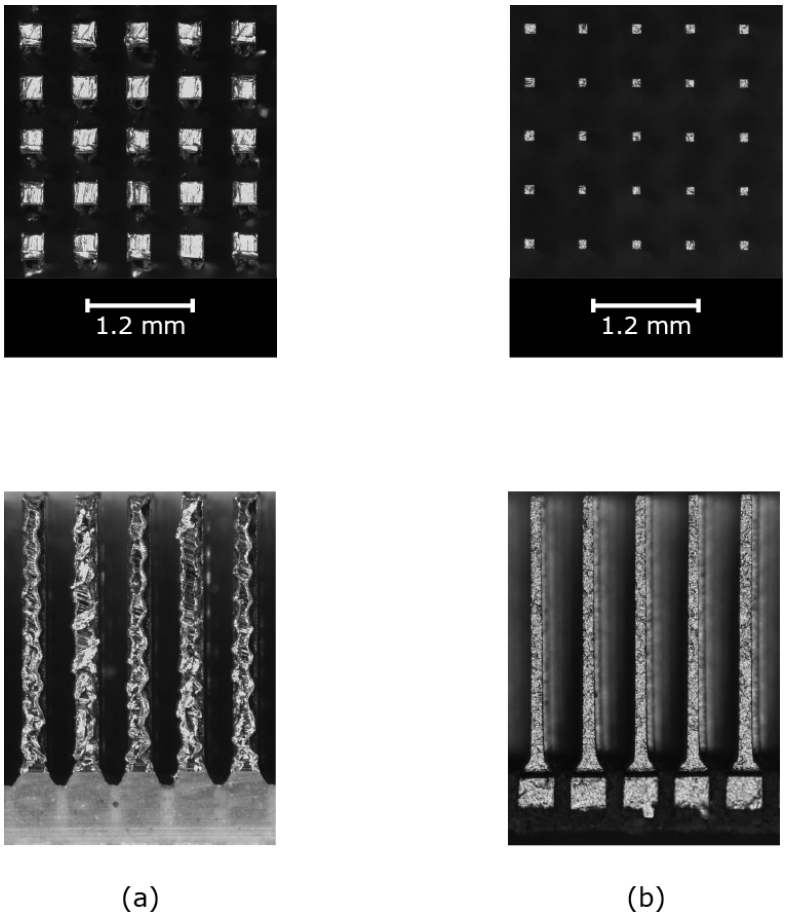

Figure 3.15: Photos after the second dicing stage: *first row*, top view; *second row*, side view. The scale bar is equal for both rows. (a) Pillars after dicing. (b) Pillars after wet-etching stage.

In the next stage a thick layer of medical grade epoxy (Hysol^{TM} M-31CL) was deposited over the structure. This epoxy was used mainly because of its biocompatibility and translucent properties, which helped on cuts alignment, and photo clarity [7]. Prior to the deposition, one gram of the two component epoxy was mixed, and the resulting air bubbles were removed in a degassing chamber for 45 minutes. After degassing, the epoxy was poured over the array, filling the empty spaces between pillars. The pouring process was performed manually and stopped as soon as the array was totally enveloped by the epoxy. The glue was left to cure for 24 hours at room temperature before further processing.

The third dicing stage was composed by two steps that removed the excess epoxy from the surface and bulk. The first step performed tips on the surface of the substrate in a

similar manner than the first prototype (Figure 3.16a). A cutting program performed 300 µm long and 300 µm wide pyramidal tips (Table 3.6).

Table 3.6: Second prototype's parameters for tips dicing.

Parameter	Value	Comments
Blade thickness	250 µm	V-shaped ZHDG
Jump #1	250 µm	Tip width (330 µm) = pillar width (330 µm)
Jump #2	350 µm	Tips spacing (1 mm) = jump #1 (330 µm) + jump #2 (670 µm)
Feed speed	0.5 mm/s	
Z-blade	3.7 mm	Tip length (300 µm) = substrate thickness (4 mm) – z-blade (3.7 mm) Z-blade (3.7 mm) = reference offset (3 mm) + z-index (0.7 mm)

The next stage was the deposition of titanium and platinum at the pillars' tips. The titanium served as an adhesive layer while platinum served as the electrode material. The thin-film covered the entire top surface of the array, this way functionalizing the tips. During deposition, the epoxy served as a mask allowing the deposition of material at the exposed tip and not the pillar. The titanium deposition was performed by e-beam at a starting pressure of 2.8×10^{-6} mbar while supplying a current of 60 mA and an electric potential of 7 kV. The platinum deposition was performed by DC sputtering at a starting pressure of 7.2×10^{-6} mbar while supplying an electric current of 33 mA, electric potential of 300 V, and a constant flow of 40 sccm of argon. The titanium deposition lasted for 5 minutes while the platinum deposition lasted for 151 minutes. The resulting layers had 70 nm and 185 nm of thickness for the titanium and platinum, respectively. The temperature at the substrate was measured for each deposition in order to avoid exceeding the constituent materials maximum working temperature. For the titanium deposition, the measured temperature at the substrate was 60ºC, while for platinum the maximum was 45ºC.

The tips were covered by a layer of platinum, which can transduce between ionic concentration and electrical potential. A last dicing step needed to be performed in order to remove the excess epoxy and shape the encapsulated pillars. Each cut was performed two times at increasing depths, this way avoiding excessive friction between the blade and the sample. If the first cut would have been performed at full depth, the sample would detach from the holder due to the excessive friction. The cutting program performed 160 µm wide and 2.9 mm long pillars, each with an approximate 20 µm wide layer of epoxy all around the pillar (Table 3.7). Smaller encapsulation layers were achieved but they required a manual row by row adjustment. The final array with epoxy insulation is shown on Figure 3.16b.

Table 3.7: Second prototype's parameters for encapsulation excess removal.

Parameter	Value	Comments
Blade thickness	250 µm	V-shaped ZHDG that performs 300 µm wide grooves in epoxy
Jump #1	460 µm	Pillar width (160 µm) = jump #1 (460 µm) – groove width (300 µm)
Jump #2	140 µm	Pillars' spacing (600 µm) = jump #1 (460 µm) + jump #2 (140 µm)
Feed speed	0.3 mm/s	Slow speed to avoid high blade-substrate friction
Z-blade #1	2 mm	Depth of the first cut (2 mm) = substrate thickness (4 mm) – z-blade #1 (2 mm)
Z-blade #2	1.1 mm	Pillar length (2.9 mm) = substrate thickness (4 mm) – z-blade #2 (1.1 mm)

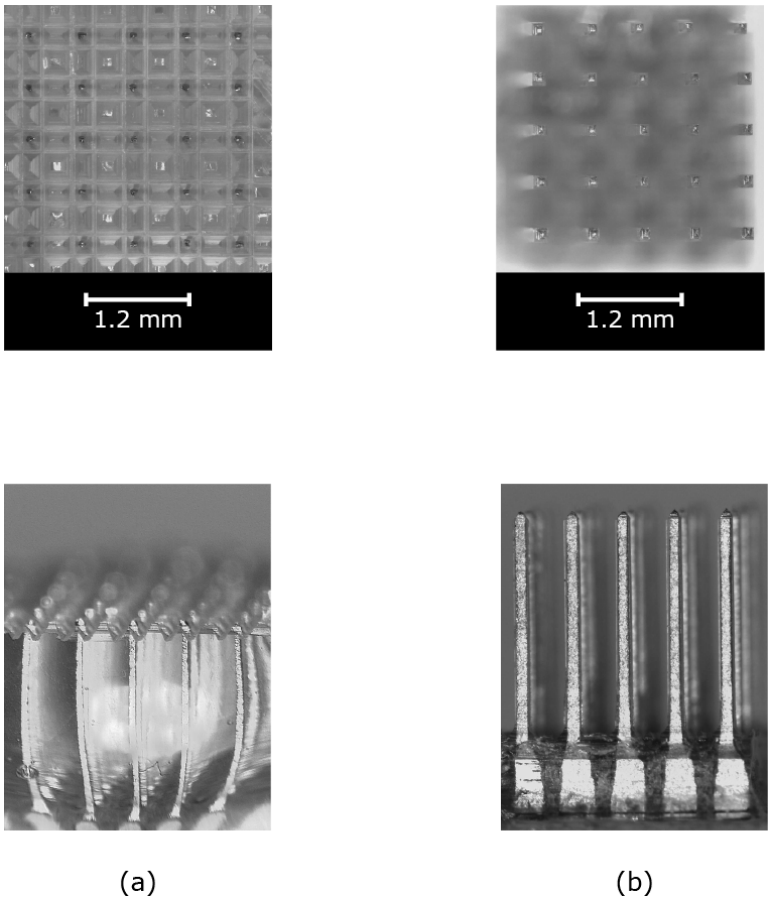

Figure 3.16: Photos after the last dicing stage: *first row*, top view; *second row*, side view. The scale bar is equal for both rows. (a) Tips at the surface of the top side after dicing. The convex shape of the epoxy generates an optical distortion on the pillars shape. (b) Encapsulated pillars after dicing.

3.3 Comparison Between Fabrication Approaches

Both fabrication approaches were able to perform tridimensional neural arrays. In terms of single array fabrication both needed approximately the same amount of time. The second approach needed less fabrication time in terms of batch fabrication, especially due to the anodizing and masking procedures.

The second approach offered other key improvements compared to the first. Instead of relying on the careful positioning of an aluminum foil for masking during thin-film deposition, it used a thick epoxy layer. This methodology increased repeatability and accuracy of the exposed tip, since it relied on the dicer's precision (2 µm for DAD 2H/6T). The width of the pillars went from 250 µm in the first prototype to 160 µm on the second, which represents a reduction of 64 %. This reduction in width is beneficial since it decreases neural tissue displacement and consequently decreases trauma after insertion. The use of platinum increases the charge density threshold when compared to gold [8].

References

[1] A. Altuna, G. Gabriel, L. Menéndez de la Prida, M. Tijero, A. Guimerá, J. Berganzo, R. Salido, R. Villa, and L. J. Fernández, "SU-8-based microneedles for in vitro neural applications," *J. Micromechanics Microengineering*, vol. 20, no. 6, Jun. 2010.

[2] Henkel AG & Co., "Hysol® 3430™ Technical Datasheet," 2008. Available at: http://www.loctite.co.uk/fullproduct-list-loctite-4995.htm?countryCode=uke&BU=industrial&parentredDotUID=productfinder&redDotUID=1000000IC7Z.

[3] Transene Company Inc., "Transene type A aluminum etchant," 2014. Available at: http://transene.com/aluminum/.

[4] D. S. Finch, T. Oreskovic, K. Ramadurai, C. F. Herrmann, S. M. George, and R. L. Mahajan, "Biocompatibility of atomic layer-deposited alumina thin films.," *J. Biomed. Mater. Res. A*, vol. 87, no. 1, pp. 100–106, Oct. 2008.

[5] S. F. Cogan, "Neural stimulation and recording electrodes," *Annu. Rev. Biomed. Eng.*, vol. 10, pp. 275–309, Jan. 2008.

[6] Henkel AG & Co., "Hysol® 9492™ Technical Datasheet," 2007. Available: http://www.loctite.co.uk/fullproduct-list-loctite-4995.htm?countryCode=uke&BU=industrial&parentredDotUID=productfinder&redDotUID=1000000J9BL.

[7] Henkel AG & Co., "Hysol® M-31CL™ Technical Datasheet," 2005. Available: http://www.loctite.co.uk/loctite-4087.htm?nodeid=8802635087873.

[8] L. A. Geddes and R. Roeder, "Criteria for the Selection of Materials for Implanted Electrodes," *Ann. Biomed. Eng.*, vol. 31, no. 7, pp. 879–890, Jul. 2003.

Chapter 4

Silicon Array Fabrication

This chapter describes the fabrication of two prototypes of neural arrays based on silicon wafers. Both prototypes relied mainly on dicing technology for fabrication of the structure. The insulation approach was different between both prototypes. Thermomigration was used in the first prototype in order to perform the insulation between pillars and create conductive paths in the n-type silicon. The second prototype relied mainly on polymer deposition for the insulation and encapsulation.

The first prototype achieved 3 mm long and 0.63 mm wide pillars, while the second achieved 4 mm long and 0.18 mm wide, resulting on approximate aspect ratios of 5:1 and 22:1, respectively.

Due to incomplete migration of aluminum in 4 mm thick silicon substrates, the first prototype did not have a complete electrical connection between pads and tips. The second prototype represented an evolution of the first, since it could perform an electrical connection between pads and tips, and also in terms of aspect ratio. Moreover, the fabrication process of the second prototype showed greater simplicity and reproducibility when compared to the first, since it relied on dicing and polymer deposition, and avoided the complexities of thermomigration process.

4.1 First Prototype

4.1.1 Fabrication Process

The first silicon prototype consisted of 100 individualized electrodes (10 rows by 10 columns) with 1 mm of spacing between them. In order to achieve such an array, the following fabrication steps were proposed:

1. Silicon wafer dicing
2. Aluminum deposition
3. Thermomigration
4. Micropillars dicing
5. Wet-etching
6. Pillars dicing
7. Encapsulation
8. Removal of encapsulation at the tips
9. Thin-film deposition

The first dicing step performed a series of 10 mm spaced cuts on an n-type, 4 mm thick wafer. The result were 10 mm × 10 mm square dies and also non-square dies due to the circular shape of the wafer (Figure 4.1a). Only the perfectly square dies were used on the following stages (Figure 4.1b).

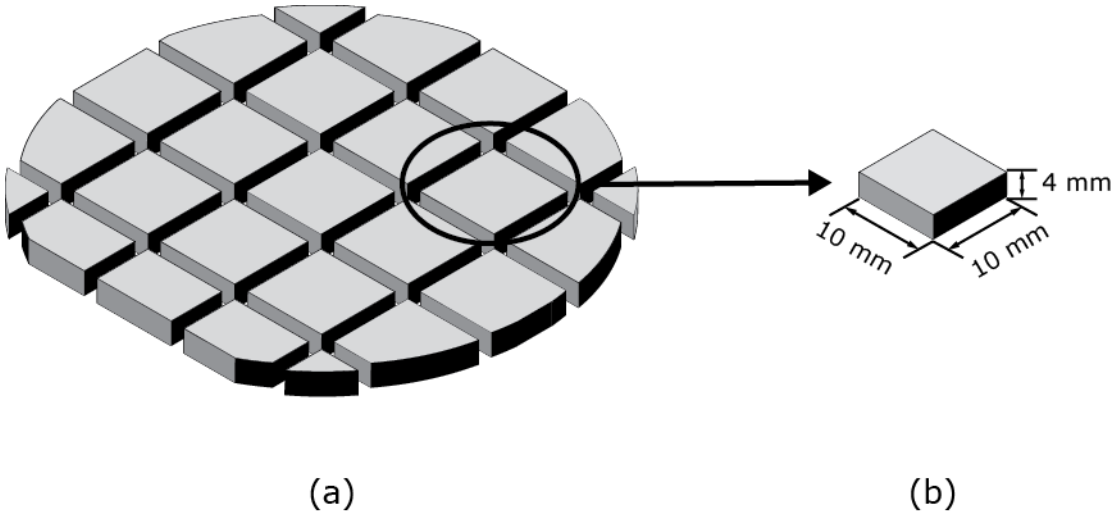

Figure 4.1: Dicing of the silicon wafer. (a) Diced wafer. (b) Single, perfectly square die.

Afterwards, a deposition of a grid patterned thin layer of aluminum on the bottom side

of the substrate was proposed (Figure 4.2). This process will be discussed in further detail on section 4.1.2.

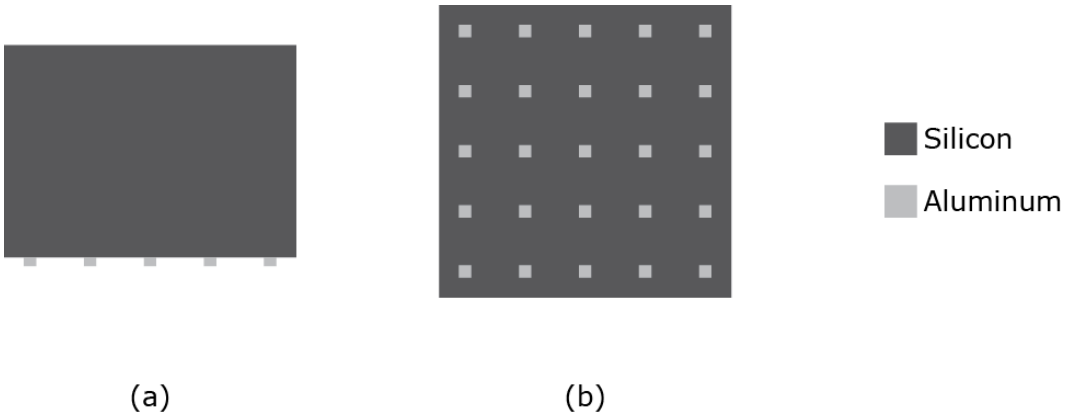

Figure 4.2: Grid patterned aluminum squares deposition over the substrate. (a) Side view. (b) Bottom view.

The sample with aluminum was subjected to a temperature gradient, which resulted in the migration of a mixture of aluminum and silicon through the wafer (thermomigration). The heat sink was cooler than the heat source, this way generating a temperature gradient between the substrate's sides. As the aluminum melted due to the temperature of the heat sink (above 550 ºC), it mixed with silicon, forming small droplets that traveled toward the heat source. The result was trails of aluminum-doped silicon.

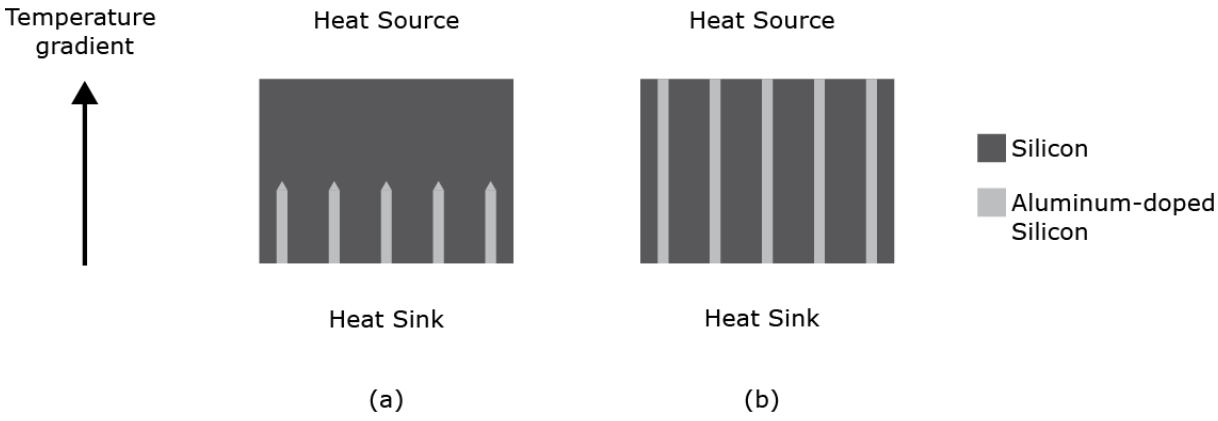

Figure 4.3: Thermomigration of aluminum on silicon. (a) Migration of the silicon-aluminum mixture from the cooler side towards the hotter side. (b) Aluminum-doped trails in silicon after the migration process.

This doping process transforms the n-type silicon into p^+-type. The p^+ symbol stands for heavily-doped silicon. The high degree of doping is useful since its low resistivity (on the order of 10^{-6} Ω/m [1]) allows the transmission of electrical signals with little attenuation. The alternation between n and p^+-type silicon creates opposing pn junctions between trails making

the individual trails electrically isolated from each other (Figure 4.4). These junctions prevent the crosstalk between electrodes that could introduce undesired signals in the readings.

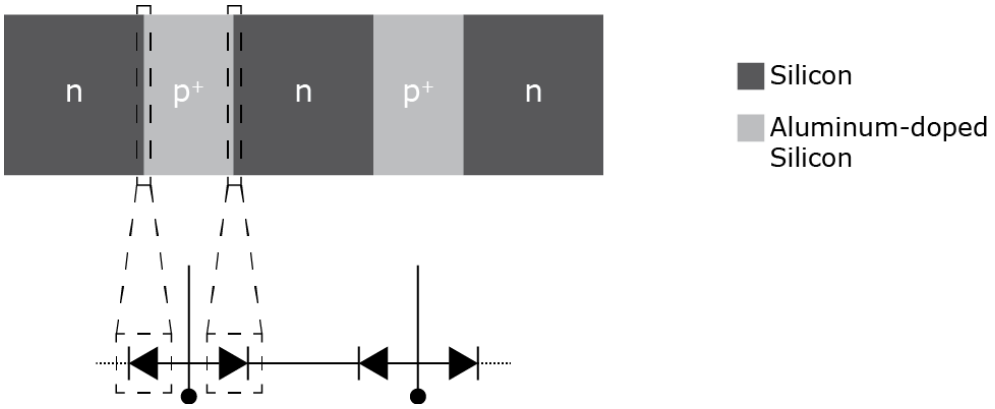

Figure 4.4: Adjacent aluminum-doped silicon trails and equivalent electric circuit. Note that no current can flow into the trails due to the back to back diodes.

The next step comprised the dicing of square micropillars at the top side (Figure 4.5a). Afterwards, a wet-etch step transformed the micropillars into micropyramids, which would serve as the tips on the final array (Figure 4.5b). The crystalline orientation of the silicon, and the etchant used, caused the anisotropic etching that shaped the micropillars into micropyramids [2].

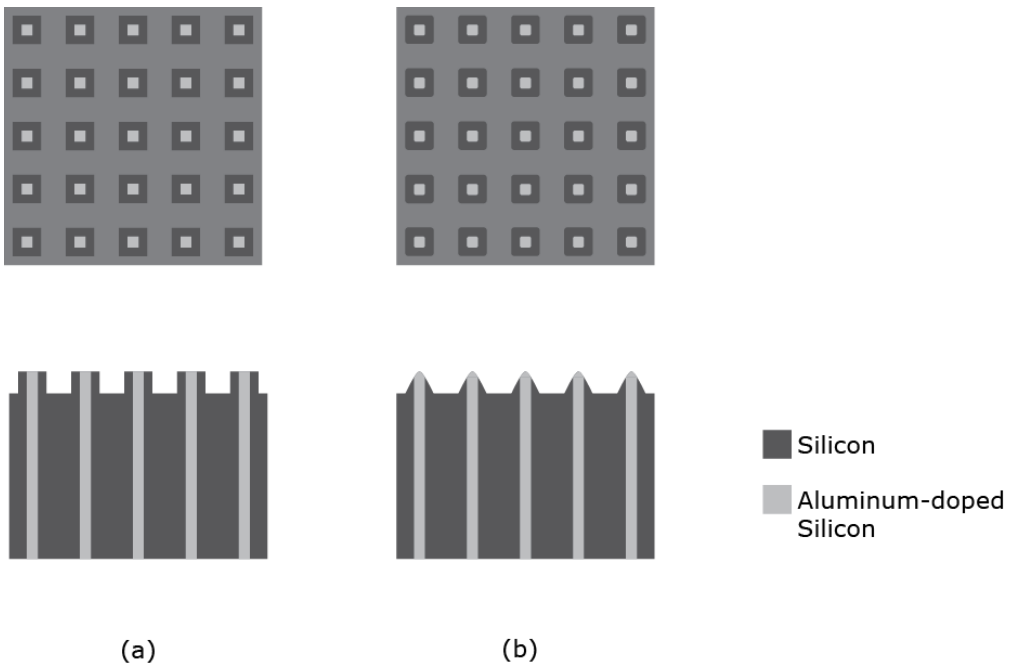

Figure 4.5: First dicing stage and wet-etching: *first row*, top view; *second row*, side view. For clarity of representation only a 5×5 array is illustrated. (a) Micropillars at the top side. (b) Micropyramids formation due to anisotropic etching.

After the tips fabrication, a dicing stage performed deep cuts on the substrate. The proposed high-aspect-ratio pillars should have an electrically conductive core caused by the aluminum doping, and be electrically isolated from each other due to the inversely polarized *pn* junctions (Figure 4.6a). Since silicon is not biocompatible, an encapsulating layer of cyanoacrylate was deposited by drop coating.

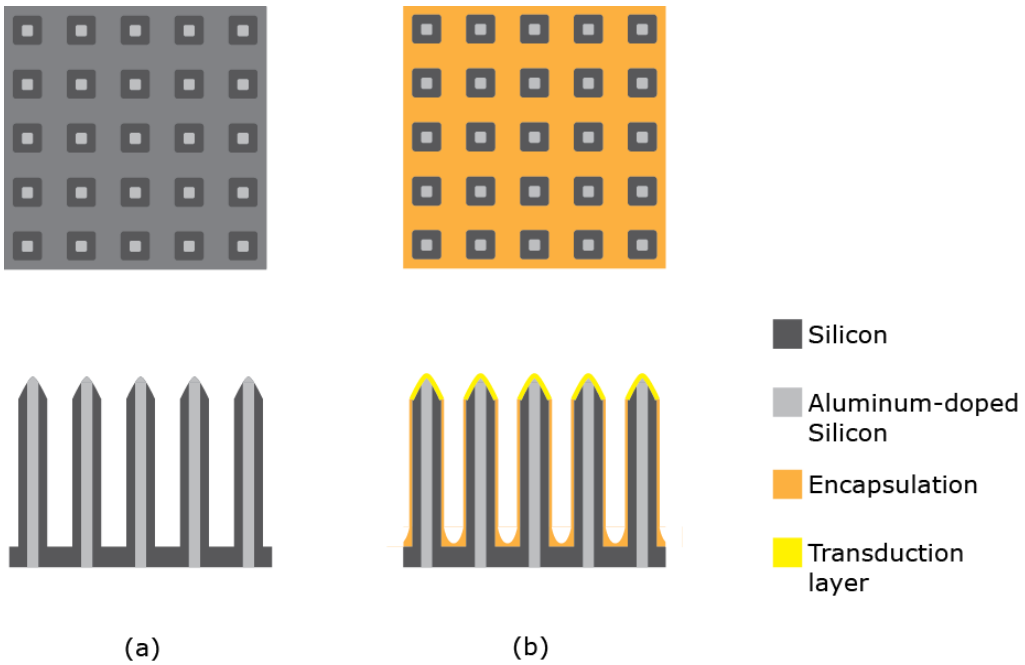

Figure 4.6: Second dicing stage and encapsulation: *first row*, top view; *second row*, side view. For clarity of representation only a 5×5 array is illustrated. (a) High-aspect-ratio pillars with a conductive core. (b) Final array with encapsulated pillars.

The two final steps comprised of the removal of cyanoacrylate at the tips, and the thin-film deposition with a mask (Figure 4.6b).

4.1.2 Experimental Results

The first step consisted on the dicing of a 4 mm thick, n-type silicon. A 150 µm thick NBC-ZB blade able to perform deep grooves, without wafer chipping or breaking, was used. Table 4.1 describes the blade and program parameter to cut 10 mm × 10 mm square dies on a 2 inch silicon wafer.

Table 4.1: First prototype's parameters for wafer dicing.

Parameter	Value	Comments
Blade thickness	150 µm	NBC-ZB that performs 170 µm wide grooves in silicon
Jump #1	10 mm	Performs 10 mm wide silicon dies
Feed speed	0.5 mm/s	Speed at which the cut is performed
Z-blade	0.1 mm	Avoid blade touching the chunk

Regarding the thermomigration tests, two different thicknesses were used for the silicon substrates; 500 µm thick for the initial tests and 4 mm thick substrates for the final tests. The silicon substrates were placed in a furnace capable of achieving a maximum temperature of 950 ºC (Figure 4.8a). The heating zone is situated at the bottom part of the furnace, while the top part is open to the exterior via a through hole in the lid (Figure 4.7a). The convection of hot air to the exterior produced a cooler side at the top while the heating zone produced a hotter side at the bottom, generating a thermal gradient. The sample was placed on a stainless steel support and was composed by the sample holder (stainless steel), the silicon substrate, and aluminum (Figure 4.7b). Figure 4.8b, shows the interior of the furnace with the support and the sample holder, used during experiments.

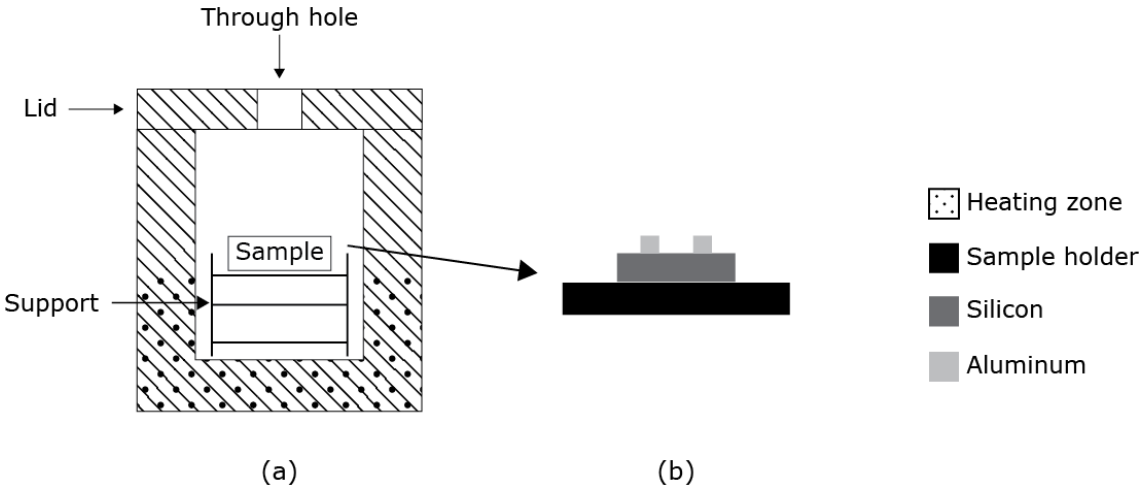

Figure 4.7: Thermomigration set-up. (a) Cross-sectional view of the furnace and sample support. (b) Sample components.

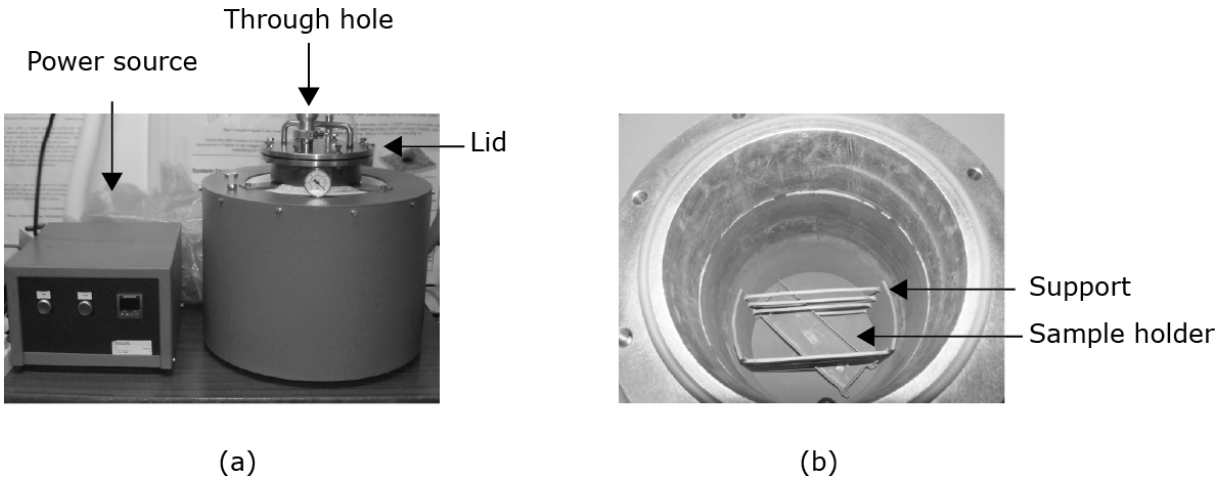

Figure 4.8: Furnace used for thermomigration. (a) External view of the furnace and power source. (b) Interior view of the furnace with pale red appearance on the heating zone.

A 500 µm n-type silicon substrate was placed over the sample holder with two pieces of aluminum facing up towards the cooler side. The lid was closed and the furnace temperature was set to 950 ºC. The samples remained inside the furnace for a total of 4.5 hours (1 hour to reach the desired temperature, 2 hours of processing, and 1.5 hours for cooling down).

Figure 4.9 shows the results after the heating procedure. Signs of aluminum melting can be observed on the top side of the substrate, while evidence of aluminum migration can be seen on the bottom side (Figure 4.9a and b). Figure 4.9c shows a considerable amount of aluminum migration through the silicon substrate. A test performed with a multimeter showed that top and bottom sides were short circuited through the aluminum, confirming that migration occurred.

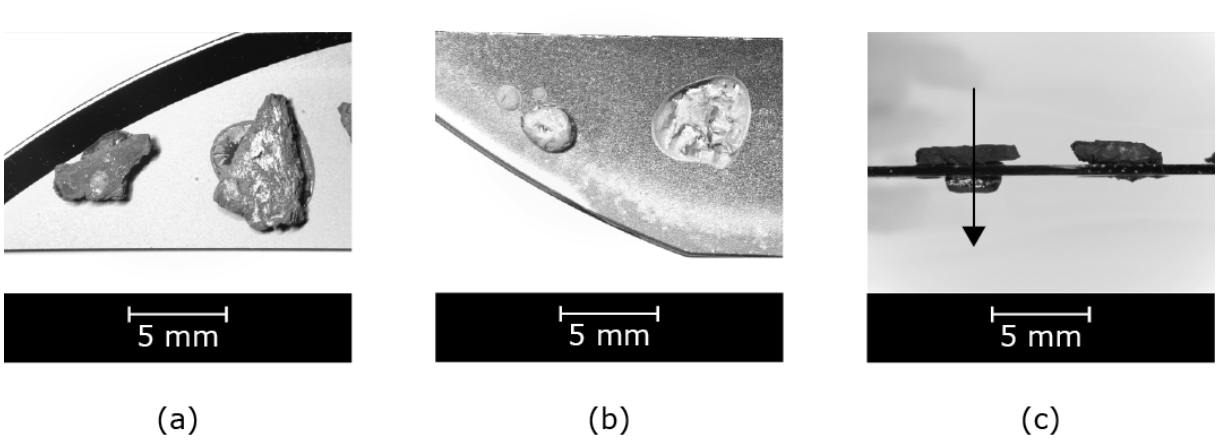

Figure 4.9: Thermomigration of aluminum on a 500 µm thick silicon substrate. (a) Top view. (b) Bottom view. (c) Side view with migration direction highlighted by an arrow.

The same set-up and heating parameters were used for migration tests on a 4 mm thick n-type silicon substrate. After the test, signs of aluminum melting could be observed at the top, while no signs of aluminum were observed at the bottom side (Figure 4.10a and b). This suggested that an incomplete migration occurred. For further investigation, the aluminum excess was removed from the top of the wafer manually and two cuts were performed over each migration zone (Figure 4.10c).

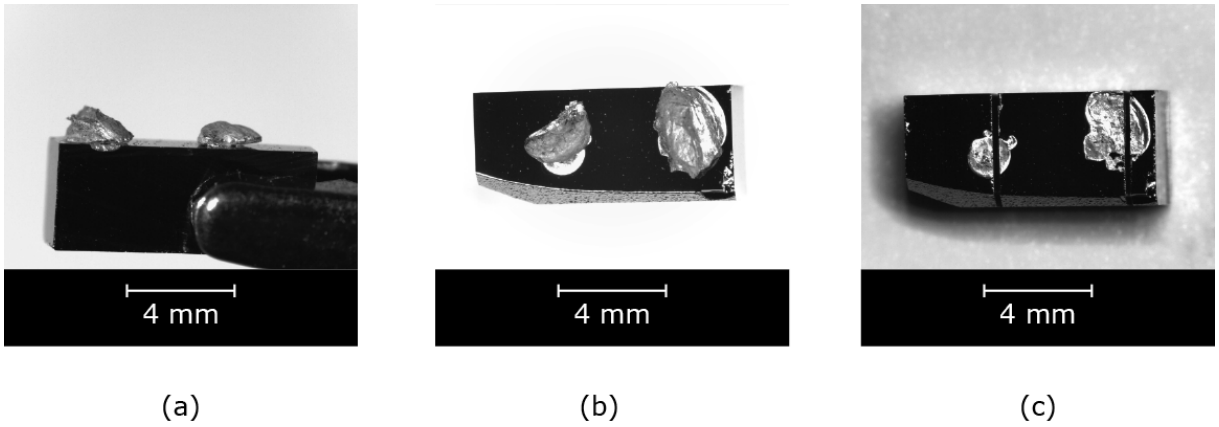

Figure 4.10: Thermomigration of aluminum on a 4 mm thick silicon substrate. (a) Side view. (b) Top view. (c) Cuts performed at aluminum migration area.

The diced cross-section showed a partial migration on the thick substrate (Figure 4.10a and b). Despite the existence of migration, the set-up and heating parameters could not achieve full migration. Further tests with different heating times, temperature oscillation and aluminum sizes, could not perform a complete migration on a 4 mm thick substrate.

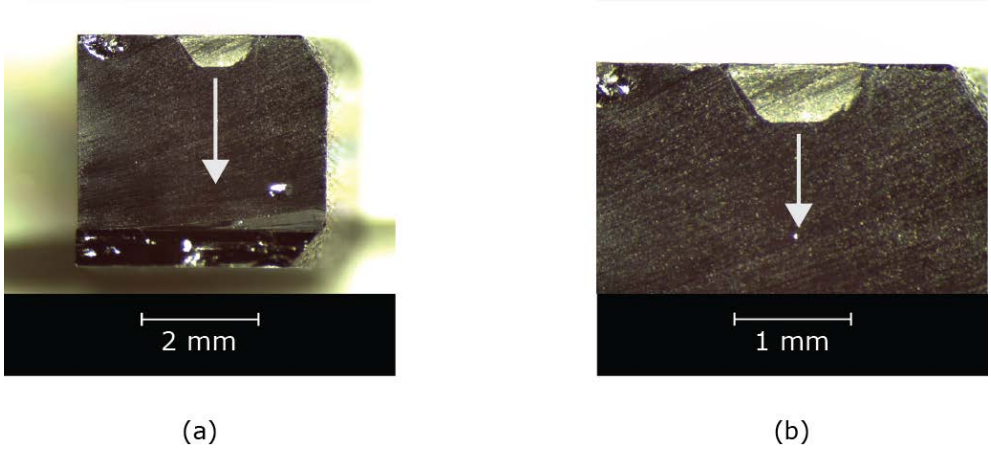

Figure 4.11: Cross sectional view of the 4 mm thick thermomigrated substrate. Migration direction is highlighted with an arrow. (a) Complete cross-section. (b) Close-up on the thermomigrated area.

Due to the unsuccessful migration with the furnace, a blowtorch was used as the heat

source. Flames with temperatures as high as 1995 ºC were achieved due to the propane gas with high levels of propylene. The blowtorch was placed beneath a stainless steel sheet support that radiated heat towards the bottom side of the sample. The top side was exposed to air, and created a thermal gradient between the top and bottom side of the sample, which generated thermomigration (Figure 4.12a). The blowtorch heated a 500 µm thick silicon substrate for 12 minutes, showing signs of partial migration (Figure 4.12b). The blowtorch gas reservoir allowed a maximum of 15 minutes of heating time.

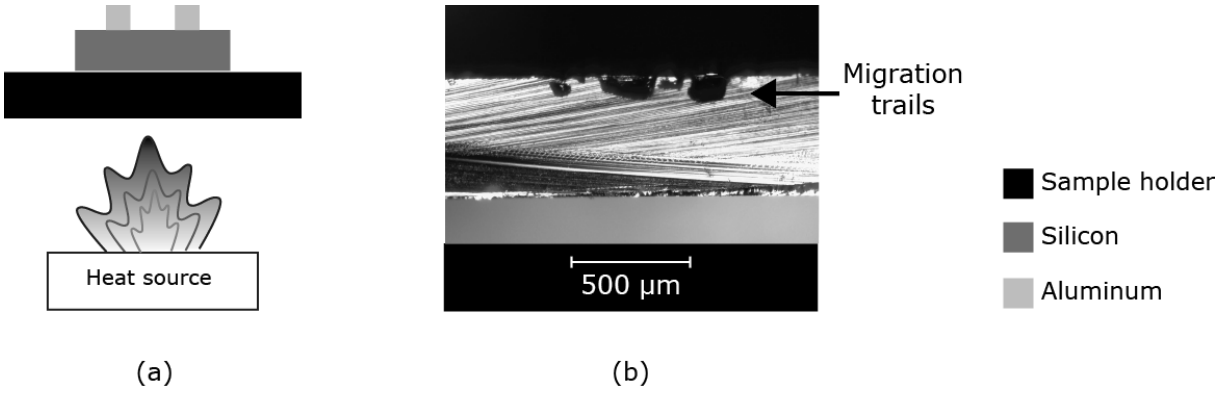

Figure 4.12: Thermomigration of aluminum on a 500 µm thick silicon substrate using a blowtorch as heat source. (a) Set-up configuration. (b) Aluminum migration in silicon.

Simultaneously to the thermomigration experiments, dicing and wet-etching tests were performed in non-migrated samples. Micropillars were diced on the top surface of a 10 mm × 10 mm × 4 mm n-type silicon substrate (Figure 4.14a). The dicing program performed 1 mm spaced, 180 µm wide, and 300 µm long silicon micropillars (Table 4.2). An illustration of the program can be on Figure 4.13.

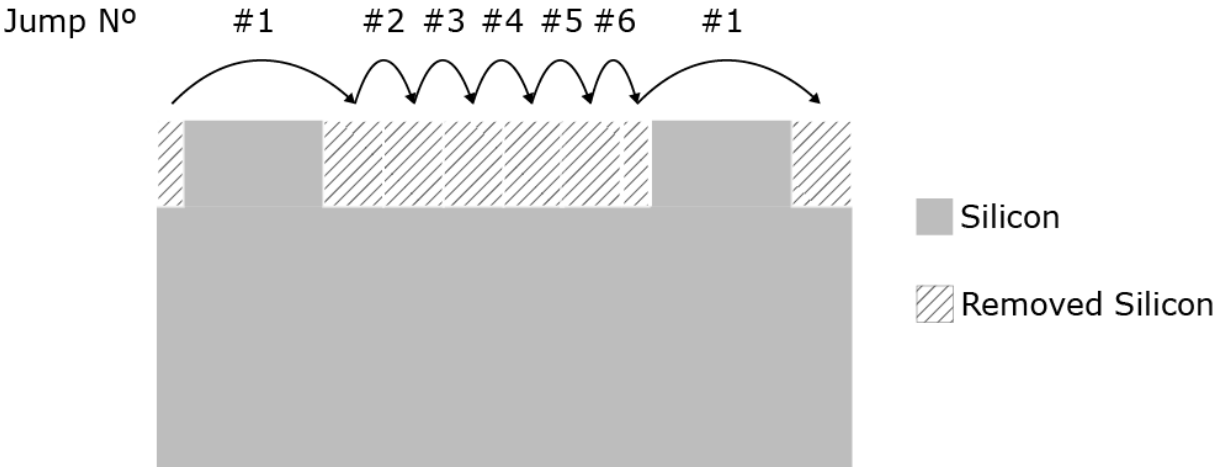

Figure 4.13: Illustration of the dicing program.

Table 4.2: First prototype's parameters for micropillars dicing.

Parameter	Value	Comments
Blade thickness	150 µm	NBC-ZB that performs 170 µm wide grooves in silicon
Jump #1	350 µm	Micropillar width (180 µm) = jump #1 (350 µm) – groove width (170 µm)
Jump #2	150 µm	
Jump #3	150 µm	
Jump #4	150 µm	
Jump #5	150 µm	
Jump #6	50 µm	Micropillars' spacing (1 mm) = sum of all jumps
Feed speed	5 mm/s	
Z-blade	3.7 mm	Micropillar length (300 µm) = substrate thickness (4 mm) – z-blade (3.7 mm)

Afterwards, the substrate underwent a wet-etching process in KOH for 4 hours. The KOH solution was kept at a constant temperature of 90ºC while being stirred with the aid of a rotating magnet. The combination of KOH and <100> n-type silicon, resulted on an anisotropic corrosion that transformed the micropillars into micropyramids (Figure 4.14b). The micropyramids were 330 µm wide and 190 µm long.

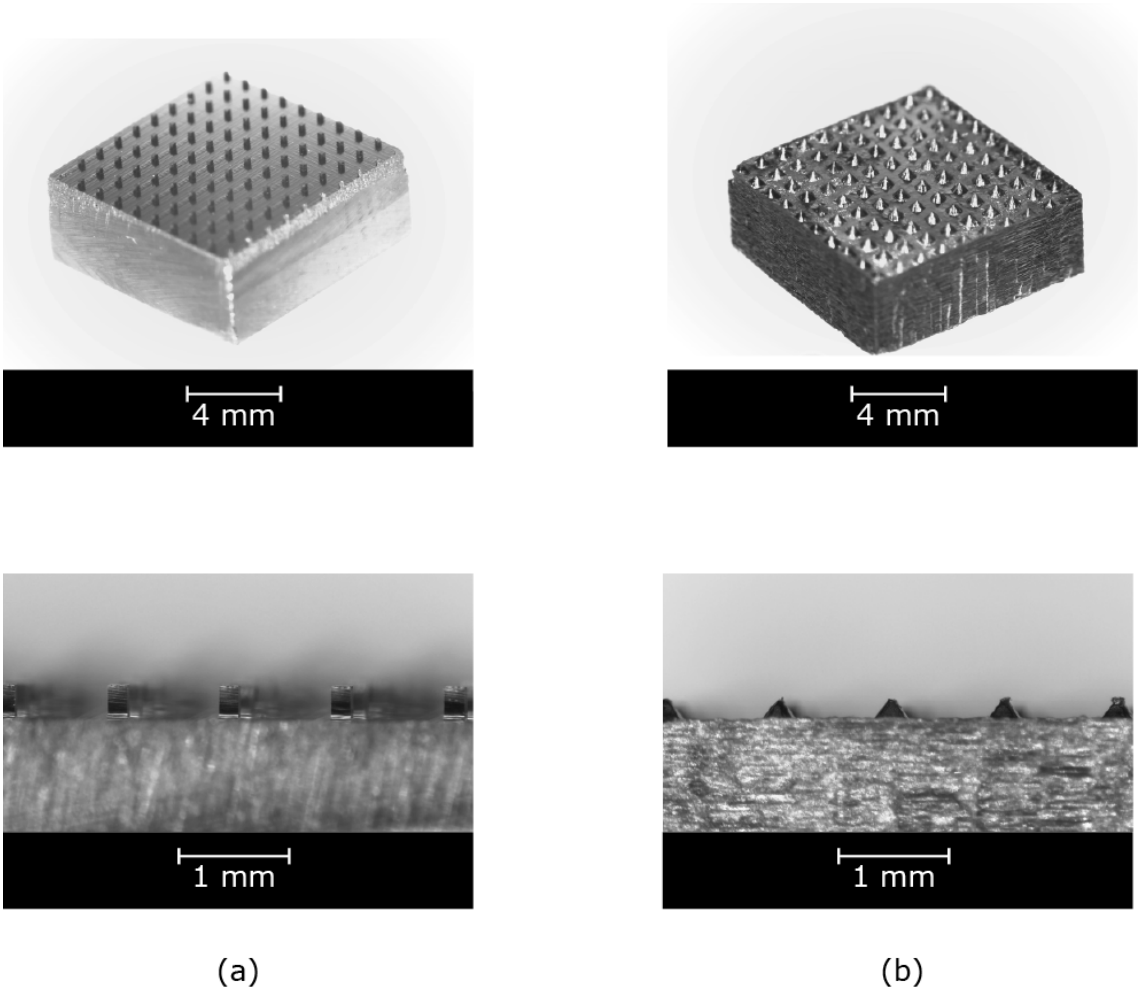

Figure 4.14: Photos after the dicing and etching step: *first row*, perspective view on the entire substrate; *second row*, partial side view. (a) Micropillars after dicing, (b) micropyramids after wet-etching step.

The next stage comprised of the dicing of long pillars with pyramidal tips. Deep grooves were cut between micropyramids (Table 4.3). The result was an array with 1 mm spaced, 3 mm long, and 630 µm wide pillars (Figure 4.15).

Table 4.3: First prototype's parameters for pillars dicing

Parameter	Value	Comments
Blade thickness	150 µm	NBC-ZB
Jump #1	800 µm	Pillar width (630 µm) = jump #1 (800 µm) – groove width (170 µm)
Jump #2	150 µm	
Jump #3	100 µm	Jump #2 and #3 removes the excess silicon between pillars
Feed speed	1 mm/s	
Z-blade	1 mm	Pillar length (3 mm) = substrate thickness (4 mm) – z-blade (1 mm)

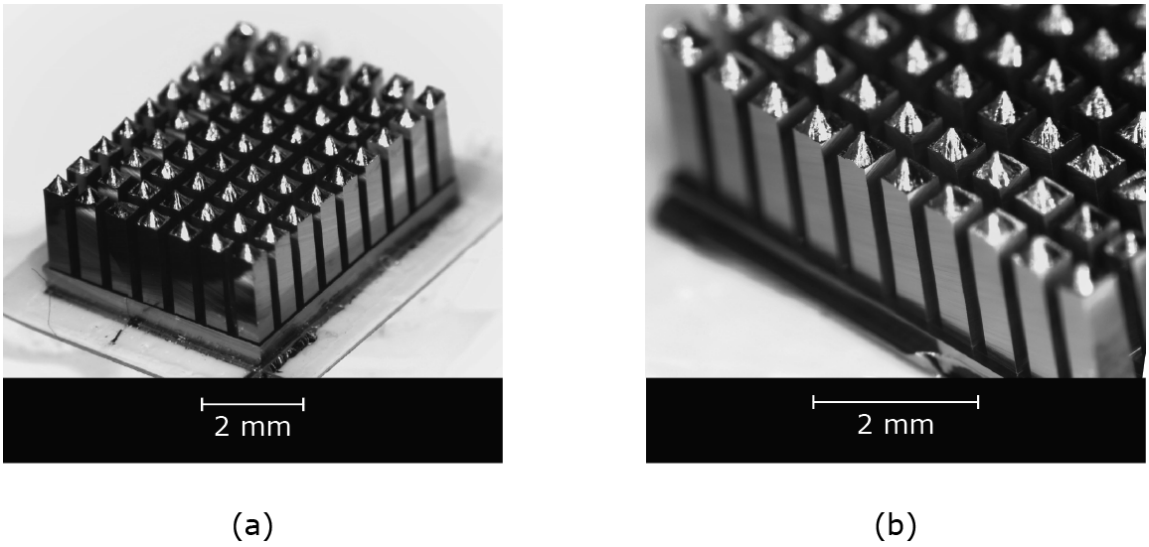

Figure 4.15: Photos of the tipped pillars. (a) Perspective view. (b) Detail on the tipped pillars.

The encapsulation tests were performed by applying consecutive drops of cyanoacrylate over the array and removing the polymer from the tips. The removal process was implemented by manually sanding the tips. These techniques showed to be unsuccessful since the drop coating could not coat evenly the pillars and the sanding could not expose the same amount of silicon on all tips.

Overall, the fabrication techniques could form tipped silicon pillars, but the migration process could not traverse the entire pillar. This shows that the dicing and wet-etching techniques are effective, while the thermomigration technique requires a custom made furnace in order to go beyond the 600 µm limit achieved by the present approach.

4.2 Second Prototype

4.2.1 Fabrication Process

A smaller array was proposed as the second prototype by decreasing the number of electrodes and their spacing. The smaller area of the array is more suitable for application on rats, and also the higher density improves the spatial resolution. The second prototype consisted of 36 individualized electrodes (6 rows by 6 columns) with 600 µm of spacing between them. The following fabrication steps were implemented:

1. Silicon wafer dicing
2. Pads region dicing
3. Adhesive deposition on pads region
4. Removal of excess adhesive on the pads region

5. Dicing of steps on silicon
6. Pillars dicing
7. Encapsulation
8. Tips dicing
9. Thin-film deposition
10. Removal of encapsulation excess

The first dicing step performed a series of cuts on a silicon wafer that resulted on 5 mm thick and 4 mm × 4 mm square substrates.

The pads region was performed by cutting the bottom side of the substrate, resulting on evenly spaced grooves (Figure 4.16a). Afterwards, a thin layer of the adhesive polymer was deposited over the substrate's bottom side (Figure 4.16b). Due to the uneven profile of the adhesive, an abrasion process was performed that made the bottom side flat, exposing the silicon pads (Figure 4.16c).

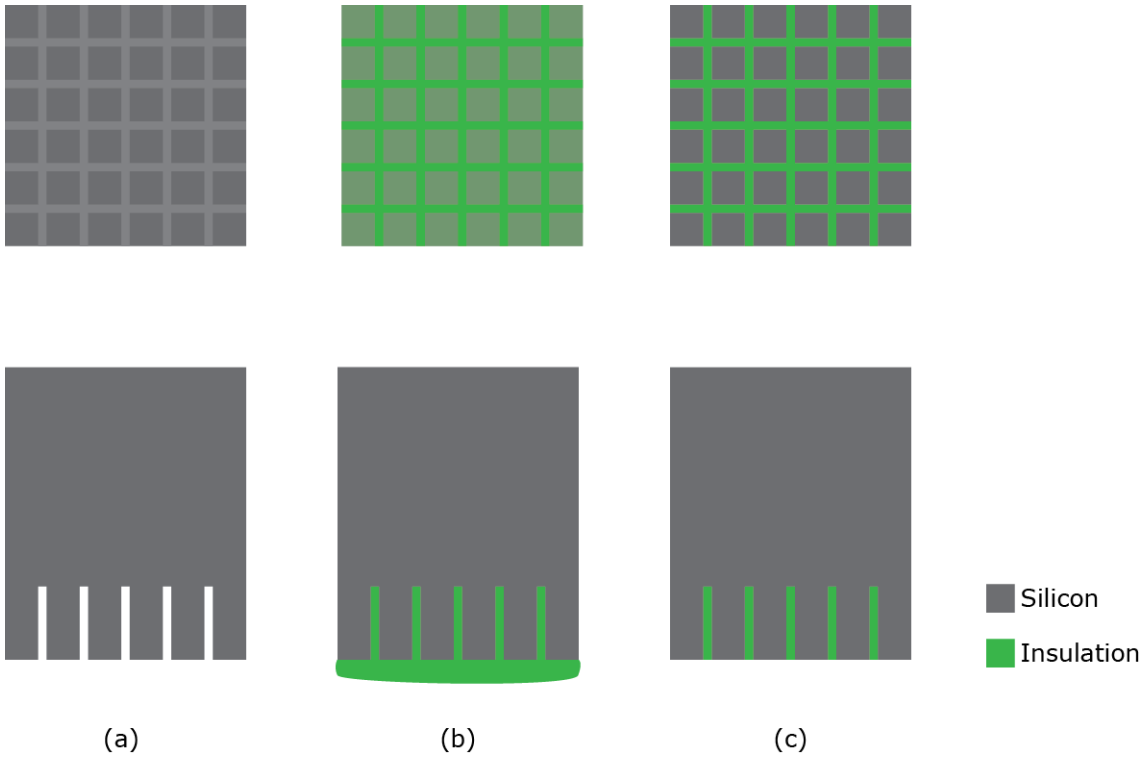

Figure 4.16: Illustration of fabrication steps two, three and four: *first row*, bottom view; *second row*, side view. Bottom side after: (a) dicing, (b) polymer deposition, and (c) abrasion.

After having the pads region defined and insulation material set on a grid pattern, the substrate's top side underwent dicing processes to perform pillars with different lengths. Successive cuts were made on the substrate's surface that accomplished three silicon

steps (Figure 4.17a). The width of the pillars was controlled by the y-axis jump, while the length of the pillars was controlled both by the z-blade and the thickness of the substrate (Figure 4.17b).

The next step added a biocompatible and electrically insulating epoxy over the top side. The material filled all empty spaces between pillars, resulting on a rigid block (Figure 4.17c).

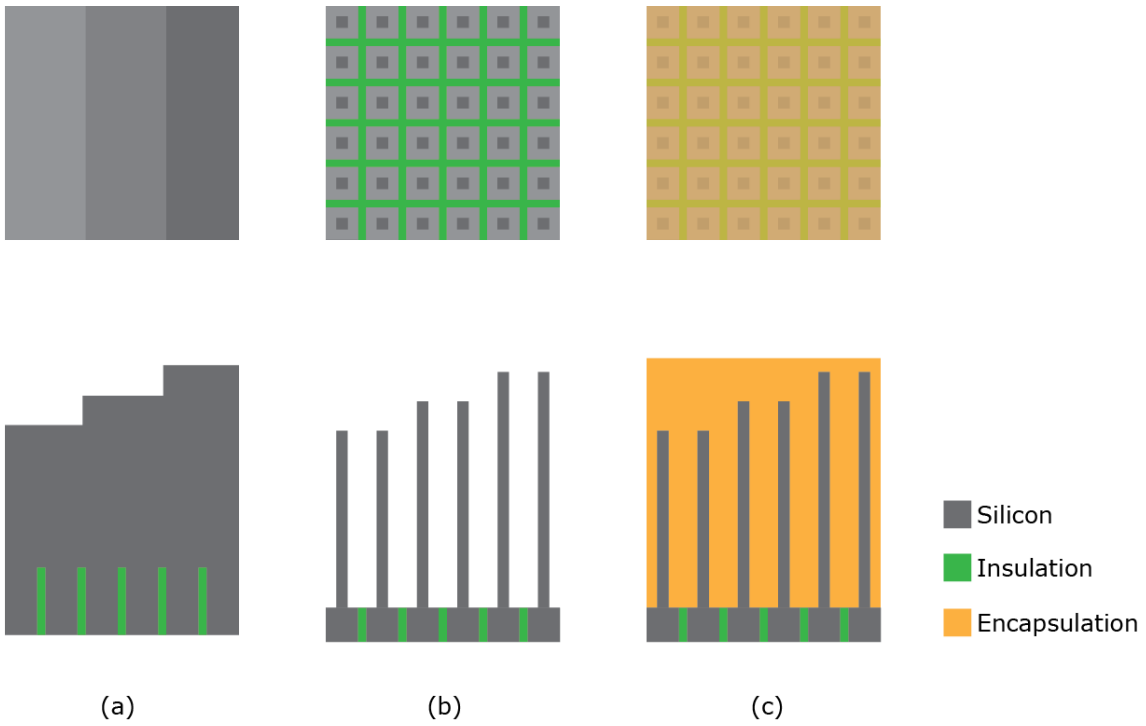

Figure 4.17: Top side dicing and encapsulation: *first row*, top view; *second row*, side view. (a) Silicon block with three steps diced on the top side. (b) Diced pillars with decreasing lengths. (c) Array encapsulation.

Afterwards, a series of cuts were performed at the top surface of the sample that removed the excess encapsulation above the pillars and performed the tips. The tips profile was determined by the shape of the beveled blade (Figure 4.18a).

In the next step, a thin layer of the platinum was deposited over the tips. This layer used thin-film deposition technique that will serve as the transducing material between brain and silicon (Figure 4.18b).

After the thin-film deposition, the excess encapsulation material between pillars was removed using the dicer. The result was an array with thin and long pillars with an electrode at each tip (Figure 4.18c).

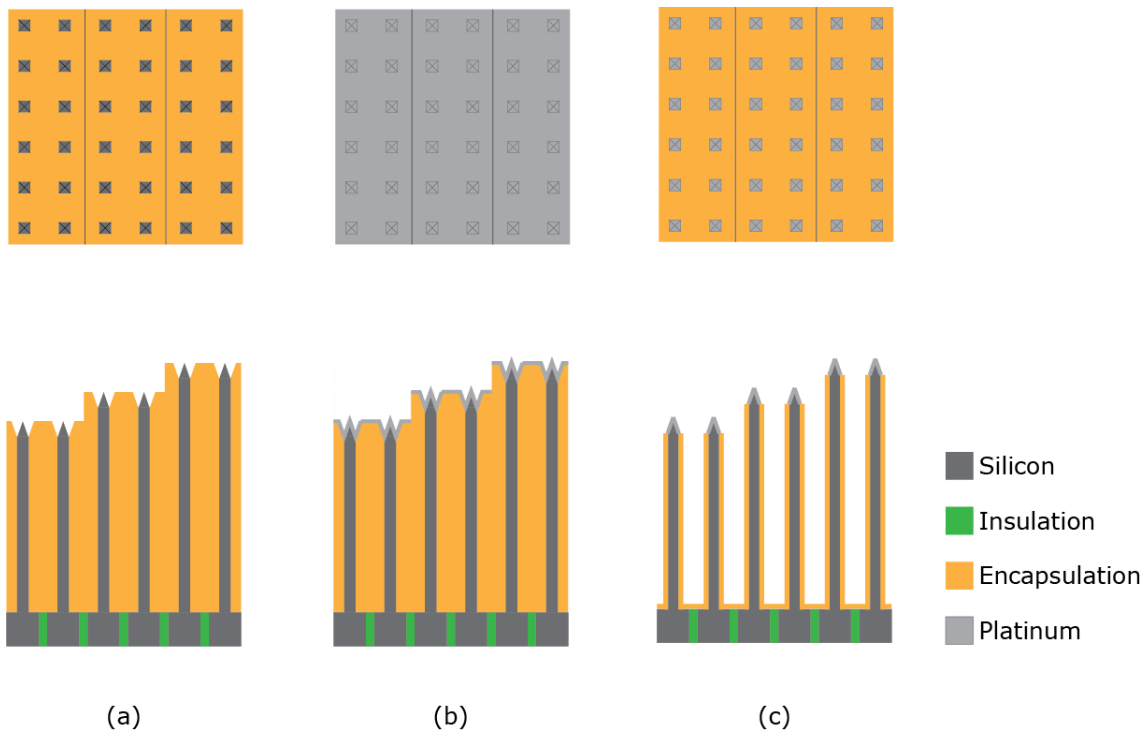

Figure 4.18: Top side final fabrication steps: *first row*, top view; *second row*, side view. (a) Tips dicing. (b) Platinum thin-film deposition. (c) Removal of encapsulation excess.

4.2.2 Experimental Results

The first dicing step cut a 4 mm thick, heavily doped, p^+-type silicon wafer. The cuts were 4 mm spaced on the first direction and 5 mm on the second (Figure 4.19a). After the cuts performed on the first direction, the wafer was rotated 90º to cut in the second direction (Figure 4.19b). The resulting dies were 4 mm × 5 mm squares and 4 mm thick. By turning each die 90º, it was possible to dice on a 4 mm × 4 mm square, and 5 mm thick silicon substrate (Figure 4.20). This step allowed 4 mm long pillars with 1 mm thick pads to be performed, using a 4 mm thick silicon wafer. The dicing steps were performed with the parameters described on Table 4.4.

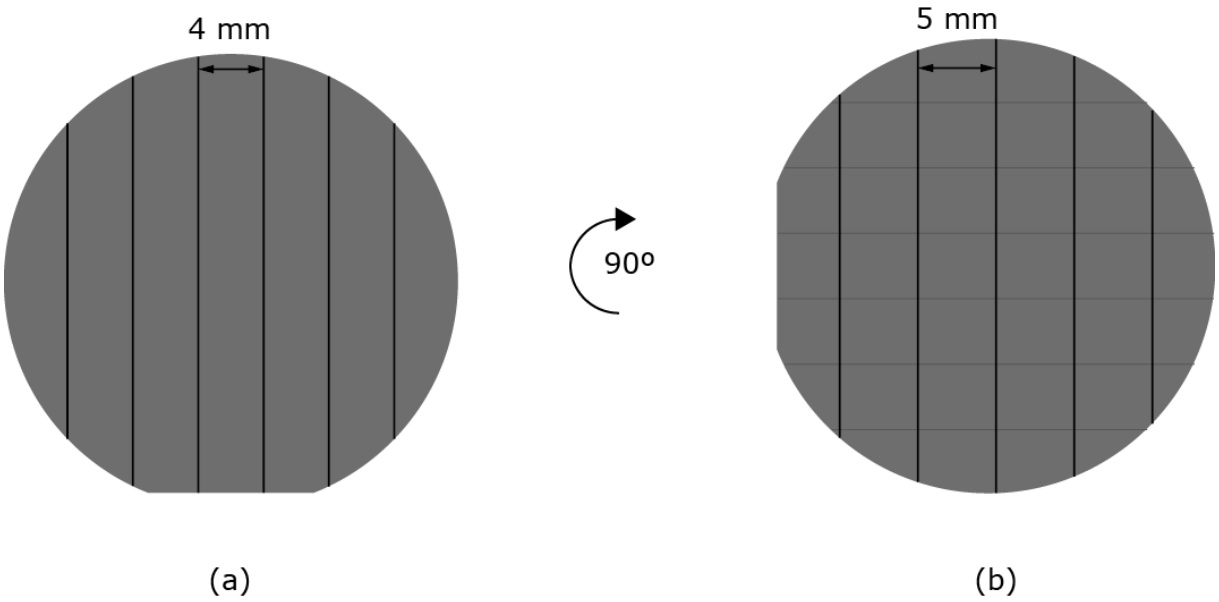

Figure 4.19: Wafer cut directions. Top view after cuts on the (a) first and (b) second direction.

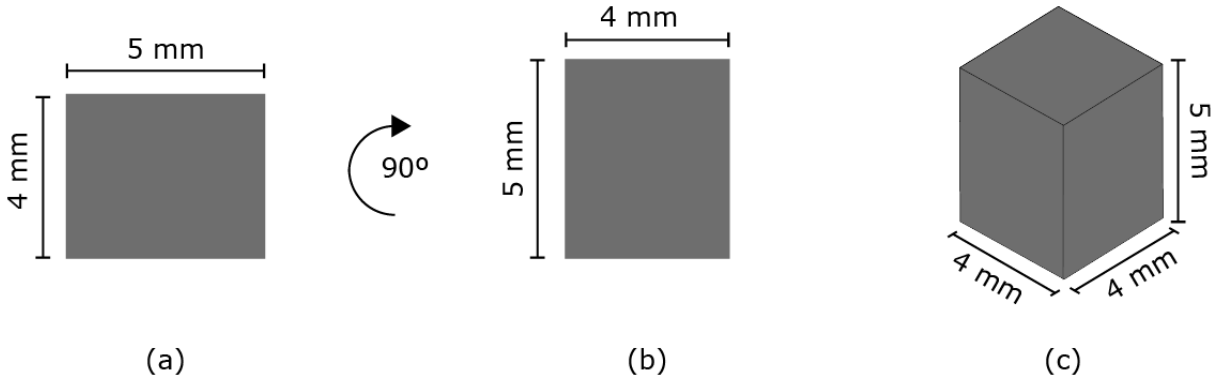

Figure 4.20: First dicing step and substrate rotation. (a) Side view before, and (b) after rotation. (c) isometric view of the substrate.

Table 4.4: Second prototype's parameters for wafer dicing.

Parameter	Value	Comments
Blade thickness	150 µm	NBC-ZB
Jump #1 (0º)	4 mm	First direction cuts represents a rotation of 0º
Jump #1(90º)	5 mm	Second direction cuts represents a rotation of 90º
Feed speed	0.3 mm/s	Slow speed due to 4 mm deep cuts
Z-blade	0.1 mm	Avoid touching the chunk

The second dicing step performed 600 µm spaced and 2 mm deep grooves (Table 4.5). The result were grid patterned grooves on the bottom side of the substrate, which delineated the pads region (Figure 4.21a).

Afterwards the grooves were filled with an epoxy resin by pressing with a small spatula against the bottom side (Hysol® 9492™). A sanding step removed the excess epoxy, exposing the pads between the grooves (Figure 4.21b).

Next, three silicon steps were diced on the surface of the substrate. The rise between steps was 500 µm. The first sequence of cuts was performed at a blade level of 4.5 mm, while the second was at 4 mm (Table 4.6). The result was a substrate with a decreasing thickness of 5 mm, 4.5 mm, and 4 mm (Figure 4.21c). The cutting parameters for the pads and silicon steps are shown in Table 4.6.

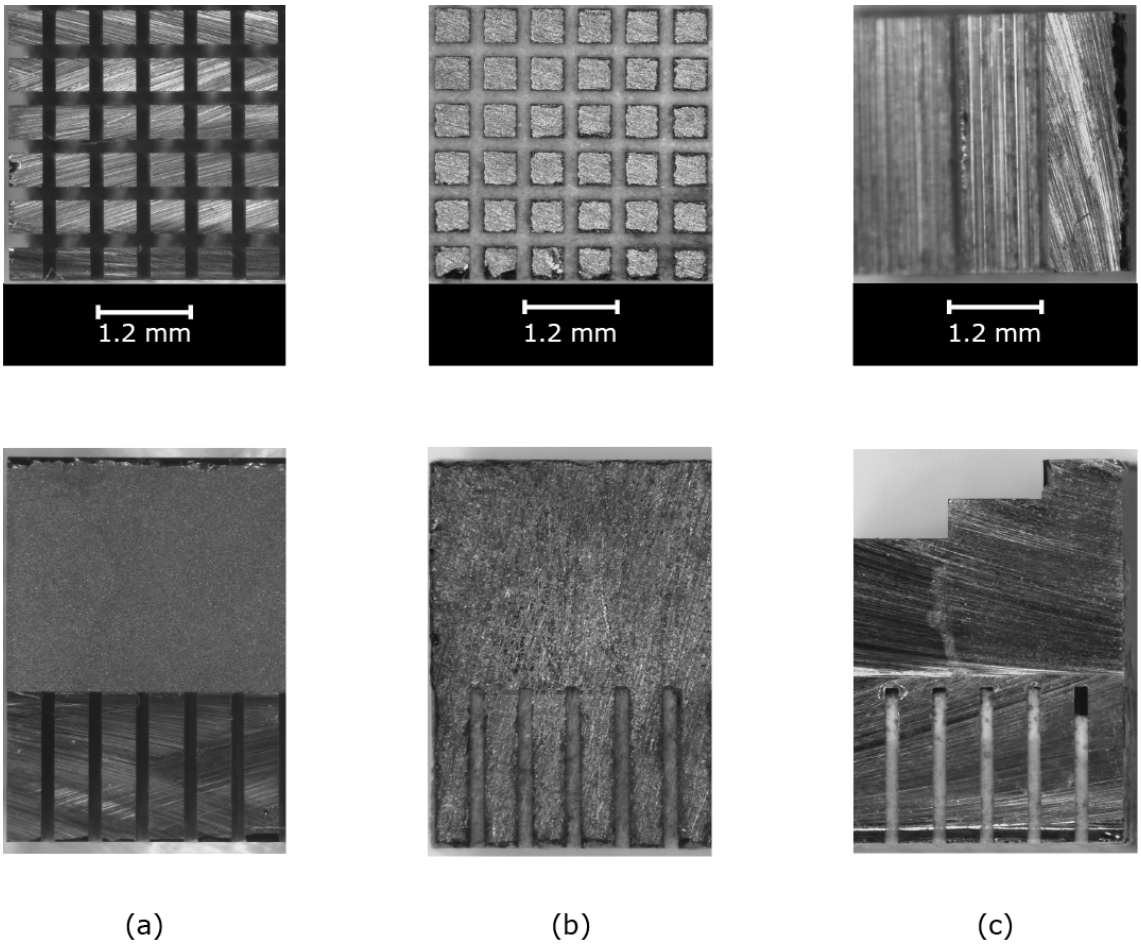

Figure 4.21: Bottom side photos and silicon steps machining. (a) Pads region after dicing, *first row*, bottom view; *second row*, side view. (b) Pads region after epoxy deposition, *first row*, bottom view; *second row*, side view. (c) Silicon steps after top side dicing, *first row*, top view; *second row*, side view. The scale bar is equal for both rows.

Table 4.5: Second prototype's parameters for pads dicing.

Parameter	Value	Comments
Blade thickness	150 µm	NBC-ZB
Jump #1	600 µm	Distance between cuts
Feed speed	0.5 mm/s	
Z-blade	3 mm	Depth of cut = sample thickness (5 mm) – z-blade (3 mm)

Table 4.6: Second prototype's parameters for silicon steps dicing.

Parameter	Value	Comments
Blade thickness	150 µm	NBC-ZB
Jump #1 − #7	150 µm	Distance between cuts
Jump #8	150 µm	Nº of jumps (8) × jump size (150 µm) = 1.2 mm
Feed speed	0.5 mm/s	
Z-blade	4.5 / 4mm	The second silicon step is performed at z-blade level of 4.5 mm while the third is 4 mm.

The next step performed silicon pillars with increasing lengths (Figure 4.23a). This was done by cutting deep grooves on the silicon substrate. The length of the pillars was determined by the thickness of the substrate. For a substrate with 5 mm, 4.5 mm, and 4 mm thick regions, 4 mm, 3.5 mm, and 3 mm long pillars were achieved. The cuts were performed with two progressive z-blade levels for both directions (Figure 4.22 a and b).

On the second cut direction, two approaches were tested. The first approach used the same parameters as the first direction, while the second approach introduced a small step on the middle of the pillar (Figure 4.22c). In a pool of 8 samples, the first approach could perform 4 mm long pillars with a success rate of 88 %, while the second was 94 %. The higher success rate from the second approach is due to the reduced amount of stress applied to the pillars. The first approach allowed 180 µm wide pillars to withstand the second direction of cut, while the second approach allowed 150 µm wide pillars. The dicing parameters for the first and second directions are described in Table 4.7 and Table 4.8, respectively.

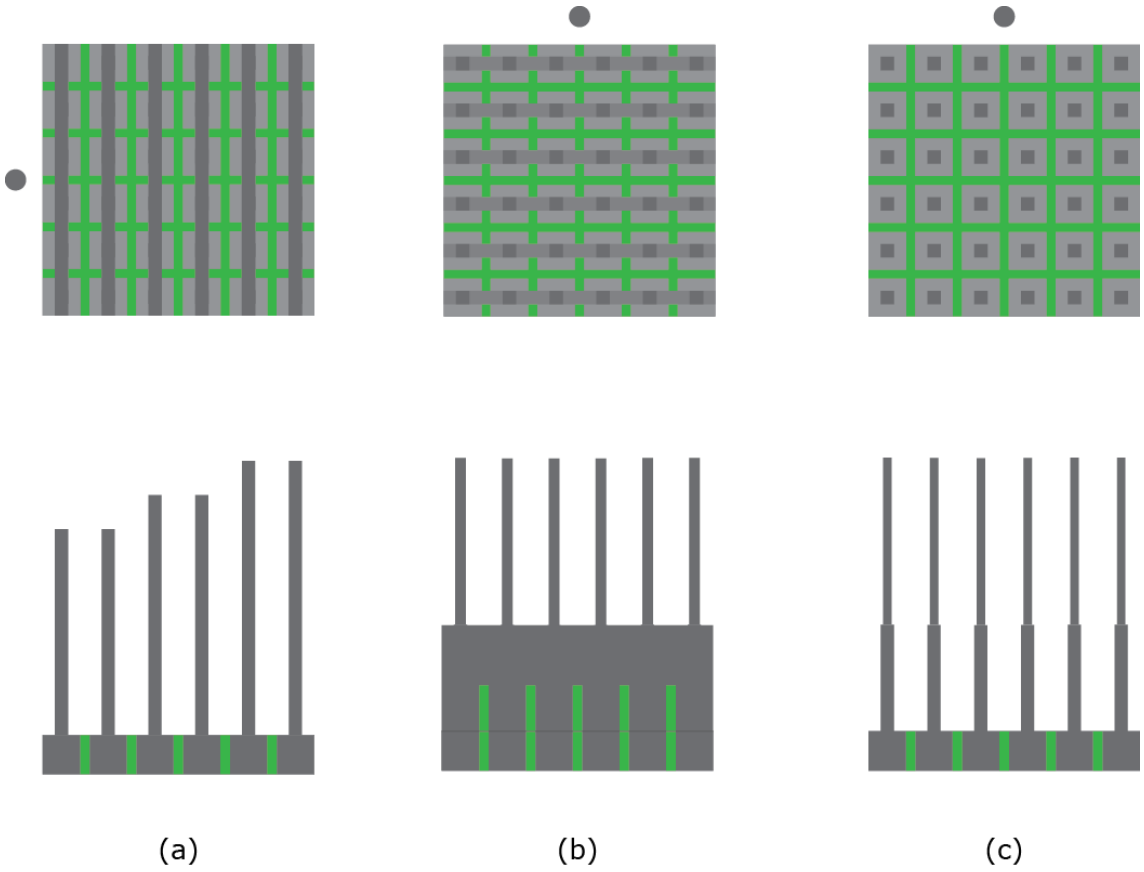

Figure 4.22: Dicing procedure to produce high-aspect-ratio silicon pillars: *first row*, top view; *second row*, side view. The grey dot represents the orientation of the array. (a) Silicon walls after first direction of cuts. (b) Short pillars after first cuts of the second direction. (c) Final pillars with a thinner profile on the upper half.

Table 4.7: Second prototype's parameters for pillars dicing (first direction).

Parameter	Value	Comments
Blade thickness	150 µm	NBC-ZB that performs 170 µm wide grooves on silicon
Jump #1	350 µm	Wall width (180 µm) = jump #1 (350 µm) – groove width (170 µm)
Jump #2	125 µm	
Jump #3	125 µm	Inter-wall space (420 µm) = jump #1 + jump #2 + groove width (170 µm)
Feed speed	0.5 mm/s	
Z-blade #1	3 mm	
Z-blade #2	1 mm	Wall length (4/3.5/3 mm) = silicon thickness (5/4.5/4 mm) – z-blade #2 (1 mm)

Table 4.8: Second prototype's parameters for pillars dicing (second direction).

Parameter	Value	Comments
Blade thickness	150 µm	NBC-ZB that performs 170 µm wide grooves on silicon
Jump #1	350 µm	Pillar width (130 µm) = jump #1 (320 µm) – groove width (170 µm)
Jump #2	150 µm	
Jump #3	150 µm	Interpillar space (470 µm) = blade thickness (170 µm) + jump #2 + jump #3
Feed speed	0.3 mm/s	Lower speed produces lower stress on the pillars
Z-blade #1	3 mm	
Z-blade #2	1 mm	Pillars length (4/3.5/3 mm) = silicon thickness (5/4.5/4 mm) – z-blade #2 (1 mm)

Afterwards, a thick layer of medical grade epoxy (Hysol^{TM} M-31CL) was deposited over the pillars, completely filling the interpillar space (Figure 4.23b) [3]. In order to avoid the epoxy from flowing to the sides, an aluminum foil was wrapped around the array, and contained the epoxy, allowing it to reach the top of the pillars (Figure 4.23c).

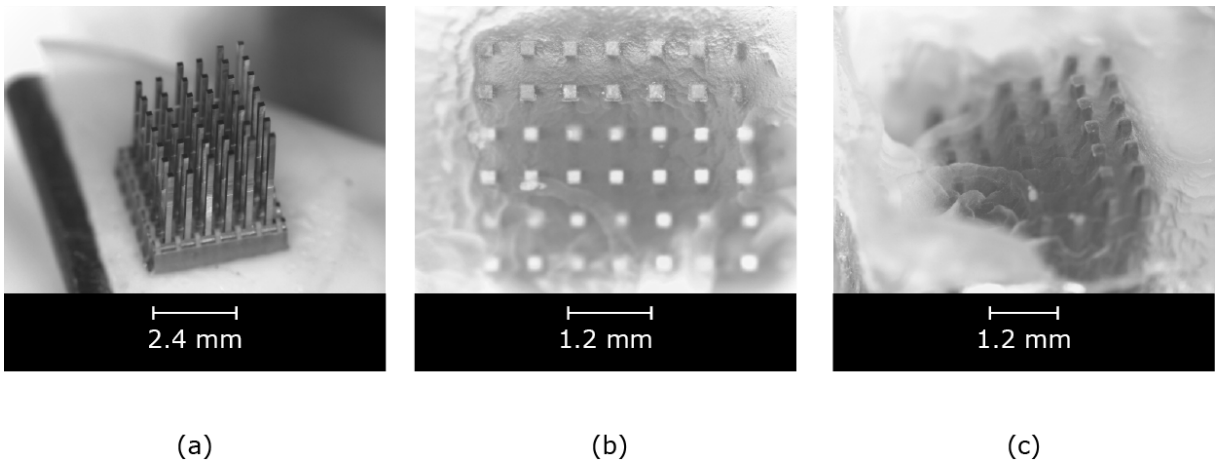

Figure 4.23: Pillars dicing and encapsulation. (a) Perspective view on the array after pillar dicing. (b) Top and (c) side view after epoxy deposition.

The tips were performed on the top side of the sample with a beveled blade (Figure 4.24). A Z09 blade was used, since NBC-ZB cannot have beveled profile. The cuts were performed at three different levels corresponding to the three steps (Table 4.9). The beveled blades created 250 µm wide and 300 µm long tips, due to the 60º angle of the tip.

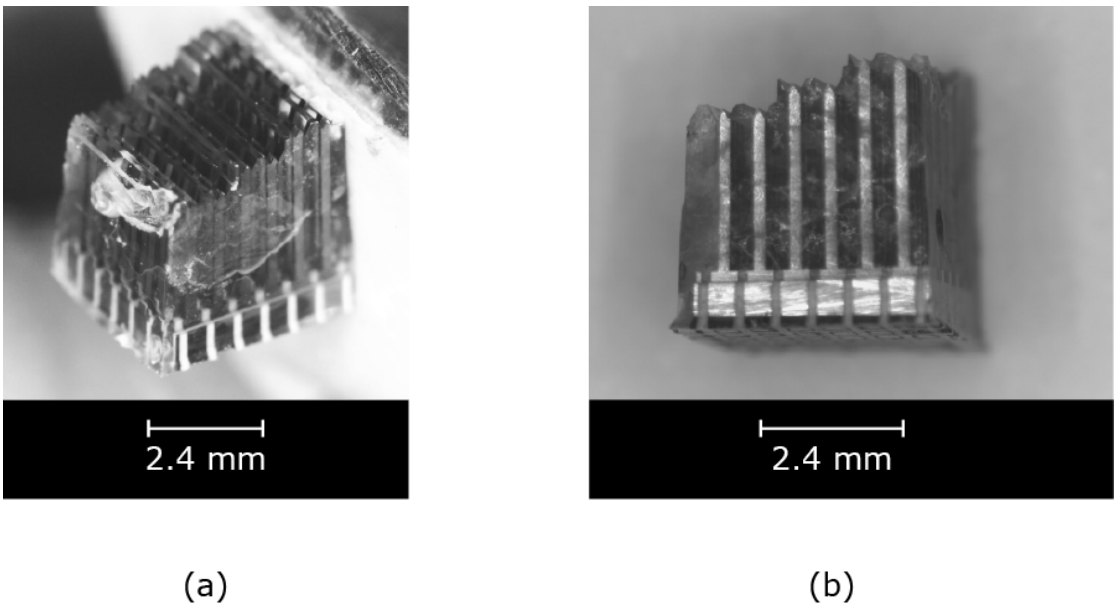

Figure 4.24: Second prototype after tips dicing. (a) Perspective view, (b) side view.

Table 4.9: Second prototype's parameters for tips dicing.

Parameter	Value	Comments
Blade thickness	250 µm	Z09 with a beveled profile
Jump #1	250 µm	Tip width (200 µm) = jump #1 (200 µm)
Jump #2	350 µm	Distance between tips(600 µm) = Jump #1 + Jump #2
Feed speed	0.5 mm/s	
Z-blade	4.7 mm / 4.3 mm / 3.7 mm	The z-blade level was 300 µm below the silicon step level. 1st level (4.7 mm) = 1st silicon step (5 mm) − 300 µm. 2nd level (4.3 mm) = 2nd silicon step (4.5 mm) − 300 µm 3rd level (3.7 mm) = 3rd silicon step (4 mm) − 300 µm

In the next step, a deposition of titanium followed by platinum was performed. The platinum was used for the transduction layer, while titanium promoted the adhesion between the silicon and platinum. The titanium deposition was performed by e-beam at a starting pressure of 3×10^{-6} mbar while supplying a current of 60 mA and an electric potential of 7 kV. The platinum deposition was performed by DC sputtering at a starting pressure of 7×10^{-6} mbar while supplying an electric current of 33 mA, electric potential of 300 V, and a constant flow of 40 sccm of argon. The titanium film was 70 nm, while the platinum was 180 nm thick. After the deposition, the entire array had a black appearance (Figure 4.25a).

Visual observation showed evidence that the tips were covered by the platinum thin-film (Figure 4.25b).

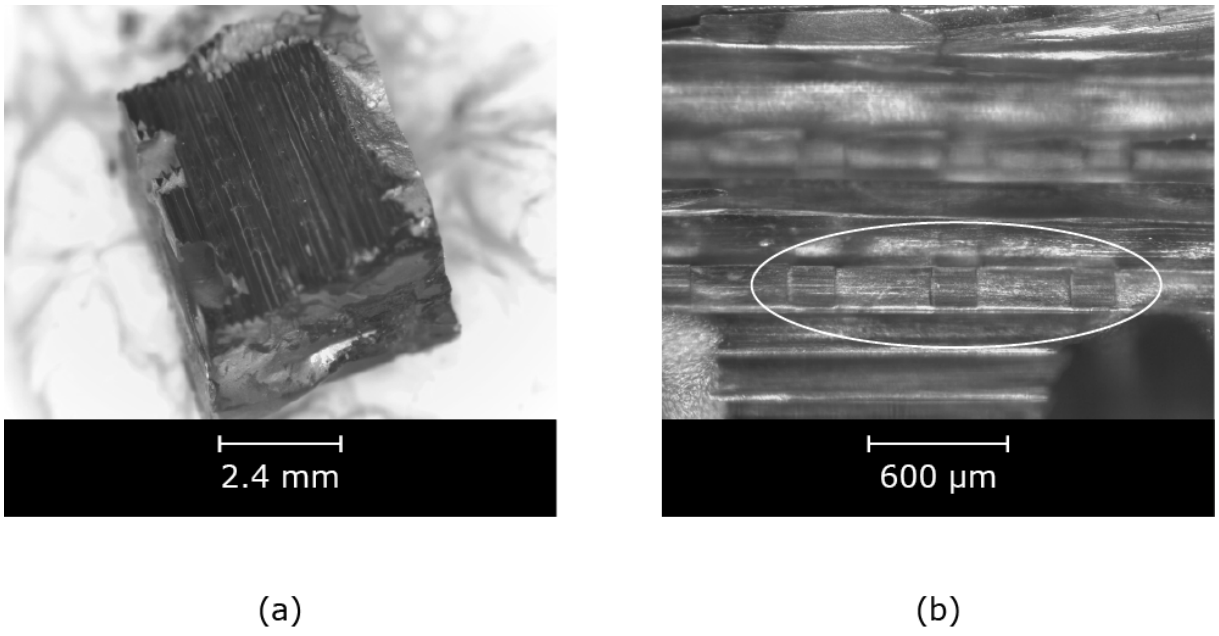

Figure 4.25: Array after deposition. (a) View of the entire array. (b) Detail of the silicon tips covered by the thin-film.

The last step shaped the final array by removing the excess encapsulation. Using the dicer to remove the epoxy between pillars, it was possible to achieve 3.9 mm long and 220 µm wide pillars with an encapsulation layer of 20 µm (Figure 4.26). Each pillar had a functional platinum electrode at the tip. The dicing parameters for removing the excess epoxy are presented on Table 4.10.

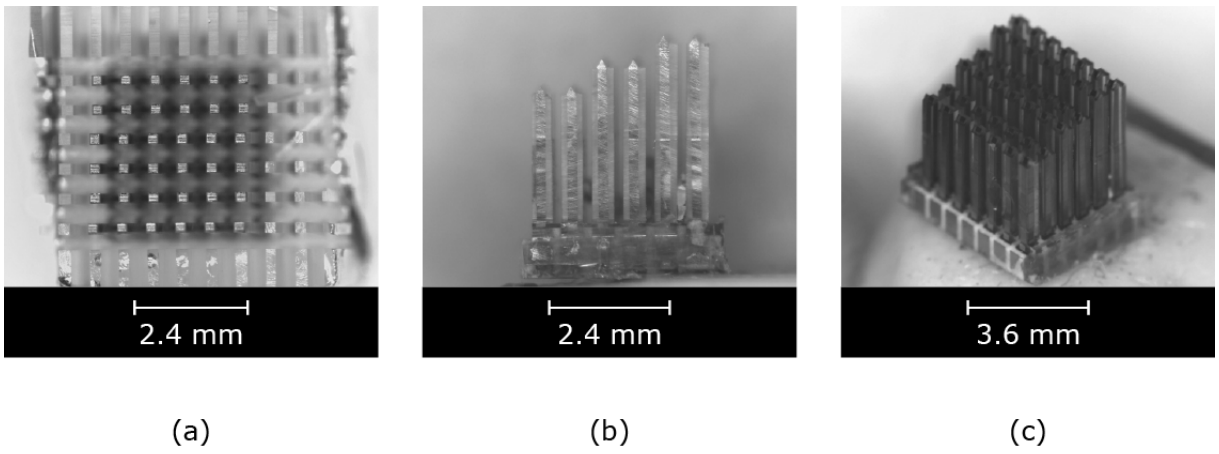

Figure 4.26: Photos of the final dicing step. (a) Top view after removing the excess between pillars. (b) Side view and (c) perspective view of the final array.

Table 4.10: Second prototype's parameters for encapsulation excess removal.

Parameter	Value	Comments
Blade thickness	250 µm	Z05 that performs 320 µm wide grooves in epoxy
Jump #1	540 µm	Pillar width (220 µm) = jump #1 (540 µm) – groove width (320 µm)
Jump #2	60 µm	Pillars' spacing (600 µm) = jump #1 (540 µm) + jump #2 (60 µm)
Feed speed	0.3 mm/s	
Z-blade #1	2 mm	Depth of the first cut (2 mm) = substrate thickness (4 mm) – z-blade #1 (2 mm)
Z-blade #2	1.1 mm	Pillar length (3.9 mm) = substrate thickness (5 mm) – z-blade #2 (1.1 mm)

The second prototype could be successfully fabricated using dicing and polymer deposition techniques. The achieved pillars had a considerable increase of aspect ratio when compared to the first prototype. Beyond this, by avoiding exotic processes such as thermomigration, higher repeatability and lower costs are possible. Overall, the second prototype represents a significant improvement over the first one.

References

[1] V. I. Rudakov and N. I. Plis, "Aluminum thermomigration technology for fabrication of silicon packages," *EuroSimE 2005. Proc. 6th Int. Conf. Therm. Mech. Multi-Physics Simul. Exp. Micro-Electronics Micro-Systems, 2005.*, no. 0852, pp. 325–329, 2005.

[2] K. E. Petersen, "Silicon as a mechanical material," *Proc. IEEE*, vol. 70, no. 5, pp. 420–457, 1982.

[3] Henkel AG & Co., "Hysol® M-31CL™ Technical Datasheet," 2005. Available: http://www.loctite.co.uk/loctite-4087.htm?nodeid=8802635087873.

Chapter 5

Electrode Array Characterization

The successfully fabricated aluminum and silicon prototypes as well as its components were structurally, mechanically, and electrochemically characterized.

The structural characterization used optical microscopy and scanning electron microscope (SEM) to measure the dimensions of the array components such as pillars, tips, and encapsulation. An energy-dispersive x-ray spectroscopy (EDS) was performed, for the chemical component analysis of the aluminum oxide encapsulation and the thin-film of gold, which was used as transduction layer on the first aluminum prototype. All optical measurements were performed by Leica M80™ stereo microscope and Leica LAS™ software. All SEM images were obtained by a FEI™ Nova NanoSEM™ 200 system and the EDS measurements were performed by an EDAX Pegasus™ system.

The mechanical characterization consisted on the implantation of the array with the aid of a dynamometer in agar gel (brain phantom that mimicked the mechanical properties of the brain) and porcine cadaver brain. Also, buckling, flexibility, and shear tests were performed. The buckling tests obtained the forces necessary to bend or break the pillars, as well as their failure mechanism. The flexural tests showed the ability of the array to bend without breaking, while the shear test acquired the resistance to bending of a single silicon pillar.

The characterization of the electrodes was performed by electrochemical impedance spectroscopy (EIS) that acquired the impedance of the thin-films of gold and platinum. Cyclic voltammetry was also performed on the platinum film in order to determine its charge injection capacity.

5.1 Structural

5.1.1 First Aluminum Prototype

The pillars' dimensions of the first aluminum prototype were measured using the microscope. Figure 5.1 shows the measurements for the pillar's length, width, and tip length. On a sample of 9 pillars, the statistical analysis showed an average length of 3.061 mm with 0.021 mm of standard deviation, and an average width of 255 µm with 18.24 µm of standard deviation (Figure 5.2).

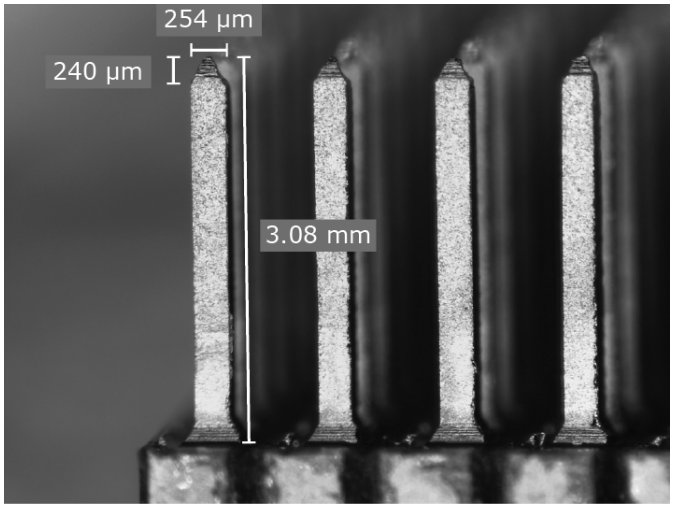

Figure 5.1: Main measurements of the first aluminum prototype.

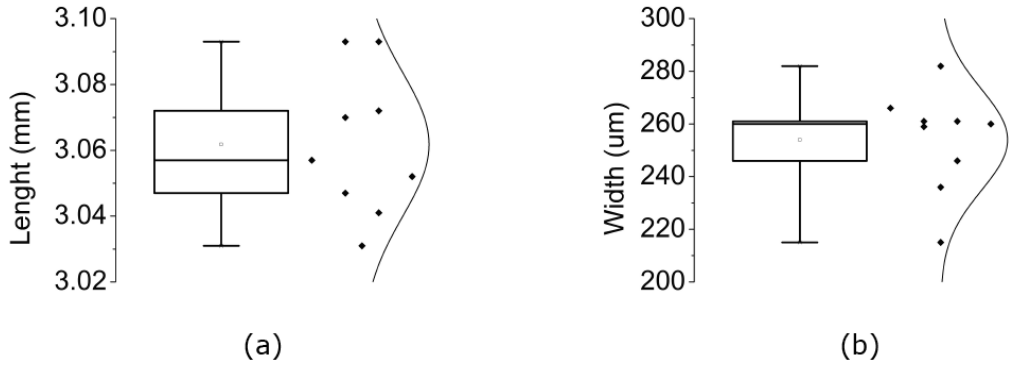

Figure 5.2: Box plot of the pillars' dimensions with measured values and normal distribution to the right: (a) length; (b) width.

An EDS measurement was performed on the pillar's surface in order to verify the existence of the aluminum oxide encapsulation layer. The EDS spectrum shows peaks corresponding to aluminum, oxygen and sulfur elements (Figure 5.3). A percentage by weight of 52% of aluminum, 43% of oxygen and 5% of sulfur was determined. These results showed that an external coating of aluminum oxide was encapsulating the pillar. The sulfur residues originated from the anodizing process, since it used a sulfuric acid solution as electrolyte.

Figure 5.4a shows a SEM image taken of the pillar's cross-section. The measured thickness of the aluminum oxide was approximately of 8 µm. The EDS spectrum shows that the surface layer had a percentage by weight of 69% of aluminum, and 31% of oxygen, while the layer underneath is composed solely by aluminum (Figure 5.4b and c). The existence of oxygen in the surface layer suggests that aluminum oxide was formed. The value of oxygen is less than half of that of aluminum. A possible cause for this, is the *pear effect*, which represents the analysis of structures that are below the surface due to the depth of penetration of the X-ray emission [1]. If the depth of penetration is superior to the thickness of the oxide layer, decreasing values of oxygen will be observed.

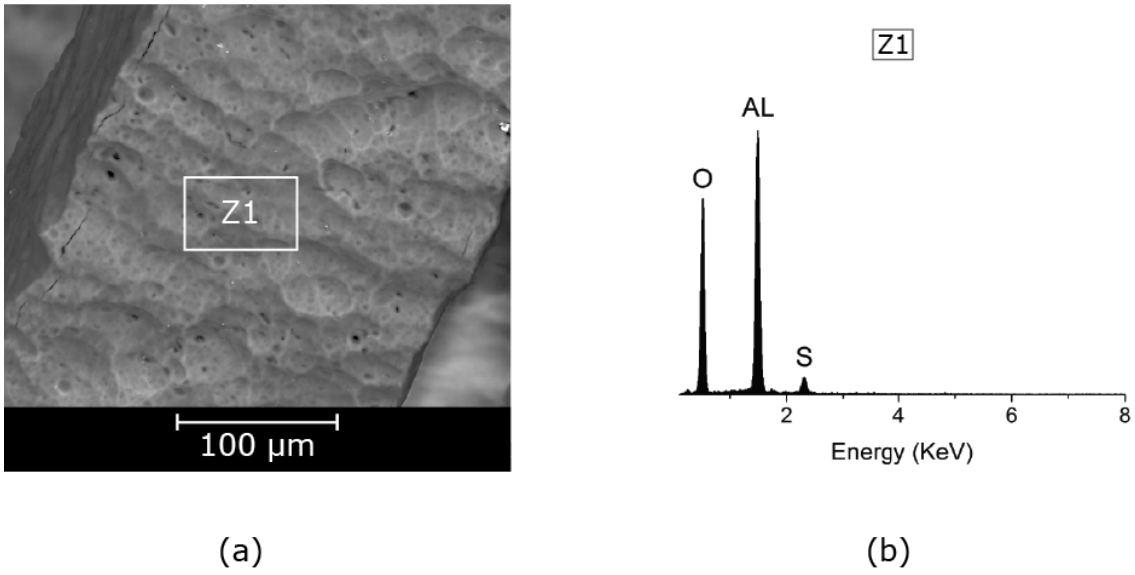

Figure 5.3: SEM image and EDS spectrum of a pillar's surface. (a) Pillar section with EDS target zone highlighted. (b) EDS spectrum of the Z1 target zone.

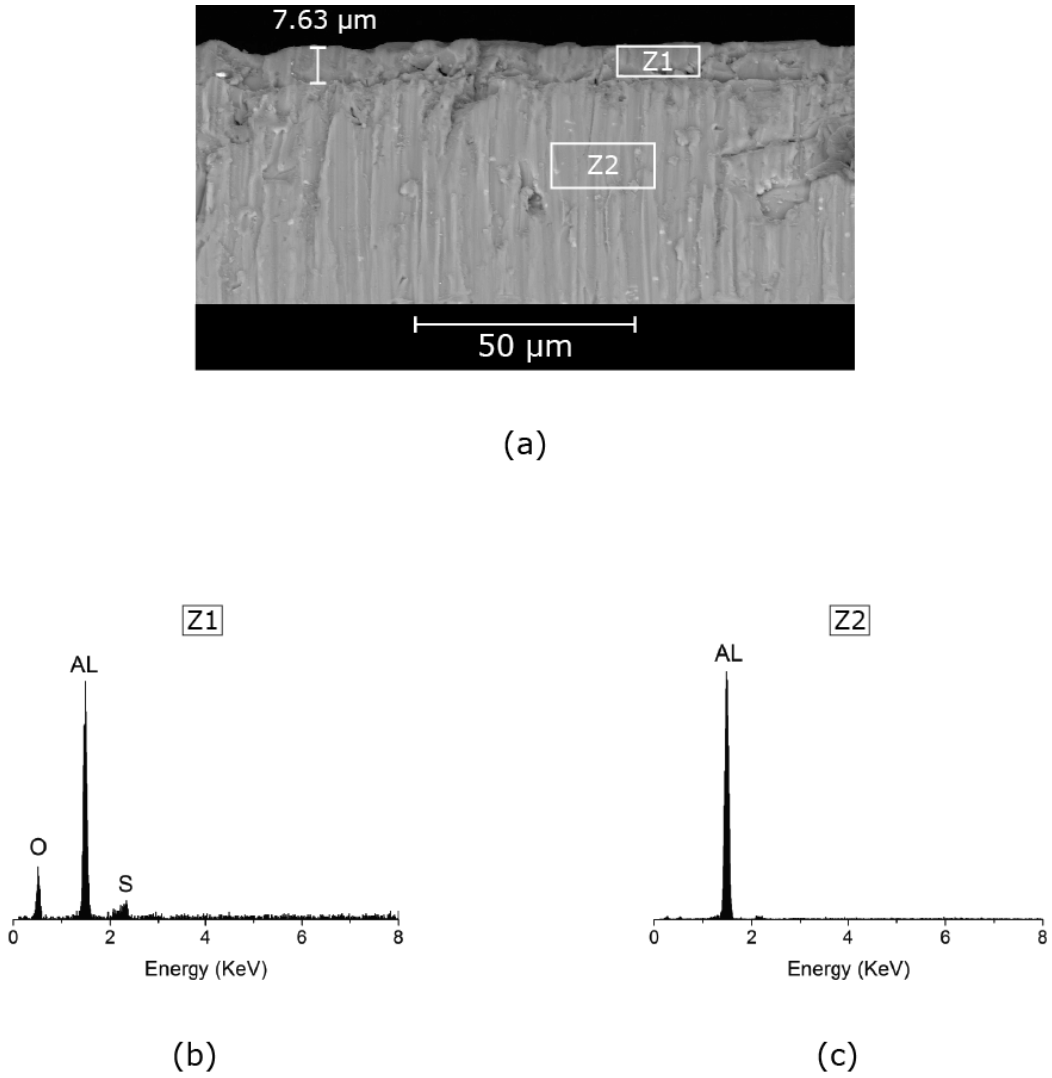

Figure 5.4: SEM image and EDS spectrum of an aluminum pillar's cross-section. (a) SEM image with aluminum oxide layer measurement and EDS target zones. EDS spectrum corresponding to zones: (b) Z1, and (b) Z2.

An EDS measurement was performed at the tip of the pillar in order to verify the quality of the thin-film of gold. The SEM image shows an incomplete covering of the tip with gold, specially at the vertex (Figure 5.5a). All obsered tips showed an incomplete coating with variation on the uncoated locations. The EDS results showed a weight percentage of 91% of gold and 9% of carbon at zone 1 (Figure 5.5a). The small amount of carbon was possibly caused by manually handling the array.

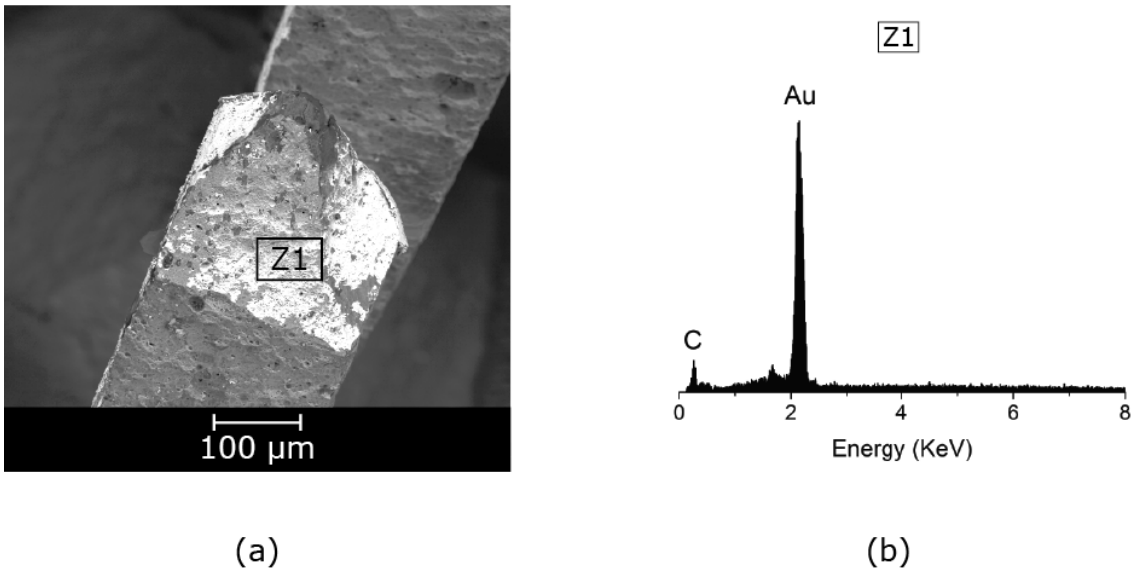

Figure 5.5: SEM image and EDS spectrum of the thin-film of gold at the tip. (a) SEM image with target EDS zone highlighted. The brighter areas are composed of gold. (b) EDS spectrum of Z1.

5.1.2 Second Aluminum Prototype

The length and width of the pillars on the second aluminum prototype were performed with using Leica microscope (Figure 5.6).

On a sample of 10 aluminum pillars, the average length was 3.09 mm and standard deviation of 0.06 mm (Figure 5.7a). The average length of the encapsulated pillars decreased to 2.88 mm with a standard deviation of 0.02 mm (Figure 5.7b). The reason for this reduction in length was caused by the removal of aluminum at the top of the pillars during tip cutting, and the encapsulation layer at the bottom.

The average width of the aluminum pillars was 117 µm with a standard deviation of 7 µm, while the encapsulated pillars were 160 µm wide, with no variation. The average encapsulation layer thickness was 22 µm, also with no variation. Despite having no observable variation under the microscope, it must be considered that the resolution limit for the measurements is 5 µm. The lack of variation in the width of the pillars suggests that the dicing procedure has a high level of repeatability.

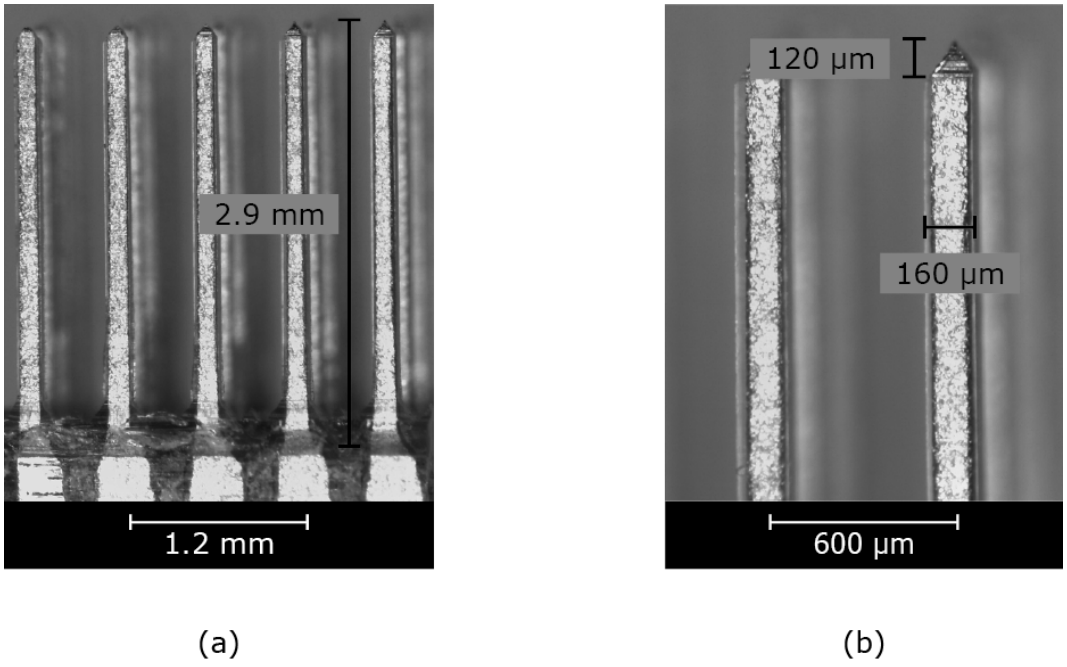

Figure 5.6: Measurements performed on the second aluminum prototype: (a) Pillar length; (b) Pillar width and tip length.

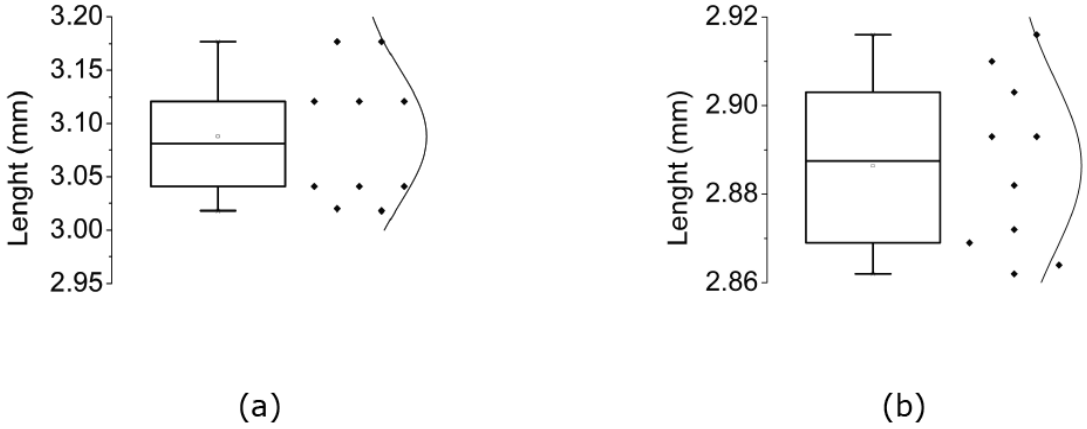

Figure 5.7: Box plot of the pillars' lengths with measured values and normal distribution to the right: (a) before encapsulation; (b) after encapsulation.

SEM images were obtained from the top part of the pillars in order to measure the tip radius and observe in detail the encapsulation condition (Figure 5.8a).

The tip radius is related with the penetration forces of the pillar, i.e., a small radius imply a small implantation force [2]. A tip radius of 9 µm was measured on the Nova SEM

system (Figure 5.8b). From 10 pillars observed, only one showed evidences of bare aluminum at the pillar (Figure 5.8c). The absence of epoxy near the tip could have been caused by the friction between the blade and the substrate, leading to detachment.

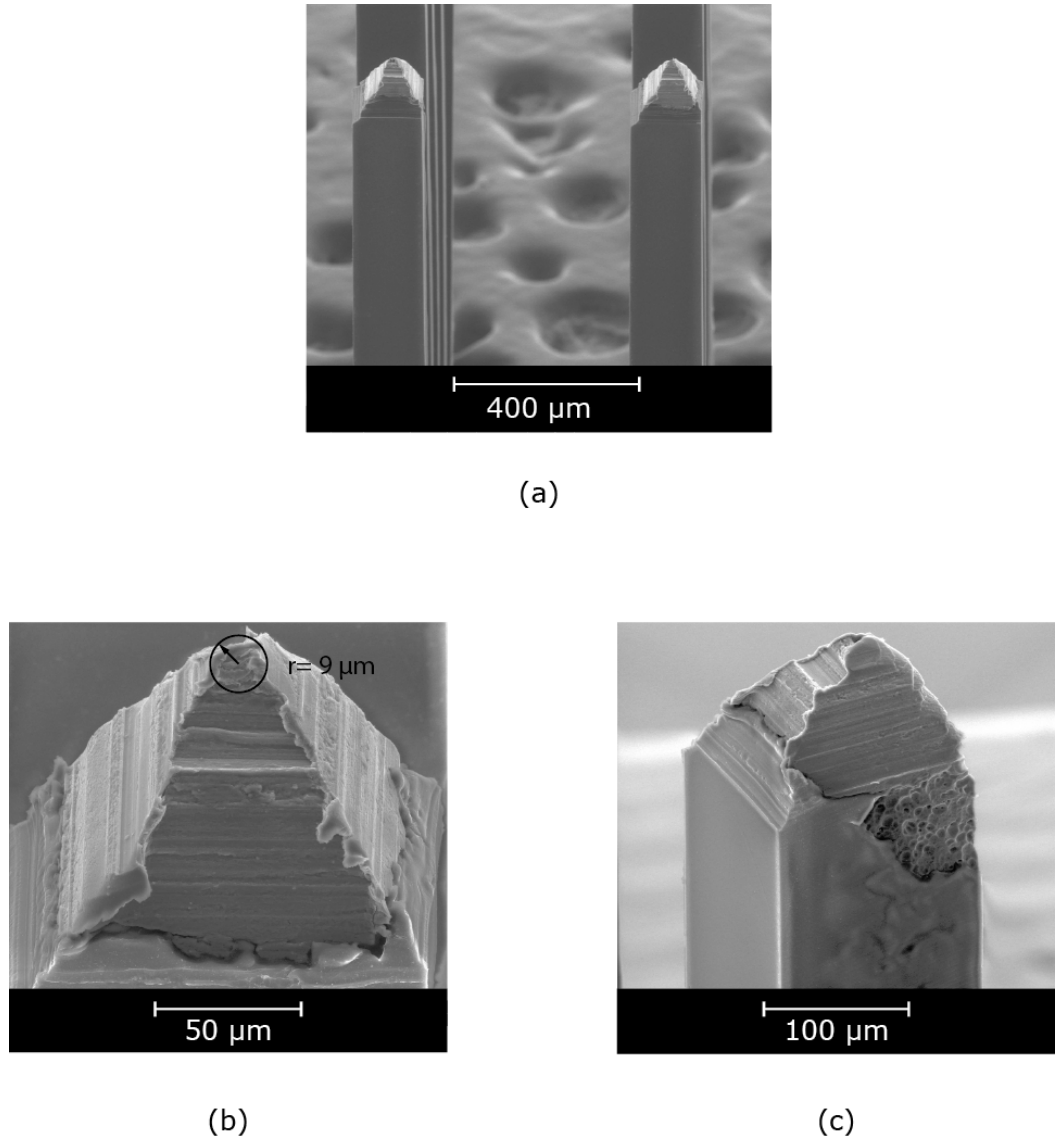

Figure 5.8: SEM images of the tip of the second aluminum prototype. (a) Aluminum pillar with epoxy encapsulation. The darker tone represents the epoxy encapsulation. (b) Tip radius. (c) Encapsulation failure close to the tip.

5.1.3 Second Silicon Prototype

Measurements of pillars' length and width were performed on the second prototype with the Leica microscope. The length and width of 24 pillars were measured; 12 with and 12 without encapsulation. The pillars without encapsulation were 4.01 mm long and 176 µm wide (Figure 5.9). The encapsulated pillars were 3.87 mm long and 214 µm wide

(Figure 5.10). The measured tip radius was of 2.5 µm (Figure 5.11). The lack of variation on the length and width of the pillars is related with the high accuracy and repeatability of the dicer. Also, the measurements are limited by a 5 µm resolution of the microscope.

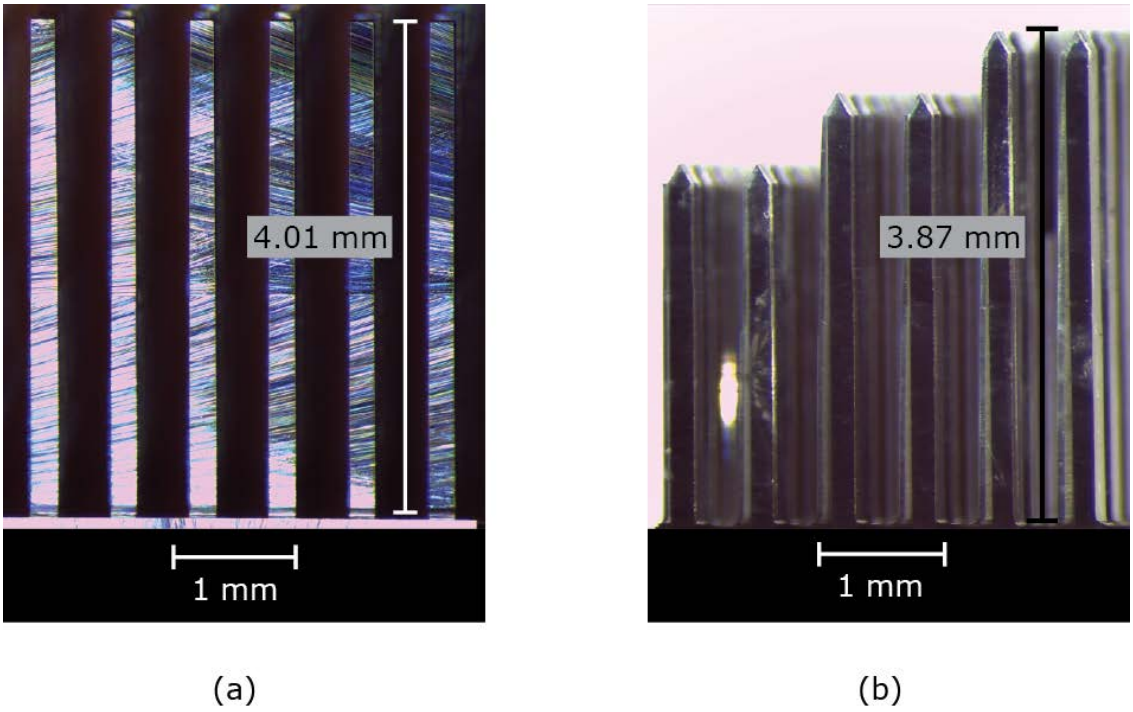

Figure 5.9: Second silicon prototype pillars' length. (a) Array of 4 mm long silicon pillars without encapsulation. (b) Final array with encapsulated pillars.

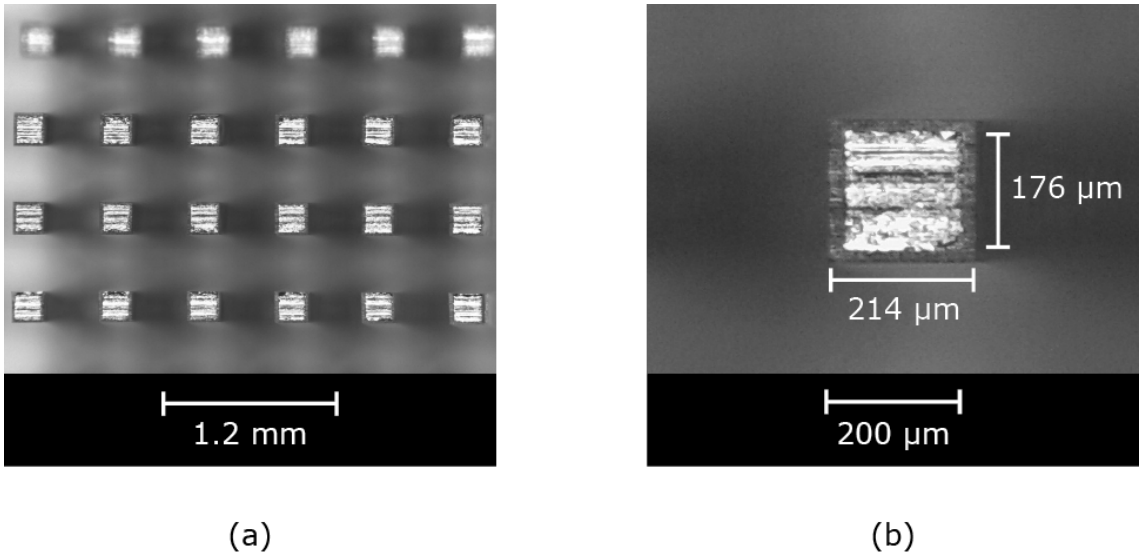

Figure 5.10: Second silicon prototype pillars' width. (a) Top view. (b) Measurements of the silicon pillar and encapsulation.

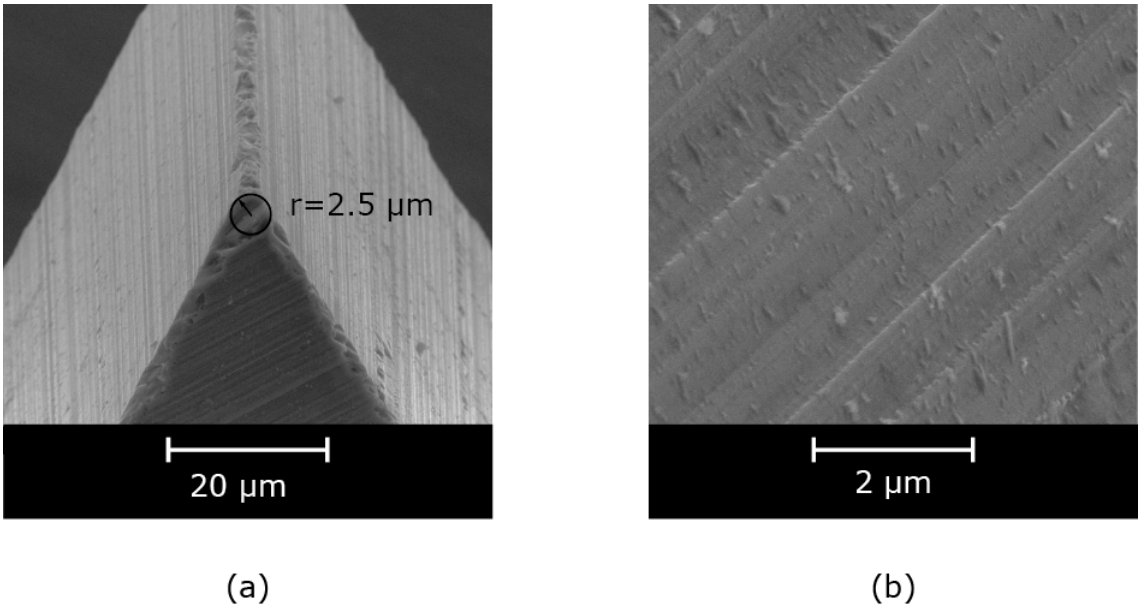

Figure 5.11: SEM image of the second silicon prototype tip. (a) Tip radius. (b) Surface of the diced silicon at the tip.

5.2 Mechanical

5.2.1 First Aluminum Prototype

The mechanical characterization of the first aluminum prototype was performed by a series of three implantation tests of the array on agar brain phantom. The implantation tests were performed on a Hounsfield H 100 KS dynamometer equipped with a 100 N load cell capable of 10 mN resolution. Figure 5.12a, shows the set-up arrangement for the implantation tests. A brain phantom with 1% of agar gel concentration, was used to mimic the mechanical properties of the brain cortex [3]. The array was attached to the dynamometer shaft, which moved down towards the agar gel at a constant speed of 0.03 mm/s. The average load necessary to implant the array was 1057 mN with a standard deviation of 62 mN, which represents approximately 11 mN per pillar (Table 5.1). The obtained plot shows a load increase on the initial stage, up to the moment where the electrodes' tips are able to pierce the gel. Afterwards, there is an abrupt drop on the required load (Figure 5.12b). This behavior suggests a bed-of-nails effect during insertion. After the electrode's full penetration there is a slight increase in the curve's slope, indicating that the array's base was being pushed against the gel.

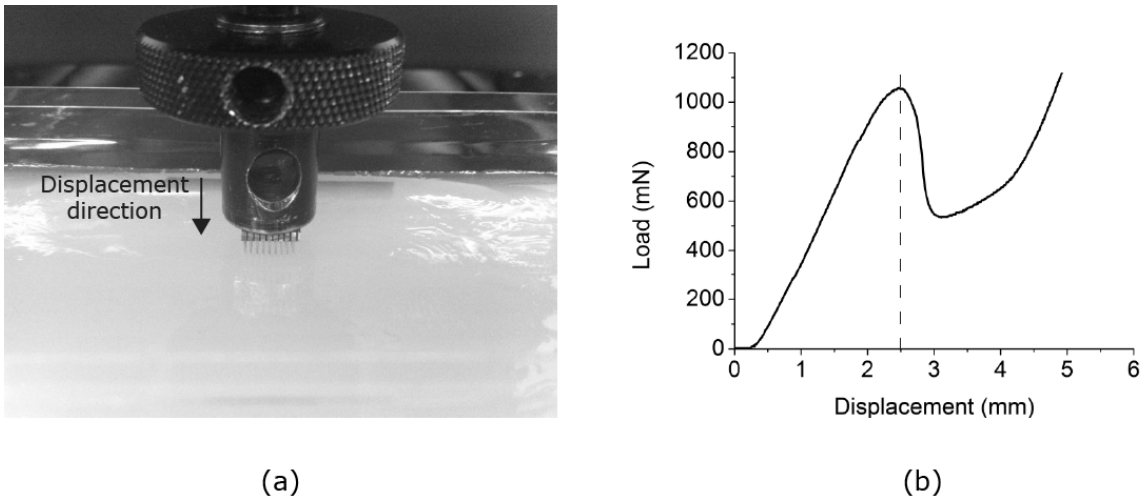

Figure 5.12: First aluminum prototype implantation tests. (a) Implantation Set-up. (b) Load versus displacement curve with implantation moment highlighted by a dashed line.

Table 5.1: First aluminum prototype implantation tests on agar.

Speed (mm/s)	Number of tests	Average load (mN)	Standard deviation (mN)	Average load per pillar (mN)
0.03	3	1057	62	11

5.2.2 Second Aluminum Prototype

The mechanical characterization of the second aluminum prototype was performed by the following tests:

- Implantation and explantation in agar gel
- Implantation and explantation in porcine cadaver brain
- Buckling load
- Flexibility

The implantation tests were performed on a Shimadzu AG-IS dynamometer equipped with a 50 N load cell capable of 5 mN resolution. The mechanical characterization used arrays with 160 µm wide, 3 mm long, tipped aluminum pillars.

Agar

Figure 5.13a, shows the set-up arrangement for the implantation tests. The tests used agar gel with a concentration of 0.5 % this way better mimicking the brain tissue [4]. In order to find an implantation parameter that is at the same time fast and that requires the minimal implantation load, three distinct speeds were used. Table 5.2, summarizes the implantation

results.

Just like on the first aluminum prototype, the load versus displacement plot shows a load peak at the implantation moment (Figure 5.13b). The load required to implant the array tends to be higher at faster implantation speeds, which suggests that lower speeds are preferable, since they would cause smaller tissue compression and thus less trauma.

Despite the difference in speed, the implantation loads per pillar decreased below 50% when compared to the first aluminum prototype, and is in the same order of magnitude reported by Das *et al.* [3]. The decrease in the load is led by the fact that the pillars on the second prototype are 64% thinner than the first prototype.

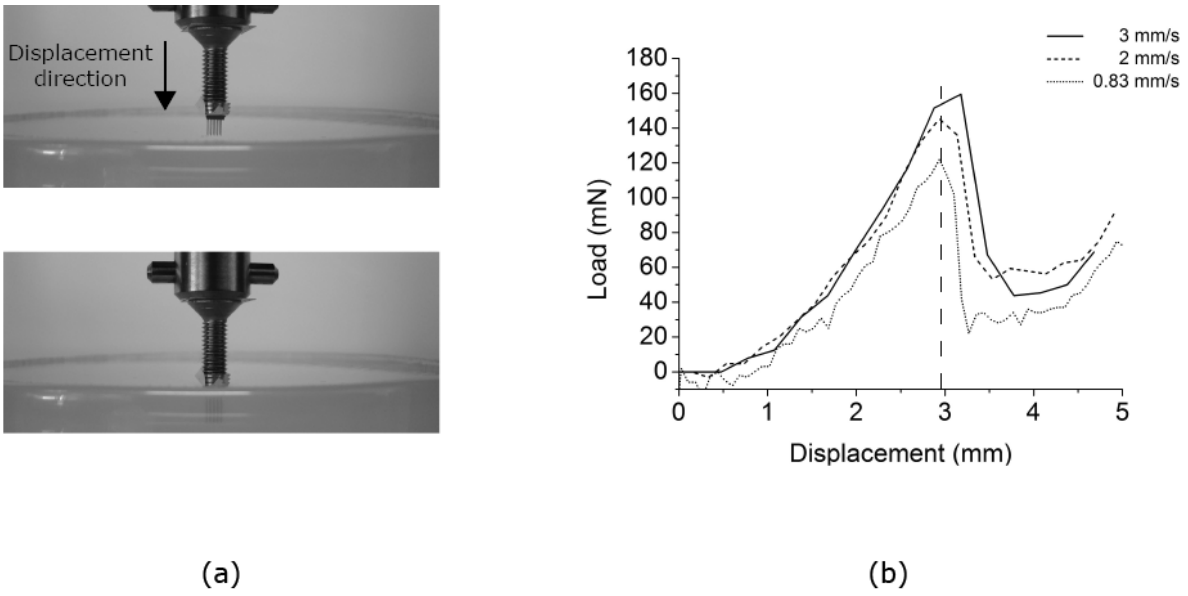

Figure 5.13: Second aluminum prototype implantation tests in agar gel. (a) Set-up, before implantation (top photo), and after implantation (bottom photo). (b) Load versus displacement for three different speeds, with implantation moment highlighted by a dashed line.

Table 5.2: Second aluminum prototype implantation tests on agar.

Speed (mm/s)	Number of tests	Average load (mN)	Standard deviation (mN)	Average load per pillar (mN)
3	4	150	2	6
2	4	145	8	5.8
0.83	4	119	8	4.76

Porcine Cadaver Brain

Implantation tests with similar parameters as the agar gel were performed on porcine cadaver brain with the *pia matter*. This innermost layer of the meninges represents the biggest barrier for implantation due to its superior robustness than the brain tissue [5]. The purpose of these tests was to evaluate pillars' robustness when penetrating the brain. The tests showed significant tissue dimpling before implantation. This suggests that a bed-of-nails effect could occur when implanting high-density arrays at the tested speeds. A slight twitch could be observed at the *pia*, when displacement depths were between 10 and 11 mm, corresponding to loads between 200 and 300 mN. This twitch indicates piercing of the pia and consequently implantation success.

Successful implantation could only be verified through explantation results, since it could not be observed from the penetration curve (Figure 5.14). The set-up and explantation curve on porcine cadaver brain are presented on Figure 5.15. The key moment during withdrawal are highlighted by a dashed line (Figure 5.15b). In moment 1, the brains' surface is in its relaxed state, in moment 2 there is a maximum tension applied and in moment 3 there is a complete detachment between the array and the tested material. Moment 1 happens because the array goes from a state of actively compressing the brain tissue to a relaxation state. The rise in tension during withdrawal is due to the drag forces between the electrodes and the surrounding brain tissue. This could be observed clearly in the cadaver brain as it followed the array trajectory originating a temporary protuberance in the region of implantation (moment 2). Next, a drop in the applied tension was observed, which led to moment 3, where the array was completely detached from the brain. The average difference between maximum tension and brain relaxation was of 57 mN with a standard deviation of 15 mN. This suggests that the array was implanted prior to removal.

Implantation tests were also performed after the removal of the *pia*. Although successful implantation could be visually observed, the load required for implantation was below the dynamometer resolution. No signs of pillar bending or breaking were observed on the arrays after explantation.

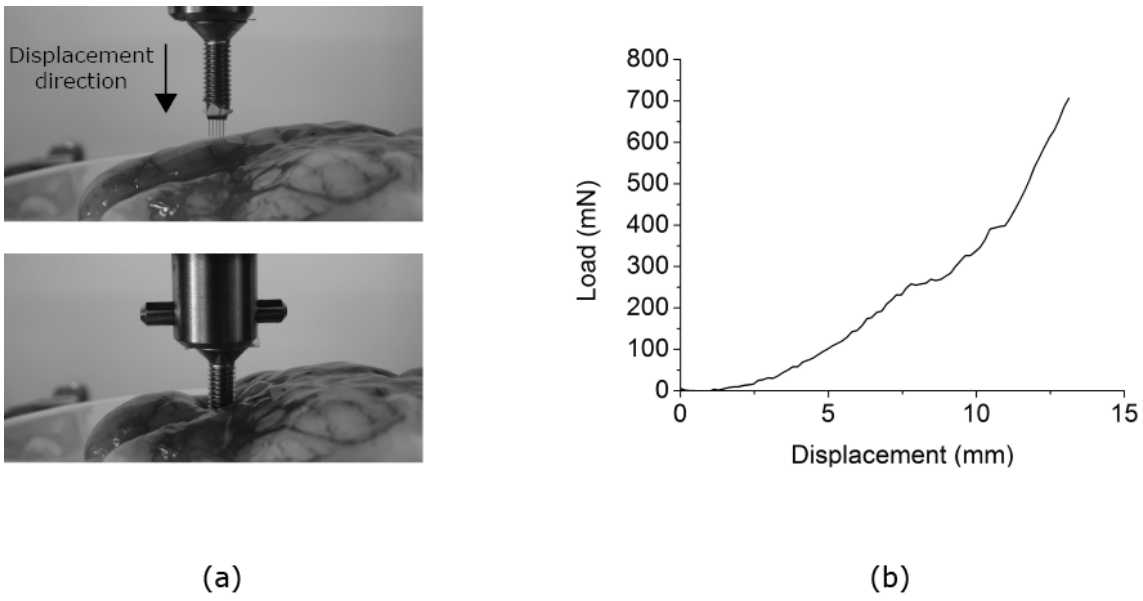

Figure 5.14: Second aluminum prototype implantation tests in porcine cadaver brain. (a) Set-up, before implantation (top photo), and after implantation (bottom photo). (b) Load versus displacement curve.

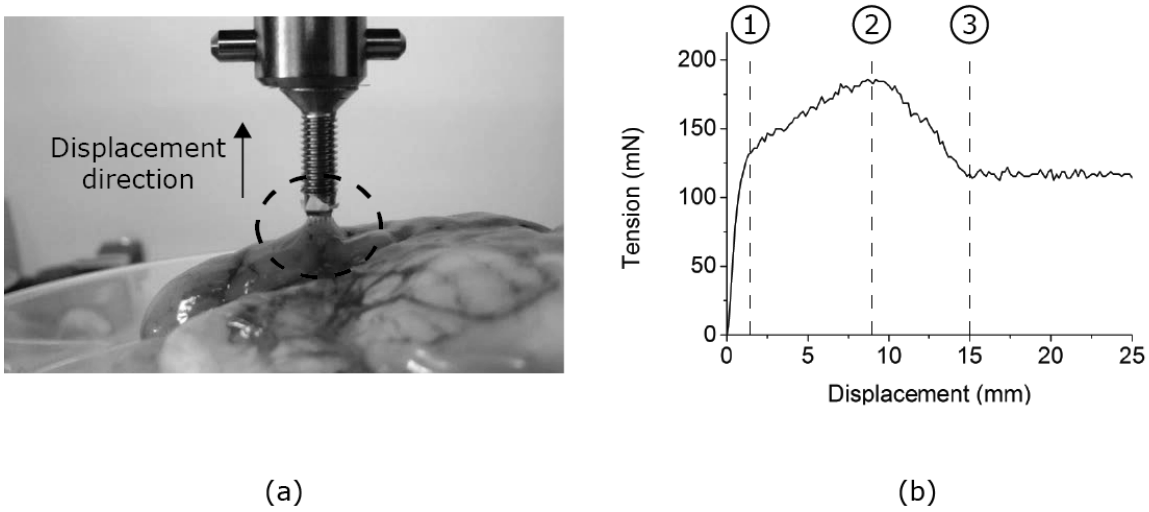

Figure 5.15: Second aluminum prototype explantation tests, on porcine cadaver brain. (a) Local protuberance highlighted at the array site due to drag forces. (b) Tension versus displacement with key moments highlighted with a dashed line: *Moment 1*, brain relaxation; M*oment 2*, maximum tension; M*oment 3*, complete detachment.

Buckling Test

A compression test was performed against a glass support to determine the force necessary to bend the pillars. Figure 5.16 shows the resulting load versus displacement curve, obtained at a displacement rate of 0.08 mm/s. The initial stage represents the descending of the array against the support while no load is applied. After mechanical contact between the array and the support, an abrupt increase in load followed was observed. After the moment where a maximum load is reached, a decrease in load was observed. The resulting peak

represents the moment when the pillars begin to bend (buckle), which occurs when a 4.5 N load is applied [6].

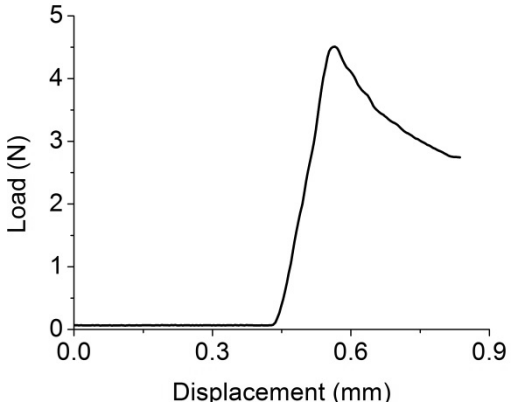

Figure 5.16: Second aluminum prototype compression curve. The observable peak represents the buckling load.

Flexibility Test

A flexibility test was performed using the three point flexural test. The tested sample was 20 mm wide and 9.6 mm long. The support was made of aluminum with 15 mm spacing between support points (Figure 5.17a). A downward load was applied at the middle of the sample until sample rupture could be observed. A maximum deflection before rupture of 0.8 mm was achieved while applying a load of 16.5 N (Figure 5.17b)

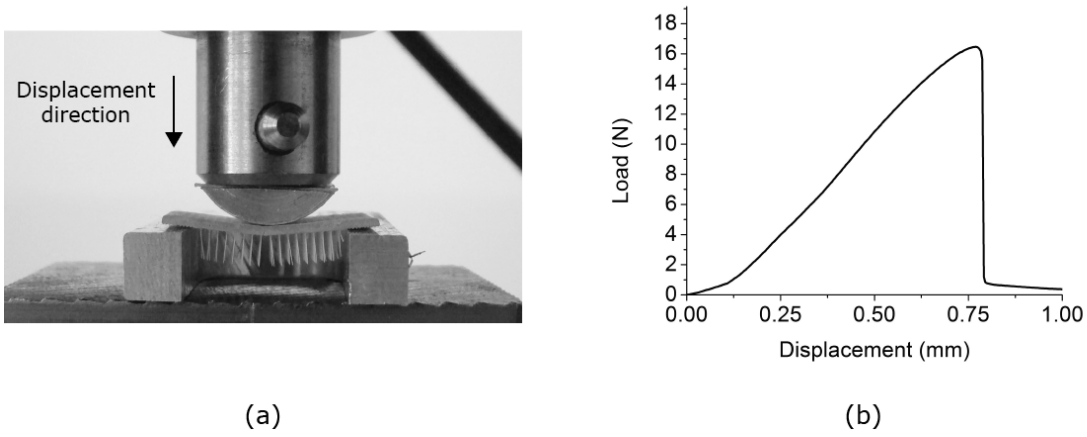

Figure 5.17: Second aluminum prototype three point flexural test. (a) Moment of rupture. (b) Load versus displacement, with an abrupt drop at rupture moment.

5.2.3 Second Silicon prototype

The mechanical characterization of the silicon prototype was performed by the

following tests:

- Implantation and explantation in agar gel
- Implantation and explantation in porcine cadaver brain
- Buckling
- Shear strength
- Flexibility

The implantation tests were performed on a Shimadzu AG-IS dynamometer equipped with a 50 N load cell capable of a 5 mN resolution. The mechanical characterization used arrays with 130 µm wide, 4 mm long, sharp silicon pillars.

Agar

Figure 5.18 shows the set-up arrangement for the implantation tests. Three different implantation speeds were performed on a 0.5 % concentration of agar gel.

Table 5.3, summarizes the implantation results.

Just like on the aluminum prototypes, the load versus displacement curve shows a peak at the implantation moment (Figure 5.18b). The same tendency of speed versus implantation load was observed with the silicon array, faster implantation speeds required higher loads.

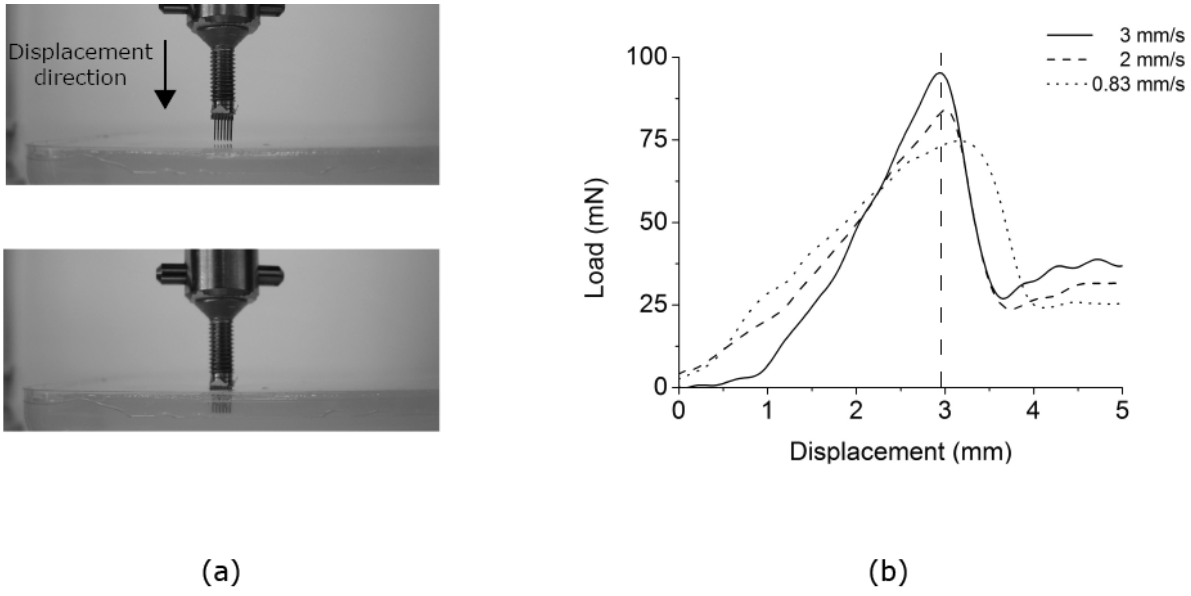

Figure 5.18: Second silicon prototype implantation tests in agar gel. (a) Set-up, before implantation (top photo), and after implantation (bottom photo). (b) Load versus displacement for three different speeds, with implantation moment highlighted by a dashed line.

Table 5.3: Silicon array implantation tests on agar.

Speed (mm/s)	Number of tests	Average load (mN)	Standard deviation (mN)	Average load per pillar (mN)
3	10	95.45	14.49	2.65
2	10	94.75	31.37	2.63
0.83	10	87.04	8.93	2.42

Porcine Cadaver brain

Six implantation tests were performed on porcine cadaver brain with the *pia matter* at 3 mm/s. The arrays had the same characteristics used in agar tests. Similarly to the aluminum arrays, significant tissue dimpling was observed before implantation. Among the 6 implantation tests on cadaver brain, two groups could be divided based on the load versus displacement curve. The first group consisted of 4 implantation tests, and had a curve with continuously increasing load (Figure 5.19a). The second group consisted of 2 implantation tests, and had an observable peak on the curve (Figure 5.19b). For the 2 tests the average load of the peak was 390 mN, and the displacement was 9.93 mm.

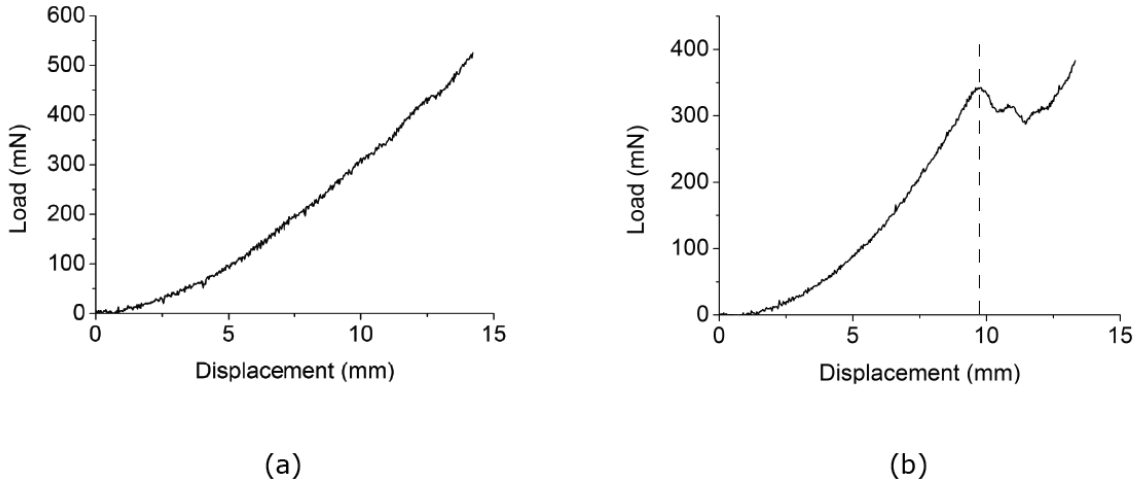

Figure 5.19: Second silicon prototype implantation tests in porcine cadaver brain. Load versus displacement curves: (a) continuously increasing load; (b) peak during implantation highlighted by a dashed line.

Just like in the aluminum arrays, successful implantation could be verified through explantation results. The set-up and withdrawal results on porcine cadaver brain are presented on Figure 5.20. The key moments during withdrawal are highlighted by a dashed line (Figure 5.20b). In moment 1 the brains' surface is in its relaxed state, in moment 2 a maximum

tension is applied, and in moment 3 there is a complete detachment between the array and the brain. A temporary protuberance could be observed in the region of implantation close to moment 2 (Figure 5.20a). This was followed by a drop in the applied tension which led to the instant where the array was completely detached from the brain (moment 3). Only 4 out of 6 explantation tests were successful. The unsuccessful implantations could be observed due to the lack of moment 2 on the tension versus displacement curve. The average difference between maximum tension and brain relaxation of the successful implantations were 49 mN with a standard deviation of 16 mN.

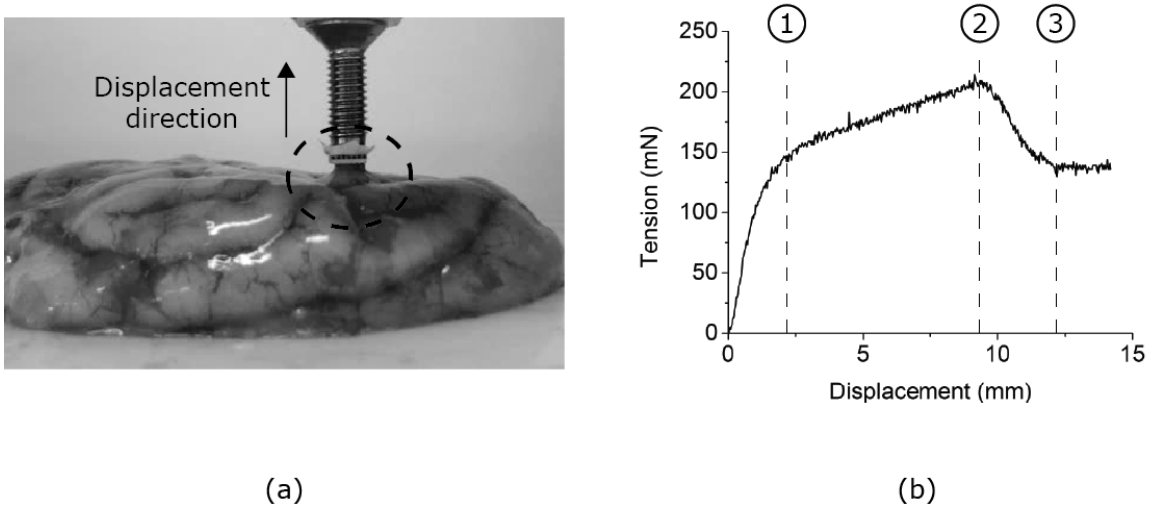

Figure 5.20: Second silicon prototype explantation tests, on porcine cadaver brain. (a) Local protuberance highlighted at the array site due to drag forces. (b) Tension versus displacement with key moments highlighted with a dashed line: *Moment 1*, brain relaxation; *Moment 2*, maximum tension; *Moment 3*, complete detachment.

Buckling and Shear Test

A compression test was performed against an aluminum support in order to determine the buckling load the pillars (Figure 5.21a). At a displacement rate of 1.67 µm/s, an abrupt drop in load is observed under the compression test (Figure 5.21b). This drop represents the breaking of pillars at a correspondent load of 59 N. Due to the stiffness of silicon, the pillars break instead of bending or buckling. This moment is represented by a peak on Figure 5.21b. A shear test was performed on a single pillar in order to determine its resistance to bending (Figure 5.21c). A load of 59 mN was necessary to break the pillar at a displacement rate of 1.67 µm/s (Figure 5.21d).

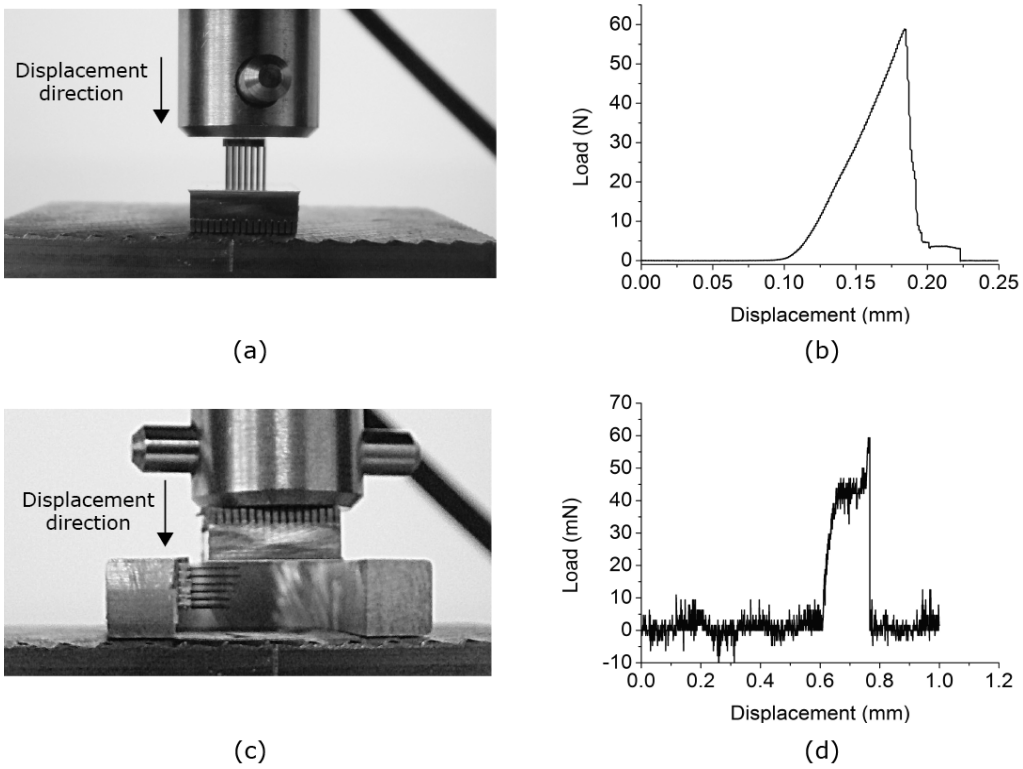

Figure 5.21: Second silicon prototype compression and shear tests. (a) Set-up of compression and (c) shear tests. (b) Load versus displacement for compression, and (d) shear tests. On both images the peak represents the moment of pillars breakage.

Flexibility Test

A flexibility test was performed using the three point flexural test. The tested sample was 19.2 mm wide and 4 mm long. The support was made of aluminum with 15 mm spacing between supporting points (Figure 5.22a). A downward load was applied at the middle of the sample until rupture could be observed. A maximum deflection before rupture of 0.3 mm was achieved while applying a load of 1.8 N (Figure 5.22b)

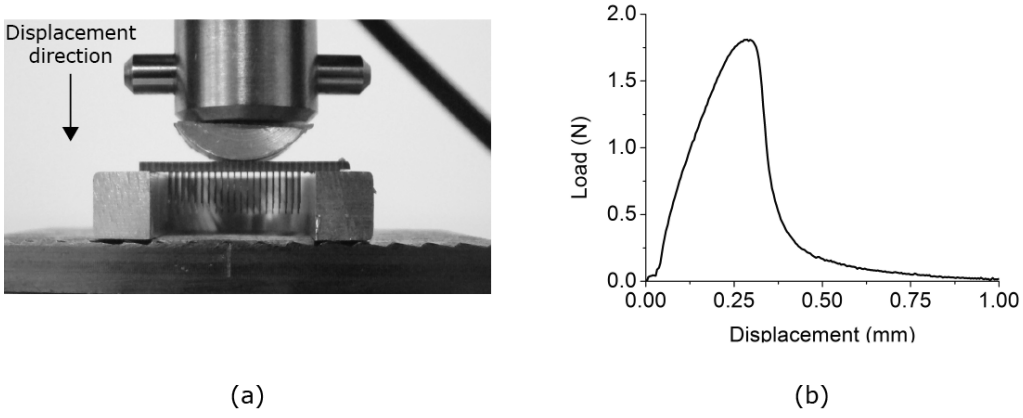

Figure 5.22: Second silicon prototype three point flexural test. (a) Moment of rupture. (b) Load versus displacement, with an abrupt drop at rupture moment. The peak represents the moment of rupture.

5.2.4 Comparison

For the agar gel, both arrays showed a tendency to decrease the implantation load with the increase of implantation speed. The observed peaks on the agar tests, suggests the existence of a layer at the surface which offers a bigger opposition than the bulk. This could be caused by a dehydration of the gel's surface due to air exposure.

The implantation load of the aluminum and silicon pillars at 3 mm/s in agar was of 6 and 2.65 mN respectively, which results on a load difference of 3.35 mN per pillar. Also, the implantation load per area of the aluminum pillars is 84% superior in comparison to the silicon pillars. Possible causes are the difference on the shape of the tip between arrays and also the stiffness of the pillars. The inferior stiffness of the aluminum pillars may provide lower shear forces on the surface of the agar thus requiring greater loads for the piercing of the agar's surface.

The compression tests showed that the average force to bend/break one aluminum and one silicon pillar was 0.18 N and 1.6 N respectively, which represents an absolute difference in force of 1.42 N. This implies that, in terms of force per area, it was necessary to employ 10 times greater force to bend/break pillars made of silicon when compared to aluminum. The underlying cause of this effect is the superior Young's modulus of silicon.

The flexural tests showed that the aluminum sample flexed 0.5 mm more than the silicon sample. This represents a deflection 3 times greater of the aluminum sample versus the silicon one. The greater flexibility of the aluminum sample could be caused by the increase of flexibility properties of the epoxy after undergoing wet-etching and also the ductility of aluminum itself.

Both arrays were able to pierce the *pia matter*, which suggest a high robustness of the pillars. The explantation data shows that the maximum tension to withdraw the aluminum pillars is almost two times superior when compared to the silicon ones. The superior surface roughness of the etched aluminum, when compared to the diced silicon, could be the cause of this increase in tension.

5.3 Electrochemical

The thin-film of gold and platinum were characterized by electrochemical impedance spectroscopy (EIS). This test is valuable for assessing the recording capabilities of the electrode by measuring its electrical impedance and phase angle. The impedance is recorded for a wide range of frequencies, particularly, the impedance at 1 kHz is of neurobiological

interest because the action potential typically lasts approximately 1 ms [7]. The phase angle describes how capacitive or resistive the interface is. Low capacitance is desirable for neural recording since it will provide an overall lower electrode impedance specially at low frequencies [8]. Figure 5.23 shows the electrical model of the electrode-electrolyte interface, also known as the simplified Randles circuit [9]. In this circuit, R_{ct} represents the charge transfer resistance, C_{dl} the double layer capacitance, and R_s the solution resistance.

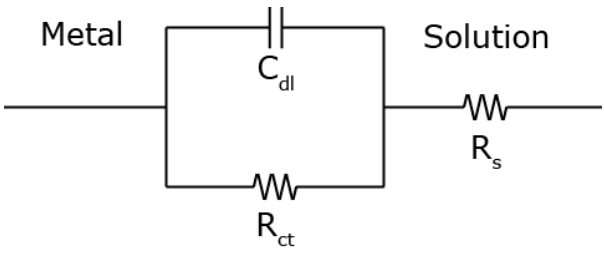

Figure 5.23: Equivalent circuit of the electrode-electrolyte interface (simplified Randles circuit).

Cyclic voltammetry (CV) was performed on the platinum thin-films in order to assess the stimulation capabilities of the electrode. The CV allows the determination of the total amount of charge per area, also known as the charge storage capacity (CSC), which is a measure of the total amount of charge available for a stimulation pulse [10]. The greater the CSC of an electrode, the greater will be its ability to deliver charge into the tissue.

The CV was only performed on the platinum thin-film, since gold is not suitable for stimulation due to its rapid dissolution in the presence of chloride ions [11,12].

For both EIS and CV, a three-electrode set-up was used (Figure 5.24). The set-up consisted of a test electrode (TE), an Ag/AgCl reference electrode (RE), and a large area (4 mm × 4 mm) platinum counter electrode (CE) [13].

In EIS test, a small sinusoidal AC wave is applied between the TE and the RE, while the electric current flows from the TE to the CE.

In the CV test, a triangular AC wave is swept cyclically between the TE and the RE between two potential limits while allowing current to flow between the TE and the CE.

In both cases there is no flow of current between the TE and the RE.

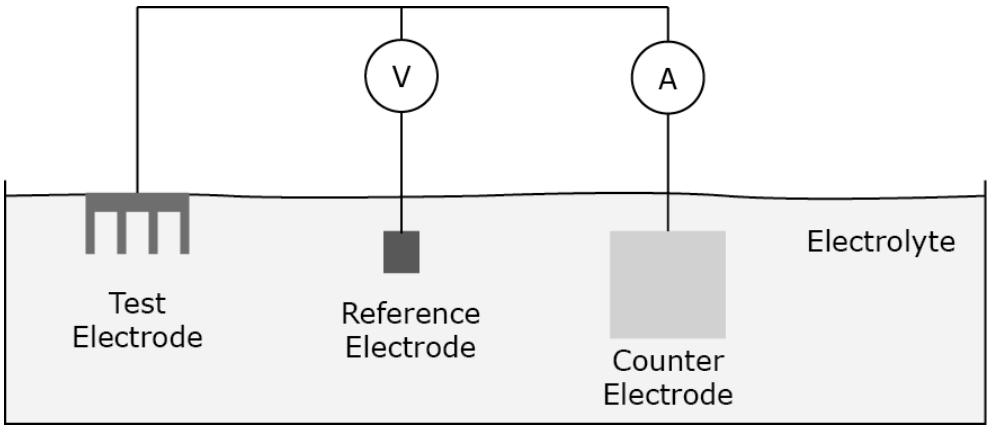

Figure 5.24: Three electrode cell configuration used for EIS and CV.

The EIS and CV were performed by a Gamry Reference 600^{TM} Potentiostat. Microscope slides were used as testing platform for the thin-film characterization. These glass slides were subjected to the same deposition parameters as the neural arrays.

5.3.1 Gold

A 300 nm thick, thermal evaporated thin-film of gold was tested for impedance and phase angle on the electrochemical cell. The electrode was subjected to a phosphate buffered saline (PBS) electrolyte with an exposed area of 4.15 cm^2. A 10 mV AC voltage was applied between the test and reference electrode, with frequencies ranging from 1 Hz to 1 MHz.

Figure 5.25a, shows the impedance of the film versus applied frequency. An accentuated decrease in impedance can be observed from 1 Hz to 100 Hz, stabilizing around 5 kΩ. At 1 kHz, the acquired impedance was 4.5 kΩ.

The electrode displays a nearly resistive (phase angle < −10º) behavior for frequencies between 1 kHz and 100 kHz and a capacitive behavior for the remaining frequencies (Figure 5.25b). The equivalent model was fitted to the impedance curve using the Levenberg-Marquardt algorithm [14] resulting on the following values: R_{ct} = 22.4 kΩ; C_{dl} = 1.96 µF; and R_s = 4.4 kΩ.

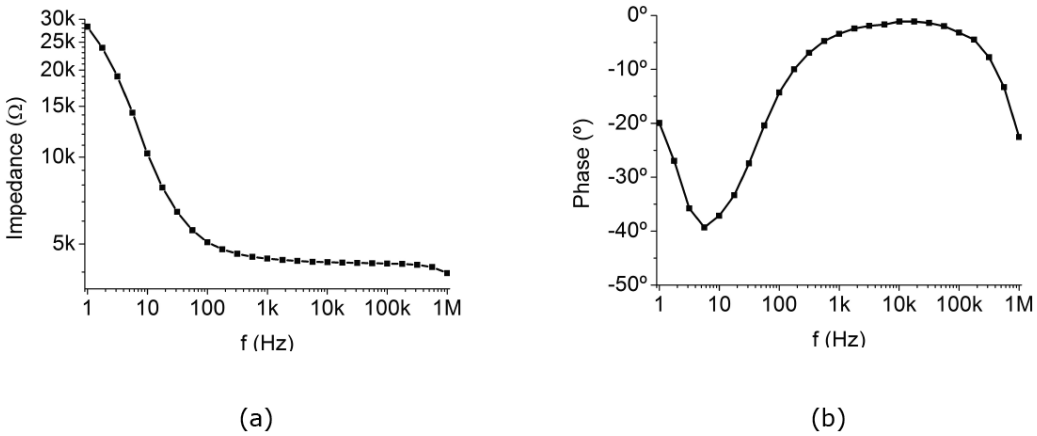

Figure 5.25: Bode plot of the EIS of the gold electrode in PBS solution: (a) impedance; (b) phase angle.

5.3.2 Platinum

A 180 nm thick, platinum thin-film was tested for impedance and phase angle on the electrochemical cell. The electrode was subjected to a 0.9% NaCl water solution (saline) with an exposed area of 0.28 cm^2. A 10 mV AC voltage was applied between the test and reference electrode, with frequencies ranging from 1 Hz to 1 MHz.

Figure 5.26a, shows the impedance of the film versus applied frequency. A continuous decrease in impedance can be observed from 1 Hz to 1 kHz with a stabilization from 10 kHz on. At 1 kHz, the acquired impedance was 1.96 kΩ.

The electrode displays a capacitive behavior from 1 Hz to 10 kHz, being nearly resistive (phase angle $< -10^{o}$) from 10 kHz on (Figure 5.26b). The equivalent model was fitted to the impedance curve using the Levenberg-Marquardt algorithm resulting on the following values: R_{ct} = 428 kΩ; C_{dl} = 306 nF; and R_s = 1.17 kΩ.

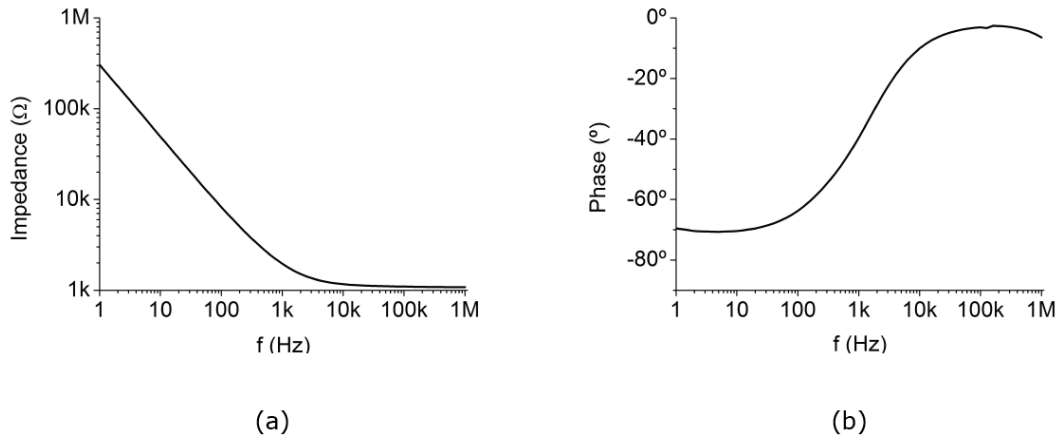

Figure 5.26: Bode plot of the EIS of the platinum electrode in NaCl solution: (a) impedance; (b) phase angle.

A cyclic voltammetry was performed on the same electrode applying a potential range between −1 V and 1.25 V (Figure 5.27). This range represents the water window for platinum and is defined as the potential region between the oxidation of water to form oxygen and the reduction of water to form hydrogen (moments 2 and 4). The oxidation of the platinum is marked by a sharp increase in current while applying 1.25 V, and the reduction is marked by the sharp decrease in current while applying −1 V. If the electrode potential passes beyond either of these two water window boundaries, all further injected charge goes into the irreversible processes of water oxidation or reduction [15].

The CSC was calculated from the time integral of the cathodic current within the water electrolysis window potential range. The cathodic current corresponds to the reduction of the electrode and is represented by the part of the curve that has negative current. The CSC corresponds to the area of the curve with negative currents (cathodic currents). The calculated CSC was 200 µC representing 700 µC/cm^2. This CSC value for Platinum, which is in accordance with other studies, demonstrates the ability of the film for stimulation purposes [10,16].

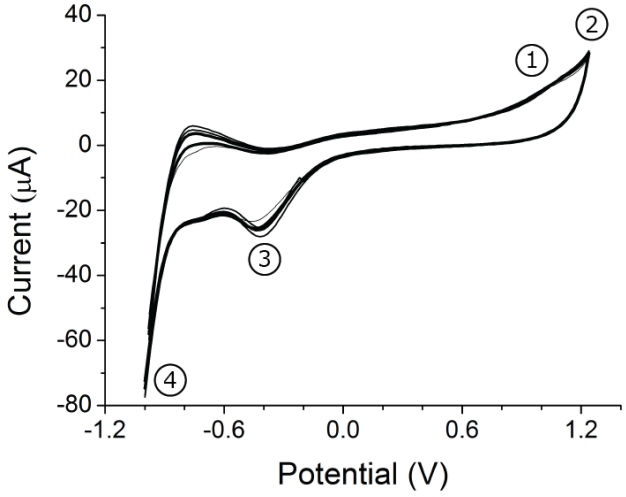

Figure 5.27: Cyclic voltammogram of Platinum in NaCl with a sweep rate of 100 mV/s. Key moments highlighted: (1) Pt oxidation; (2) O_2 release; (3) Pt reduction; and (4) H_2 generation.

References

[1] O. Arnould and F. Hild, “On the measurement by EDX of diffusion profiles of Ni/Cu assemblies,” *arXiv Prepr. arXiv0712.3636*, no. March, 2007.

[2] A. Altuna, G. Gabriel, L. Menéndez de la Prida, M. Tijero, A. Guimerá, J. Berganzo, R. Salido, R. Villa, and L. J. Fernández, "SU-8-based microneedles for in vitro neural applications," *J. Micromechanics Microengineering*, vol. 20, no. 6, Jun. 2010.

[3] R. Das, D. Gandhi, S. Krishnan, L. Saggere, and P. J. Rousche, "A benchtop system to assess cortical neural interface micromechanics.," *IEEE Trans. Biomed. Eng.*, vol. 54, no. 6 Pt 1, pp. 1089–1096, Jun. 2007.

[4] R. Pomfret, G. Miranpuri, and K. Sillay, "The Substitute Brain and the Potential of the Gel Model," *Ann. Neurosci.*, vol. 20, no. 3, Jul. 2013.

[5] A. A. Sharp, A. M. Ortega, D. Restrepo, D. Curran-Everett, and K. Gall, "In vivo penetration mechanics and mechanical properties of mouse brain tissue at micrometer scales," *IEEE Trans. Biomed. Eng.*, vol. 56, no. 1, pp. 45–53, Jan. 2009.

[6] A. T. Beck and A. S. Dória, "Reliability Analysis of I-Section Steel Columns Designed According to New Brazilian Building Codes," *J. Braz. Soc. Mech. Sci. Eng.*, no. 2, pp. 152–159, 2008.

[7] E. Kandel, J. Schwartz, and T. Jessell, *Principles of neural science*, 5th Ed. McGraw-Hill Medical, 2000.

[8] D. Zhou and E. Greenbaum, *Implantable Neural Prostheses Vol 2*. Springer, 2009.

[9] W. Franks, I. Schenker, P. Schmutz, and A. Hierlemann, "Impedance characterization and modeling of electrodes for biomedical applications.," *IEEE Trans. Biomed. Eng.*, vol. 52, no. 7, pp. 1295–1302, Jul. 2005.

[10] S. F. Cogan, "Neural stimulation and recording electrodes," *Annu. Rev. Biomed. Eng.*, vol. 10, pp. 275–309, Jan. 2008.

[11] S. Myllymaa, K. Myllymaa, and R. Lappalainen, "Flexible implantable thin film neural electrodes," *Recent Adv. Biom. Eng.*, 2009.

[12] G. E. Loeb and C. Gans, *Electromyography for Experimentalists*. University of Chicago Press, 1986.

[13] S. Negi, R. Bhandari, and F. Solzbacher, "Morphology and Electrochemical Properties of Activated and Sputtered Iridium Oxide Films for Functional Electrostimulation," *J. Sens. Technol.*, vol. 2, no. September, pp. 138–147, 2012.

[14] D. Marquardt, "An Algorithm for Least-Squares Estimation of Nonlinear Parameters," *J. Soc. Ind. Appl. Math.*, vol. 11, no. 2, pp. 431–441, 1963.

[15] D. R. Merrill, M. Bikson, and J. G. R. Jefferys, "Electrical stimulation of excitable tissue: design of efficacious and safe protocols.," *J. Neurosci. Methods*, vol. 141, no. 2, pp. 171–198, Feb. 2005.

[16] K. G. Shah, V. M. Tolosa, A. C. Tooker, S. H. Felix, and S. S. Pannu, "Improved chronic neural stimulation using high surface area platinum electrodes.," *Annu. Int. Conf. IEEE Eng. Med. Biol. Soc.*, pp. 1546–1549, Jan. 2013.

Chapter 6

Conclusion

The present work showed the design parameters, fabrication approaches, and characterization of tridimensional neural electrodes. Four prototypes were developed, two using aluminum and the other two using silicon. The second prototype of each material represented an evolution from the first prototype and will be referred from now on as aluminum and silicon array.

The primary objective was the fabrication of a high-density array with the ability to reach areas of the brain below the cortex in the rat. This animal is commonly used as model for neurological studies and has a cortex thickness of approximately 2 mm [1]. Deeper structures of the brain such as the hippocampus could be more effectively studied by such devices. Also, commercially available, microfabricated, tridimensional arrays are either limited to a recording depth of 2 mm or require manual assembly of its parts [2–4].

The secondary objective was the development of a fabrication approach that required fewer steps than commercially available probes and at the same time avoided costly technologies such as reactive ion etching (RIE) and chemical vapor deposition (CVD).

Both objectives were achieved with success. High-aspect-ratio pillars with lengths of 3 mm and 4 mm were accomplished by the aluminum and silicon arrays, respectively. The silicon array relied basically on dicing technology and polymer deposition, while the

aluminum array needed an extra step of wet-etching, providing a simple and cost-effective fabrication approach.

6.1 Aluminum vs. Silicon

Both aluminum and silicon showed some strengths and weaknesses as structural material of the array.

Aluminum pillars have greater electrical conductivity and mechanical flexibility than doped silicon. Its high-electrical conductivity allows low signal loss and thus better quality signals. Its superior flexibility reduces the mechanical mismatch between brain tissue and pillars, decreasing the amount of local inflammation and neurodegeneration [5]. However, aluminum showed some disadvantages, such as the difficulty of dicing high-aspect-ratio pillars and the accumulation of aluminum residues at the blade.

High-aspect-ratio silicon pillars could be cut with the dicer without residue formation. They had a buckling load 10 times superior to aluminum. This significant difference is due to the greater Young's modulus of silicon. This superiority allows pillars with higher aspect-ratios to sustain the same amount of load without bending. Being the standard semiconductor material, silicon has been widely used as neural probe and is fully compatible with standard CMOS processes [6,7]. These two facts offer greater processing knowledge on this material, and also, a wide variety of available microfabrication techniques without the need of adaptations [8]. On the other hand, silicon pillars could easily break during cutting due to its brittleness, which required special dicing procedures.

6.2 Fabrication

Dicing

The dicing technology was effective at making high-aspect-ratio pillars with consistent width. Actually, the variation of the 4 mm long silicon pillars was below the 5 µm resolution of the microscope. The performance of tips using this technology avoided others more costly technologies [9–11]. It also allowed the same equipment to perform multiple steps of fabrication, reducing its overall complexity.

The dicing of high-aspect-ratio structures required special concerns in terms of blade type, depth and speed of cut. Aluminum and silicon offered different challenges when

performing high-aspect-ratio pillars.

Aluminum pillars required a minimum width of 280 µm in order for 3 mm long pillars to withstand the cut. Smaller widths or longer lengths resulted in pillars bending. Also, the right choice of blade thickness, bond type and diamond grit size was essential. Only blades with large grit size (≥ 23 µm) were successful at dicing aluminum, while small grit size (3 µm), even at slow speeds would invariably lead to blade breakage.

Silicon allowed higher aspect-ratio pillars than aluminum. Although 130 µm wide pillars were successfully performed through dicing, they required cuts with increasing depths in order to avoid pillar breakage. This approach allowed 94% of the measured pillars to withstand the cuts. Only a blade with flexible bond type (NBC) and small grit size could achieve these results. Other blades such as Z09 and ZHDG with equal or greater grit size would drastically decrease the number of intact pillars. Probable reasons for this decrease were the relative big grits and the stiffness of the blades' bond which would cause chipping of the silicon and increase cutting vibration, eventually leading to pillars breakage.

For both materials, very slow cutting speeds (0.3-0.5 mm/s) had to be applied in order to result in pillar integrity. In fact, on the last dicing stage, the cuts usually required the minimum speed allowed by the equipment (0.3 mm/s). Low speeds were also mandatory to maintain good quality of cut and blade integrity. Wavy cuts and blade breakage was observed with NBC blades when cutting 4 mm deep grooves in silicon with speeds equal to or above 1 mm/s. From literature, grooves with a maximum aspect ratio of 20:1 were mentioned but in this work, grooves with 27:1 were successfully performed at very low speeds [12].

Encapsulation

The encapsulation with medical grade epoxy (Hysol^{TM} M-31CL) required a special degassing procedure in order to avoid entrapment of air bubbles. Air is added in the epoxy when the two components are mixed. Besides removing the air bubbles, the degassing period also decreased the epoxy viscosity, since the polymer curing starts at the moment of mixing. A balance between degassing time and viscosity was attained at 45 minutes, since longer periods would make the resin too viscous to flow into the interpillar space. Another concern was the use of small amounts (< 2 g) of resin in order to avoid excessive heat generated by the chemical reactions while curing. Larger quantities would result in pillars bending or cracking due to thermal expansion.

Thermomigration

The two proposed thermomigration approaches could only dope 800 µm thick layers of silicon. The inability to dope 4 mm thick silicon wafers showed to be unfeasible by these

two approaches. In order to perform the migration of aluminum in such thick substrates, an apparatus able to produce a more stable and a greater temperature gradient would be necessary. Systems have been developed to successfully perform the migration of aluminum in silicon. Issues concerning trail merging, poor yield, low interelectrode impedance, and set-up complexity have been reported on such systems [13–15].

General approach

The fabrication approach of the silicon array relies on dicing, polymer and thin-film deposition, while the aluminum array requires an extra step of wet-etching. Both arrays avoid the used of techniques usually required in the fabrication of tridimensional neural electrodes such as photolithography, RIE and CVD, which represents a simpler and cheaper fabrication methodology [6,8].

6.3 Characterization

Through optical and scanning electron microscopy the pillars' aspect-ratio, tips' morphology, encapsulation, and thin-film morphology were analyzed. Observations with a 60x magnification under the optical microscope showed no width variation for both aluminum and silicon arrays after encapsulation. At this magnification details below 5 µm were imperceptive, which implies that width variations below 5 µm were achieved. The same behavior could be observed on the length of the silicon pillars. On the other hand, the aluminum pillars showed a variation in length mainly due to tip differences. The ductility of aluminum introduced these tip variations, since with the passing of the blade small differences would appear at the tip.

The determination of successful implantation of the array in porcine cadaver brain showed some challenges, since during implantation the force versus displacement curve did not show clear evidences of penetration. The success of implantation was confirmed through the explantation tests, since a local protuberance and a detachment instant could be observed on the tension versus displacement curve. Displacements of three to four times the length of the arrays were necessary for implantation to occur. The amount of dimpling before implantation suggests that the *pia matter* behaved as a penetration barrier. These results indicates that high-velocity implantation techniques such as impaction insertion are better suited to implant a dense array of needles without massive tissue dimpling and compression [16].

The compressive tests on both arrays showed that silicon pillars could withstand

10 times greater axial loads than aluminum pillars. This implies that silicon pillars thinner than aluminum could support the same amount of compressive load without breaking. This is valuable since pillars with small cross-section result in small insertion trauma.

Gold and platinum films were electrochemically tested on a three electrode cell. Both gold and platinum showed a decrease in impedance with the increase of frequency, due to their capacitive behavior. At high frequencies the acquired impedance was mainly due to the solution resistance. Only platinum could behave as stimulation electrode, since charge injection on the gold film would quickly destroy it. A charge injection capacity of 700 $\mu C/cm^2$ was observed for the platinum film.

6.4 Future work

Further work would be necessary to connect the array to external devices. Through the use of interconnecting technologies such as wire bonding, it would be possible to electrically link each electrode to external instrumentation. This link would allow the EIS measurement directly on the array therefore allowing a better control of the electrode's impedance. Also, the wired connection would allow the acquisition of signals on live animals such as rats and comparison to commercial electrodes.

The addition of signal processing electronics and wireless communication electronics embedded on the array would be the next step after the wired connection since this would decrease the risk of infections due to transcutaneous connections. Also, by being completely integrated with the body, with no external connections it would add greater mobility to the test subject and ubiquity to the device. In order to add these features, technologies such as flip-chip bonding, and polymer encapsulation should be employed [17].

The deposition of uniform films on the electrode surface should be addressed by using techniques such as rotating substrates on PVD systems. Other approach would be the electrodeposition of biocompatible polymers capable of charge injection such as PEDOT [18].

A more conclusive test should be done to determine array implantation. Techniques such as high-resolution computer tomography could be performed to confirm implantation success with a greater accuracy.

The development of a fabrication procedure able to decrease the cross-section of the pillars would be valuable, since this would produce a smaller immune response [19]. Decreasing the pillars cross-section would allow a greater density of electrodes, which is valuable in the neuroprosthetics field [20].

A future improvement to the device would be the addition of light emitting capabilities. The ability to stimulate neurons with light has proven to be of great value to neuroscientists, in an emerging field called optogenetics. The incorporation of light guides along the pillars or micro light emitting diodes at their tip could add the desired optical capabilities to the array. These features would require a significant increase in fabrication complexity of the array [21].

Also, the ability to perform chemical sensing in the brain could bring some insights on the continuous electrical and chemical interactions of the brain. Possible schemes could use electrochemistry, hydrogels, or plasmonic crystals [22–24]. Chemical interaction could be performed with the addition of drug delivery capabilities like microchannels or biodegradable carriers [25,26].

References

[1] G. Paxinos and C. Watson, *The Rat Brain in Stereotaxic Coordinates - Part 1*, Sixth Edit. Elsevier Inc., 2007.

[2] R. A. Normann, "Technology insight: future neuroprosthetic therapies for disorders of the nervous system," *Nat. Clin. Pract. Neurol.*, vol. 3, no. 8, pp. 444–452, 2007.

[3] M.-Y. Cheng, M. Je, K. L. Tan, E. L. Tan, R. Lim, L. Yao, P. Li, W.-T. Park, E. J. R. Phua, C. L. Gan, and A. Yu, "A low-profile three-dimensional neural probe array using a silicon lead transfer structure," *J. Micromechanics Microengineering*, vol. 23, no. 9, Sep. 2013.

[4] S. Musallam, M. J. Bak, P. R. Troyk, and R. A Andersen, "A floating metal microelectrode array for chronic implantation.," *J. Neurosci. Methods*, vol. 160, no. 1, pp. 122–7, Feb. 2007.

[5] V. S. Polikov, P. A. Tresco, and W. M. Reichert, "Response of brain tissue to chronically implanted neural electrodes.," *J. Neurosci. Methods*, vol. 148, pp. 1–18, Oct. 2005.

[6] K. D. Wise, "Silicon microsystems for neuroscience and neural prostheses," *IEEE Eng. Med. Biol. Mag.*, October, 2005.

[7] K. C. Cheung, "Implantable microscale neural interfaces," *Biomed. Microdevices*, vol. 9, no. 6, pp. 923–938, Dec. 2007.

[8] M. Hajjhassan, V. Chodavarapu, and S. Musallam, "NeuroMEMS: Neural Probe Microtechnologies," *Sensors*, vol. 8, pp. 6704–6726, 2008.

[9] S. Kim, R. Bhandari, M. Klein, S. Negi, and L. Rieth, "Integrated wireless neural interface based on the Utah electrode array," *Biomed. Microdevices*, pp. 453–466, 2009.

[10] G. E. Perlin and K. D. Wise, "Ultra-compact integration for fully-implantable neural microsystems," in *IEEE 22nd International Conference on Micro Electro Mechanical Systems,(MEMS)*, 2009.

[11] J. Du, M. L. Roukes, and S. C. Masmanidis, "Dual-side and three-dimensional microelectrode arrays fabricated from ultra-thin silicon substrates," *J. Micromechanics Microengineering*, vol. 19, no. 7, Jul. 2009.

[12] Devin Martin, "The Evolution of Wafer Dicing," *The International Magazine for te Semiconductor Packaging Industry*, vol. 18, no. 5, 2014.

[13] K. E. Jones, P. K. Campbell, and R. A. Normann, “A Glass / Silicon Composite Intracortical Electrode Array,” *Ann. Biomed. engeneering*, pp. 423–437, 1992.

[14] B. Morillon, J.-M. Dilhac, C. Ganibal, and C. Anceau, “Realization of Deep P+ Zones by Al Thermomigration in a Temperature Gradient RTP Furnace,” in *199th Meeting of the Electrochemical Society, March, Washington, DC*, 2001.

[15] H. E. Cline, “Thermomigration of aluminum-rich liquid wires through silicon,” *J. Appl. Phys.*, vol. 47, no. 6, 1976.

[16] P. J. Rousche and R. a Normann, “A method for pneumatically inserting an array of penetrating electrodes into cortical tissue.,” *Ann. Biomed. Eng.*, vol. 20, no. 4, pp. 413–422, Jan. 1992.

[17] A. Sharma, L. Rieth, P. Tathireddy, R. Harrison, H. Oppermann, M. Klein, M. Töpper, E. Jung, R. A. Normann, G. Clark, and F. Solzbacher, “Long term in vitro functional stability and recording longevity of fully integrated wireless neural interfaces based on the Utah Slant Electrode Array,” *J. Neural Eng.*, vol. 8, no. 4, Aug. 2011.

[18] X. Cui and D. Zhou, “Poly (3, 4-ethylenedioxythiophene) for chronic neural stimulation,” *Neural Syst. Rehabil. Eng.*, vol. 15, no. 4, pp. 502–508, 2007.

[19] A. Fujishiro, H. Kaneko, T. Kawashima, M. Ishida, and T. Kawano, “In vivo neuronal action potential recordings via three-dimensional microscale needle-electrode arrays.,” *Sci. Rep.*, vol. 4, Jan. 2014.

[20] D. A. Schwarz, M. A. Lebedev, T. L. Hanson, D. F. Dimitrov, G. Lehew, J. Meloy, S. Rajangam, V. Subramanian, P. J. Ifft, Z. Li, A. Ramakrishnan, A. Tate, K. Z. Zhuang, and M. A. L. Nicolelis, “Chronic, wireless recordings of large-scale brain activity in freely moving rhesus monkeys,” *Nat. Methods*, May 2013, Apr. 2014.

[21] T. Kim, J. G. McCall, Y. H. Jung, X. Huang, E. R. Siuda, Y. Li, J. Song, Y. M. Song, H. A. Pao, R.-H. Kim, C. Lu, S. D. Lee, I.-S. Song, G. Shin, R. Al-Hasani, S. Kim, M. P. Tan, Y. Huang, F. G. Omenetto, J. A. Rogers, and M. R. Bruchas, “Injectable, Cellular-Scale Optoelectronics with Applications for Wireless Optogenetics,” *Science*, vol. 340, pp. 211–216, Apr. 2013.

[22] E. van der Wouden, E. Tolner, M. Odjik, W. Olthuis, A. van den Maagdenburg, M. Ferrari, and A. van den Ber, “Development of a neural probe to measure potassium during a cortical spreading depression in-vivo,” in *Transducers conference*, Jun. 2013.

[23] M. Guenther, T. Wallmersperger, and G. Gerlach, “Piezoresistive Chemical Sensors Based on Functionalized Hydrogels,” *Chemosensors*, vol. 2, no. 2, pp. 145–170, Jun. 2014.

[24] M. E. Stewart, C. R. Anderton, L. B. Thompson, J. Maria, S. K. Gray, J. a Rogers, and R. G. Nuzzo, “Nanostructured plasmonic sensors.,” *Chem. Rev.*, vol. 108, no. 2, pp. 494–521, Feb. 2008.

[25] O. Frey, P. D. van der Wal, S. Spieth, O. Brett, K. Seidl, O. Paul, P. Ruther, R. Zengerle, and N. F. de Rooij, “Biosensor microprobes with integrated microfluidic channels for bi-directional neurochemical interaction.,” *J. Neural Eng.*, vol. 8, no. 6, Dec. 2011.

[26] A. P. Alivisatos, A. M. Andrews, E. S. Boyden, M. Chun, G. M. Church, K. Deisseroth, J. P. Donoghue, S. E. Fraser, J. Lippincott-Schwartz, L. L. Looger, S. Masmanidis, P. L. McEuen, A. V Nurmikko, H. Park, D. S. Peterka, C. Reid, M. L. Roukes, A. Scherer, M. Schnitzer, T. J. Sejnowski, K. L. Shepard, D. Tsao, G. Turrigiano, P. S. Weiss, C. Xu, R. Yuste, and X. Zhuang, “Nanotools for neuroscience and brain activity mapping.,” *ACS Nano*, vol. 7, no. 3, pp. 1850–1866, Mar. 2013.

Annex

Journal Publications

1. A. C. Peixoto, A. F. Silva, N. S. Dias, and J. H. Correia, “High-aspect-ratio neural electrode array fabrication using thermomigration process,” *Procedia Engineering*, pp. 1–4, 2012.
2. A. C. Peixoto, S. B. Goncalves, A. F. Silva, N. S. Dias, and J. H. Correia, “Neural Electrode Array Based on Aluminum: Fabrication and Characterization,” *IEEE Sensors Journal*, vol. 13, no. 9, pp. 3319–3324, 2013.
3. A. C. Peixoto, S. B. Goncalves, F. Pinho, A. F. Silva, N. S. Dias, and J. H. Correia, “Flexible three-dimensional microelectrode array for neural applications,” Sensors Actuators A Physical, vol. 217, pp. 21–28, Sep. 2014.
4. S. B. Goncalves, A. C. Peixoto, A. F. Silva, and J. H. Correia “Fabrication and mechanical characterization of long and different penetrating length neural microelectrode arrays” *Journal of Micromechanics and Microengineering*” (in press)

The full papers are attached in the following pages.

Available online at www.sciencedirect.com

ScienceDirect

Procedia Engineering 00 (2012) 000–000

Procedia Engineering

www.elsevier.com/locate/procedia

Proc. Eurosensors XXVI, September 9-12, 2012, Kraków, Poland

High-aspect-ratio neural electrode array fabrication using thermomigration process

A.C. Peixoto[a]*, A.F. Silva[b], N.S. Dias[c,d], J.H. Correia[a]

[a]*Department of Industrial Electronics, University of Minho, Guimarães, Portugal*
[b]*MIT Portugal Program, School of Engineering, University of Minho, Guimarães, Portugal*
[c]*Life and Health Sciences Research Institute (ICVS), University of Minho, Braga, Portugal*
[d]*DIGARC, Polytechnic Institute of Cávado and the Ave, 4750-810 Barcelos, Portugal*

Abstract

A novel fabrication process for a high-aspect-ratio recording and stimulation intracortical neural microelectrode array is described. Using a combination of dicing and KOH wet-etching, microspikes are formed on the surface of a *n*-type (100), 4 mm thick, silicon wafer. Deep 3 mm cuts are performed in order to produce sharped tip pillars of high-aspect-ratio (0.2x0.2x3 mm). Thermomigration is employed as a selective doping technique performing electrically insulated pillars due to the *pn* back biased junctions formed between each pair of *n*-type substrate and p^+ migrated trails. Gold is deposited over the spikes in order to have a good ionic interface with the neural tissue, while the remaining surface is passivated with a biocompatible layer of cyanoacrylate. The final result is a deep penetrating electrode array with potential new applications in neuroprosthetics' research field.

Keywords:Invasive neural electrode; Microelectrode array, thermomigration, silicon.

1. Introduction

Invasive neural electrodes are widely used tools in neuroscience to study the behavior and function of the central nervous system at cellular level. There is also a growing interest in the clinical application of

* Corresponding author. Tel.: +351-253-517374; fax: +351-253-510189.
E-mail address: alexandre.peixoto@dei.uminho.pt.

stimulation and recording neural electrodes. Several successful applications of implantable neural prostheses, such as cardiac pacemakers, cochlear implants and deep brain stimulators, are commercially available. Many disorders can be treated with these neural prostheses (e.g. irregular heart rate, deafness and Parkinson's disease).

Recent scientific advances in the neuroprosthetics therapies' field and the need to gain scientific insights on how populations of neurons interact in the complex and distributed systems that generate behavior, triggered the development for long penetrating electrodes.

Intracortical microelectrode arrays can offer a selective access to individual nervous cell activity and also provide a greater spatial resolution than previously achieved with individual electrodes. Many spike-shaped microelectrodes based on silicon that can be safely inserted into the brain have been successfully developed [1].

However, in order to selectively stimulate and record from single or multiple neurons each electrode in the array must be electrically independent from the others. A physical phenomenon known as thermomigration is used to selectively dope the silicon, creating conductive trails across the silicon wafer. After the doping procedure, a biocompatible ionic transducer is deposited over the electrodes' tips, while the remaining surface of the array is insulated with a biocompatible material.

In this paper, it is presented a neuronal electrode array fabrication process based on the thermomigration technique.

2. Selective doping

Liquid droplets in a solid migrate in a thermal gradient because atoms of the solid dissolve into the liquid at the hot interface of the droplet, diffuse across the droplet, and deposit on the cold interface of the droplet. The resulting flux of dissolved solid atoms from the hot to the cold side of the droplet causes the droplet to migrate towards the hot end of the crystal [2].

This droplet movement applied to semiconductor and metal is often called thermomigration. The selective doping starts with the deposition of aluminum pads over an *n*-type silicon wafer. The aluminum pads deposited on the cold surface form droplets of silicon-aluminum liquid alloy, which tend to migrate along the temperature gradient towards the hot surface.

As the droplets move through the wafer, the silicon, now doped to saturation with aluminum, recrystallizes behind the droplets. Eventually the droplets traverse the entire thickness of the wafer, and deposit themselves on the hot surface. As aluminum is a *p*-type dopant, this process leaves a trail of p^+-type silicon in the *n*-type wafer [3].

Figure 1: Aluminum migration due to thermal gradient; a) Liquid alloy formation; b) Migration of silicon-aluminum liquid alloy towards hot surface.

(a) *(b)*

3. Fabrication procedure

The fabrication process starts by dicing 0.2x0.2x0.3 mm pillars on a 4 mm thick *n*-type (100) silicon wafer (*Figure 2b and Figure 3a*). In order to create sharp tips, the substrate with an array of pillars undergoes a KOH wet-etch process for 4 hours (*Figure 2c and Figure 3b*). The etching stage was performed with a 30 % KOH solution at 90 ºC.

On the following step, a thin-film of photolithographically patterned aluminum squares is deposited on the bottom surface of the silicon substrate (*Figure 2d).* With a heat source underneath the substrate and a cooling convection system above it, a strong thermal gradient (0.02 ºC/μm [4]) is formed across the wafer and the thermomigration process starts. With a minimum of 660 ºC in the cold surface, the aluminum squares melt and form a silicon-aluminum liquid alloy which migrates through the silicon wafer's cross-section and establishes a conductive channel (*Figure 2e*).

A second dicing procedure is performed in order to create high-aspect-ratio 0.4x0.4x3 mm pillars with sharp tips (*Figure 2g and Figure 3c*). Because of the pillars' high-aspect-ratio and the silicon brittleness, the cutting speed needed to be below 1 mm/s. These pillars are electrically insulated from each other by the resulting back to back *pn* junction, which is formed between any pair of p^+ trails (*Figure 2f*).

Lastly the tips are coated with gold which is a good ionic transducer, and the remaining surface is passivated by depositing a biocompatible layer of cyanoacrylate (*Figure 2h*) [6].

Figure 2: Fabrication steps; a)Silicon substrate; b) Diced micropillars; c) Etched micropillars; d) Aluminum deposition; e) p+ trails due to thermomigration; f) Interelectrode insulation due to back biased pn junction; g) Diced sharped pillars; h) Gold deposition and polymer coating.

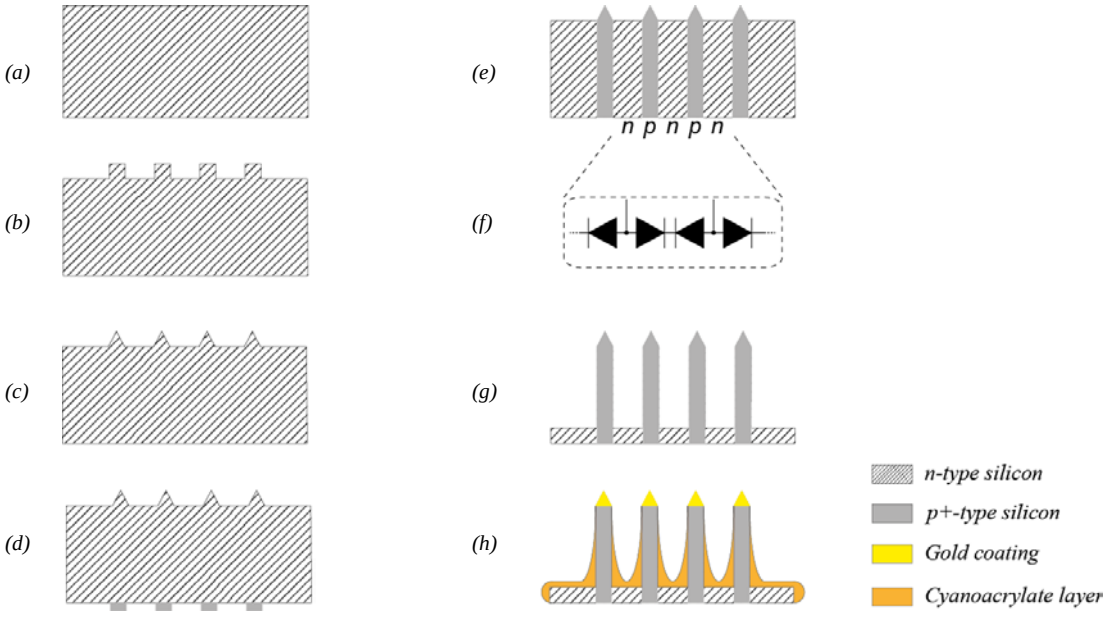

Figure 3: Photos of the fabricated prototype; a) Diced micropillars; b) Etched micropillars; c) Final electrode array.

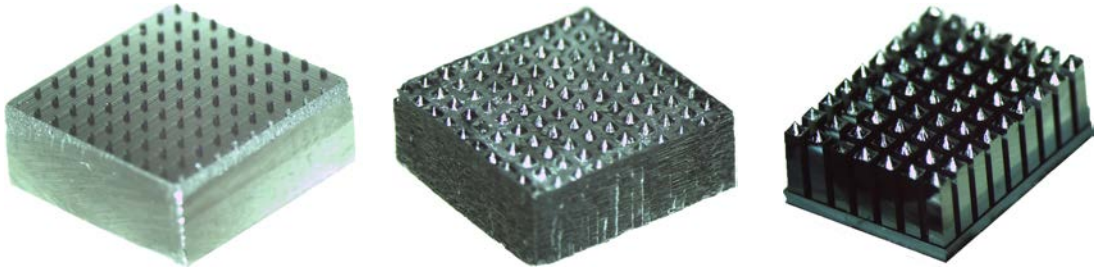

(a) *(b)* *(c)*

4. Conclusion

A process to fabricate an invasive microelectrode array that enables deep reaching and individually addressable electrode has been presented. The fabrication procedure ensures a final structure with high-aspect-ratio electrodes. The presented approach of multi-dicing steps and thermomigration provides a consistent method of high-reproducibility. The method requires KOH as etchant instead of a HF, HNO_3 mixture, a hazardous acid, needing extra safety requirements, commonly used for etching highly-doped *p*-type silicon wafers.

The thermomigration phenomenon enables not only the definition of local conductive paths across the wafer for the biopotential signal drive, but also the formation of *pn* junctions for interelectrode insulation. The conductive channel uniformity is highly dependent on the temperature conditions that the wafer is subjected to. An evenly distributed heat below the wafer will practically eliminate irregularities in the doped trails, leaving behind only minor deviations.

The presented technique is a strong alternative for microelectrode array fabrication by combining KOH wet-etch and silicon dicing on a high-yield process.

Acknowledgements

This work was supported by FCT with the reference project FCOMP 01 0124-FEDER-010909 (FCT/PTDC/SAU-BEB/100392/2008).

References

[1] M. Hajjhassan, V. Chodavarapu, and S. Musallam, “NeuroMEMS: Neural Probe Microtechnologies,” *Sensors*, vol. 8, pp. 6704-6726, 2008.

[2] H. E. Cline and T. R. Anthony, “High-speed droplet migration in silicon,” *journal of applied physics*, vol. 47, no. 6, pp. 2325-2331, 1976.

[3] P. K. Campbell, K. E. Jones, R. J. Huber, K. W. Horch, and R. a Normann, “A silicon-based, three-dimensional neural interface: manufacturing processes for an intracortical electrode array,” *IEEE transactions on bio-medical engineering*, vol. 38, no. 8, pp. 758-68, Aug. 1991.

[4] M. Eslamian and M. Z. Saghir, “Thermodiffusion (thermomigration) and convection in molten semiconductor–metal layers,” *International Journal of Thermal Sciences*, vol. 50, no. 7, pp. 1232-1242, Jul. 2011.

[5] L. F. Mondolfo, *Aluminum alloys: structure and properties*. Butter Worths, 1976.

[6] R. T. Moretti Neto, I. Mello, A. B. D. S. Moretti, C. R. C. Robazza, and A. A. C. Pereira, “In vivo qualitative analysis of the biocompatibility of different cyanoacrylate-based adhesives,” *Brazilian Oral Research*, vol. 22, no. 1, pp. 43-47, Mar. 2008.

Neural Electrode Array Based on Aluminum: Fabrication and Characterization

Alexandre Coumiotis Moreira Peixoto, Sandra Beatriz Gonçalves, Alexandre Ferreira Da Silva, Nuno S. Dias, and J. Higino Correia, *Member, IEEE*

***Abstract*— A unique neural electrode design is proposed with 3 mm long shafts made from an aluminum-based substrate. The electrode is composed by 100 individualized shafts in a 10 × 10 matrix, in which each aluminum shafts are precisely machined via dicing-saw cutting programs. The result is a bulk structure of aluminum with 65° angle sharp tips. Each electrode tip is covered by an iridium oxide thin film layer (ionic transducer) via pulsed sputtering, that provides a stable and a reversible behavior for recording/stimulation purposes, a 40 mC/cm^2 charge capacity and a 145 Ω impedance in a wide frequency range of interest (10 Hz–100 kHz). Because of the non-biocompatibility issue that characterizes aluminum, an anodization process is performed that forms an aluminum oxide layer around the aluminum substrate. The result is a passivation layer fully biocompatible that furthermore, enhances the mechanical properties by increasing the robustness of the electrode. For a successful electrode insertion, a 1.1 N load is required. The resultant electrode is a feasible alternative to silicon-based electrode solutions, avoiding the complexity of its fabrication methods and limitations, and increasing the electrode performance.**

***Index Terms*— Invasive electrode, recording, stimulation, iridium oxide, aluminum, electrode array, sharp tips.**

I. Introduction

THE ability to access deep areas of the brain to record the electrical activity or to perform functional stimulation is a key feature to understand the neurophysiological processes and to restore nervous system's lost functionalities [1].

This became possible with the development of neural interfaces. They have been designed to establish a connection between the neurons (electrically active cells of the nervous system) and the electronic system that handles the biopotentials. One may find neural interfaces in limb prostheses for spinal cord injury and stroke, bladder prostheses, cochlear auditory prostheses, retinal and cortical visual prostheses, cortical recording for cognitive control of assistive devices, and deep brain stimulation for essential tremor in Parkinson's disease [2].

In order to establish a neural interface it is necessary to transduce a signal between the electrical domain (electronic circuit) to the biological domain (neurons) and vice-versa. This is accomplished using an electrode in which a charge transduction occurs between the electrons species of the electrode material and the ions species of the electrolyte.

Nonetheless, the neural electrodes differ from the standard biopotentials electrodes. The neural solutions are known to be invasive, of small size, and multichannel. One can define a set of features that neural electrodes should comply with, namely: electrodes should remain stable for long periods of time; its cross section should be as small as possible in order to displace or damage as little tissue as possible during insertion; and the implantable electrode should have a large density of transduction ports to interface with different neurons.

In this neurophysiologic field, two neural electrodes designs stand out: the Michigan probe [3] and the Utah probe [4].

The Michigan probe is a multi-point electrode type. The electrode is composed by an array of shafts that in each one, there are several transduction ports individually addressable. The result is a map of the electrical activity at multiple depths of the brain (along the shaft depth). However, this electrode designs presents a fabrication process highly complex with a low production yield. Furthermore, the fragility of each shank leads to breaks during the insertion, and consequently tissue damage [5].

The Utah probe is characterized by an array of shafts, with a single transduction point at the shafts' tip. Its fabrication process is based on the micromachining of silicon wafers via physical and chemical processes. Depending on the wafer (if type p or n), exotic processes are required as thermomigration to establish conductive paths across the wafer [6], or instead, glass fusion to isolate each shaft from the surrounding shafts in the same array [7]. Either way, the Utah's fabrication processes have strict requirements as high temperature ovens for fusing glass or even specially designed ovens for the thermomigration technique. Moreover, it requires the use of wet-etching to sharpen the shafts' tips. Overall, these mentioned processes end up resulting in a low reproducibility rate.

Manuscript received December 14, 2012; revised June 3, 2013; accepted June 5, 2013. Date of publication June 19, 2013; date of current version July 30, 2013. The work of A.C. Peixoto was supported in part by the Portuguese Foundation for Science and Technology under Grant SFRH/BD/89509/2012, and the FCT with the reference Project FCOMP 01 0124-EDER-010909 under Grant FCT/PTDC/SAU-BEB/100392/2008. The associate editor coordinating the review of this paper and approving it for publication was Prof. Carlo Morabito.

A. C. M. Peixoto, S. B. Gonçalves, and J. H. Correia are with the Department of Industrial Electronics, University of Minho, Guimaraes 4800-058, Portugal (e-mail: alexandre.peixoto@dei.uminho.pt; sbeatriztg@gmail.com; higino.correia@dei.uminho.pt).

A. F. Da Silva is with the MIT Portugal Program, School of Engineering, University of Minho, Guimarães 4800-058, Portugal (e-mail: asilva@dei.uminho.pt).

N. S. Dias is with the Life and Health Sciences Research Institute, University of Minho, Braga 4710-057, Portugal, and also with DIGARC, Portugal Polytechnic Institute of Cavado and Ave, Barcelos 4750-810, Portugal (e-mail: ndias@dei.uminho.pt).

Color versions of one or more of the figures in this paper are available online at http://ieeexplore.ieee.org.

Digital Object Identifier 10.1109/JSEN.2013.2270034

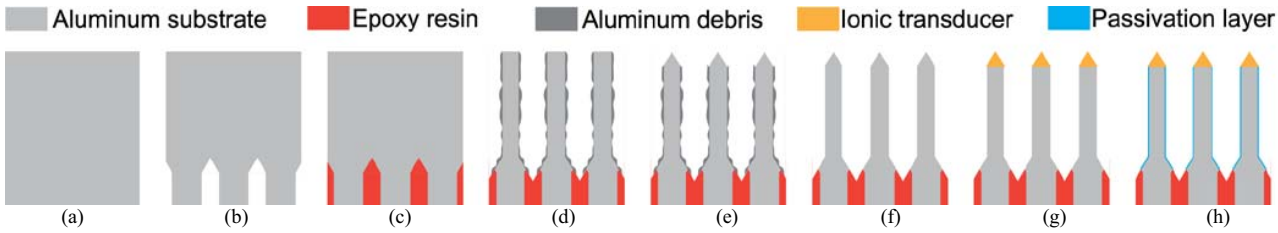

Fig. 1. Fabrication steps: (a) Aluminum substrate; (b) Pads region delimitation; (c) Pads' groves filling with epoxy resin; (d) Shafts cutting stage; (e) Shafts sharpening; (f) Shafts cleaning via etching stage; (g) IrO2 thin-film deposition at the shafts' tips; (h) Electrode passivation.

Moreover, in both approaches a maximum penetration depth of 1.5 mm has been reported [5].

A new fabrication approach is proposed, using a different bulk material for the electrode substrate, different techniques that provide high-production yield, reproducibility, and an electrode with 3 mm range of depth. The presented electrode design is made from an aluminum-based bulk substrate, with iridium oxide (IrO2) as ionic transducer at each shaft tip and coated with a passivation layer of aluminum oxide. The fabrication steps are described in detail and the electrode is fully characterized (morphologically, mechanically and electrically).

II. Electrode Design

When designing a neural electrode, it is important to consider the need for a stationary solution, capable of providing high-spatial resolution interface with the neurons [8] and reaching several points of interest [9] with increasing penetration depths. Moreover, due to the invasive nature of neural electrodes, it becomes imperative, for Chronic applications, to ensure mechanical, chemical and electrical long-term stability.

The electrode requirements define the constraints regarding materials to be used, fabrication processes and overall electrode shape.

The single-channel matrix design has proven to be the most adequate design for implantable neural electrodes [10] due to its robustness and flexibility.

The fabrication of the electrode should be compatible with large-scale manufacturing solutions and therefore, a simple and highly reproducible process was sought. The two major techniques selected were a combination of dicing with wet-etching. By using the dicing with a special designed saw that presents a wedge shape, it would be possible to establish a cutting plan that would create the sharp tips and the long shafts. The wet-etching would only be applied for cleaning purposes, removing all the scrap material that piles up in the cuts.

In combination with the fabrication technique, a different bulk material was selected. Instead of using the standard silicon wafer, it was decided to use an aluminum piece as bulk. Aluminum, being a ductile and easy to machine material, offers some advantages over silicon commonly used in the production of neural prosthesis. Aluminum is a natural good conductor, offering very low resistivity (28.2 nΩ.m) [11]. This characteristic offers an electrical advantage over doped silicon, which has been reported to have a resistivity at best of 50,000 nΩ.m [12], which is a difference of 3 orders of magnitude between aluminum and doped silicon.

However, aluminum has two main drawbacks: non-biocompatibility and low Young's modulus. Although aluminum is used as body material and conductive channel for the biopotentials, it is required to coat/passivate it not only to ensure that no aluminum is in contact with neural tissue due to toxicity reasons but also to guarantee that only the tip is performing the signal interface with the neurons and not the entire shaft. The aluminum ductility may be a concern, depending on the aspect ratio of the fabricated shaft. But, since one desires long shafts with low widths, the ductility may induce the shaft to bend during the insertion. In order to avoid these two issues, an anodization procedure is proposed. It is possible to anodize the aluminum, creating an external coating of aluminum oxide. The result is a covering that not only is biocompatible and therefore solving the cytotoxicity issues but that also has a superior Young's modulus compared to the aluminum that enhances the structural robustness of the entire electrode [13], [14].

It is necessary to select the material to perform the ionic transduction at the shaft's tip site as neither aluminum nor doped silicon are able to perform the charge transfer at the electrode-electrolyte interface. There are several suitable materials, which include silver/silver chloride (Ag/AgCl) [15], titanium nitride (TiN), platinum (Pt) [16] and iridium oxide (IrO2) [17]. Nonetheless, IrO2 has been proven to be one of the most promising and preferred materials for electrodes [18], [19] due to its high charge delivery capacity, low constant impedance over the entire frequency range for neural stimulation and biocompatibility [20].

III. Electrode Fabrication

The fabrication procedure for the proposed electrode design (Figure 1) uses a combination of different techniques, namely: dicing, polymer deposition, wet-etching and electrolytic passivation.

The dicing stage comprises a cutting plan to delineate and to shape the wafer in order to establish the structural shape of the intended electrode array matrix. The cutting plan is divided into four sub-stages, all of them performed on a Disco DAD 2H/6T dicing machine, equipped with Disco ZHDG blades capable of performing 3 mm deep, 0.250 mm wide cuts and V-shaped grooves. The substrate was an aluminum square chunk, 99 % pure, 10 mm wide and 5 mm thick.

The first series of cuts is performed on the backside of the aluminum chunk (Figure 1b) and intends to outline each

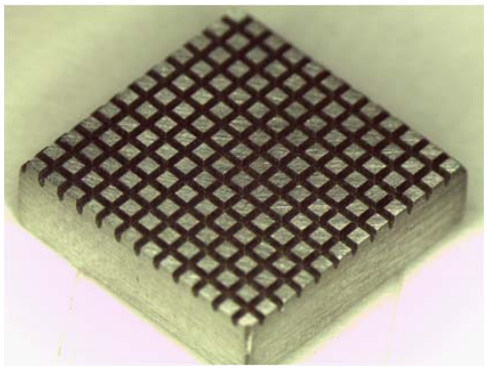

Fig. 2. Definition of the pads regions on the aluminums wafer's backside.

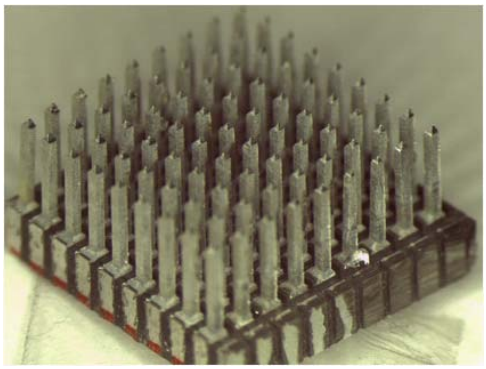

Fig. 3. Electrode matrix structure after the etching stage.

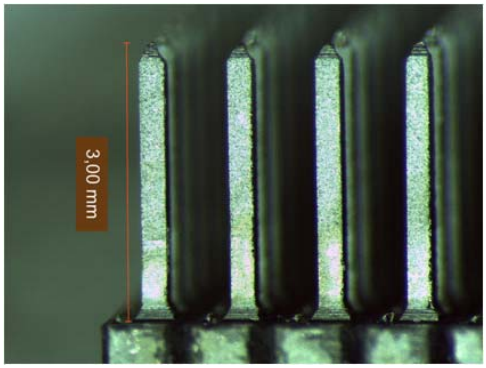

Fig. 4. Detailed view of a set of the 3 mm long shafts.

pad Region. These pads will be the connecting sites for interrogating each electrode tip. The cuts have a grid profile, in which the cut is 2.5 mm deep and 1 mm spaced (Figure 2).

Afterwards, the resultant cavities are filled with an epoxy-resin (Figure 1c) that will serve as electrical insulation between electrodes in the final structure and will also be the structural element that provides structural integrity to the electrode matrix and keep it as a whole and single component. The polymer is slowly laid over the backside center, forcing the air inside the groves to be pushed out as the polymer fills the grooves. After the polymer cure, the backside surface is grinded and polished to remove the excess of polymer, resulting in a smooth surface.

The epoxy-resin was the selected material due to its high-level of adhesion to aluminum and chemical resistance.

With the backside defined, the fabrication steps are now dedicated to creating the sharp shafts (Figure 1d–f).

First, a cut plan is performed to machine a matrix of 3 mm high and 350 μm wide pillars (Figure 1d). The space between pillars is in accordance to the distance between pads. In this case, a 1 mm space was set in order to create a 10 $\times$ 10 electrode matrix in a 10 mm wide square aluminum chunk. Higher electrode densities are possible but it is necessary to adjust the spacing value.

After the first stage of cuts, the shafts present a straight square profile that need to be sharpened to facilitate the implantation. The shafts are sharpened by passing the cutting blade on the top of the pillar, near its edge.

After the cut, a large amount of aluminum debris piles in the space between the pillars and in order to clean it, the electrode is immersed on type-A aluminum etchant at 50 °C for 30 minutes (Figure 1f) [21]. As the etchant also attacks the shafts' aluminum, it is therefore necessary to take it into account and have a wider shaft width that will be thinned when immersed in the etching bath. The result is a clean electrode matrix structure of high-aspect ratio shafts as shown in Figure 3. A detailed view of the final shafts is showed in Figure 4.

At this point the electrode's shafts are not yet functionalized. So far, one has the main electrode body fully conductive but not able to perform the charge transduction.

In order to deposit the ionic transducer at the shafts' tips, an aluminum foil was pressed against them exposing only the very tips. This foil is placed with the aid of two fiber glass sheets. The upper sheet has 500 μm holes with 1 mm spacing between them, allowing the shafts to pass through it while the lower sheet has no holes. Controlling the distance between these two sheets there are four precision screws and bolts at each corner. By placing the foil below the upper sheet and controlling the number of turns in each nut, the exposed region is precisely controlled.

Prior to the iridium oxide deposition, a thin layer of 50 nm titanium (Ti) is deposited by DC sputtering. The Ti layer will promote the adhesion of the iridium film to the aluminum. The iridium oxide is deposited by pulsed Sputtering in a 3.5 sccm oxygen flow at 180 W (50 kHz).

In the last fabrication stage, the aluminum shafts need to be passivated via anodizing. The process is performed by submersing the shafts in a sulfuric acid solution while injecting a 13 mA/cm^2 current density through the electrode shafts (anode) and a platinum electrode (cathode).

A close up image of the aluminum oxide protective layer can be seen on Figure 5.

IV. Results

A. Morphology

Figure 6 shows the main measurements that define each shaft tip. The shaft features include a 3 mm high and 250 μm wide shank, with a square-base pyramidal shape tip with a 65° vertex. In a population of 69 samples the average angle was 65° with a standard deviation of 5.67°, while the average

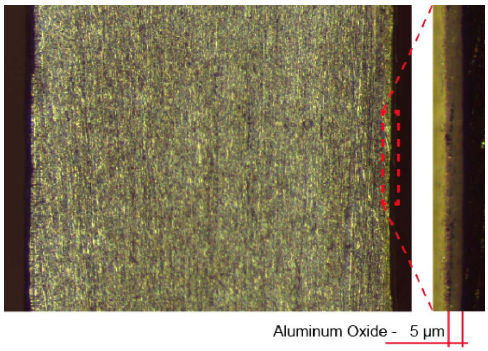

Fig. 5. Anodized shafts cross-section with a detailed view of the aluminum oxide protective layer.

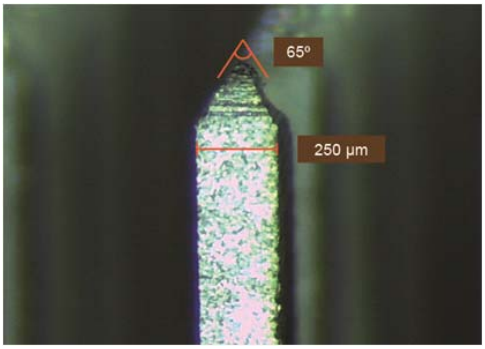

Fig. 6. Detailed view of single shaft tip.

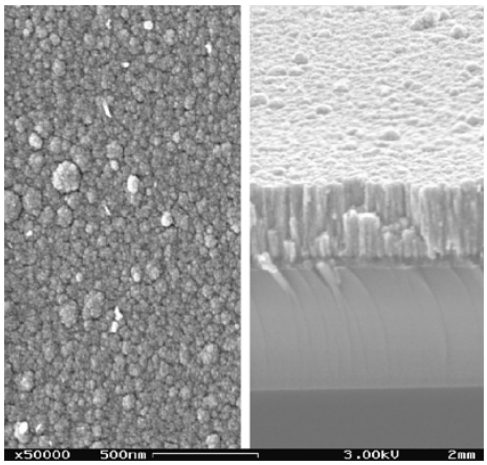

Fig. 7. SEM image of the IrO2 thin-film (top and cross-section view).

height was 3 mm with a standard deviation of 50 μm. The average tip radius was of 9 μm.

The shaft base is an aluminum block of 0.7 $\times$ 0.7 $\times$ 0.2 mm^3 for a 10 $\times$ 10 electrode matrix in a 10 mm square substrate.

Figure 7 shows in detail the surface and cross-section of the iridium oxide thin-film deposited at the shaft tip. The images were obtained by scanning electron microscope technique and it is possible to identify a grainy structure with a coherent morphology.

B. Mechanical

The mechanical analysis focused on the load required to implant the electrode and on the electrode robustness. The tests

Fig. 8. Mechanical test arrangement.

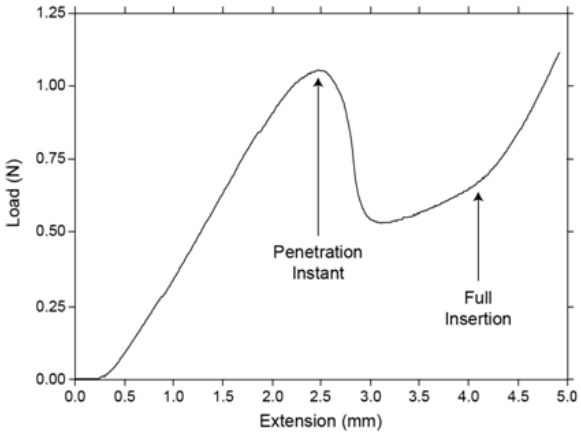

Fig. 9. Electrode's implantation mechanical response.

were performed on a Hounsfield H 100 KS dynamometer equipped with a 100 N load cell and capable of a resolution of 10 mN. The neural tissue mechanical properties were mimicked via agar-agar gel (1% solution) [22]. Figure 8 shows the setup arrangement for the implantation analysis.

The crosshead was set to move at a constant displacement rate of 30 μm/s towards the gel (compressive load), while the required load was being acquired.

The obtained plot (Figure 9) shows a load increase on the initial stage while still subjected to the material gel resistance up to the moment where the electrodes' tips are able to pierce the gel. From this moment beyond there is a fast decrease of the required load to fulfill the entire electrode implantation. This suggests a bed-of-nails effect during insertion. On the final stage there is a slightly higher increase slope related to the material resistance when the electrode was already fully inserted and the crosshead continued the displacement.

The required load, according to the obtained data, is approximately 1.13 N with a 13 % variation among samples. These values are similar to results reported in other studies [23].

The electrodes were also removed from the gel after the test to evaluate their integrity and effect on the gel. None of the tested samples showed any sign of break or bended shafts. The pierced holes on the gel seemed to partially recover from insertion.

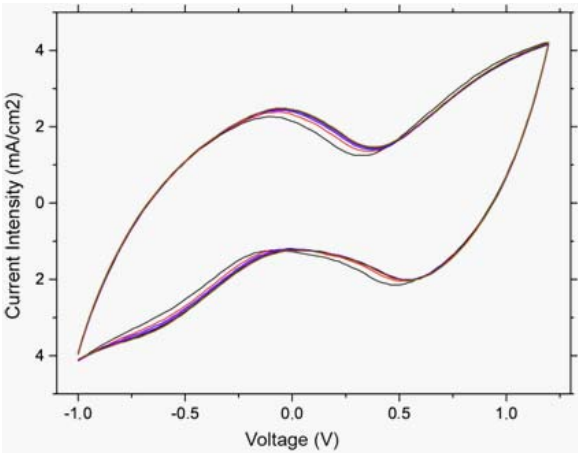

Fig. 10. Cyclic voltammetry measurements for different activation cycles.

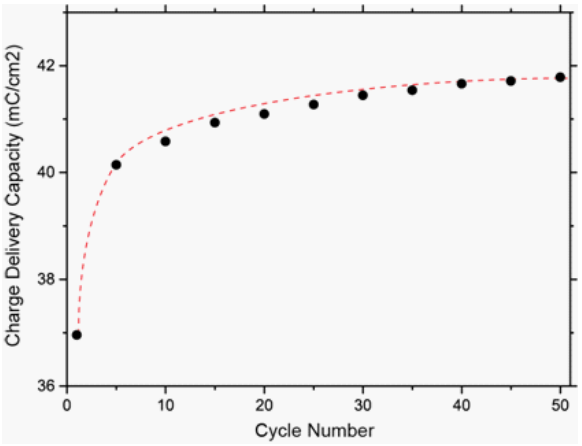

Fig. 11. Charge delivery capacity in dependence of the cycle number.

C. Electrical

The electrochemical analysis of the electrodes were performed on a Gamry Reference 600^{TM} Potentiostat/ Galvanostat. In an electrochemical cell, with a NaCl solution (0.9 % by weight), the thin-film of IrO2 that performs the electrode-electrolyte interface underwent cyclic voltammetry and impedance analysis.

The cyclic voltammogram (Figure 10) shows a reversible behavior, with minimum changes after several activation cycles. The reversibility of the process enables the electrode to be safely used for stimulation purposes.

Figure 11 shows how the charge delivery capacity changes along the activation cycles of the electrode, providing a look on how the electrode would perform along its lifecycle. Due to the electrochemical reactions occurring in the surface of the electrode its structure is modified resulting in this variation. The first cycles led to a fast increase of charge delivery capacity, which gradually reaches a plateau value.

The general shapes of the impedances before and after activation of 50 cycles are shown in the *Bode* plot of Figure 12. The cutoff frequency which represents the transition from the capacitive region to the resistive region, shifts to lower frequencies with activation. Successive activation cycles move the cutoff frequency further to lower frequencies but, the effects are not as pronounced.

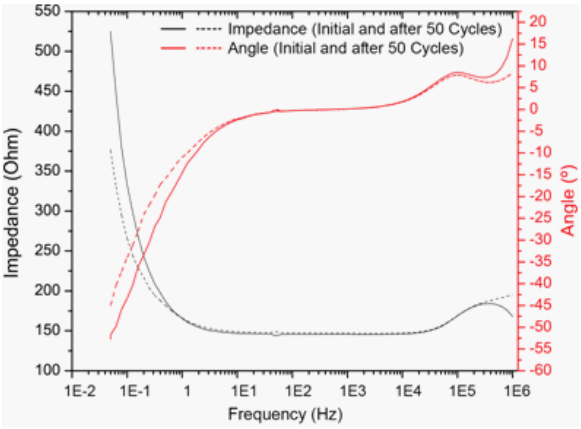

Fig. 12. Bode plot before and after activation with 50 cycles.

By lowering the cutoff frequency, the electrode gains a wider frequency range of low impedance useful for functional electro-stimulation. This way, the diffusion control plays a slighter role in impedance behavior of activated samples, meaning that, at lower frequencies, the electrode impedance is dominated by the double layer capacitance [24].

On Figure 12's secondary axis is possible to identify the behavior of the sample according to the signal frequency. For frequencies up to 100 Hz, the sample presents a capacitive component, and above 10 kHz it has a inductive component. But, for frequencies between 1 kHz and 10 kHz, the samples are purely resistive, since the *theta* is null, and in this frequency range, the impedance value is around 145 Ohm.

V. Conclusion

An electrode array with 3 mm long shafts made from an aluminum based substrate is fabricated.

The aluminum-based substrate proves to be a feasible alternative to silicon-based electrode solution by overcoming its limitations and its fabrication complexity. Nonetheless, it was necessary to establish a fabrication method capable of precise machining and to define solution to overcome the aluminum own limitations: biocompatibility and ductility.

The proposed fabrication procedure proved to be consistent and reproducible. Moreover, it enables the fabrication of shafts with heights well above the ones reported in bibliography.

The result was a robust invasive neural electrode matrix with 3 mm long shafts. The electrode can be easily implanted, requiring 1.1 N load at its base. The deposition of IrO2 films as the ionic transducer showed the required performance for its application, with a consistent reversible electrochemical behavior, and 40 mC/cm2 charge delivery capacity and a impedance of 145 Ohm in the same frequency range as the stimulation protocols.

Overall, the proposed electrode design becomes an eligible alternative for biopotentials recording and stimulation applications.

References

[1] B. S. Wilson and M. F. Dorman, "Interfacing sensors with the nervous system: Lessons from the development and success of the cochlear implant," *IEEE Sensors J.*, vol. 8, no. 1, pp. 131–147, Jan. 2008.

[2] S. F. Cogan, "Neural stimulation and recording electrodes," *Annu. Rev. Biomed. Eng.*, vol. 10, pp. 275–309, Jan. 2008.

[3] K. D. Wise, "Wireless integrated microsystems: Wearable and implantable devices for improved health care," in *Proc. Int. Solid-State Sens., Actuat., Microsyst. Conf.*, Jun. 2009, pp. 1–8.
[4] A. Sharma, L. Rieth, P. Tathireddy, R. Harrison, H. Oppermann, M. Klein, M. Töpper, E. Jung, R. Normann, G. Clark, and F. Solzbacher, "Long term in vitro functional stability and recording longevity of fully integrated wireless neural interfaces based on the Utah Slant electrode array," *J. Neural Eng.*, vol. 8, no. 4, p. 045004, Aug. 2011.
[5] M. Hajjhassan, V. Chodavarapu, and S. Musallam, "NeuroMEMS: Neural probe microtechnologies," *Sensors*, vol. 8, no. 10, pp. 6704–6726, 2008.
[6] P. K. Campbell, K. E. Jones, R. J. Huber, K. W. Horch, and R. A. Normann, "A silicon-based, three-dimensional neural interface: Manufacturing processes for an intracortical electrode array," *IEEE Trans. Biomed. Eng.*, vol. 38, no. 8, pp. 758–768, Aug. 1991.
[7] K. E. Jones, P. K. Campbell, and R. A. Normann, "A glass/silicon composite intracortical electrode array," *Ann. Biomed. Eng.*, vol. 20, no. 4, pp. 423–437, 1992.
[8] T. A. Fofonoff, S. M. Martel, N. G. Hatsopoulos, J. P. Donoghue, and I. W. Hunter, "Microelectrode array fabrication by electrical discharge machining and chemical etching," *IEEE Trans. Biomed. Eng.*, vol. 51, no. 6, pp. 890–895, Jun. 2004.
[9] R. Bhandari, S. Negi, L. Rieth, R. A. Normann, and F. Solzbacher, "A novel method of fabricating convoluted shaped electrode arrays for neural and retinal prostheses," *Sens. Actuators. A, Phys.*, vols. 145–146, nos. 1–2, pp. 123–130, Jan. 2008.
[10] R. A. Normann, "Technology insight: Future neuroprosthetic therapies for disorders of the nervous system," *Nature Clinical Pract. Neurol.*, vol. 3, no. 8, pp. 444–452, 2007.
[11] J. Cutnell and J. Kenneth, *Physics*, 3rd ed. New York, NY, USA: Wiley, 1995.
[12] R. Sharma, P. Tathireddy, S. Lee, L. Rieth, E. Bamberg, and A. Dorval, "Procedia engineering application-specific customizable architectures of Utah neural interfaces," *Engineering*, vol. 25, pp. 1–4, Feb. 2011.
[13] D. S. Finch, T. Oreskovic, K. Ramadurai, C. F. Herrmann, S. M. George, and R. L. Mahajan, "Biocompatibility of atomic layer-deposited alumina thin films," *J. Biomed. Mater. Res. Part A*, vol. 87, no. 1, pp. 100–106, Oct. 2008.
[14] K. E. Petersen, "Silicon as a mechanical material," *Proc. IEEE*, vol. 70, no. 5, pp. 420–457, May 1982.
[15] J. A. McLaughlin, E. T. McAdams, and J. Anderson, "Novel dry electrode ECG sensor system," in *Proc. 16th Annu. Int. Conf. IEEE Eng. Med. Biol. Soc.*, Nov. 1993, pp. 800–804.
[16] A. Ivorra, R. Gómez, N. Noguera, R. Villa, A. Sola, L. Palacios, G. Hotter, and J. Aguiló, "Minimally invasive silicon probe for electrical impedance measurements in small animals," *Biosens. Bioelectron.*, vol. 19, no. 4, pp. 391–399, Dec. 2003.
[17] S. F. Cogan, T. D. Plante, and J. Ehrlich, "Sputtered iridium oxide films (SIROFs) for low-impedance neural stimulation and recording electrodes," in *Proc. Conf. Proc. IEEE Eng. Med. Biol. Soc.*, vol. 6. Sep. 2004, pp. 4153–4156.
[18] R. B. McIntosh, P. E. Mauger, and S. R. Patterson, "Capacitive transducers with curved electrodes," *IEEE Sensors J.*, vol. 6, no. 1, pp. 125–138, Feb. 2006.
[19] J. P. Carmo, N. Sé. Dias, H. R. Silva, P. M. Mendes, C. Couto, and J. H. Correia, "A 2.4-GHz low-power/low-voltage wireless plug-and-play module for EEG applications," *IEEE Sensors J.*, vol. 7, no. 11, pp. 1524–1531, Nov. 2007.
[20] B. Wessling, W. Mokwa, and U. Schnakenberg, "RF-sputtering of iridium oxide to be used as stimulation material in functional medical implants," *J. Micromech. Microeng.*, vol. 16, no. 6, pp. 142–148, Jun. 2006.
[21] *Material Safety Data Sheet for Aluminum Etchant Type A*, Transene Co., Rowley, MA, USA, 1987.
[22] Z.-J. Chen, G. T. Gillies, W. C. Broaddus, S. S. Prabhu, H. Fillmore, R. M. Mitchell, F. D. Corwin, and P. P. Fatouros, "A realistic brain tissue phantom for intraparenchymal infusion studies," *J. Neurosurgery*, vol. 101, no. 2, pp. 314–322, 2004.
[23] M. Han, P. S. Manoonkitiwongsa, C. X. Wang, and D. B. McCreery, "In vivo validation of custom-designed silicon-based microelectrode arrays for long-term neural recording and stimulation," *IEEE Trans. Biomed. Eng.*, vol. 59, no. 2, pp. 346–354, Feb. 2012.
[24] B. Wessling, W. Mokwa, and U. Schnakenberg, "RF-sputtering of iridium oxide to be used as stimulation material in functional medical implants," *J. Micromech. Microeng.*, vol. 16, no. 6, pp. S142–S148, Jun. 2006.

Alexandre Coumiotis Peixoto received the Degree in electrical engineering and the master's degree in electrical engineering from the University of Trás-os-Montes e alto Douro, Vila Real, Portugal, in 2008 and 2010, respectively. He is currently pursuing a Ph.D. degree in biomedical engineering with the University of Minho, Guimarães, Portugal.

Sandra Beatriz Gonçalves received the Degree in biomedical engineering (Integrated Masters) with the major in medical electronics from the University of Minho, Guimarães, Portugal, in 2012. She is currently a Researcher with the University of Minho.

Alexandre Ferreira Da Silva graduated, in 2007, in Biomedical Engineering at University of Minho, Braga, Portugal. He obtained in 2011 the PhD degree in Leaders for Technical Industries, at the same institution, under the MIT-Portugal Program within the Engineering Design and Advanced Manufacturing (EDAM) focus-area. Presently, he is an assistant professor for the MIT Portugal's EDAM focus-area at University of Minho. His main research interests are related to the design and development of medical devices, and micro/nano fabrication technologies.

Nuno Sérgio Dias (S'06) received the Degree in industrial electronics and computers from the University of Minho, Braga, Portugal, in 2004, and the Ph.D. degree in industrial electronics from the University of Minho, Guimarães, Portugal, in 2009, in collaboration with the Center for Neural Engineering, Pennsylvania State University, State College, PA, USA. His Ph.D. thesis focused on Brain–Machine Interface Based on Biotelemetry and Dry Electrodes. He is currently a Post-Doctoral Researcher with the Life and Health Sciences Research Institute - ICVS, University of Minho. He is a member of the IEEE Industrial Electronics Society and the IEEE Engineering in Medicine and Biology Society.

José Higino Correia (S'96–M'00) received the Degree in physical engineering from the University of Coimbra, Coimbra, Portugal, in 1990, and the Ph.D. degree from the Laboratory for Electronic Instrumentation, Delft University of Technology, Delft, The Netherlands, in 1999, working in microsystems for optical spectral analysis. He is currently a Full Professor with the Department of Industrial Electronics, University of Minho, Braga, Portugal. He was the General-Chairman of Eurosensors in 2003 and MME in 2007. His current research interests include micromachining and microfabrication technology for mixed-mode systems, solid-state integrated sensors, microactuators and microsystems. He is a member of the IEEE Industrial Electronics Society.

Sensors and Actuators A 217 (2014) 21–28

Contents lists available at ScienceDirect

Sensors and Actuators A: Physical

journal homepage: www.elsevier.com/locate/sna

Flexible three-dimensional microelectrode array for neural applications

A.C. Peixoto[a,*], S.B. Goncalves[a], F. Pinho[a], A.F. Silva[b], N.S. Dias[c,d,e], J.H. Correia[a]

[a] Department of Industrial Electronics, University of Minho, Campus of Azurem, 4800-058 Guimaraes, Portugal
[b] MIT Portugal Program, University of Minho, School of Engineering, Campus of Azurem, Guimarães, Portugal
[c] Life and Health Sciences Research Institute (ICVS), School of Health Sciences, University of Minho, 4710-057 Braga, Portugal
[d] DIGARC, Polytechnic Institute of Cávado and Ave, 4750-810 Barcelos, Portugal
[e] ICVS/3B's – PT Government Associate Laboratory, Braga/Guimarães, Portugal

ARTICLE INFO

Article history:
Received 19 March 2014
Received in revised form 24 June 2014
Accepted 24 June 2014
Available online 2 July 2014

Keywords:
Aluminum
Neural electrode
Microfabrication
Dicing
Flexible

ABSTRACT

A neural electrode array design is proposed with 3 mm long sharpened pillars made from an aluminum-based substrate. The array is composed by 25 electrically insulated pillars in a 5 × 5 matrix, in which each aluminum pillar was precisely machined via dicing saw technique. The result is an aluminum structure with high-aspect-ratio pillars (19:1), each with a tip radius of 10 μm. A thin-film of platinum was deposited via sputtering technique to perform the ionic signal transduction. Each pillar was encapsulated with an epoxy resin insulating the entire pillar excluding the tip. This process resulted in mechanically robust electrodes each capable of withstanding loads up to 200 mN before bending. The array implantation tests were conducted on agar gel at speeds of 50 mm/min, 120 mm/min and 180 mm/min which resulted in average implantation forces of 119 mN, 145 mN and 150 mN, respectively. Insertion and withdrawal tests were also performed in porcine cadaver brain showing a necessary force of 66 mN for successful explantation. A three point flexural test demonstrated a displacement of 0.8 mm before array's breakage. The electrode's impedance was characterized showing a near resistive impedance of 385 Ω in the frequency range from 2 kHz to 125 kHz. The resultant array, as well as the fabrication technique, is an innovative alternative to silicon-based electrode solutions, avoiding some fabrication methods and limitations related to silicon and increasing the mechanical flexibility of the array.

1. Introduction

The ability to access areas of the brain in order to record neural electrical activity or to perform functional stimulation is a key feature to understand the neurophysiological processes and to restore the nervous system's lost functionalities [1]. Advances in microtechnologies allowed the development of micrometer size instruments to interact with neural tissue. These instruments, known as neural electrodes, are usually invasive, of small size, and with multiple channels.

Currently, there are many neural electrode approaches and designs [2]. The Michigan probe [3] and the Utah array [4] stand out due to their high-density of electrodes, tridimensional nature and efficacy in long term recording.

These two approaches are based on silicon microfabrication. This implies that their fabrication is heavily dependent on CMOS technology, which is readily and easily available due to the massification of consumer electronics. Due to this fact, there's a significant advantage on using standard microfabrication techniques. However, this implies that the entire process will be based on silicon.

Despite the many advantages of silicon, brittleness stands out as a major disadvantage when interacting with biological tissues. A logical evolution toward bio-integration would be the use of materials with superior flexibility than silicon.

Both arrays are commercially available but are limited to cortical regions, due to the size of the electrodes being restricted to 1.5 mm. Longer electrodes have been achieved by using μ-wire electrical discharge machining [5]. Longer electrodes like these would allow the exploration of other brain structures of great importance for neurophysiology, such as the hippocampus [6]. Rats are commonly used as animal models by neurobiologists to better understand the human brain [7]. In rats the hippocampus is situated between 2 and 4 mm below the surface [8]. In this paper

* Corresponding author. Tel.: +351 967947793.
E-mail addresses: ID3251@alunos.uminho.pt, alexbr82@gmail.com (A.C. Peixoto).

http://dx.doi.org/10.1016/j.sna.2014.06.020
0924-4247/

we describe an array consisting of 25 electrodes, each able to reach 3 mm below the brain surface. At this depth the electrodes are able to reach the hippocampus. Aluminum was used as structural material and also as electrical conductor for the acquired signals. Epoxy resin was used as encapsulation and also as structural adhesive between micropillars. The combination of these two materials allows greater flexibility than silicon. A sputtered thin-film of platinum was used as the transduction layer between signal acquisition electronics and neural activity. By introducing materials with higher degree of flexibility than silicon, this approach decreased the mechanical mismatch between the brain and the array, reducing possible trauma due to brain mechanical dynamics [9]. By avoiding some advanced microfabrication techniques such as reactive ion etching and chemical vapor deposition, the present approach is more cost-effective than the two aforementioned alternatives. Although using alternative materials, the processes are based on standard microfabrication techniques, this means that the arrays can be manufactured in batches with a throughput yield similar to silicon. The fabrication steps are described in detail, the array is morphologically and mechanically characterized, and the platinum thin-film electrodes are electrochemically characterized.

This paper also offers a significant improvement in several aspects over a previously described aluminum array [10]. The present encapsulation process relies on the deposition and selective removal of the resin around each pillar, while in the previous version an anodizing process was used. While the present approach performs a uniform and sealed layer the previous relies on aluminum oxide, which has nanopores that are inherent of the anodizing process [11]. Also, the present approach is simpler since it avoids the need of a special set-up to inject a controlled current from the array to the cathode while submerged in and acidic solution [12]. The reproducibility is increased in the present version, because it relies on the precision of the dicing machining to deinsulate the tips and control the electrode's active area. The new array has a density of 2.8 electrodes per mm^2which is more than double the density of the previous version. Higher electrodes densities allows higher spatial resolution of the brain activity, which is of great value to better understand brain functions [13]. Finally, the pillars' aspect-ratio almost doubled going from 12:1 to 19:1. This reduction in the pillar's cross-section is very important since it is crucial for neural electrodes to displace the minimum quantity of neural tissue [6].

2. Array design

Due to the various applications of invasive electrodes in neurophysiology, the array's design should be made according to a specific application. Arrays with high-density are preferred when used for applications such as neuroprosthetics or for mapping the interaction between diverse brain's regions [2,10]. The described array has 25 electrodes, one at each tip of a micropillar, with a spacing of 600 μm between each, resulting in an electrode density of 2.8 electrodes per mm^2.

It is also important that the micropillars cause minimum tissue trauma due to insertion and subsequent tissue displacement. It was a major concern to design a probe that would displace the smallest volume of brain tissue during insertion. This implies that the pillars should have the smallest cross section possible. Each micropillar has a cross section of 160 μm × 160 μm and 3 mm of length, which results in a high-aspect-ratio of 19:1. Each micropillar has a pyramidal profile with a tip radius of 10 μm. These sharp tips reduce the insertion force for penetration, subsequently reducing insertion trauma by minimizing tissue dimpling and compression [15].

The thin and long profile of the pillars requires that their mechanical properties should withstand the axial forces needed for penetration without buckling or breaking, as well as to withstand the shear stresses due to imperfect insertion, namely, angled penetration and movement during penetration. Each pillar consists of a combination of an aluminum pillar and a thick epoxy coating all around the pillar. The aluminum has a compressive strength of approximately 70 N/mm^2 while the epoxy has a compressive strength of 65 N/mm^2 [12,13]. Although with a significantly smaller compressive and shear strength than silicon, aluminum and epoxy offer superior strength than the soft and viscoelastic brain tissue (Table 1). Also the penetration forces of cylindrical probes ranging from 100 μm to 200 μm in diameter have been reported to be below 15 mN in the rat brain [15]. For this magnitude of forces, both materials have the mechanical properties to withstand penetration without bending, as shown in the results section. In the case of imperfect insertions, the probes can be subjected to shear forces, which could bend them and lead to breakage. Aluminum and epoxy are ductile materials; this property gives the probes a greater degree of flexion than silicon.

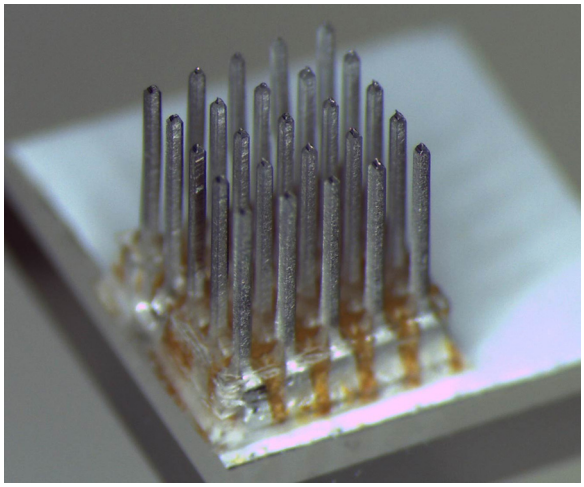

Fig. 1. Perspective view of the 5 × 5 electrode array.

Signal quality is of great importance, since neural signal have a magnitude of power in the order of few micro-watts. At this scale, signal attenuation due to electrical resistance becomes important, therefore the conducting material should have the least possible amount of resistance. Aluminum is inherently an excellent electrical conductor with resistivity values of approximately 26.9 nΩ m, which makes it an appropriate choice for conducting electrical signals [17].This characteristic offers an electrical advantage over doped silicon, which has been reported to have a resistivity of 50 μΩ m[18], which is a difference of 3 orders of magnitude between aluminum and doped silicon. Table 1 compares the different materials properties.

It was necessary to select a material to perform the ionic transduction at each tip since aluminum is not adequate to perform the charge transfer at the electrode–electrolyte interface. Platinum has been widely used as a neural electrode for recording and stimulation, with evidences of chemical stability in saline, highly polarizable, and with relative high charge-injection limits [18–20]. A thin-film of Platinum was deposited via DC sputtering at each electrode, allowing the transduction of electrical signals from the neuronal tissue. Fig. 1 shows a perspective view of the final array.

3. Array fabrication

The fabrication process for the proposed electrode design used a combination of standard CMOS processes such as wafer dicing, wet-etching, thin-film deposition; and also non-standard processes such as microcasting and adhesive bonding. Although the

Table 1
Material properties comparison.

Parameter	Unit	Brain [19]	Aluminum [17]	Hysol 3430 [16]	Silicon [20]
Young's modulus	GPa	19×10^{-6}	70	3.21	190
Shear strength	MPa	–	75	–	7000
Resistivity	Ω m	–	2.69×10^{-8}	3×10^{15}	700×10^{-6}[a]
Compressive strength	N/mm^2	16×10^{-3}	70	65	8300
Cost	–	–	$	$	$$

[a] Highly doped silicon [18].

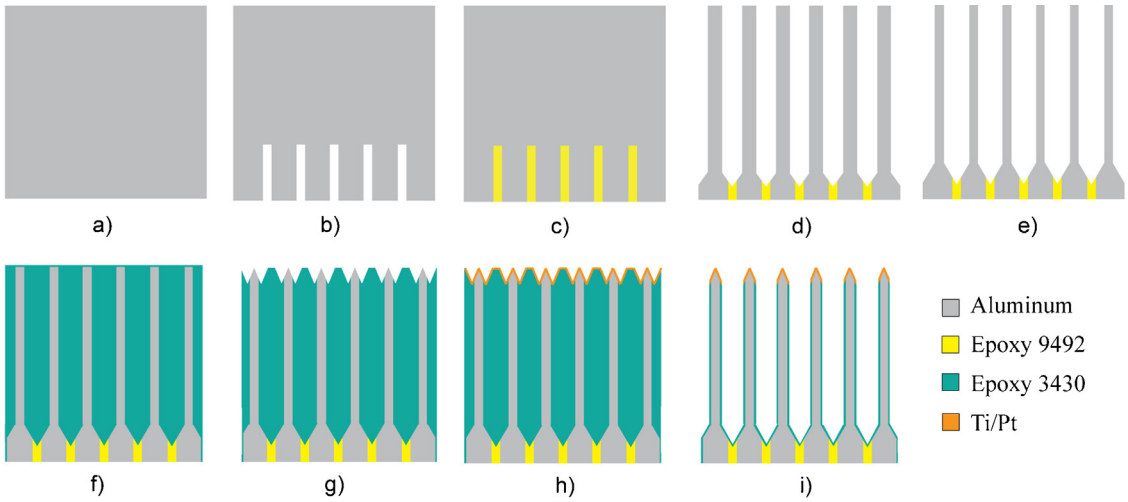

Fig. 2. Fabrication steps.

wafer dicing is usually performed on silicon, our process technology applied it for dicing aluminum and epoxy resin.

All dicing steps were performed on a Disco DAD 2H/6T dicing machine, equipped with Disco ZHDG blades capable of performing 3 mm deep, 350 μm wide cuts and V-shaped grooves. The substrate used was a 99% pure aluminum block, 25 mm wide and 4 mm thick (Fig. 2a).The first series of cuts were performed on one of the surfaces that we will define as the "backside" of the array. These cuts outlined the pads' region. These pads made the electrical connection between each electrode tip and the acquisition electronics. The cuts have a grid pattern with a spacing of 600 μm and depth of 1 mm (Fig. 2b). Afterwards, the resultant cavities were filled with an epoxy resin (Hysol 9492) that serves as electrical insulation between each pillar, individualizing all the electrodes and also acting as the structural bond between pillars [24]. The polymer was injected over the backside, forcing out any air remaining inside the grooves and replacing the empty space between pads with the epoxy resin. After the curing of the polymer, the backside surface was abraded with small grit sandpaper to remove the excess polymer, resulting in a smooth surface (Fig. 2c).

The epoxy resin was selected as the bonding material due to its high-level of adhesion to aluminum, excellent electrical insulation and chemical resistance [25].

With the backside defined, the substrate was turned over in order to create the pillars. A program was performed to cut a matrix of 3 mm deep and 250 μm wide pillars (Fig. 2d). Each pillar was centered with each pad. After this dicing stage, a significant amount of burr was formed at the pillars' edges. In order to remove the burr and also to decrease the pillars' cross section, the array was immersed in 20 mL of aluminum etchant at 50 °C for 70 min [26]. The etchant was constantly circulating through the pillars with the aid of a magnetic stirrer. As a result of the etching step, extremely thin aluminum pillars were achieved (Fig. 2e). The pillars' dimensions will be discussed in further detail in the next section. Although visually, the epoxy appeared to be slightly discolored by the etching bath, it remained strong enough for normal handling.

A second step of casting was performed, this time to completely fill the space between pillars with epoxy resin (Fig. 2f). The next cutting step had a twofold purpose: one was to sharpen the pillars' tips to facilitate insertion into the brain tissue and the second was to guarantee the deposition of the Platinum thin-film only on the tips. The tips were formed by passing a V-shaped blade on the top of each pillar (Fig. 2g).

In the resulting surface was deposited a layer of 70 nm of titanium (Ti) followed by a 200 nm layer of platinum (Pt). The Pt layer will allow an efficient charge transfer between the electrode and electrolyte (neural tissue) while Ti serves as an adhesive layer. The Ti layer was deposited using electron beam evaporation at a starting pressure of 2.8×10^{-6} mBar while supplying a current of 60 mA and a potential of 7 kV. The duration of the deposition was 5 min and the maximum temperature measured at the substrate was 60 °C. The Pt layer deposited using DC sputtering at a starting pressure of 3.3×10^{-6} mBar while supplying a current of 60 mA and a potential of 7 kV. The duration of the deposition was 3 min and the maximum temperature measured at the substrate was 45 °C (Fig. 2h).

Afterwards, a third step of dicing was performed to remove the excess epoxy, resulting in the high-aspect-ratio pillars. The resulting pillars have a core of aluminum to serve as a pathway for neural signals to be transmitted from the tips to the pads. The epoxy layer serves as an electrical insulator, blocking the aluminum core to receive unwanted neural activity (Fig. 2i). Photos of the fabrication steps are shown in Fig. 3.

4. Results

4.1. Morphological

A total of 4 arrays were used for the measurement of the array's dimensions. After the wet etching process the aluminum pillars

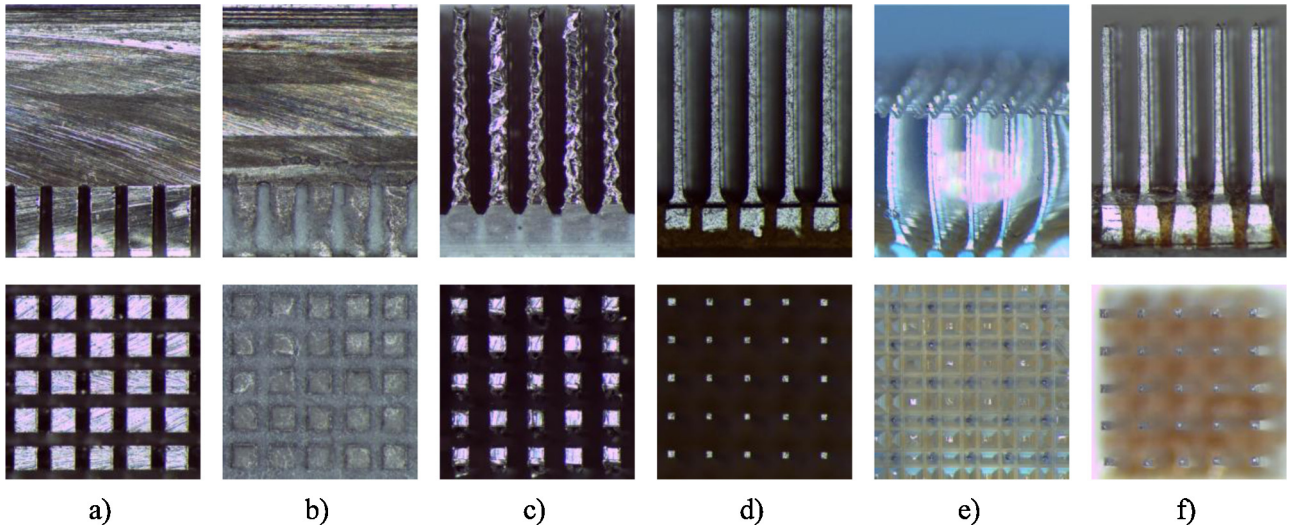

Fig. 3. Structure fabrication. First row photos correspond to the side view and second row photos correspond to either top or bottom view: (a) aluminum substrate with pads region delimitation; (b) pads' grooves filled with epoxy resin; (c) pillars after dicing stage; (d) pillars after the wet-etching step; (e) casted array with tips (optical distortion due to the convex shape of the epoxy); (f) final array structure.

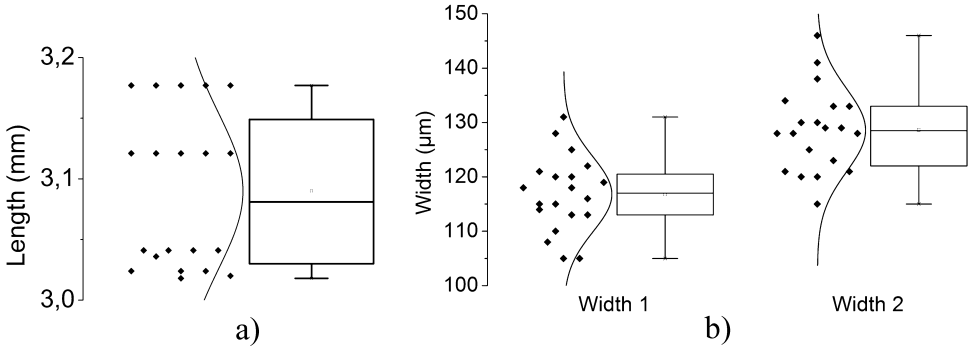

Fig. 4. Box plot with normal distribution of the aluminum pillars after wet-etching: (a) length of the pillars; (b) width of the pillars in the first direction and second direction (width 1 and width 2).

were measured to verify the variation that the corrosion introduces to their main dimensions. In a population of 20 samples, the average length was 3.09 mm with a standard deviation of 0.06 mm. Since aluminum is ductile and each cut creates small amounts of burr at the pillars' edges, it was important to observe the different widths between the first and second series of cuts when creating the pillars (Fig. 3c). These cuts are perpendicular so there should be a small difference in widths between two perpendicular sides of each pillar. For these measurements, 20 samples positioned at the perimeter of each array were used. All widths were measured at middle height of each pillar. The average width was 117 µm for the first direction and 129 µm for the second direction; both standard deviations were of 7 µm. The width difference between the two directions showed no statistical significance ($p < 0.05$; *T*-test). Fig. 4 shows the box plot for each group of measurements.

Fig. 5 shows the main dimensions that define each pillar with the epoxy coating. The pillars are 3 mm long and 160 µm wide, with a pyramidal shaped tip. The encapsulating epoxy is approximately

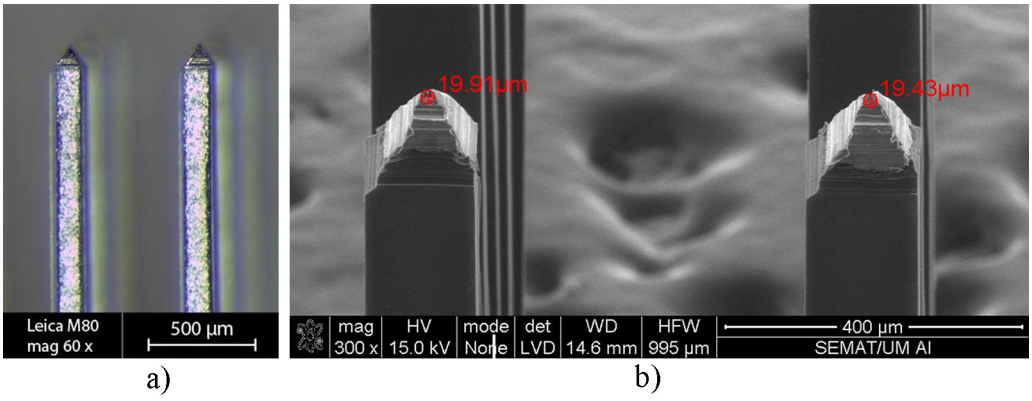

Fig. 5. Detailed view of the final pillars: (a) pillars lateral view coated with an epoxy layer; (b) tip morphology.

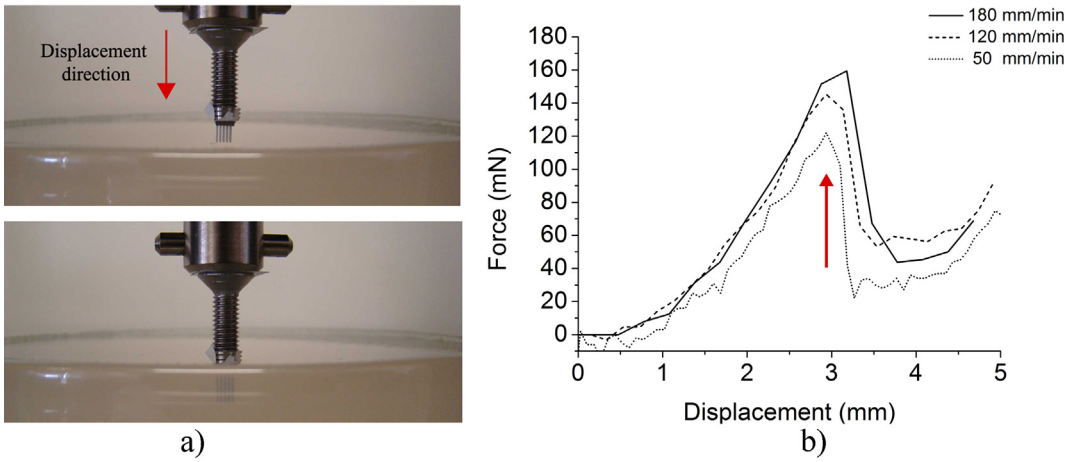

Fig. 6. Mechanical insertion tests on 0.5% agar gel: (a) insertion setup. Top picture, array before implantation, bottom picture, array fully implanted; (b) force versus displacement for the three tested speeds. The penetration moment is highlighted with a red arrow. (For interpretation of the references to color in this figure legend, the reader is referred to the web version of the article.)

20 μm thick. We have achieved alignment accuracies of 30 μm between the wafer's upper and back sides and of 6 μm between the epoxy layer and the aluminum pillar. The level of accuracy depends on the optical magnification of the dicer's microscope.

The measured tip radius was 10 μm. The pillars' base is an aluminum block of 400 μm × 400 μm × 750 μm. The tip measurement was performed in a FEI Nova NanoSem™ 200. All other measurements were performed with Leica M80™ stereo microscope and Leica LAS™ software.

4.2. Mechanical

The mechanical tests focused on the force required to implant and explant the array on agar brain phantom and also on porcine cadaver brain. The tests were performed on a Shimadzu AG-IS dynamometer equipped with a 50 N load cell capable of a 5 mN resolution. Agar gel has been widely used as an in vitro alternative for brain tissue [27–29]. The insertion mechanics were tested in 0.5% agar gel which mimics the brain cortex. Fig. 6a shows the setup arrangement for the implantation tests. The array was attached to the dynamometer shaft, which moved downward toward the agar gel at a predetermined speed. The shaft was set to move at three different speeds, namely, 180 mm/min, 120 mm/min and 50 mm/min. Fig. 6b shows the force applied versus the array's displacement toward the gel.

In Fig. 6b was observed an increase on the force applied on the initial stage while still subjected to the gel's resistance until the moment where the electrodes' tips appear to pierce the surface. Beyond this moment, as expected, there was an abrupt drop in the required load. After the electrode's full penetration there was a slight increase in the curve's slope, indicating that the array's base was pushing against the gel. It could be concluded that the maximum force coincided with the necessary load for piercing the gel and beginning implantation. By increasing the implantation speed, the force needed to penetrate the agar increased as well. The acquired data is summarized in Table 2.

Between the three tested speeds there is a maximum variation of force of 1.24 mN per electrode. The average implantation force is considerably lower than our previous thicker probe [10] and in the same order of magnitude of Das et al. [29]. Implantation tests with similar parameters as the agar gel were performed on porcine cadaver brain with the purpose of testing the array robustness, these tests showed significant tissue dimpling without implantation success. Penetration of the *dura mater* and subsequent implantation on the brain was only possible when displacements of four times the length of the electrodes were applied, which suggests that for a high-density electrode matrix it is necessary the use of impact insertion techniques to avoid massive tissue dimpling and compression before penetration [30]. Successful implantation could only be verified through explantation data, since it could not be observed from the penetration curve. Fig. 7a shows the withdrawal data on porcine cadaver brain while Fig. 7b shows the data related to the agar gel. Each figure shows the key moment highlighted by a red arrow. Moment 1 is where the brains' surface is in its relaxed state, in moment 2 there is a maximum tension applied and in moment 3 there is a complete detachment between the array and the tested material. Moment 1 happens because the array goes from a state of actively compressing the brain tissue to a relaxation state. The rise in tension during withdrawal is due to the drag forces between the electrodes and the surrounding material. This could be observed clearly in the cadaver brain as it followed the array trajectory originating a temporary protuberance in the region of implantation (moment 2). This was followed by a drop in the applied tension which led to the instant where the array was completely detached from the brain (moment 3). For the brain, the difference in force between brain relaxation and maximum tension was of 66 mN. This suggests that the array was fully implanted prior to removal. Besides this analysis the full implantation in agar could also be observed visually (Fig. 6a bottom).

A destructive test was performed against a glass substrate to acquire the force needed to bend the pillars. At a displacement rate of 5 mm/min, the measured buckling load was 5 N. This buckling load is inferior to silicon probes since aluminum has inferior Young's modulus [31].

A flexibility test was performed using the three point flexural test. The tested sample was 20 mm wide and 9.6 mm long. The

Table 2
Statistical data of the implantation tests.

Implantation speed (mm/mim)	Number of samples	Average maximum force (mN)	Standard deviation (mN)	Average maximum force per electrode (mN)
50	4	119	8	4.76
120	4	145	8	5.8
180	4	150	2	6

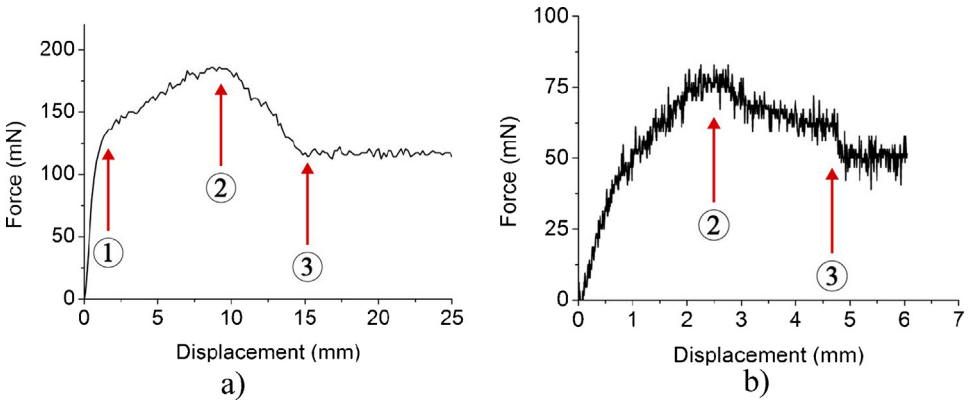

Fig. 7. Withdrawal results with key moments highlighted by red arrows. Moment 1, brain relaxation; moment 2, maximum tension; moment 3 complete detachment; (a) porcine cadaver brain; (b) agar gel.

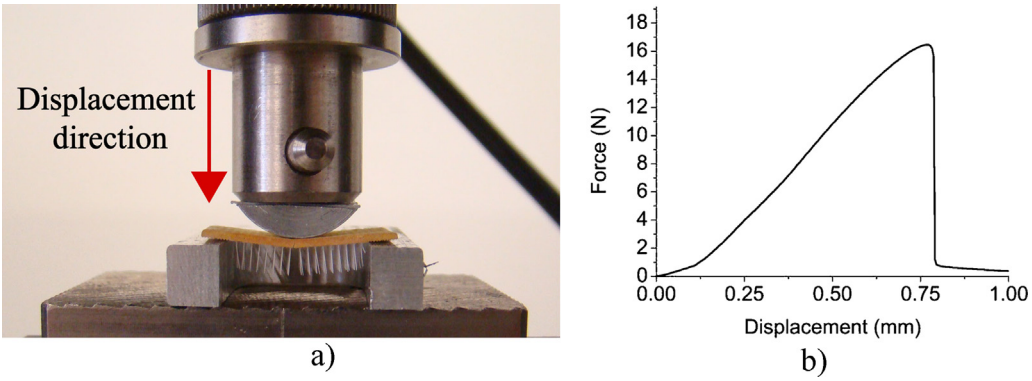

Fig. 8. Three point flexural test set up and results; (a) aluminum base with 15 mm spacing between support points. The picture was taken at the moment of rupture. (b) Force versus displacement graph.

support was made of aluminum with 15 mm spacing between support points (Fig. 8a). A downward force was applied in the middle of the sample with a cylindrical aluminum support until sample rupture could be observed. A maximum deflection before rupture of 0.8 mm was achieved (Fig. 8b).

4.3. Electrochemical

The electrochemical impedance characteristics of the platinum thin-film were obtained using a Gamry Reference 600™ Potentiostat/Galvanostat. A three-electrode chemical cell configuration with an Ag/AgCl reference electrode and a large area platinum counter electrode were used. The corresponding area of the platinum thin-film tested as the working electrode was of 38.4 mm^2. The electrolyte used was a saline solution with a concentration of 0.9% of NaCl. The experiment was carried out at room temperature. The alternate current excitation voltage was 10 mV with a frequency range from 1 Hz to 1 MHz. Fig. 9a shows the Bode plot of the impedance magnitude versus frequency for the platinum thin-film. Three readings of the same sample were performed for increased measurement reliability. At 1 kHz the average impedance was 385 Ω. The impedance at this specific frequency is of neurobiological interest because the neuronal cell's action potential has a duration close to 1 ms, and therefore, provides the attenuation introduced by the electrode for this range of frequencies. The electrode exhibits a near-resistive phase angle in the frequency range between 2 kHz and 125 kHz (Fig. 9b), and a capacitive behavior for the remaining frequencies.

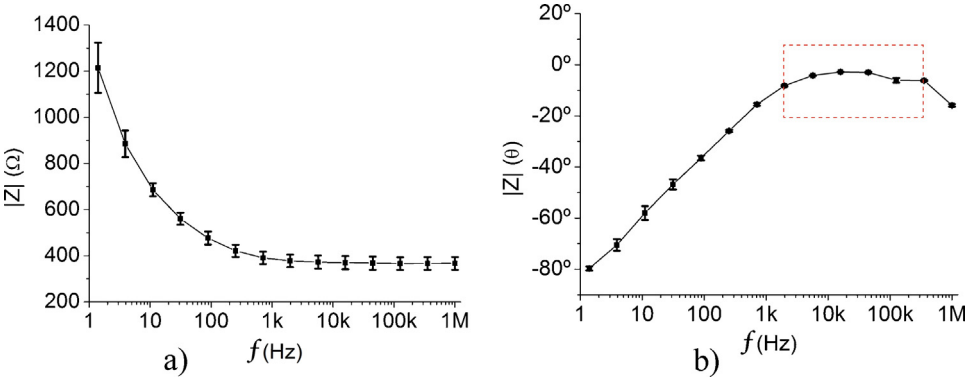

Fig. 9. Bode plot of the electrochemical impedance spectroscopy of the electrode in saline solution: (a) magnitude; (b) phase angle with highlight of the near resistive region.

5. Conclusions

The present work demonstrated that despite the challenges of micromachining aluminum, it is possible to fabricate high-aspect-ratio structures employing only dicing and wet-etching techniques. The aluminum-based substrate proved to be a possible alternative to silicon-based arrays by offering some advantages in terms of flexibility and electrical conductivity. The fabrication approach is cost-effective by avoiding advanced microfabrication techniques. Although the wet-etching step introduces some variations in the pillar's width, the encapsulating process corrects these variations by relying in the dicing machine's high resolution. The electrode array has the ability to penetrate deeper than commercially available arrays and is not subject to breakage during insertion. The result was a robust invasive neural electrode array with 3 mm long pillars with the ability to penetrate agar brain phantom and porcine cadaver brain tissue. Results showed that increasing implantation speeds would increase penetration forces in agar gel proportionally. The three point flexural test showed the ability of the array to bend made possible by the combination of aluminum and epoxy resin at its base. The platinum coating demonstrated through the electrochemical tests in saline solution to have the required performance for neural tissue interface. The present fabrication method can be applied to other metals, allowing alternate structural materials instead of silicon in the design of neural array. Overall, the proposed design and fabrication procedure is an eligible alternative for neural signal recording and stimulation systems and also offers a contribution to the future of flexible implantable devices.

Acknowledgments

A.C. Peixoto is supported by the Portuguese Foundation for Science and Technology under grant SFRH/BD/89509/2012. This work was supported by FCT with the reference project FCOMP 01 0124-FEDER-010909 (FCT/PTDC/SAU-BEB/100392/2008). The authors wish to thank Professor Senentxu Lanceros-Mendez for kindly granting access to the Shimadzu dynamometer and also to Pedro Libânio Martins for the valuable suggestions and technical assistance during the implantation tests.

References

[1] R.A. Normann, Technology insight: future neuroprosthetic therapies for disorders of the nervous system, Nat. Clin. Pract. Neurol. 3 (8) (2007) 444–452.
[2] K.C. Cheung, Implantable microscale neural interfaces, Biomed. Microdevices 9 (December (6)) (2007) 923–938.
[3] K.D. Wise, Wireless integrated microsystems: wearable and implantable devices for improved health care, in: Solid-State Sensors, Actuators and Microsystems Conference, 2009, pp. 1–8.
[4] A. Sharma, L. Rieth, P. Tathireddy, R. Harrison, H. Oppermann, M. Klein, M. Töpper, E. Jung, R.A. Normann, G. Clark, F. Solzbacher, Long term in vitro functional stability and recording longevity of fully integrated wireless neural interfaces based on the Utah Slant Electrode Array, J. Neural Eng. 8 (August (4)) (2011).
[5] P. Tathireddy, D. Rakwal, E. Bamberg, F. Solzbacher, Fabrication of 3-dimensional silicon microelectrode arrays using micro electro discharge machining for neural applications, in: Solid-State Sensors, Actuators and Microsystems Conference. Transducers, 2009, pp. 1206–1209.
[6] J. Csicsvari, D.A. Henze, B. Jamieson, K.D. Harris, A. Sirota, P. Barthó, K.D. Wise, G. Buzsáki, Massively parallel recording of unit and local field potentials with silicon-based electrodes, J. Neurophysiol. 90 (2) (2003) 1314–1323.
[7] N.A. Fineberg, M.N. Potenza, S.R. Chamberlain, H.A. Berlin, L. Menzies, A. Bechara, B.J. Sahakian, T.W. Robbins, E.T. Bullmore, E. Hollander, Probing compulsive and impulsive behaviors, from animal models to endophenotypes: a narrative review, Neuropsychopharmacology 35 (February (3)) (2010) 591–604.
[8] G. Paxinos, C. Watson, The Rat Brain in Stereotaxic Coordinates – Part 1, 6th ed., Elsevier Inc., 2007.
[9] T. Kim, J.G. McCall, Y.H. Jung, X. Huang, E.R. Siuda, Y. Li, J. Song, Y.M. Song, H.A. Pao, R.-H. Kim, C. Lu, S.D. Lee, I.-S. Song, G. Shin, R. Al-Hasani, S. Kim, M.P. Tan, Y. Huang, F.G. Omenetto, J.A. Rogers, M.R. Bruchas, Injectable, cellular-scale optoelectronics with applications for wireless optogenetics, Science 340 (April (6129)) (2013) 211–216.
[10] A.C. Peixoto, S.B. Goncalves, A.F. Silva, N.S. Dias, J.H. Correia, Neural electrode array based on aluminum: fabrication and characterization, IEEE Sens. J. 13 (9) (2013) 3319–3324.
[11] J. Zahavi, M. Metzger, Electron microscope study of breakdown and repair of anodic films on aluminum, J. Electrochem. Soc. 119 (11) (1972) 1479.
[12] J. Yahalom, T.P. Hoar, Galvanostatic anodizing of aluminium, Electrochim. Acta 15 (June (6)) (1970) 877–884.
[13] M.A. Nicolelis, A.A. Ghazanfar, B.M. Faggin, S. Votaw, L.M. Oliveira, Reconstructing the engram: simultaneous, multisite, many single neuron recordings, Neuron 18 (April (4)) (1997) 529–537.
[15] A.A. Sharp, A.M. Ortega, D. Restrepo, D. Curran-Everett, K. Gall, In vivo penetration mechanics and mechanical properties of mouse brain tissue at micrometer scales, IEEE Trans. Biomed. Eng. 56 (January (1)) (2009) 45–53.
[16] Henkel AG & Co., Hysol® 3430TM Technical Datasheet, 2008, Available at: http://www.loctite.co.uk/fullproduct-list-loctite-4995.htm?countryCode=uke&BU=industrial &parentredDotUID=productfinder&redDotUID=1000000IC7Z
[17] R. Cobden, A. Banbury, Aluminium: physical properties, characteristics and alloys, TALAL (1994) 60.
[18] R. Sharma, P. Tathireddy, S. Lee, L. Rieth, Application-specific customizable architectures of Utah neural interfaces, Procedia Eng. 25 (2011) 1016–1019.
[19] B. Rashid, M. Destrade, M. Gilchrist, Mechanical characterization of brain tissue in compression at dynamic strain rates, J. Mech. Behav. Biomed. Mater. (2012).
[20] K.E. Petersen, Silicon as a mechanical material, Proc. IEEE 70 (5) (1982) 420–457.
[24] Henkel AG & Co., Hysol® 9492TM Technical Datasheet, 2007, Available at: http://www.loctite.co.uk/fullproduct-list-loctite-4995.htm?countryCode=uke&BU=industrial &parentredDotUID=productfinder&redDotUID=1000000J9BL
[25] DSM Engineering Plastics, Gluing Guide, 2013, Available at: www.dsm.com/content/dam/dsm/automotive/en_US/documents/gluing-guide.pdf
[26] Transene Co. Inc., Material safety data sheet for aluminum etchant Type A, Rowley, MA, 1987.
[27] Z.-J. Chen, G.T. Gillies, W.C. Broaddus, S.S. Prabhu, H. Fillmore, R.M. Mitchell, F.D. Corwin, P.P. Fatouros, A realistic brain tissue phantom for intraparenchymal infusion studies, J. Neurosurg. 101 (2) (2004) 314–322.
[28] R. Pomfret, G. Miranpuri, K. Sillay, The substitute brain and the potential of the gel model, Ann. Neurosci. 20 (July (3)) (2013).
[29] R. Das, D. Gandhi, S. Krishnan, L. Saggere, P.J. Rousche, A benchtop system to assess cortical neural interface micromechanics, IEEE Trans. Biomed. Eng. 54 (June (6 Pt 1)) (2007) 1089–1096.
[30] P.J. Rousche, R.A. Normann, A method for pneumatically inserting an array of penetrating electrodes into cortical tissue, Ann. Biomed. Eng. 20 (January (4)) (1992) 413–422.
[31] M. Hajj-Hassan, V.P. Chodavarapu, S. Musallam, Microfabrication of ultra-long reinforced silicon neural electrodes, Micro Nano Lett. 4 (January) (2009) 53–58.

Biographies

A.C. Peixoto graduated, on 2008, in electrical Engineering, at University of Trás-os-Montes e alto Douro, Vila Real, Portugal. He obtained in 2010 the Master's degree in electrical engineering, at the same institution. Presently, he is pursuing a PhD on biomedical engineering at University of Minho, Guimarães, Portugal.

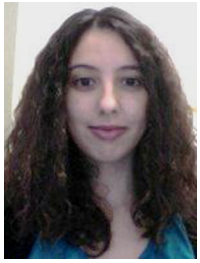

S.B. Goncalves graduated, on 2012, in biomedical engineering (integrated masters) with the major in medical electronics, at University of Minho, Portugal. Presently, she is a researcher at University of Minho.

F. Pinho graduated, on 2002, in physical therapy and in industrial electronics engineering on 2009. Presently he is an assistant professor at InstitutoPolitécnico de Saúde do Norte (IPCA) and is also pursuing a PhD on biomedical engineering at University of Minho, Guimarães, Portugal.

A.F. Silva graduated, in 2007, in biomedical engineering (integrated masters) with the specialization in medical electronics, at University of Minho, Braga, Portugal. He obtained in 2011 the PhD degree in leaders for technical industries, at the same institution, over the MIT-Portugal Program within the Engineering Design and Advanced Manufacturing (EDAM) focus-area. Presently, he is an assistant professor to the MIT Portugal's EDAM focus-area at University of Minho.

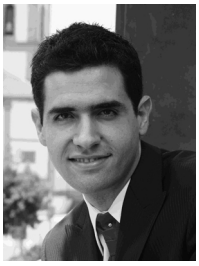

N.S. Dias graduated in industrial electronics and computers at University of Minho, Portugal in 2004. In 2009, he obtained the PhD degree in industrial electronics from the University of Minho, Guimarães, Portugal, in collaboration with the Center for Neural Engineering at The Pennsylvania State University, State College, PA, USA. During his PhD, Nuno developed a brain–machine interface based on biotelemetry and dry electrodes. He is currently pursuing a post-doc position at ICVS/3Bs Associate Laboratory, University of Minho, Braga, Portugal.

J.H. Correia graduated in physical engineering from University of Coimbra, Portugal in 1990. He obtained in 1999 a PhD degree at the Laboratory for electronic instrumentation, Delft University of Technology, The Netherlands, working in the field of microsystems for optical spectral analysis. Presently, he is a full professor in Department of Industrial Electronics, University of Minho, Portugal. He was the General-Chairman of Eurosensors 2003 and MME 2007, Guimarães, Portugal. His professional interests are in micromachining and microfabrication technology for mixed-mode systems, solid-state integrated sensors, microactuators and microsystems.

IOP Publishing Journal of Micromechanics and Microengineering
J. Micromech. Microeng. **25** (2015) 055014 (9pp) doi:10.1088/0960-1317/25/5/055014

Fabrication and mechanical characterization of long and different penetrating length neural microelectrode arrays

S B Goncalves[1], A C Peixoto[1], A F Silva[2] and J H Correia[1]

[1] Department of Industrial Electronics, University of Minho, Guimaraes, Portugal
[2] MIT Portugal Program, School of Engineering, University of Minho, Guimaraes, Portugal

E-mail: sgoncalves@dei.uminho.pt

Received 6 July 2014, revised 29 August 2014
Accepted for publication 2 September 2014
Published 17 April 2015

Abstract

This paper presents a detailed description of the design, fabrication and mechanical characterization of 3D microelectrode arrays (MEA) that comprise high aspect-ratio shafts and different penetrating lengths of electrodes (from 3 mm to 4 mm). The array's design relies only on a bulk silicon substrate dicing saw technology. The encapsulation process is accomplished by a medical epoxy resin and platinum is used as the transduction layer between the probe and neural tissue. The probe's mechanical behaviour can significantly affect the neural tissue during implantation time. Thus, we measured the MEA maximum insertion force in an agar gel phantom and a porcine cadaver brain. Successful 3D MEA were produced with shafts of 3 mm, 3.5 mm and 4 mm in length. At a speed of 180 mm min^{-1}, the MEA show maximum penetrating forces per electrode of 2.65 mN and 12.5 mN for agar and brain tissue, respectively. A simple and reproducible fabrication method was demonstrated, capable of producing longer penetrating shafts than previously reported arrays using the same fabrication technology. Furthermore, shafts with sharp tips were achieved in the fabrication process simply by using a V-shaped blade.

Keywords: neural electrodes, dicing technology, mechanical characterization

(Some figures may appear in colour only in the online journal)

1. Introduction

Invasive neural interfaces capable of communication with neural tissue are emergent therapeutics. This approach relies on electrodes implanted inside the brain, restoring lost neural function by recording and/or electrically stimulating a large number of small groups of neurons. Deep brain stimulation (DBS) has proved to have beneficial effects in a variety of neurological conditions, such as Parkinson's disease, essential tremor, dystonia, Tourette's syndrome, chronic pain, epilepsy, depression and obsessive compulsive disorder (OCD) [1, 2]. Cochlear [3] and retinal [4] implants are also widely used in the therapy of deafness and blindness, respectively. More recently, studies have been trying to achieve control of artificial limbs through implantable electrodes [5, 6].

Current fabrication methods of 3D microprobe array structures can be divided into three principal branches: silicon bulk etched microprobe array; polymer-constructed array; and 3D arrays assembled from 2D parts [7]. Three dimensional microelectrode arrays (MEA) based on silicon technologies are receiving a growing amount of interest, since they enable a pronounced increase in the number of recording sites per probe shaft [8]. Two well-known silicon-based configurations of invasive neural microelectrodes are the Michigan probe and the Utah Electrode Array (UEA), which are nowadays still the reference point to several studies [9, 10]. The Michigan configuration includes single-shaft, multi-shaft and 3D layouts with multiple recording sites per electrode [10]. On the other hand, the UEA configuration comprises a 3D array of one hundred needle-shaped microelectrodes and each shaft has an

Table 1. Comparison of design parameters between some silicon-based 3D MEA.

Reference	Array dimension	Array fabrication method	Number of electrodes per shaft	Number of shafts	Length (mm)	Width (μm)	Thickness(μm)
[8]			9	1, 4	8	140	100
[14]	2D	Dry silicon	3	4	10	100	50
[15]		etching process	8	4, 8	7–8	—	—
[16]			188	1, 4	4	180	300
[20]			16 (8 × 8)	2	5	190	50
[7]		Silicon	4	16 (4 × 4)	6	100	250
[17]	3D array	micromachining	1	128 (8 × 16)	1–2.5	40	15
[18]	by 2D parts	and	1	16 (4 × 4)	1.2	50	12
[19]	assembly	assembly	8	32 (4 × 8)	3.3	144	80
[21]		processes	5	16 (4 × 4)	2, 4.5, 8	140	100
[22]			4	16 (4 × 4)	4	60	—
[25]	3D	Wet-etching	4	4 (2 × 2)	4	200	30
[24]	array	μ-WEDM[a]	1	100 (10 × 10)	5, 9	200	200

active tip that communicates with the neural tissue. Currently, UEA electrodes have a maximum length of 1.5 mm, which restricts their application to surface structures of the cerebral cortex [11–13].

The desire to increase scientific insight into the interaction of neuron populations has triggered the need for longer penetrating electrodes. Therefore, in the last decade several approaches based on different technologies were developed to produce invasive neural interfaces with deeper electrode shafts. Most of these approaches include planar microfabricated 2D MEA [8, 14–16] or 3D structures that are assembled by layers of 2D arrays [7, 17–22]. However, both approaches have disadvantages, when compared to technologies that simply rely on silicon wafer micromachining like the UEA array [23].

Planar electrodes have an inherent 2D nature, recording along a single plane of the brain, which prevents the full neurons and cell activity information in 3D space. On the other hand, 3D MEA ensure the simultaneous monitoring and stimulation of neural activity within a targeted volume of brain tissue with a high spatial resolution. This allows for more realistic and complete information of neural networks. Although 3D arrays resulting from assembly techniques are capable of performing as 3D interfaces, they have some drawbacks. They require complex assembly steps and vertical interconnection to produce 3D structures. Besides this, they have a low structure strength and a large implantable opening [7]. Multiple active sites along the shafts are easily achieved.

Some efforts have been made to obtain 3D MEA with long electrodes based on silicon wafers micromachining which also include microwire electrical discharge machining [24] and self-assembled probes using a heat treatment processes [25] to achieve the final 3D array design. We have previously presented [26] an approach to fabricate 3D MEA with shaft lengths up to 3 mm, which use aluminum as the bulk material instead of silicon. Table 1 compares the 3D MEA with regard to their design parameters.

In this paper we will focus on technologies that rely on wafer dicing to define the 3D array and to achieve longer electrode shafts. The final 6 × 6 matrix comprises three different lengths for the shafts, the longest being 4 mm and the shortest 3 mm. The fabrication process is characterized by its simplicity, low-cost and reproducibility. Since depths of up to 4 mm are reached, the proposed electrode matrix enables the recording/stimulation of deeper neural structures than the cerebral cortex, such as a rat's hippocampus. This neural structure is a frequently used research model for exploring both normal and pathological conditions of the nervous system, including the processes involved in memory and learning as well as neurodegenerative diseases [27].

Mechanical characterization of the final array was also performed using a 0.5% agar gel phantom and a porcine cadaver brain, in order to measure the MEA's maximum insertion and withdrawal forces. Mechanical characterization of arrays is essential, since some of the leading hypotheses for the failure of neuroprosthesis relate to acute injury caused by insertion [28].

2. MEA design

The developed neural MEA consists of 36 sharp electrode probes fabricated on a silicon substrate. The structure comprises three different electrode lengths: 3 mm, 3.5 mm and 4 mm. Its structure is divided into three regions: a support base region, the electrode body (shaft) and a piercing region (sharp tip) that is simultaneously the recording/stimulating region, as shown in figure 1(*a*). The square support base region measures 3.45 × 3.45 mm^2 and the electrode's shaft is 150 μm wide. The base region is supported by an epoxy filling, which also allows interelectrode electrical isolation. The wide electrode shaft is designed to be robust enough to withstand implantation. After the insulation process of the array, each shaft ends up with a width of 180 μm along the electrode length. The sharp tip at the shaft's end corresponds to a recording/stimulating region which is covered by a titanium (Ti) and platinum (Pt) layer. Ti serves as the adhesion promoter for the Pt thin film, which is the material that interfaces with the neural tissue. Pt was selected due to it's biocompatibility and impedance characteristics [29]. The

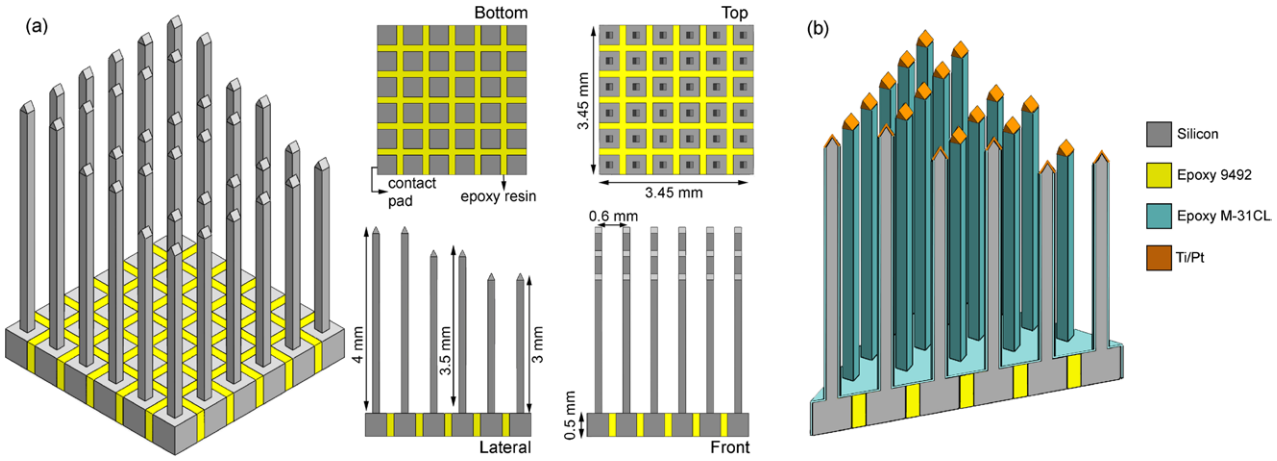

Figure 1. (*a*) 3D schematic of the MEA after the dicing saw process to create the array design. At this step of the fabrication process the high-aspect-ratio and different penetrating lengths of electrodes can be seen; (*b*) transversal cut of the 3D final array showing the insulation and transduction layers.

electrode tips are placed 600 μm from each other. Figure 1(*b*) shows the schematic of the final 3D MEA design.

3. Fabrication process

Figure 2 illustrates the process flow of the 3D MEA fabrication, whose design is exclusively accomplished by a dicing saw that patterns the silicon substrate. The cutting stages are performed on a Disco DAD 2H/6T dicing machine, equipped with a Disco NBC–ZB diamond grit blade capable of performing cuts 4 mm deep and 150 μm wide at a cutting speed of 0.3 mm s^{-1}. Some modifications had to be made in the way the dicing machine performs the *Z*-axis calibration in order to cut samples that are higher than the 2 mm limit of the machine. By placing an aluminum spacer between the blade and the sample holder, it is possible to cut at heights up to 4 mm. This spacer is manually introduced just for the set-up of the machine and is removed afterwards. The height of the spacer is the difference between the pretended height and the 2 mm limit.

The array is fabricated out of a [1 0 0] p-type boron-doped silicon wafer with 1.3 mΩ.cm resistivity and a thickness of 5 mm (figure 2(*a*)). The fabrication process starts by making a set of 1.5 mm deep cuts on the backside of the silicon substrate to create squared pad regions with dimensions of 0.45 × 0.45 × 1.5 mm^3 (figure 2(*b*)). The pad regions represent the electrical contacts of each electrode in the array. The next step consists of filling the grooves with a non-conductive epoxy resin (Loctite® Hysol 9492) in order to electrically isolate each electrode from its neighbours (figure 2(*c*)). The epoxy excess is removed through grinding and polishing. After cutting the electrode shafts, the epoxy resin is used to cluster all shafts in a single structure.

Afterwards, the front side of the silicon substrate is diced to produce three steps with different heights. This is accomplished by multiple closely-spaced dicing cuts, in order to remove all the silicon between cuts. Each of these closely-spaced cuts produces a step that is 0.5 mm shorter than the previous one. Thus, the set of cuts for the higher shafts are performed at the substrate's surface, followed by a set of cuts 0.5 mm deeper and so on, as shown in figure 2(*d*). The next step consists of the shaft's formation, which results in a 6 × 6 matrix. Two sets of deep orthogonal cuts are made on the upper side of the silicon substrate. The backside pads that are initially 1.5 mm deep are reduced at this step to a thickness of 0.5 mm, connected by a 0.15 mm wide layer of epoxy 9492. The result of this dicing step is 36 0.15 × 0.15 mm^2 wide shafts with penetrating depths of 3 mm, 3.5 mm and 4 mm (figure 2(*e*)). This technology also allows other combinations of shaft lengths, suitable for other applications.

After the shafts are properly shaped and electrically insulated from each other, it is necessary to encapsulate the array. This is accomplished by placing the array into a square mold filled with a medical epoxy adhesive (Loctite® M-31CL™), which after curing will result in a complete covering of the array with a biocompatible resin [30] (figure 2(*f*)). The pad regions provide electrical access to each shaft, so the medical epoxy layer in the array's backside is removed through grinding and polishing.

In order to smooth the process of the electrodes' implantation into the neural tissue, sharpening of the shaft tips is performed. Since the blunt shafts comprise different lengths, this step has to be completed once again at increasing depths with an index of 0.5 mm between cuts. Therefore, graded and sharpened shafts are produced, as shown in figure 2(*g*). This dicing step is accomplished by a V-shape 250 μm thick Disco Z09 blade that makes a 60° angle with the surface. The cutting speed is 0.5 mm s^{-1}. The sharp tips formation is accomplished at this step so the area of the transduction layer can be properly controlled, exposing only the sharp tips of the shafts.

The next step is the deposition of the transduction layer in order to convert the silicon shafts into active electrodes for recording or stimulation (figure 2(*h*)). The transduction layer consists of 50 nm of Ti and 200 nm of Pt layers. The Pt layer will allow an efficient charge transfer between the electrode and the neural tissue while Ti serves as an adhesive layer. The Ti layer was deposited using electron beam evaporation at a

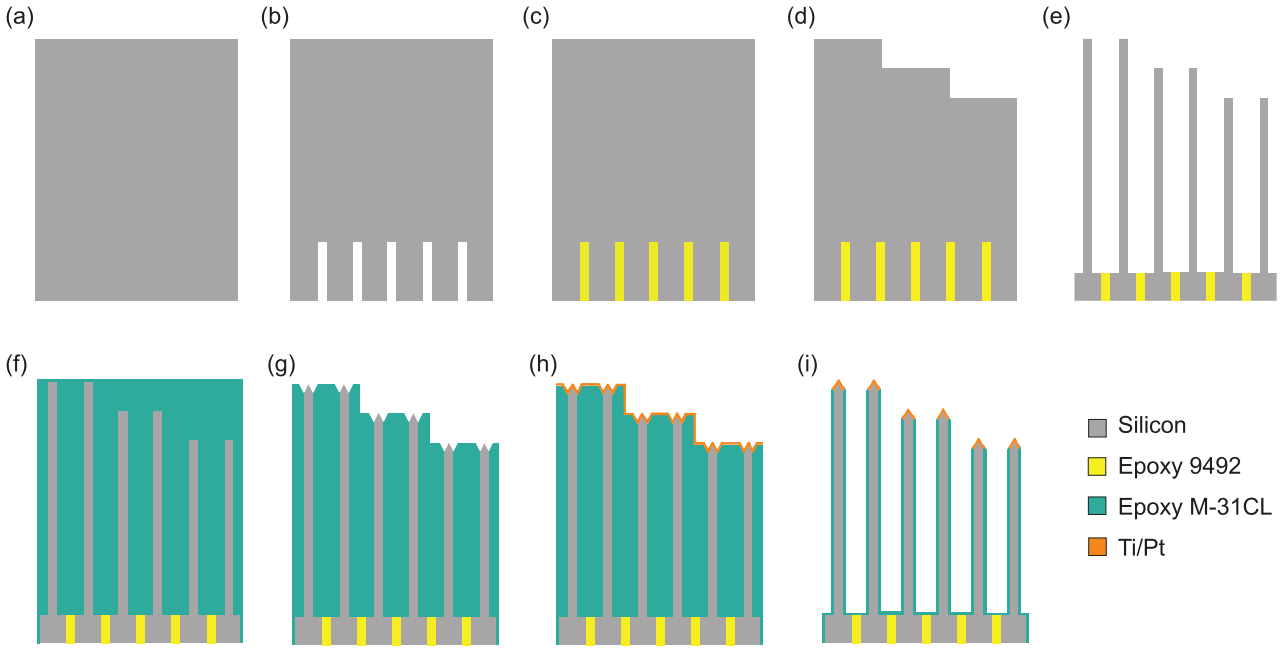

Figure 2. Cross-sectional drawings of the fabrication steps. (*a*) Silicon substrate; (*b*) pads' region fabrication; (*c*) adhesive filling with epoxy 9492 resin; (*d*) silicon steps produced by closely-spaced cuts; (*e*) blunt shafts with lengths of 4 mm (left), 3.5 mm (centre) and 3 mm (right), spaced 0.6 mm apart; (*f*) array's encapsulation by medical epoxy M-31CL resin; (*g*) diced sharp shaft tips at different depths; (*h*) deposition of Ti/Pt layers; (*i*) medical epoxy removal by dicing.

starting pressure of 8.6×10^{-6} mBar while supplying a current of 8 mA and a potential of 7 kV. The duration of the deposition was 2 min (deposition rate approximately 5 Å s^{-1}) and the maximum temperature measured at the substrate was 60 °C. The Pt layer was deposited using DC sputtering at a starting pressure of 1×10^{-2} mBar while supplying a 40 sccm of Argon, a current of 40 mA and a potential of 302 V. The duration of the deposition was 251 min (deposition rate approximately 0.15 Å s^{-1}) and the maximum temperature measured at the substrate was 37 °C. Both depositions are performed in the same vacuum environment, so that the Pt layers are deposited over the Ti layers before they are exposed to the atmosphere.

The final 3D array is accomplished by removing the excess of the medical epoxy. Once again two sets of deep orthogonal cuts are made on the upper side of the silicon substrate, leaving each shaft with a thin layer of medical epoxy (figure 2(*i*)). The result of this dicing step is thirty-six 180×180 μm^2 wide shafts with penetrating depths of 3 mm, 3.5 mm and 4 mm.

4. Results

4.1. Fabrication process

The results of the 3D MEA fabrication are shown in figure 3, which comprises transversal and 3D views of each fabrication step. All photos and measurements were performed with a Leica M80™ stereo microscope and Leica LAS™ software. Figure 3(*a*) shows the thick silicon substrate which undergoes a dicing process to create the 3D MEA. The dicing step result to create the electrical contact pads is shown in figure 3(*b*) at multiple views. The initial pad regions are $0.45 \times 0.45 \pm 0.013$ mm^2 wide and 1.5 ± 0.027 mm deep.

The result of filling the grooves with epoxy resin is shown in figure 3(*c*). In figure 3(*d*) one can see the staircase effect on the upper side of the silicon substrate, in order to produce flat shafts. The shafts created are 4 ± 0.017 mm, 3.5 ± 0.009 mm and 3 ± 0.014 mm deep and 0.15 ± 0.005 mm wide as shown in figure 3(*e*). At this stage, the final contact pad lengths are set to 0.5 ± 0.043 mm. The results of the insulation process are shown in figure 3(*f*) and one can see that the total shaft area is encapsulated by the medical epoxy layer. In figure 3(*g*), the result of dicing the sharp tips is shown. Figure 4 shows the array's shafts with the sharp tips, which have lengths of 0.15 ± 0.006 mm and a radius tip of 2.41 μm. The tip measurement was performed in a FEI Nova NanoSem™ 200. The final 3D MEA can be seen in figure 3(*h*).

A 6×6 matrix of electrodes with different penetrating depths spacing each electrode by 600 μm and insulated by a 15 ± 3.6 μm layer of a medical epoxy resin was successfully produced. The final characteristics of the array are summarized in table 2. During the final cutting step, only the shaft's body undergoes a dicing process. Thus, Ti/Pt transduction layers on the shaft's tips are able to withstand this step. Although we have presented a detailed process flow with a single array sample, the proposed 3D arrays are compatible with a batch-scale fabrication process.

4.2. Mechanical characterization

The 3D MEA robustness was characterized by measuring the compressive failure forces of the shafts and the array's bending force. We also measured the load required to implant and extract the array into a substrate of 0.5% agar gel and a porcine cadaver brain. A total of five porcine cadaver brain

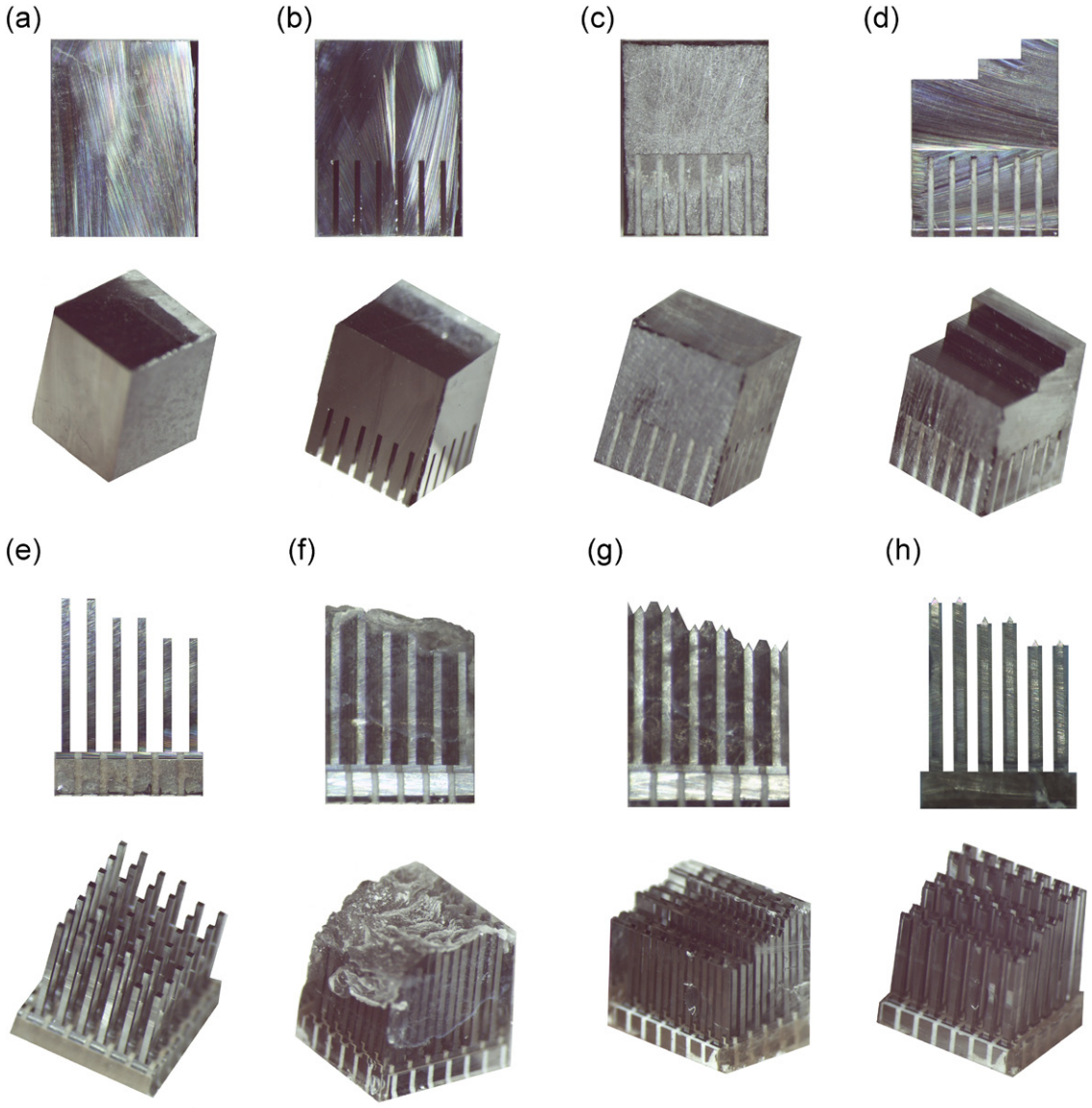

Figure 3. Transversal (top) and 3D photos (bottom) of the array fabrication steps. (*a*) Silicon substrate; (*b*) diced contact pads; (*c*) filling with epoxy 9492 resin; (*d*) diced substrate's upper side to produce three steps; (*e*) diced blunt shafts with lengths of 4 mm (left), 3.5 mm (center) and 3 mm (right), spaced 0.6 mm apart; (*f*) array's insulation by medical epoxy resin; (*g*) diced sharp shaft tips at different depths; (*h*) medical epoxy removal by dicing, producing a 6 × 6 matrix of electrodes.

samples were used. They were conserved at −18 °C for 12 h and 30 min before the mechanical tests they were preserved at 5 °C. During the tests, both gel and brain tissue were exposed to the room temperature.

The tests were performed on a Shimadzu AG-IS dynamometer equipped with a 50 N load cell capable of a 5 mN resolution. For the longitudinal compressive failure force tests, due to the high forces involved a 500 N load cell with 50 mN resolution was used. The implantation and withdrawal tests include three different speeds. Only 4 mm shafts composed the tested 6 × 6 arrays in order to represent the worst case scenario.

The array's mechanical characterization focused on its robustness. The electrodes' compressive failure forces were measured as well as the array's base bending force. The setup photo and load versus displacement graphic results are shown in figure 5. In longitudinal compression tests (figure 5(*a*)), the shafts withstand a load of approximately 68.37 ± 8.63 N before breakage. Figure 5(*b*) shows the axial compression failure tests on single shafts. The array is horizontally placed in a support made of aluminum with a 15 mm spacing between support points. An aluminum block made a downward displacement until it reaches the shaft at 2/3 of its height. The results show that up to 60 mN is required to break a single shaft. In order to measure the array's base bending force, a three point flexural test was used. The tested sample was 19.2 mm wide and 4 mm long (figure 5(*c*)). A downward force was applied in the middle of the sample with a cylindrical aluminum support until sample rupture could be observed. A maximum deflection before a rupture of 0.3 mm was achieved with a required load of 1.8 N.

We also measured the array's insertion and withdrawal forces (10 separate samples for each test) into two different

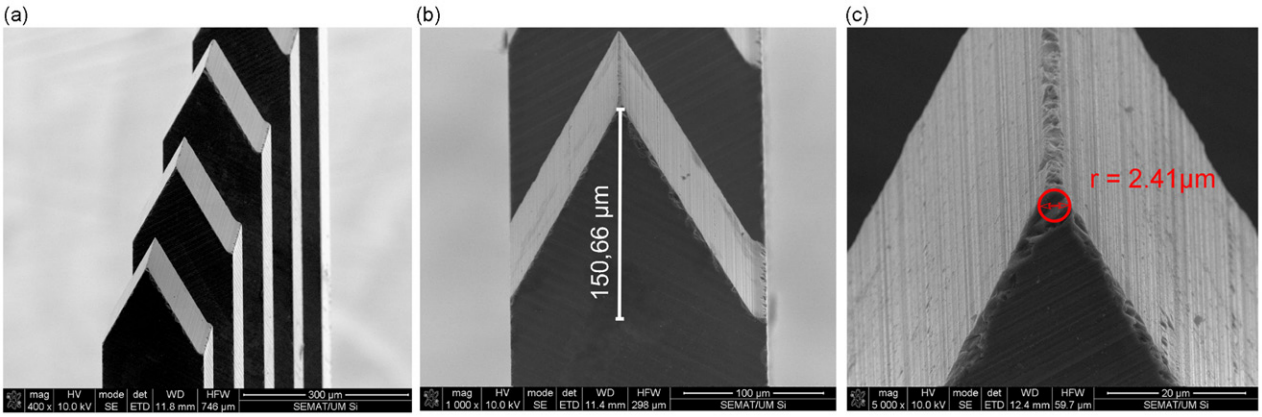

Figure 4. SEM images of (*a*) the array's sharp shafts, (*b*) the tip's height of approximately 150 μm and (*c*) the radius tip of 2.41 μm.

Table 2. Summary of geometrical properties of the fabricated 3D probes arrays.

Array's dimensions	3.45 × 3.45 mm^2	**Shaft width**	180 μm
Contact pad width	0.45 × 0.45 mm^2	**Shaft length**	3, 3.5 and 4 mm
Contact pad height	500 μm	**Tip length**	150 μm
Space between shafts	600 μm	**Tip radius**	2.41 μm

substrates: 0.5% agar gel and a porcine cadaver brain. Agar gel was used as an in vitro alternative for brain tissue [31, 32]. Figures 6(*a*) and (*d*) demonstrates the setup arrangement for the implantation analysis on agar and brain tissue, respectively. The array was attached to the dynamometer shaft (positioned perpendicular to the substrate surface), which moved downward towards the substrate at a predetermined speed. After penetration, the dynamometer shaft paused for 30 s before initiating the withdrawal tests, where the probe returned to its initial position, removing it from the tissue. The shaft was set to move at three different speeds, namely, 180 mm min^{-1}, 120 mm min^{-1} and 50 mm min^{-1}. The surfaces of the substrates were determined by manually lowering the array until a small force was registered on the load cell. The array was then raised slightly just until the load on the probe returned to zero.

Figures 6(*b*) and (*e*) shows the force applied versus the array's displacement towards the gel and brain, respectively. Each figure shows the key moment highlighted by a number. In both insertion tests, we observed an increase in the force applied on the initial stage while the array is still subjected to the gel or brain's resistance until the moment where the electrode tips pierce the surface. Beyond this moment, as expected, there was an abrupt drop in the required load, which corresponds to moment 1, identified in the figures. After the electrode's full penetration there was a slight increase in the curve's slope, indicating that the array's base was pushing against the gel or brain's surface (moment 2). The withdrawal test results on agar and the brain are shown in figures 6(*c*) and (*f*), respectively. In moment 3 there is a maximum tension applied until a complete detachment between the array and the tested material is accomplished (moment 4). The rise in tension during withdrawal is due to the drag forces between the electrodes and the surrounding material. Table 3 summarizes the acquired data on the implantation and withdrawal tests.

4.3. Electrochemical characterization

In vitro electrochemical impedance spectroscopy (EIS) was used to perform electrochemical characterization. The surface area of the Pt films was 0.02 mm^2. The impedance measurements were performed in a Gamry system (Gamry Instruments, Reference 600™), using a standard three-electrode configuration. A large-area platinum foil (40 × 40 × 0.25 mm^3) was used as a counter electrode and an Ag|AgCl reference electrode. The electrolyte employed was a 0.9% NaCl solution. Impedance (Z) was measured for frequencies from 1 Hz to 1 MHz at a constant 10 mV AC voltage. All measurements were made at room temperature.

At 1 kHz, *in vitro* EIS measurements showed an average impedance of 68 kΩ for Pt thin-films. The impedance at this specific frequency is of neurobiological interest because the neuronal cell's action potential has a duration close to 1 ms and therefore, provides the attenuation introduced by the electrode for this range of frequencies. Figure 7(*a*) shows the Bode plot of the impedance magnitude versus frequency for the sputtered Pt thin-film. Three readings of the same sample were performed for increased measurement reliability. The electrode exhibits a capacitive behaviour in all the frequency ranges (figure 7(*b*)).

5. Discussion and conclusion

This paper proposed a different fabrication method of 3D silicon-based neural MEA with long electrodes of different penetrating depths. The 3D arrays were patterned relying only on dicing saw technology and successfully producing a matrix of 6 × 6 electrodes. Arrays of up to 4 mm long, 180 μm wide and individually addressable were fabricated. The described fabrication process is simple, reproducible and robust enough for batch fabrication.

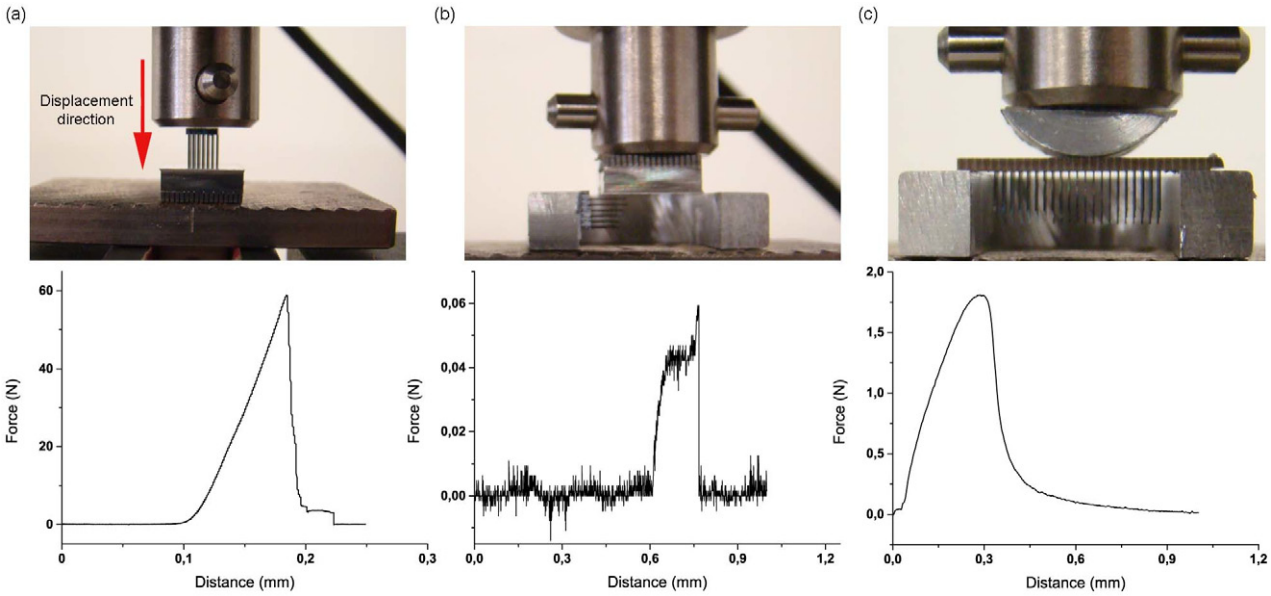

Figure 5. Mechanical failure tests. The first row of photos corresponds to the setup arrangement and the second row to the force versus displacement graphic for the three tests. (*a*) Longitudinal and (*b*) axial compressive force and (*c*) bending force.

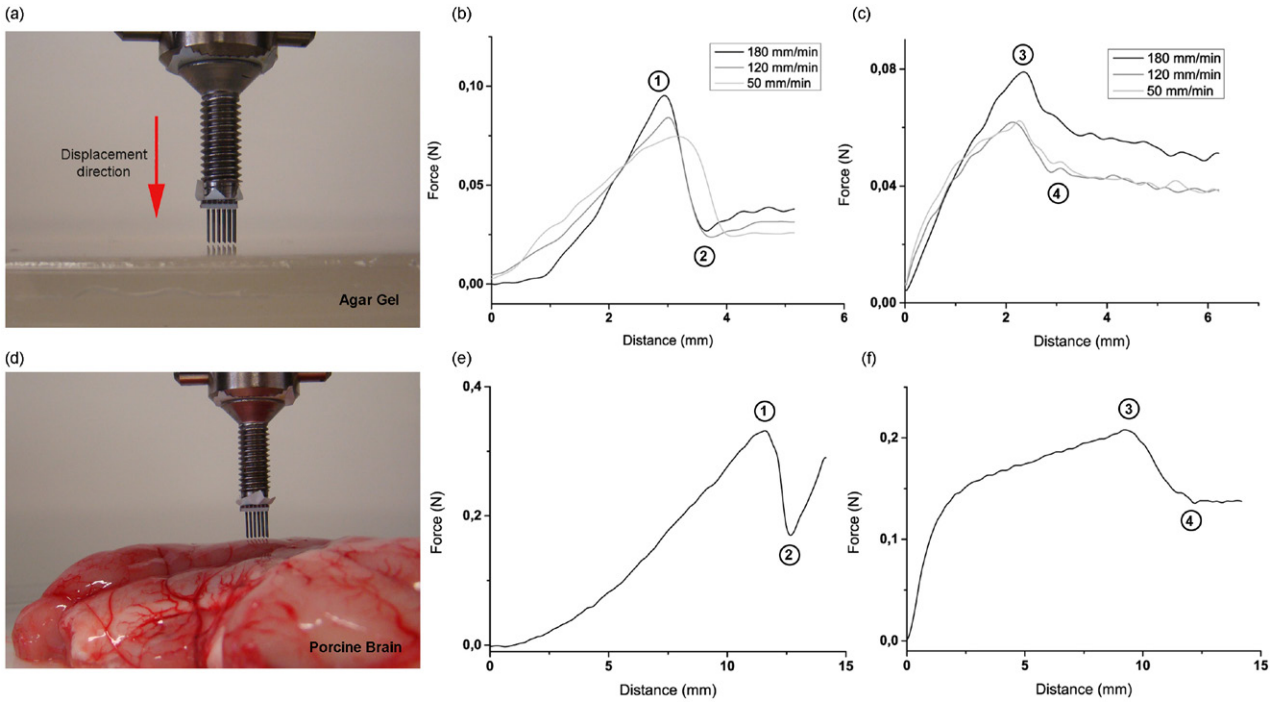

Figure 6. Experimental setup photo used in the mechanical tests on (*a*) 0.5% agar gel. Displacement versus force graphic for the (*b*) insertion and (*c*) removal tests on agar gel at different speeds. (*d*) Setup photo for the tests on the porcine cadaver brain. Displacement versus force graphic for the (*e*) insertion and (*f*) removal tests on the porcine brain at a velocity of 180 mm min^{-1}.

Wang *et al* [25] presented a self-assembled array probe based on silicon wet-etching micromachining to produce the array design and use heat treatment processes to achieve the final probe. Although it creates shafts 4 mm deep, this technology is limited to the number of shafts in the array (see table 1). Rakwal *et al* [24] introduced a fabrication process (μ-WEDM) capable of producing a 10 × 10 array with shaft lengths up to 9 mm. Although this sounds like a promising method, it is not standard industry technology. On the other hand, the fabrication process used in this paper employs standard micromachining technology. Moreover, the reported sharp tips have been realised through silicon etching processes [33, 34]. The proposed fabrication method avoids etching processes, producing the sharpened shaft tips with a set of dicing cuts using a V-shaped blade.

The final 3D probe also comprisees different shaft lengths: 4, 3.5 and 3 mm. This technology is compatible with different lengths and also a superior number of different shaft heights

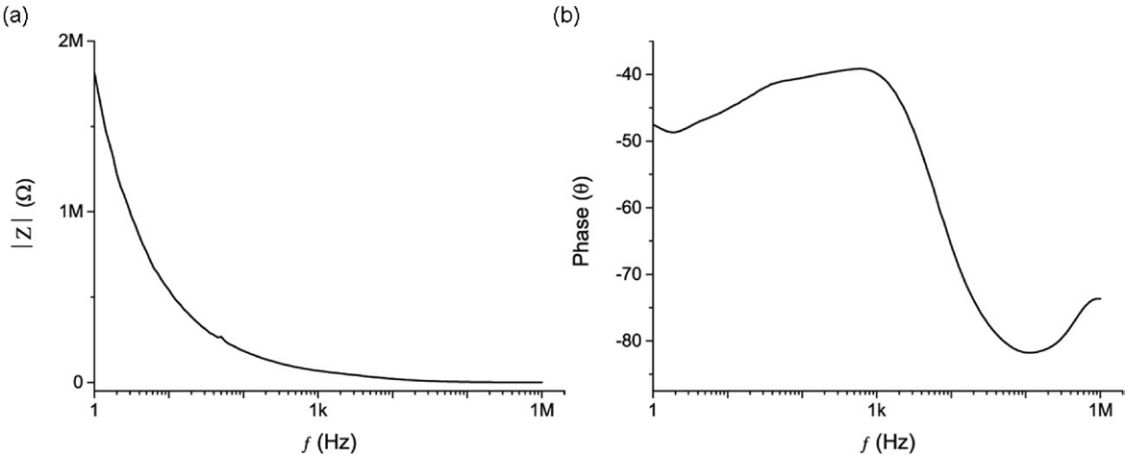

Figure 7. Bode plot of the EIS tests in saline solution: (*a*) magnitude; (*b*) phase angle.

Table 3. Statistical data of the implantation and withdrawal tests. The number of samples was 10 for each test. The presented values correspond to the average maximum force measured in each test.

Material	Speed (mm min^{-1})	Implantation force (mN)	Force per electrode (mN)	Withdraw force (mN)	Force per electrode (mN)
0.5% Agar Gel	50	87.04 ± 8.93	2.42	68.6 ± 7.58	1.91
	120	94.75 ± 31.37	2.63	68.57 ± 9.49	1.93
	180	95.45 ± 14.49	2.65	74.23 ± 8.25	2.06
Porcine brain	180	444.54 ± 90.37	12.5	250.53 ± 30.54	6.96

that may be changed depending on the desired application. Probes with different penetrating depths allow us to reach a wider spatial region and decrease the number of redundant electrodes, providing a more selective recording and stimulating of the neural tissue. For *in vivo* applications, the brain's opening required to implant the proposed MEA is defined by the backside end of the array, which is approximately 3.45 × 3.45 × mm^2. This are more favourable results compared to the reported compact array, with opening areas of 5.7 × 4 mm^2 [19] and 5 × 5 mm^2 [21].

The mechanical characterization shows a robust MEA. Results showed that the longer shafts withstand a longitudinal compressive load of approximately 68 N before the electrodes break and it requires a 1.8 N load before the array's base rupture. The electrodes are more fragile when an axial compression is applied, breaking with a 60 mN load. Nevertheless, the insertion force required to penetrate the brain reported in literature is of the order of several mN [28, 35, 36], which indicates that these MEA are strong enough to withstand the forces required at implantation time.

Many designs of long probes fail (crack or shatter) during implantation as they are unable to withstand the insertion axial forces, retraction forces and tension forces of the brain tissue [37]. Thus, the array's insertion and withdrawal forces have been quantified using a brain cortex phantom (0.5% agar gel) and a porcine cadaver brain. In both the agar gel and brain tissue, none of the tested samples showed any sign of shaft breakage during and after the mechanical tests.

In the agar tests different penetration and withdrawal speeds were applied. Although average load values seemed to increase along with the increased speed of the test, the large standard deviation values (especially at 120 mm min^{-1}) do not allow it to reach a correlation between the increased speed and load. However, low insertion speeds are expected to result in lower required loads, since they have the advantage of generating minimal vibration and mechanical shock to the tissue inserted while inserting electrodes, allowing the implantation surface to accommodate the probe more successfully [28, 35]. Also, as expected, higher loads are consistently required to pierce the arrays into the substrates than to withdraw them, since the only force involved in withdrawing tests are the drag forces between the electrodes and the surrounding material. However, by comparing agar and brain tissue results, we can conclude that the insertion and withdrawal results are highly dependent on the insertion material. This is because agar gel phantoms do not incorporate the heterogeneous composition of neural tissue, which will have considerable impact on the dynamics of insertion and tissue deformation. Brain tissue insertion tests performed at a lower speed (50 mm min^{-1} and 120 mm min^{-1}) showed significant tissue dimpling without implantation success. High speed insertion tests (180 mm min^{-1}) were successful, resulting in maximum forces with a magnitude six times higher than with agar to penetrate the electrodes. This difference in magnitude can be explained by the required force to pierce the brain's dura matter layer.

Jensen *et al* [35] demonstrated that the insertion forces increase with the number of shafts within the array. Thus, the results obtained are consistent with those reported in the order of several mN, higher in magnitude due to the increased number of shafts (36 electrodes). In both agar and brain tissue, the required insertion and withdrawal forces per electrode are

within this range. The results on the agar gel and the brain's maximum force per electrode are in the same of magnitude obtained by Das *et al* [32]. Other studies [28, 36] have been performed in order to measure the insertion forces in a rat's brain, obtaining lower magnitudes of force than those obtained in this paper. These results were achieved due to the fact that the dura matter were removed previous to the insertion test and only pia matter had to be penetrated at implantation time.

Overall, the proposed design and fabrication procedure is an eligible alternative for long 3D MEA technology that allows neural signal recording and stimulation. It also offers a contribution to future studies addressing the importance of additional insertion parameters for optimal device insertion.

Acknowledgments

ACP is supported by the Portuguese Foundation for Science and Technology (SFRH/BD/89509/2012). This work was also supported by FCT with the project reference FCOMP-01-0124-FEDER-010909 (FCT/PTDC/SAU-BEB/100392/2008).

References

[1] Perlmutter J and Mink J 2006 *Annu. Rev. Neurosci.* **29** 229–57
[2] Mogilner A, Benadib A and Rezai A 2001 *Thalamus Relat. Syst.* **1** 255–67
[3] Wilson B and Dorman M 2008 *Hearing Res.* **242** 3–21
[4] Yanai D, Weiland J, Mahadevappa M, Greenberg R, Fine I and Humayun M 2007 *Am. J. Ophthalmol.* **143** 820–7
[5] Collinger J, Wodlinger B, Downey J, Wang W, Tyler-Kabara E, Weber D, McMorland A, Velliste M, Boninger M and Schwartz A 2013 *Lancet* **381** 557–64
[6] Hochberg L, Serruya M, Friehs G, Mukand J, Saleh M, Caplan A, Branner A, Chen D, Penn R and Donoghue J 2006 *Nature* **442** 164–71
[7] Chang C and Chiou J 2010 *Sensors* **10** 4238–52
[8] Ruther P, Herwik S, Kisban S and Seidl K 2010 *IEEJ Trans. Electr. Electron. Eng.* **5** 505–15
[9] Normann R A 2007 *Nat. Rev. Neurol.* **3** 444–52
[10] Wise K 2005 *IEEE Eng. Med. Biol. Mag.* **24** 22–9
[11] Bhandari R, Negi S, Rieth L, Normann R and Solzbacher F 2009 *J. Micromech. Microeng.* **19** 035004
[12] Song Y *et al* 2005 *IEEE Trans. Neural Syst. Rehabil. Eng.* **13** 220–6
[13] Wark H *et al* 2013 *J. Neural Eng.* **10** 045003
[14] Hajj-Hassan M, Chodavarapu V and Musallam S 2009 *Micro Nano Lett.* **4** 53–8
[15] Kindlundh M, Norlin P and Hofmann U 2004 *Sensors Actuators* B **102** 51–8
[16] Seidl K, Herwik S, Torfs T, Neves H, Paul O and Ruther P 2011 *J. Microelectromech. Syst.* **20** 1439–48
[17] Bai Q, Wise K and Anderson D 2000 *IEEE Trans. Biomed. Eng.* **47** 281–9
[18] Bai Q and Wise K 2001 *IEEE Trans. Biomed. Eng.* **48** 911–20
[19] Yao Y, Gulari M, Wiler J and Wise K 2007 *J. Microelectromech. Syst.* **16** 977–88
[20] Du J, Roukes M and Masmanidis S 2009 *J. Micromech. Microeng.* **19** 075008
[21] Herwik S *et al* 2009 *J. Micromech. Microeng.* **19** 074008
[22] Perlin G and Wise K 2010 *J. Microelectromech. Syst.* **19** 1409–21
[23] Jones K, Campbell P and Normann R 1992 *Ann. Biomed. Eng.* **20** 423–37
[24] Rakwal D, Heamawatanachai S, Tathireddy P, Solzbacher F and Bamberg E 2009 *Microsyst. Technol.* **15** 789–97
[25] Wang M, Maleki T and Ziaie B 2010 *J. Micromech. Microeng.* **20** 035013
[26] Peixoto A, Goncalves S, Silva A, Dias N and Correia H 2013 *IEEE Sensors J.* **13** 3319–24
[27] Kjonigsen L, Leergaard T, Witter M and Bjaalie J 2011 *Front. Neuroinform.* **5** 2
[28] Paralikar K and Clement R 2008 *IEEE Trans. Biomed. Eng.* **55** 2258–67
[29] Boretius T, Jurzinsky T, Koehler C and Kerzenmacher S 2011 *Conf. Proc. IEEE Engineering in Medicine and Biology Society* pp 5404–7
[30] Henkel A G & Co. 2005 Loctite® M-31CL™ Technical Data Sheet Available: www.henkel.co.uk/2838_UKE_HTML.htm?nodeid=8797726048257
[31] Pomfret R, Miranpuri G and Sillay K 2013 *Ann. Neurosci.* **20** 118–22
[32] Das R, Ghandi D, Krishnan S, Saggere L and Rousche P 2007 *IEEE Trans. Biomed. Eng.* **54** 1089–96
[33] Wu J, Feng W, Tang W and Zeng F 2006 *Conf. Proc. IEEE Engineering in Medicine and Biology Society* pp 3166–9
[34] Bhandari R, Negi S, Rieth L, Normann R and Solzbacher F 2008 *Sensors Actuators* A **145–6** 123–30
[35] Jensen W, Yoshida K and Hofmann U 2006 *IEEE Trans. Biomed. Eng.* **53** 934–40
[36] Sharp A, Ortega A, Restrepo D, Curran-Everett D and Gall K 2009 *IEEE Trans. Biomed. Eng.* **56** 45–53
[37] Hajj-Hassan M, Chodavarapu V and Musallam S 2008 *Sensors* **8** 6704–26